Pulling apart mitotic spindle positioning in the *C. elegans* early embryo

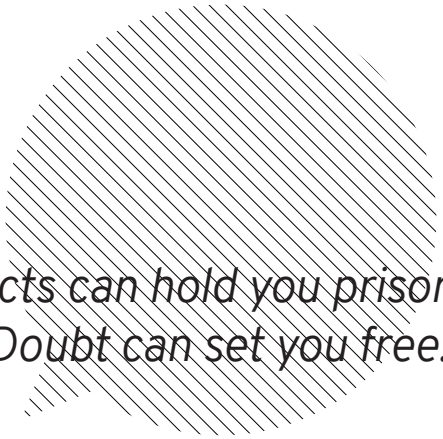

'Facts can hold you prisoner.
Doubt can set you free.'

Drian van der Woude in his winning essay for the Robbert Dijkgraaf essay award 2017

ISBN: 978-90-393-7022-3

Printed by: Gildeprint, Enschede
Layout and design: Buro Brouns
Cover image: Lars-Eric Fielmich

Copyright © 2018 by L. Fielmich. All rights reserved.

Pulling apart mitotic spindle positioning in the *C. elegans* early embryo

Mitotische spoel positionering ontleden in het vroege *C. elegans* embryo

(met een samenvatting in het Nederlands)

Proefschrift

ter verkrijging van de graad van doctor aan de Universiteit Utrecht
op gezag van de rector magnificus, prof.dr. H.R.B.M. Kummeling,
ingevolge het besluit van het college voor promoties in het openbaar te verdedigen
op woensdag 12 september 2018 des middags te 12.45 uur

door

Lars-Eric Fielmich

geboren op 19 januari 1987 te Nieuwegein, Nederland

Promotor: prof. dr. S.J.L. van den Heuvel

Table of Contents

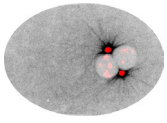

1

Introduction: Polarity control of spindle positioning in the *C. elegans* embryo

Lars-Eric Fielmich and Sander van den Heuvel

Developmental Biology, Department of Biology, Faculty of Sciences, Utrecht University, Padualaan 8, 3584 CH Utrecht, The Netherlands.

An adapted version of this manuscript was published as a review in *Cell Polarity: Role in Development and Disease in 2015*

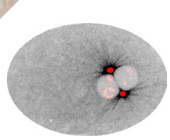

Abstract

Cell and tissue polarity guide a large variety of developmental processes, including the choice between symmetric and asymmetric cell division. Asymmetric divisions create cell diversity and are needed for maintenance of tissue specific stem cells. Symmetric divisions, on the other hand, promote exponential cell proliferation. Polarized cells can divide symmetrically, when cleavage takes place along the polarity axis. Alternatively, polarized cells can divide asymmetrically. To control this decision, developmental cues position the mitotic spindle, which instructs the plane of cell cleavage. In animal cells, positioning of the spindle depends on evolutionarily conserved interactions between a heterotrimeric G protein alpha subunit, TPR-GoLoco domain protein, and NuMA-related coiled-coil protein. This trimeric complex recruits the dynein microtubule motor and captures astral microtubules at the cortex. The interplay between dynein and depolymerizing microtubules generates cortical pulling forces that promote aster movement and spindle positioning. Through mechanisms that are poorly understood, cell polarity and other developmental signals control the microtubule-pulling forces to instruct the orientation and plane of cell division. In this chapter, we review the current understanding of the connection between cell polarity and spindle positioning, with a focus on studies of the early *C. elegans* embryo. The nematode *C. elegans* develops through highly reproducible symmetric and asymmetric cell divisions and has contributed significantly to the knowledge of cell polarity and spindle positioning in asymmetric cell division.

Spindle positioning and asymmetric cell division

When cells divide, chromosome segregation is followed by cleavage of the cytoplasm. The microtubule spindle apparatus instructs the cytokinetic furrow to form perpendicular to, and usually midway through, the central spindle. By positioning the spindle with respect to the polarity axis of the cell or tissue, daughter cells are formed at the proper place, with the right size and developmental fate. Hence, accurate spindle positioning is critical for tissue integrity, morphogenesis, and the balance between symmetric and asymmetric division of stem cells and tissue-specific progenitor cells. How cell polarity information is translated into proper spindle positioning has been a subject of intense study over the past fifteen years. Information from a variety of systems has resulted in a general model for spindle positioning in animal cells (For reviews: (Galli and van den Heuvel, 2008; Knoblich, 2010; Morin and Bellaïche, 2011). While some aspects are understood in considerable detail, cell-type dependent variations are still emerging, and many questions remain unanswered even for the best-studied systems.

The distinction is often made between intrinsic and extrinsic asymmetric division (Horvitz and Herskowitz, 1992) (Fig. 1). In intrinsic asymmetric division, anterior-posterior, apical-basal or planar polarity guides the asymmetric distribution of cell fate determinants in mitosis. By also aligning the mitotic spindle with this polarity axis, cytoplasmic cleavage segregates the localized components into a single daughter cell. Thus, intrinsic asymmetric division generates different daughter cells during the cell division process. As an alternative mode of asymmetric division, external signals may instruct a different fate in daughter cells that are initially identical after division. As an example, tissue-specific stem cells may depend on contact with a niche for maintenance of the uncommitted state. If the spindle orients perpendicular to the niche during cell division, a single daughter cell will remain associated with the niche as an uncommitted stem cell, while the other daughter cell loses this interaction and initiates a differentiation program (Fig. 1). Thus, spindle positioning is crucial for both intrinsic and extrinsic asymmetric division, to unequally partition determinants or properly position daughter cells, respectively.

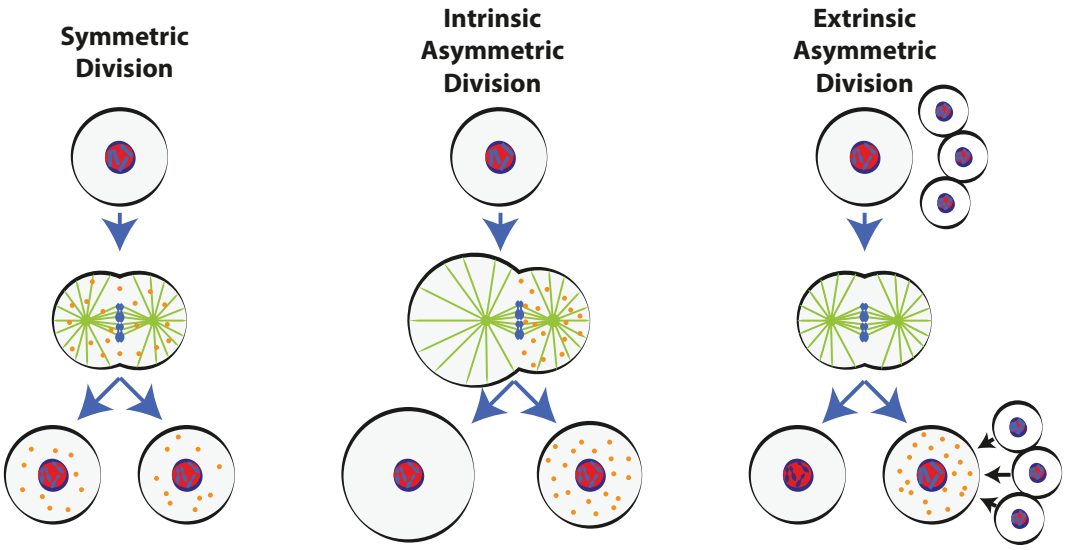

Figure 1 Symmetric and asymmetric cell division. The left panel illustrates a symmetric cell division in which cell fate determinants (orange) are distributed equally over the two daughter cells. In the middle panel, an intrinsic asymmetric cell division is depicted. The plane of cell cleavage and asymmetric localization of fate determinants in the mitotic mother cell ensure that cell division creates daughter cells with different cytoplasmic determinants and cell fates. Off center positioning of the spindle causes the division to be asymmetric in size as well. The final panel illustrates an extrinsic asymmetric division. The two daughter cells do not inherit different fate determinants during mitosis but receive different extrinsic signals that promote their distinct cell fates.

Spindle positioning has been best studied in the context of asymmetric cell division in invertebrate models. While this review focuses on the nematode *C. elegans*, other examples should be mentioned to illustrate the importance of this process. Excellent examples are the *Drosophila* central nervous system and larval brain, which are formed through repetitive rounds of intrinsic asymmetric division of neuroblasts (NBs). The embryonic NBs become specified within a polarized epithelium known as ventral neuroectoderm (Knoblich, 2010; Morin and Bellaïche, 2011). They delaminate from this epithelium and go through several rounds of asymmetric divisions in which the spindle aligns along the apical-basal polarity axis. Critical in spindle orientation is expression of the Inscuteable adaptor protein upon NB specification. Inscuteable forms a link between proteins that determine apical cell polarity and proteins that anchor astral microtubules, thereby ensuring apical-basal orientation of the spindle. The apical daughter cells are larger and retain self-renewing capacity, while the smaller basal cells (known as ganglion mother cells) undergo one symmetric division to form two neurons. Remarkably, the size asymmetry does not follow from asymmetric spindle positioning, but from asymmetry in spindle geometry during anaphase (Kaltschmidt et al., 2000). Consequently, the cell cleavage plane is placed towards the basal side. Cell cleavage in neuroblasts can also occur independently of the spindle, presumably induced by basally enriched acto-myosin (Cabernard et al., 2010).

Another well-studied model for asymmetric division are the *Drosophila* sensory organ precursor (SOP, also called pI) cells. SOP cells generate the mechanosensory organs of the peripheral nervous system of the fly. These organs consist of a sensory hair, connected to a socket cell and neuron, which is surrounded by a glial-like sheath cell (Knoblich, 2010; Morin and Bellaïche, 2011). To form these four different cells, SOP cells go through two rounds of intrinsic asymmetric cell division. These divisions are coordinated with the anterior-posterior (A-P) body axis of the fly to align the orientation of sensory bristles. Hereto, Frizzled (Fz)-dependent planar cell polarity (PCP) signaling aligns the spindle along the A-P body axis in mitotic SOP cells. During this divi-

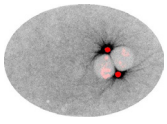

sion, the Notch-antagonist Numb localizes to the anterior cell cortex and becomes asymmetrically segregated to the anterior pIIb cell. This cell continues to divide to form a neuron and sheath cell, while division of the posterior pIIa cell creates the hair and socket cell of the sensory organ.

Stem cell divisions in the male and female *Drosophila* germline provide examples of niche-dependent asymmetric divisions. The mechanisms that control these divisions differ from the focus of this chapter and are therefore not discussed. Insight obtained in *C. elegans* studies has substantially contributed to the molecular understanding of asymmetric divisions in mammals, in particular those that occur during mammalian skin and brain development. Development of the mouse skin from a single to multilayered structure (stratification) coincides with a switch from symmetric to mostly asymmetric divisions around day 14 of embryogenesis (E14) (Lechler and Fuchs, 2005; Williams et al., 2011). The spindle orients in the plane of the epithelium during symmetric divisions. Asymmetric division involves rotation of the spindle to align with the apical-basal axis of cell polarity, and leads to formation of a differentiating daughter cell above the basal cell layer. The mammalian brain develops from neuroepithelial progenitor cells (Fietz and Huttner, 2011). These cells are connected by adherens junctions close to their apical surface. Cell cycle dependent apical-basal movements of the cell nuclei create a pseudostratified epithelium. When these cells enter mitosis, the nucleus is always at the apical side. Initially, the mitotic spindle orients within the plane of the epithelium and symmetric divisions expand the pool of progenitors. Similar to skin development, a switch to asymmetric division leads to neurogenesis, which peaks around day E14-E15 of mouse embryogenesis and coincides with subtle spindle rotations. Because the apical surface is narrow, even a subtle spindle rotation leads to the creation of a daughter cell that lacks apical surface and adherens junction attachment (Fietz and Huttner, 2011). This cell initiates neural differentiation either directly or after further division. In all these examples, apical polarity and spindle positioning use molecular mechanisms that have been discovered in substantial part through studies of the early *C. elegans* embryo.

Spindle positioning in the early *C. elegans* embryo

The nematode *C. elegans* develops through a highly reproducible pattern of asymmetric and symmetric divisions. Division of the *C. elegans* zygote has served as a particularly informative model for the concerted steps that are required for intrinsic asymmetric cell division: establishment of polarity, asymmetric localization of fate determinants and proper positioning of the spindle to instruct the plane of cell cleavage. The *C. elegans* oocyte is not polarized before fertilization. Sperm entry initiates a symmetry-breaking event, which defines the posterior end and leads to formation of the embryonic A-P axis. The anterior PAR protein complex consists of the PDZ-domain proteins PAR-3 and PAR-6 in association with atypical protein kinase C (PKC-3). This complex occupies the oocyte cortex at the time of fertilization (Fig. 2). Two posterior PAR proteins, the PAR-2 ring finger protein and PAR-1 MARK family Ser/Thr kinase, are present in the cytoplasm at that time, because PKC-3 phosphorylates PAR-2 and prevents its cortical local-ization. While this distribution is stable, fertilization-dependent processes disturb the equilibrium. A sperm-derived Rho-GAP, CYK-4, and cortical depletion of the Rho-GEF ECT-2 by maturated sperm-derived centrosomes disrupt the acto-myosin cytoskeleton and cause it to retract towards the opposite (anterior) pole. Coincident with this acto-myosin flow, anterior PAR proteins are removed from the posterior cortex. Moreover, microtubules nucleated at the mature centrosomes bind PAR-2 and protect it from PKC-3 phosphorylation. This allows PAR-2 to occupy the cortex and to recruit PAR-1 near the paternal pronucleus (Fig. 2). PAR-1 then phosphorylates PAR-3, which antagonizes posterior localization of the anterior PAR complex. The mutual antagonism between the anterior and posterior PAR proteins results in a new equilibrium with PAR-3–PAR-6–PKC-3 occupying the anterior half of the cortex, while PAR-2 and PAR-1 occupy the posterior half (Cowan and Hyman, 2007; Hoege and Hyman, 2013).

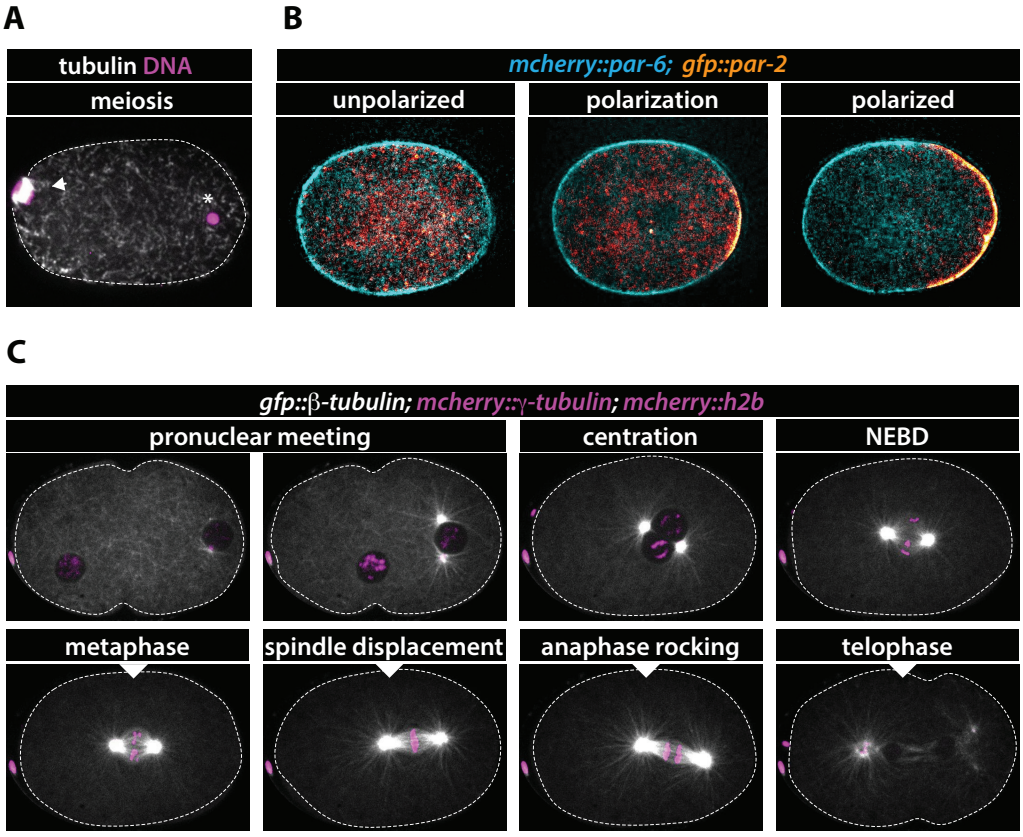

Figure 2 Establishment of polarity in the *C. elegans* zygote. **(A)** Immunohistochemical staining of wild type *C. elegans* embryo with antibodies recognizing tubulin, DNA is stained with DAPI. At the moment of fertilization by the male sperm (*), the oocyte is stalled in prophase of meiosis I (arrowhead) and PAR polarity proteins are distributed uniformly **(B first panel)**. **(B middle panel)** Sperm entry breaks symmetry and marks the future posterior pole of the embryo. Cortical actomyosin starts to retract anteriorly. Coincident with the actin flow, anterior PAR proteins are removed from the posterior cortex, allowing for cortical localization of posterior PAR proteins. **(B right panel)** Polarization is complete when an equilibrium between the opposing PAR-domains is reached. **(C)** The oocyte finishes meiosis I and II after sperm entry, resulting in two polar bodies and one maternal pronucleus. After the pronuclei have met in the posterior, the pronuclei-centrosomal complex centrates and rotates while assembling the mitotic spindle along the A-P PAR-polarity axis. At the embryonic midplane, the nuclear envelopes break down and chromosomes become aligned at the metaphase plate (inverted triangle). Higher posterior pulling forces acting on the spindle cause the spindle to displace posteriorly, positioning the cleavage plane off-center. This sequence of events, initiated by male sperm entry, results in a division that is unequal in size and contents.

Polarity establishment coincides with two consecutive highly asymmetric meiotic divisions. These divisions produce two small polar bodies, as the compact meiotic spindle segregates the chromosomes in close proximity to the cortex (Fig. 2). Subsequently, the haploid maternal pronucleus migrates to the posterior to meet the paternal pronucleus, followed by movement of the adjoined nuclei towards the center (centration). The pronuclei-centrosomal complex rotates during this anterior migration, coincident with spindle assembly along the A-P axis of the zygote (P0). Following nuclear envelope breakdown, the spindle aligns the chromosomes at the

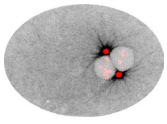

metaphase plate in the middle of the zygote. The spindle relocates slightly towards the posterior in metaphase and during elongation in anaphase. During this translocation, the posterior pole shows extensive lateral oscillations, named 'rocking', while the anterior pole remains relatively fixed. The off-center placement of the spindle results in an unequal first division that gives rise to a larger anterior blastomere (AB) and smaller posterior daughter (P1) (Fig. 2, 3). Coincidently, cytoplasmic determinants become unequally partitioned, creating intrinsic differences between the AB somatic blastomere and P1 germline precursor cell. All these asymmetries depend on A-P polarity. In embryos that lack PAR protein function, the spindle remains in the center of the zygote and cell cleavage is symmetric in size and fate. Inactivation of anterior PAR complex function results in rocking of both spindle poles and exaggerated spindle elongation (Kemphues et al., 1988). In contrast, inactivation of posterior PAR function causes both spindle poles to remain quite stationary, resembling the normal behavior of the anterior pole.

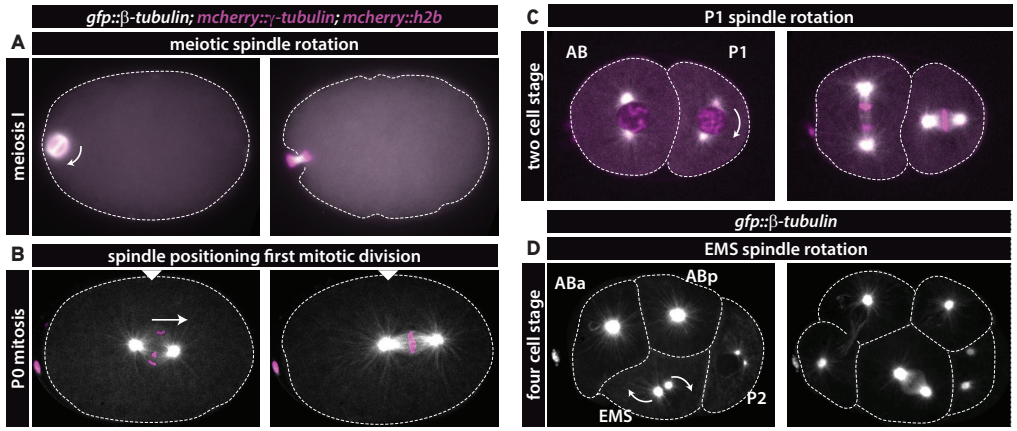

Figure 3 Asymmetric cell divisions in the *C. elegans* early embryo. **(A)** During meiosis, the oocyte divides highly asymmetrically because the meiotic spindle locates close to the cell cortex and rotates such that small polar bodies are formed, and a large zygote remains. **(B)** During the first mitotic division, pulling forces are asymmetric in P0, resulting in a larger AB and smaller P1 blastomere. **(C)** In P1, the spindle rotates and aligns with the A-P polarity axis as in P0. **(D)** In the four-cell embryo, ABa and ABp divide under a slight angle to generate left-right asymmetry. The EMS spindle rotates under influence of extrinsic signals emanating from the P2 cell. These rounds of asymmetric division are highly reproducible and regulated, making them a strong experimental model for studies of asymmetric cell division.

The P1 blastomere re-establishes opposing PAR-protein domains. The duplicated centrosomes migrate around the nucleus in AB and P1, to initiate a transverse spindle position (Fig. 3). In P1, however, the nucleus and associated centrosomes rotate by 90º, to align with the A-P polarity axis in prometaphase and promote asymmetric cell division (Fig. 3). This division generates another precursor of the germline (P2), which continues cell-autonomously controlled asymmetric division, just like its daughter germline precursor cell P3. In contrast, asymmetric division of EMS, a precursor of endoderm (intestine) and mesoderm, requires signaling from the neighboring P2 blastomere at the four-cell stage. This involves a Wnt/Fz pathway and parallel acting MES-1/SRC-1 tyrosine kinase signaling. These pathways coordinate spindle orientation along the long axis of the embryo with endoderm specification in the daughter cell that contacts P2 (Bei et al., 2002). Division of ABa and ABp, the other two blastomeres of the four-cell embryo, uses a small rotation of the spindle to divide left-right under a slight angle, to create repro-

ducible left-right asymmetry of the animal (Bergmann et al., 2003). The right daughter cell of this division, ABar, rotates its spindle again dependent on a Wnt-signal from the neighboring C blastomere. In summary, the position of the spindle and cleavage plane is highly regulated in *C. elegans* and critical in generating the proper cell lineages throughout development. While substantial insight has been obtained in the proteins that contribute to spindle positioning, the coordination with cell polarity is only partly understood.

The molecular components of cortical force generation

In animal cells, pulling forces that act between the cell cortex and astral microtubules position the spindle in mitosis. These forces are generated by depolymerization of the microtubule plus-ends, in association with dynein minus-end directed motor proteins. The dynein motor is recruited to the cortex by a trimeric protein complex that is conserved throughout the animal kingdom. In *C. elegans*, the complex contains a GOA-1 or GPA-16 heterotrimeric G-protein α-subunit, which functions as a cortical anchor. The TPR and 'G-Protein Regulator' motif proteins GPR-1/2 form a bridge between Gα at the membrane and the LIN-5 coiled-coil protein. LIN-5 interacts directly or indirectly with subunits of the cytoplasmic dynein complex (Fig. 4). Genetic studies place PAR polarity proteins upstream of Gα–GPR-1/2–LIN-5 in the control of spindle positioning. Multiple possible links between polarity regulators and the pulling force complex have been suggested, but a comprehensive picture of spatiotemporal control of spindle positioning has yet to emerge.

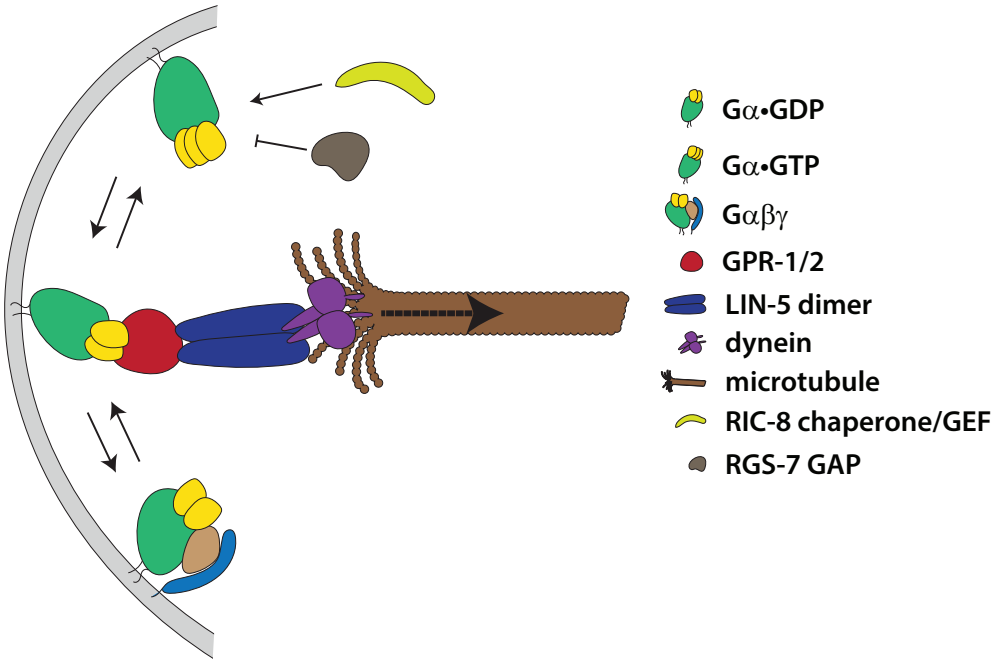

Figure 4 Model illustrating the generation of cortical pulling forces at microtubule plus ends. Dynein is tethered to the cortex by a trimeric complex of Gα·GDP-GPR-1/2-LIN-5. Cortical pulling forces are generated by microtubule de-polymerization and dynein minus-end directed motor activity. The GEF protein RIC-8 facilitates the GDP/GTP exchange on GOA-1 Gα and promotes GPA-16 Gα plasma membrane localization. The GAP RGS-7 catalyzes Gα GTPase activity.

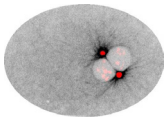

Non-canonical G-protein signaling

G-protein signaling has long been known as a major route to convey extracellular signals over the plasma membrane. In this pathway, ligand binding induces a transmembrane G-protein coupled receptor (GPCR) to act as a guanine nucleotide exchange factor (GEF). Exchange of GDP to GTP causes dissociation of the receptor-associated Gα·GDP–Gβγ complex, allowing Gα·GTP and Gβγ to activate downstream targets. Surprisingly, spindle positioning turned out to use a receptor-independent non-canonical G-protein pathway. The first support for heterotrimeric G protein contribution to spindle positioning came from the Plasterk group, who found that inactivation *of gpb-1*, one of two *C. elegans* Gβ genes, randomizes mitotic spindle orientation in early divisions, and thus perturbs the tightly regulated process of asymmetric cell division (Zwaal et al., 1996). Subsequently, Miller and Rand found that mutation of *goa-1* $G\alpha_o$ also affects the position and orientation of the mitotic spindle in early *C. elegans* embryos (Miller and Rand, 2000). While this phenotype is low penetrant, combining mutations and/or RNA-mediated interference (RNAi) of *goa-1* and *gpa-16* $G\alpha_{i/o}$ causes near complete absence of spindle positioning and results in symmetric division of the one-cell embryo (Gotta and Ahringer, 2001). Thus, the GOA-1 and GPA-16 Gα subunits (together referred to as Gα) act redundantly in spindle positioning. Finally, RNAi of one of two *C. elegans* Gγ-subunit genes, *gpc-2* (Gγ-2) was found to cause spindle defects com-parable to *gpb-1* RNAi (Gotta and Ahringer, 2001). At that time, a complete heterotrimeric G-protein, consisting of GOA-1/GPA-16 Gα, GPB-1 Gβ, and GPC-2 Gγ subunits, had been implicated in asymmetric cell division in *C. elegans*. There was no evidence, however, for contribution of a G-protein coupled receptor (GPCR), and transmembrane signaling appeared unlikely in a one-cell embryo.

Support for non-canonical G-protein signaling in asymmetric cell division came simultaneously from studies in *Drosophila*. Inscuteable was found to control asymmetric NB divisions in association with the Partner of Inscuteable (Pins) protein and a Gα subunit (Schaefer et al., 2000). In addition, $G\alpha_i$ and Pins, but not Inscuteable, were shown to determine the division orientation of SOP cells in *Drosophila* (Bellaïche et al., 2001; Schaefer et al., 2001). Thus, cell autonomous control of spindle positioning in the *C. elegans* zygote and *Drosophila* NB, and division orientation control by planar cell polarity all turned out to use a novel form of G protein signaling.

TPR-GPR domain proteins

Three groups simultaneously identified additional positive regulators of Gα in the control of asymmetric division of the *C. elegans* zygote (Colombo et al., 2003; Gotta et al., 2003; Srinivasan et al., 2003). The G-protein regulator (GPR) genes *gpr-1* and *gpr-2* were first observed to affect spindle positioning in a high-throughput RNAi screen of all Chromosome III encoded genes (F22B7.13, C38C10.4; (Colombo et al., 2003)). Independently, GPR-1 and GPR-2 proteins were co-immunopurified with the spindle positioning protein LIN-5 (Srinivasan et al., 2003). The *gpr-1* and *gpr-2* coding sequences share 96% nucleotide identity; hence RNAi for one inhibits the other gene simultaneously. The predicted proteins are 97% identical and are commonly referred to together as GPR-1/2 or simply GPR. Importantly, GPR-1/2 are related to *Drosophila* Pins and part of a protein family that includes the closely related mammalian LGN (Leu-Gly-Asn repeat enriched protein) and AGS3 (activator of G-protein signaling), as well as *C. elegans* AGS-3. These proteins all contain multiple N-terminal Tetratricopeptide (TPR) protein interaction motifs and at least one C terminal GoLoco/GPR domain (Colombo et al., 2003; Gotta et al., 2003; Srinivasan et al., 2003).

The GPR/GoLoco domain interacts with $G\alpha_{i/o}$·GDP, inhibits GDP release and competes with Gβγ association. Crystal structure studies showed that Gβγ and the GPR/GoLoco motif interact with Gα·GDP through overlapping binding sites (Kimple et al., 2002). Hence, spindle positioning was initially thought to depend on Gβγ release (Gotta et al., 2003; Schaefer et al., 2001).

In *C. elegans*, RNAi of *gpr-1/2* closely mimics *goa-1/gpa-16* RNAi, which indicates that GPR-1/2 act positively with Gα. In contrast, *gpb-1* Gβ and *gpc-2* Gγ RNAi do not resemble *gpr-1/2* RNAi or alter the *goa-1/gpa-16* RNAi phenotype. Such observations demonstrated that, rather than Gβγ, interaction between Gα·GDP and GPR-1/2 is required for spindle positioning in asymmetric cell division (Colombo et al., 2003; Gotta et al., 2003; Srinivasan et al., 2003). This confirmed alternative use of G-protein signaling in spindle positioning, as Gα·GDP instead of Gα·GTP is the active form. Gα·GDP interacts with a GPR^{Pins} family member, which in turn uses the TPR motifs, and possibly a linker between the TPR and GPR/GoLoco domains, to recruit additional spindle positioning proteins to the membrane.

LIN-5$^{Mud/NuMA}$

Another important component of the cortical pulling complex in *C. elegans* is the LIN-5 protein, which is the functional equivalent of mammalian NuMA (Nuclear Mitotic Apparatus), and *Drosophila* Mud (Mushroom body defect). The *lin-5* gene was defined by 'lineage-abnormal' mutations (Albertson, 1978). Homozygous *lin-5* mutants are sterile, but when derived from heterozygous parents complete normal embryonic development. Postembryonic cell divisions fail in mitosis in these mutants; chromosomes may not fully align at the metaphase plate, anaphase and cytokinesis do not occur, yet cells exit from mitosis at the normal time and enter the next round of DNA synthesis, centrosome duplication and mitotic entry (Albertson, 1978; Lorson et al., 2000; Sulston and Horvitz, 1981). Dependent on the lineage, postembryonic blast cells in *lin-5* mutants continue abortive mitoses and become highly polyploid. Embryonic development in these mutants is driven by maternal product, as knock down of *lin-5* by RNAi and temperature shift of *lin-5(ev571*ts*)* mutants cause complete embryonic lethality (Lorson et al., 2000).

The extended central domain of the LIN-5 protein is predicted to form an α-helical coiled-coil structure (Lorson et al., 2000). While the amino-acid sequence provided little functional information, immunopurification followed by mass spectrometry revealed that LIN-5 and GPR-1/2 form part of a protein complex (Srinivasan et al., 2003). The strong overlap in phenotype also support joint functions: *gpr-1/2* and *lin-5* RNAi each cause reduced spindle elongation, lack of posterior movement of the spindle in anaphase and failure to undergo normal asymmetric division of the zygote (Gotta et al., 2003; Srinivasan et al., 2003). The characteristic oscillations and flattening of the posterior spindle pole that normally occur during spindle migration are also absent after *gpr-1/2* and *lin-5* knock down, and the spindle does not rotate in the P1 blastomere. Chromosome segregation and cytokinesis continue for two or three rounds of cell division, giving rise to dead embryos with a few highly polyploid nuclei. The physical association between LIN-5 and GPR-1/2, as well as interaction between GPR-1/2 and Gα, and the strong resemblance in *lin-5*, *gpr-1/2* and *goa-1/gpa-16* RNAi phenotypes all supported a model in which the encoded proteins act together to control the mitotic spindle position. In addition, *lin-5* is also required for meiotic spindle rotation, independently of *gpr-1/2* and *goa-1/gpa-16* Gα (Lorson et al., 2000; van der Voet et al., 2009).

The trimeric Gα–GPR–LIN-5 complex recruits dynein to the cortex

The subcellular localizations of LIN-5 and GPR-1/2 show strong overlap and mutual dependence. The proteins are present at the spindle poles, in the cytoplasm, at the cell cortex, and, specifically in metaphase, at kinetochore microtubules. GPR-1/2 fails to localize in the absence of LIN-5, and LIN-5 loses its cortical localization when GPR-1/2 or Gα are gone (Lorson et al., 2000; Srinivasan et al., 2003; van der Voet et al., 2009). The combined data support that $G\alpha_{i/o}$·GDP, GPR-1/2 and LIN-5 form a trimeric complex needed for spindle positioning in *C. elegans* (Fig. 4). Similarly, *Drosophila* Pins associates with $G\alpha_i$ and the $LIN\text{-}5^{NuMA}$-related protein Mud in NBs and

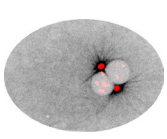

epithelial cells (Bowman et al., 2006; Izumi et al., 2004; Siller and Doe, 2009). Moreover, mammalian LGN recruits the NuMA protein to the cell cortex and simultaneously interacts with $G\alpha_i$ (Du and Macara, 2004). Each of these complexes is critical for spindle positioning and orienting cell division, in mammals in particular in the developing skin and brain (Lechler and Fuchs, 2005; Williams et al., 2011). Thus, an evolutionarily conserved mechanism appears to control positioning of the cell division plane in all animals.

Observations in the one-cell *C. elegans* embryo provided additional functional insights. It was found that the Gα–GPR–LIN-5 complex is needed for the generation of pulling forces that act from the cortex at astral microtubules. Such external forces can be made visible by means of spindle midzone severing with a UV-laser (Grill et al., 2001). Following spindle severing, the spindle poles move outward with increased speed towards the cell periphery. Importantly, the posterior pole moves with a higher velocity and over a larger distance than the anterior pole. This indicates asymmetry in pulling forces, which depends on A-P polarity; *par-2* mutant embryos are 'anteriorized' and show anterior and posterior pole movements with the same low peak velocity as the wild type anterior pole. Vice versa, *par-3* mutant embryos are 'posteriorized' with both sides showing high pulling forces (Grill et al., 2001). Knockdown of *Gα*, *gpr-1/2* or *lin-5* largely eliminates these pulling forces (Nguyen-Ngoc et al., 2007; van der Voet et al., 2009), while specific loss of LIN-5 from spindle poles has no effect (van der Voet et al., 2009). Thus, cortical localization of LIN-5, through Gα–GPR-1/2 interaction, is needed for the pulling forces that position the spindle in mitosis.

Gα–GPR–LIN-5 contribute to cortical pulling forces through recruitment of a dynein motor complex to the cell periphery (Couwenbergs et al., 2004; Nguyen-Ngoc et al., 2007). Dynein anchored by Gα–GPR–LIN-5 attaches microtubule plus ends to the cell cortex, while depolymerization of the microtubule ends is thought to be largely responsible for force generation (Kozlowski et al., 2007; Laan et al., 2012; Nguyen-Ngoc et al., 2007). Myristoylation of the Gα subunit allows membrane attachment of the complex, and, based on analysis of human NuMA, the N-terminal part of LIN-5^{NuMA} mediates dynein interaction (Kotak et al., 2012). While these molecular interactions are conserved in the animal kingdom, variations are used in development. In meiosis of the *C. elegans* female pronucleus, LIN-5 and dynein are needed to rotate the meiotic spindle in order to expel the polar bodies. Instead of Gα–GPR-1/2, a complex of ASPM-1 (Abnormal Spindle-like, Microcephaly associated) and Calmodulin anchors LIN-5 and dynein at the spindle poles to mediate this rotation (van der Voet et al., 2009). In planar cell polarity, the Frizzled receptor and Dishevelled effector orient the spindle and division plane. Dishevelled interacts with Mud in *Drosophila* SOP cells, and with NuMA during zebrafish gastrulation to engage the dynein motor complex in this process (Morin and Bellaïche, 2011). Thus, the LIN-$5^{Mud/NuMA}$ coiled-coil protein acts as a general dynein adaptor in spindle positioning. This adaptor also functions as an important target of spatiotemporal regulation of spindle pulling forces.

Regulation of Cortical Force Generation in the *C. elegans* one-cell embryo

The asymmetric localization of PAR proteins in the *C. elegans* embryo causes the spindle to migrate off center in mitosis. As compared to *Drosophila* NBs and SOP cells, the distribution of cortical pulling force proteins is more dynamic and less asymmetric in the *C. elegans* zygote, and a combination of several factors may determine the plane of cell cleavage. Below, we review the mechanisms that have been proposed to contribute to asymmetric pulling forces in the one-cell *C. elegans* embryo.

Gα Regulators

During delamination of the *Drosophila* NB, polarity of the neuroepithelium is maintained and apically localized PAR3–PAR6–aPKC recruits Inscuteable to the apical side of the cell. Pins and $G\alpha_i$ accumulate at the same side, presumably recruited by Inscuteable, thus cell polarity corresponds directly to asymmetry in cortical force generators. By contrast, the GOA-1 and GPA-16 $G\alpha_{i/o}$ subunits show uniform localization at the cortex of the *C. elegans* zygote (Colombo et al., 2003; Gotta et al., 2003; Srinivasan et al., 2003). Nevertheless, regulation of the active versus inactive state of the heterotrimeric G protein could create asymmetry in pulling forces. The activity of G proteins depends on the associated guanosine nucleotide, GTP or GDP. As for canonical G protein signaling, GEF and GAP proteins have been identified that affect GOA-1 and GPA-16 $G\alpha_{i/o}$ activity in spindle positioning. However, GPR-1/2 associates specifically with $G\alpha_{i/o}$·GDP, behaves as a GDP-dissociation inhibitor (GDI) and competes with Gβγ in Gα·GDP binding. While regulation of the GTP binding and hydrolysis cycle is clearly critical in pulling force generation, it remains puzzling if and how this level of Gα regulation contributes to the spatiotemporal control of spindle positioning.

The Gα GTPase cycle is essential for pulling force generation

An important regulator of Gα in spindle positioning is the 'resistant to inhibitors of cholinesterase 8' (RIC-8) protein. The *ric-8* gene was identified in a genetic screen for factors that mediate neurotransmitter release, a process regulated by heterotrimeric G protein signaling (Miller et al., 1996). Remarkably, *ric-8* and *goa-1* showed closely related functions during spindle positioning in the early embryo (Miller et al., 2000). Insight in the molecular function of RIC-8 came from studies that identified mammalian RIC-8A and RIC-8B as binding partners of $G\alpha_{i/o/q}$ (Tall et al., 2003). Further analysis revealed that RIC-8A exhibits potent GEF activity and associates with the Gα·GDP monomer and nucleotide free transition state, but not with Gα·GTP or the trimeric Gα·GDP–Gβγ complex. RIC-8 interacts with GOA-1 as well as GPA-16 Gα in *C. elegans* and is a GEF for GOA-1 *in vitro*. The RIC-8 protein is present uniformly in the cytoplasm and weakly at the cortex. Strong inactivation of *ric-8*, by combined mutation and RNAi, causes loss of pulling forces in the early *C. elegans* embryo and resembles *goa-1/gpa-16* double RNAi or knockdown of other components of the LIN-5 complex (Afshar et al., 2004). Thus, RIC-8 acts as a general positive regulator of Gα-mediated spindle positioning.

It appears paradoxical that the RIC-8 GEF and GPR-1/2 GDI proteins display opposite biochemical activity while both promote spindle-pulling forces. GEF requirement may indicate that the Gα subunit needs to go through the GTP binding-hydrolysis cycle in this process. Mammalian RIC-8A does not activate Gα·GDP–Gβγ trimers, but catalyzes nucleotide exchange of free Gα·GDP and Gα·GDP in complex with a GoLoco/GPR motif protein and NuMA (Tall and Gilman, 2005). Thereby, RIC-8 triggers the dissociation of the Gα·GDP–LGN–NuMA complex. Thus, force generation may involve dissociation of the pulling force complex or generation of Gα·GTP. A different model came from observations in NBs and SOP cells in *Drosophila*, and of *RIC-8A* and *RIC-8B* knock out mouse ES cells (David et al., 2005; Gabay et al., 2011; Hampoelz et al., 2005; Wang et al., 2005). These studies showed that RIC-8 is needed for plasma membrane association of newly synthesized Gα subunits. Acting as a molecular chaperone, RIC-8 might use the nucleotide switch to dissociate from the properly folded and ER membrane associated Gα·GTP molecule. *C. elegans* GOA-1 and GPA-16 show differential interactions with RIC-8. RIC-8 acts as a GEF for GOA-1 but not GPA-16, and RIC-8 controls the cortical localization and protein level of GPA-16, but not GOA-1 (Afshar et al., 2004, 2005). As *ric-8* RNAi resembles the *goa-1/gpa-16* double knockdown phenotype, both chaperone and GEF activities of RIC-8 may contribute to pulling force generation.

Contribution of a GTP-binding/hydrolysis cycle in non-canonical G-protein signaling is further supported by involvement of a possible Gα GAP (GTPase Activating Protein). Examining all *C. elegans* proteins with 'regulator of G-protein Signaling' (RGS) GTPase activation domains, RGS-7 was rec-

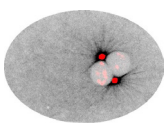

ognized for its essential function in embryonic development (Hess et al., 2004). One-cell embryos lacking *rgs-7* function showed increased movement and rocking of the posterior spindle pole and exaggerated asymmetric division. Severing of the spindle midzone with a UV-laser beam demonstrated that the increased posterior displacement of the spindle results from decreased anterior pulling forces in *rgs-7* mutant embryos. RGS-7 is present at the cortex, though only detectable from the two-cell stage onward (Hess et al., 2004). It remains unknown why loss of an apparently uniformly distributed RGS-7 protein reduces only anterior pulling forces. However, genetic and biochemical experiments strongly support that RGS-7 acts as a GAP for GOA-1.

The Gβγ dimer is also an important negative regulator of pulling force generation, as it competes with GPR-1/2 for Gα·GDP. As mentioned above, RNAi of *gpb-1* and *gpc-2* cause abnormal centrosome movements and spindle orientation. Based on combined RNAi with *Gα*, this phenotype results from hyperactive Gα that is no longer sequestered by Gβγ, and not from loss of Gβγ-specific effector signaling (Tsou et al., 2003). Spindle severing experiments showed that *gpb-1* RNAi increases spindle pulling forces in the anterior (Afshar et al., 2004, 2005). Thus, asymmetry in Gβγ could contribute to asymmetry in pulling forces and posterior displacement of the spindle in mitosis. A recent study showed dynamic regulation of cortical GPB-1 levels and trafficking through both early endosomes and recycling endosomes (Thyagarajan et al., 2011). In metaphase of the zygote, trafficking rates are higher in the anterior than the posterior and more GPB-1 remains present in endosomal vesicles in the posterior (Fig. 5). Thus, a larger fraction of the uniformly distributed Gα protein may be available for GPR-1/2 association in the posterior. This provides a potential mechanism for spatiotemporal regulation of spindle positioning.

GPR-1/2 Regulators

Since the discovery of the GPR-1/2 proteins, asymmetry in their localization has been proposed to be responsible for asymmetric pulling forces (Colombo et al., 2003; Gotta et al., 2003). However, our group did not detect statistically relevant posterior enrichment of GPR-1/2 (or LIN-5) in metaphase, while spindle pulling forces are clearly higher in the posterior at that stage (Berends et al., 2013; Galli et al., 2011a; Srinivasan et al., 2003). The localization of GPR-1/2 is quite dynamic and likely subjected to regulatory mechanisms. GPR-1/2 and LIN-5 become anteriorly enriched during polarity establishment and prophase of the first mitotic division, which contributes to pronuclear centration (Park and Rose, 2008; Tsou et al., 2003). Subsequently, GPR-1/2 and LIN-5 redistribute to become higher at the posterior cortex in mitosis. This enrichment is limited but detectable in anaphase, however, it may either follow or cause asymmetry in pulling forces (Berends et al., 2013; Colombo et al., 2003; Gotta et al., 2003; Srinivasan et al., 2003). Moreover, asymmetry in cortical dynein localization has not been detected during any phase of *C. elegans* zygotic division (Kotak et al., 2012; Nguyen-Ngoc et al., 2007). Thus, the question if asymmetric distribution of the pulling force complex is responsible for asymmetric spindle positioning has not been conclusively answered.

Localization of GPR-1/2 requires not only Gα but also LIN-5 (Gotta et al., 2003; Srinivasan et al., 2003). A mechanism proposed for mammalian LGN may explain this dual dependence (Du and Macara, 2004). The N-terminal TPR domains of LGN and C-terminal GoLoco/GPR motifs engage in intramolecular interactions that cause a closed protein conformation. Binding of either $G\alpha_i$ or NuMA abolishes this intramolecular interaction and allows for simultaneous binding of the other partner (Du and Macara, 2004). Structural studies indicate that the LGN GoLoco domains interact in tandem with the LGN TPR repeats (Pan et al., 2013). Given that GPR-1/2 has only few confirmed TPR and GoLoco/GPR motifs, it is unclear whether the conformational switch model proposed for LGN should apply to GPR-1/2 as well. The dependence on both Gα and LIN-5 supports that GPR-1/2 uses a related mechanism for its cortical localization.

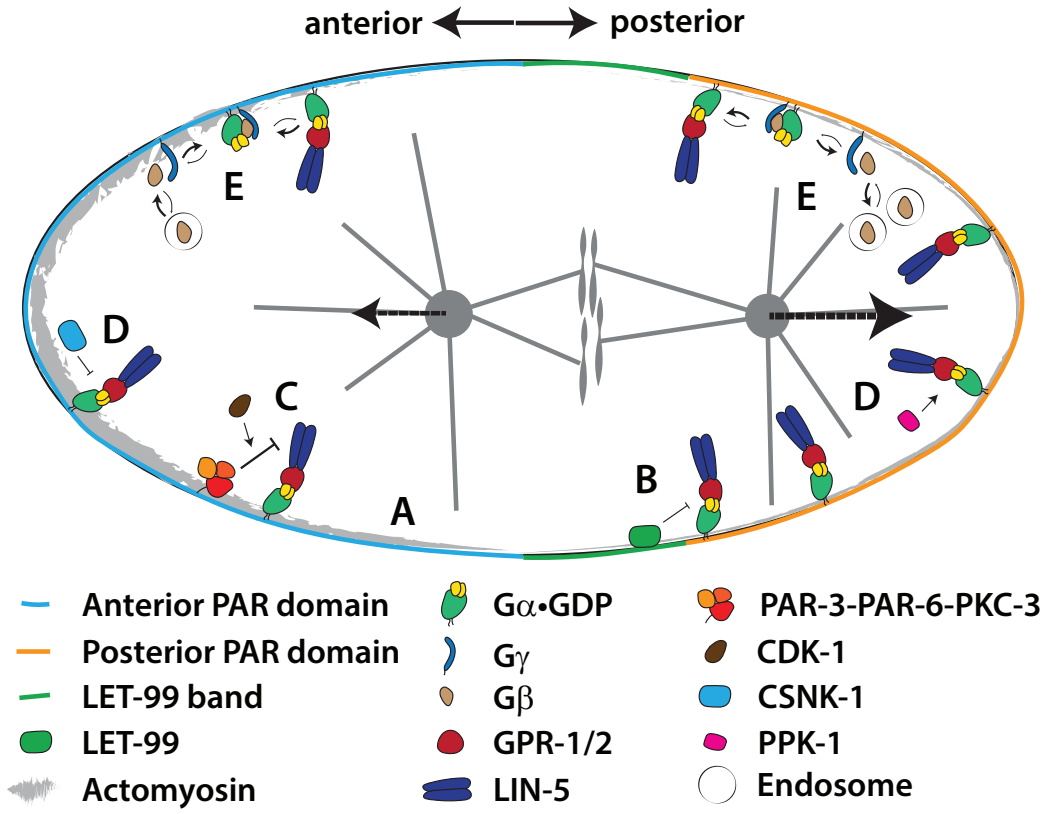

Figure 5 Model illustrating the mechanisms discussed in the text that contribute to asymmetric spindle pulling forces in the *C. elegans* zygote. **(A)** The cortex of the *C. elegans* zygote P0 is divided in an anterior and posterior PAR polarity domain. During polarization, actomyosin contracts and accumulates in the anterior half of the cell. The resulting stiffer anterior cortex reduces pulling force generation. **(B)** A posterior lateral band LET-99 antagonizes GPR-1/2-LIN-5 localization and generates a third cortical puling force domain. **(C)** PKC-3 phosphorylates LIN-5 directly and thereby negatively regulates anterior cortical pulling forces. This phosphorylation is possibly primed by CDK-1 phosphorylation. **(D)** Anterior CSNK-1 reduces force generation and restricts the PIP2 generating kinase PPK-1, a positive regulator of cortical pulling forces, posteriorly. **(E)** GPR-1/2 competes with Gβ for Gα. Gβ traffics continuously through recycling endosomes. The Gβ trafficking rates are asymmetric, resulting in higher anterior and lower posterior cortical Gβ levels to compete with GPR-1/2 for Gα.

An additional regulatory protein might induce asymmetry in GPR-1/2 function. LET-99 is a DEP (Dishevelled/EGL-10/Pleckstrin) domain protein that antagonizes cortical localization of Gα–GPR-1/2 (Bringmann et al., 2007; Park and Rose, 2008; Tsou et al., 2003). The *let-99* mutant phenotype resembles aspects of the *gpb-1* RNAi phenotype and indicates negative regulation of cortical Gα–GPR-1/2. Both anterior and posterior PAR proteins inhibit LET-99 at the cortex, which restricts LET-99 localization to a cortical band at about 60% of the long axis of the one-cell embryo. Identification of the LET-99 band has resulted in a cortical force model with three instead of two (anterior and posterior) domains. Negative regulation of force generation in the posterior LET-99 band (possibly in combination with asymmetric distribution of cortical

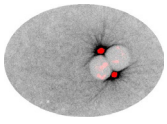

GPR-1/2) results in net anterior pulling forces during pronuclear centration, and net posterior pulling forces from metaphase onwards (Fig. 5) (Couwenbergs et al., 2004; Krueger et al., 2010; Tsou et al., 2003). This indicates the possibility that not anterior-posterior GPR-1/2 asymmetry per se, but rather reduced pulling on astral microtubules that reach the LET-99 lateral band, is responsible for a net increase in posterior pulling forces and spindle displacement in mitosis.

An RNAi screen for defects in pronuclear and spindle movements identified Casein Kinase-1 (CSNK-1) as a pulling force regulator (Panbianco et al., 2008). CSNK-1 is membrane associated and enriched in the anterior of the *C. elegans* zygote in a PAR-dependent manner. CSNK-1 negatively regulates the localization of GPR-1/2–LIN-5, possibly indirectly by confining the PIP2-generating PIP2 Kinase PPK-1 to the posterior. PPK-1 or PIP2 may positively regulate the localization of GPR-1/2–LIN-5 (Fig. 5), although neither GPR-1/2 nor LIN-5 has a known PIP2 binding domain (Panbianco et al., 2008). The protein phosphatase PPH-6 and its associated subunit Sit4p-Associated Protein-1 (SAP-1) also promote GPR-1/2 localization and spindle pulling forces in anaphase (Afshar et al., 2010). Co-depletion of CSNK-1 and PPH-6 resembles the PPH-6/SAPS-1 depleted phenotype of decreased cortical GPR-1/2 localization and spindle forces. Thus, CSNK-1 may act on PPH-6 to inhibit GPR-1/2–LIN-5 localization in the anterior. While the exact molecular mechanisms remain unclear, both kinases and phosphatases contribute to regulation of GPR-1/2 localization.

LIN-5 Regulators

Because Gα–GPR–LIN-5 form a trimeric complex, the regulation of Gα and GPR-1/2 levels described above also applies to cortical localization of LIN-5. In addition, LIN-5 is also subjected to specific controls. Immunopurification followed by mass spectrometry showed extensively phosphorylation of LIN-5 at 25 different residues (Galli et al., 2011a). Stable isotope labeling combined with kinase knock down and quantitative phosphopeptide analysis revealed that four LIN-5 serine residues are phosphorylated directly by the atypical Protein Kinase C 3 (PKC-3), in a cyclin-dependent kinase 1 (CDK-1) dependent manner (Fig. 5). PKC-3 is part of the anterior PAR complex, while CDK-1 is a key positive regulator of mitotic entry, thus establishing a direct connection between the LIN-5 complex, PAR polarity and cell-cycle progression. Phosphorylation of LIN-5 by PKC-3 occurs in the anterior, peaks in metaphase and then disappears rapidly (Galli et al., 2011a). Spindle midzone severing experiments in combination with non-phosphorylatable and phosphorylation-mimicking LIN-5 mutations demonstrated that the PKC-3 specific phosphorylation of LIN-5 inhibits pulling forces. This spatiotemporal regulation coincides with the switch from anterior directed movement of the pronuclei-centrosomal complex during centration to posterior migration of the spindle in metaphase/anaphase.

To promote symmetric cell division, apically localized aPKC antagonizes spindle pulling forces in polarized *Drosophila* and mammalian epithelial cells (Guilgur et al., 2012; Hao et al., 2010). Maldin-Darby canine kidney (MDCK) cells in 3D culture form organized cysts with a single luminal epithelial layer. To instruct a planar spindle position, aPKC phosphorylates LGN^{Pins}, which creates a 14-3-3 protein binding site and prevents association with $G\alpha_i$ (Hao et al., 2010). Thus, phosphorylation of pulling force complex components by aPKC provides a direct way to coordinate the cell division plane with cell polarity in worms, flies and mammals. Similarly, mitotic kinases are likely to couple cell cycle progression and pulling force generation through phosphorylation of $LIN\text{-}5^{NuMA}$ or GPR^{LGN}. The LIN-5 phosphorylation by PKC-3, described above, depends indirectly on CDK-1 (Galli et al., 2011a). CDK-1 phosphorylation possibly activates PKC-3 or might prime LIN-5 for subsequent phosphorylation by PKC-3. Direct phosphorylation of NuMA by CDK-1 has been implicated in dynein localization in mammalian cells grown in culture (Kiyomitsu and Cheeseman, 2013; Kotak et al., 2013). NuMA phosphorylation by CDK-1 during metaphase negatively affects cortical dynein levels and is antagonized by the continuously active protein phosphatase

PPP2CA. This mechanism explains an observed increase in cortical dynein levels from metaphase to anaphase, following inactivation of CDK-1. Additional phosphorylations by cell-cycle and polarity kinases will probably contribute to spatiotemporal control of cortical pulling forces.

Dynein

Recruitment of cytoplasmic dynein appears the most important function of the LIN-5 complex. Dynein acts in association with various regulator and adaptor proteins, including the multiple subunit dynactin complex (Raaijmakers et al., 2013). Components of cytoplasmic dynein as well as dynactin are conserved between *C. elegans* and mammals and include potential adaptors for LIN-5 association as well as other regulators of localization and activity (O'Rourke et al., 2007; Raaijmakers et al., 2013). For example, the dynein adaptor Lissencephaly 1 (LIS-1) is required for cortical pulling forces (Nguyen-Ngoc et al., 2007). *In vitro* studies have shown that LIS-1 promotes dynein's continued association with microtubules (Huang et al., 2012). Continued attachment to depolymerizing microtubule ends is likely needed for pulling force generation.

Dynein acting independently of the LIN-5 pulling force complex has been proposed to contribute to centration movements (Kimura and Kimura, 2011). The dynein light chain protein Dynein Roadblock (DYRB-1) anchors organelles for transport along microtubules. Because of the resistance of the viscous cytoplasm this generates a dragging force at centrosomes. This mechanism may contribute to centration because microtubules extending towards the anterior are longer and the majority of organelles are anterior of the maternal and paternal pronucleus at the time of meeting (Kimura and Kimura, 2011). Another mechanism proposed to contribute to centration of the pronuclei-centrosomal complex is sliding of microtubules along the cortex, when microtubules are not attached end-on but laterally by a cortical LIN-5-dynein complex (Gusnowski and Srayko, 2011). Lateral sliding is more prominent during centration than during anaphase, and also more evident in the anterior than the posterior part of the embryo. It is unclear whether this sliding is actively regulated or a consequence of the geometry of the spindle and angle under which microtubules reach the cortex. Pushing forces of microtubules that buckle up against the cortex without being captured by dynein may further promote centration of the pronuclei-centrosomal complex (Laan et al., 2012).

Microtubule Dynamics

The generation of cortical pulling forces depends strongly on the dynamic instability of microtubules. This is supported by the finding that pulling force generation is lost after administration of microtubule stabilizing drugs (Nguyen-Ngoc et al., 2007). Microtubule plus tips grow with an estimated speed of ~0,5 µm/s and de-polymerize with a speed of ~0,84 µm/s during catastrophe (Kozlowski et al., 2007). Live observations of embryos expressing plus-end tracking EBP-2::GFP have shown that catastrophe rarely occurs before a growing microtubule reaches the cortex. When reaching the cortex, however, catastrophe follows within one to two seconds(Kozlowski et al., 2007). Microtubules often reach the cortex as bundles of multiple filaments, which can be captured by pulling force complexes. In vitro experiments have indicated that a single depolymerizing microtubule generates six to ten times as much force as a motor protein (~50 pN, a single dynein motor ~7 to 8 pN) (Grishchuk et al., 2005; Kozlowski et al., 2007). It is possible that dynein motor activity is only required to maintain contact with the depolymerizing microtubule (Laan et al., 2012).

Force generators that are anchored in a more rigid cortex are less able to maintain contact with the depolymerizing microtubule and thus produce less force (Kozlowski et al., 2007). So far, there is no experimental evidence showing an asymmetry in spindle geometry between the

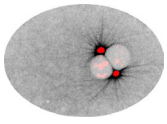

anterior and posterior part of the *C. elegans* zygote. However, F-actin is enriched at the anterior cortex when the zygote enters mitosis. This most likely increases cortical rigidity and must therefore decrease the forces generated by anterior pulling force complexes. Indeed, several groups observed substantially increased pulling forces in the anterior after actin depletion by drug treatment (Afshar et al., 2010; Berends et al., 2013; Redemann et al., 2010). Thus, in addition to regulation of the pulling force complex, a difference in the cortical rigidity caused by actin accumulation provides a possible cause of pulling force asymmetry.

Concluding remarks

Through controlled spindle positioning, polarized cells decide between symmetric and asymmetric cell division, and create daughter cells of the correct sizes at the appropriate positions. Studies in worms, flies and mammals have provided detailed descriptions of representative symmetric and asymmetric cell divisions. By now, most of the basic players in polarity establishment and spindle positioning may be identified. It remains incompletely understood, however, how cell and tissue polarity translate to proper positioning of the mitotic spindle. While the one-cell *C. elegans* embryo offers a relatively simple and well-tractable model, providing a complete answer to this question has proven to be remarkably difficult. Polarity dependent differences in pulling force component localization, phosphorylation, antagonist association and actin accumulation have all been described to contribute to the lower anterior compared to posterior pulling forces that position the spindle during asymmetric division of the *C. elegans* zygote. Importantly, the identified principles appear to be conserved and to apply broadly to regulation of the cell division plane in other cell types and organisms.

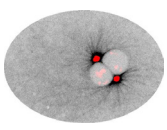

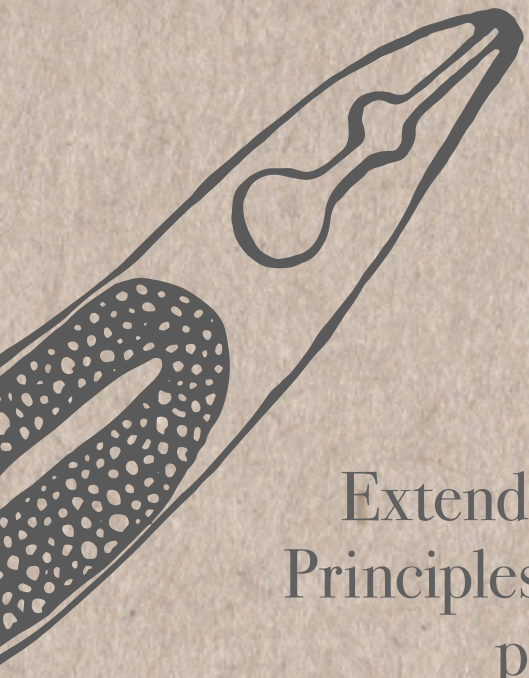

2

Extended introduction: Principles of mitotic spindle positioning

Lars-Eric Fielmich and Sander van den Heuvel

Developmental Biology, Department of Biology, Faculty of Sciences, Utrecht University, Padualaan 8, 3584 CH Utrecht, The Netherlands.

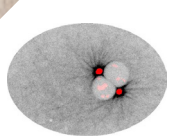

Introduction

The previous chapter introduced how cellular polarity regulates asymmetric spindle positioning, with a strong emphasis on the *C. elegans* zygote. This chapter will expand on this topic with some additional information to provide more context for the work described in this thesis.

Balance of forces

We all began our life as just a single cell: a fertilized egg or zygote. This popular opening for a developmental biology seminar was once a revolutionary finding. More than a century ago, Hertwig and Fol were the first to describe how the life of an animal starts with the fusion of the egg and sperm cell. While studying sea urchin and frog early embryos, Hertwig noticed that their round cells divide at random angles. However, when he compressed the embryos he noticed that the spindle apparatus aligned with the induced long axis of the cell. This led him to formulate the long-axis or 'Hertwig rule', which states that cells align their division orientation with their long axis (Hertwig, 1884). Over the course of more than a century, the Hertwig rule has proven to hold true as a basic principle for cell division orientation from invertebrates to mammals (Gray et al., 2004).

What are the mechanisms that position the spindle in the cell center and make the asters seek the long axis? There are three major forces that contribute to mitotic spindle positioning: 1) a pushing force by astral microtubules (AMTs) that grow against the cell cortex, 2) a pulling force by shrinking AMTs that are anchored at the cell cortex, and 3) a cytoplasmic drag force by microtubule motor-dependent transport along AMTs. In general, the pushing force and the cytoplasmic drag force contribute to spindle centering, whereas cortical pulling generates the dominant decentering force. Many studies describe these forces, *in vivo*, *in vitro*, and *in silico*. These generally agree on an AMT-length dependent effect: the centering forces on a centrosome are highest in the direction of the longest AMTs (Garzon-Coral et al., 2016; Grill et al., 2003; Hamaguchi and Hiramoto, 1986; Kimura and Onami, 2005; Kozlowski et al., 2007; Laan et al., 2012; Minc et al., 2011; Pécréaux et al., 2016; Shinar et al., 2011; Wühr et al., 2010). Pushing, pulling, and drag forces act simultaneously, but their individual contribution is influenced by physiological and physical variables such as centrosome-cortex distance, number of AMTs, and number of active cortical force generators. Thus, although general principles apply, the relative contribution of each mechanism to center the spindle may vary between cell types. The following paragraphs explore how dragging, pushing, and pulling contribute to spindle centering.

Spindle centering:

to drag …

The principle that spindle centering can be achieved by forces that originate from interactions with the cytoplasm rather than the cortex is most apparent in sea urchin (*Clypeaster japonicus*), frog (*Xenopus laevis*), and zebrafish (*Danio rerio*) early embryos. The cells in these systems are extremely large, so that the AMTs of the metaphase spindle do not reach the cell cortex, yet the mitotic spindle reliably finds the center of the cell (Hamaguchi and Hiramoto, 1986; Wühr et al., 2010). The observation that spindles move in the direction of the (experimentally induced) longer AMTs in a dynein dependent manner supports the following model: movement of the microtubule motor dynein towards the centrosome causes cytoplasmic drag along AMTs, resulting in a force directed away from the centrosome (Fig. 1 A). This was supported by 3D computer models that replicated both spindle centering and alignment along the long axis as a result of

cytoplasmic drag force (Kimura and Onami, 2005; Shinar et al., 2011). Because longer AMTs can harbor more dynein motors, this provides an explanation for why the centering force is stronger in the direction of the longer AMTs. *In vivo* experiments in *C. elegans* zygotes confirmed that transport of vesicles towards the centrosome contributes to spindle centering during prometaphase. More specifically, spindle centering was strongly affected by knock-down of the dynein light-chain subunit *dyrb-1* (dynein roadblock) and endosome surface proteins *rab-5* and *rab-7* (Kimura and Kimura, 2011). Thus, the cytoplasmic drag force is a conserved mechanism that contributes to spindle centering.

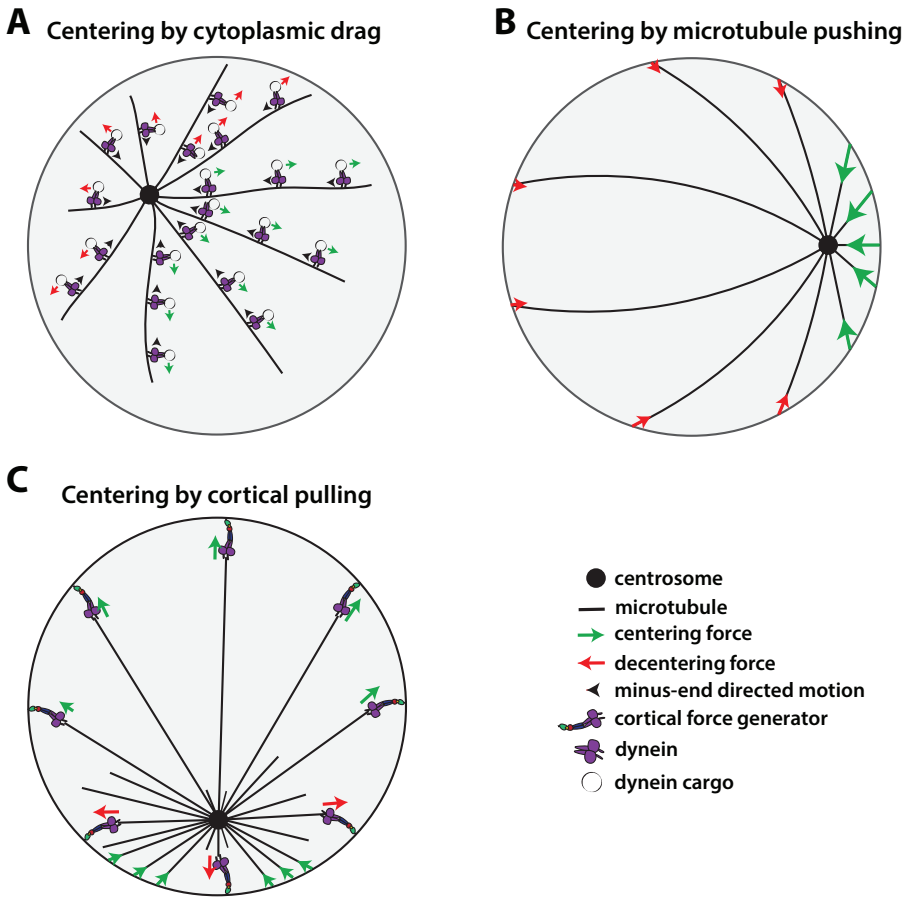

Figure 1 Schematic illustrations of the microtubule-dependent centrosome centering mechanisms. **(A)** Dynein motility towards the centrosome generates friction with the cytoplasm and an effective drag force away from the centrosome. Cytoplasmic drag forces are highest in the direction of the longest microtubules because longer microtubules harbor more dynein motors. **(B)** When a growing microtubule reaches the cell boundary, it can generate pushing forces while continuing to grow. Shorter microtubules are more rigid and less likely to buckle. Microtubule pushing forces are therefore highest in the direction of the longer microtubules. **(C)** A wider array of microtubules from a centrosome reaches the further cortex and could result in pulling force in that direction. However, this can only occur if cortical dynein levels are sufficiently low to assure that the greater number of microtubules that reaches the nearer cortex does not lead to stronger pulling towards the nearer cortex. Microtubules that do not anchor to a cortical force generator can generate pushing force.

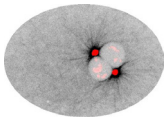

… to push …

The metaphase spindle of the *C. elegans* zygote is positioned in the center of the cell with remarkable precision: cell-to-cell variability is only ~1% (Pécréaux et al., 2016). This high accuracy can be explained by the collective pushing of many AMTs against the cell boundary that reduces variability (Howard and Garzon-Coral, 2017; Pécréaux et al., 2016). Microtubules are stiff polymers that are commonly nucleated from a microtubule organizing center (MTOC – the centrosome is the MTOC for the spindle) and stochastically alternate between growing and shrinking phases. These microtubule dynamics are most prominent at the microtubule plus-end; the microtubule minus-end is relatively stable, especially when it is associated with an MTOC (Akhmanova and Steinmetz, 2015; Vleugel et al., 2016a). The metaphase spindle of the *C. elegans* zygote contains about 16.000 AMTs (Redemann et al., 2017). Due to the stochastic nature of microtubule dynamics, the number of AMTs decreases exponentially with distance from the centrosome and ~200 AMTs contact the cell cortex at any given time in metaphase (Kozlowski et al., 2007; Pécréaux et al., 2016). These high numbers reduce stochastic noise and underlie the low variability in spindle centering.

A microtubule that reaches the cell cortex still has space to polymerize as a result of Brownian motion, thereby generating a pushing force of ~5 pN against the cortex (Dogterom and Yurke, 1997; Laan et al., 2012; Vleugel et al., 2016a). A microtubule can buckle and push or undergo catastrophe and shrink back towards the centrosome when it reaches a boundary, dependent on the ratio between the elastic force (to bend a microtubule) and stall force (to stop microtubule polymerization) (Kozlowski et al., 2007; Laan et al., 2012). Shorter microtubules are more rigid and less likely to buckle. The cortex nearest the MTOC is thus not only reached by more but also stiffer microtubules; therefore, microtubule pushing creates a centering force that, like cytoplasmic drag force, scales with AMT length (Fig. 1 B) (Howard and Garzon-Coral, 2017; Laan et al., 2012; Wu et al., 2017). Pushing forces are also expected to scale with cell size. Indeed, spindle centering forces by microtubule pushing are approximately twice as high in the *C. elegans* AB and P1 blastomeres as in the zygote P0 (Garzon-Coral et al., 2016). Despite higher AMT pushing forces in smaller cells, the centering effect of AMT pushing may be stronger in larger cells. This is the result of greater force differences between AMTs pushing against the nearer (short and rigid AMTs) and further (buckling AMTs) cortex (Howard and Garzon-Coral, 2017; Kozlowski et al., 2007). In conclusion, AMT pushing can be a precise spindle centering mechanism that varies with cell/spindle scale.

… or to pull?

Cortical pulling forces are a prominent player in spindle positioning, but can they also establish and maintain the spindle in the cell center? That the strongly decentering cortical pulling force contributes to spindle centering was proposed based on the following reasoning. For a decentered centrosome, a wider array of AMTs radiates towards the further cortex; hence, a larger fraction of the cell's cortical force generators pulls the centrosome towards the center (Kozlowski et al., 2007; Laan et al., 2012) (Fig. 1 C). On the other hand, relatively more AMTs reach the nearer cortex resulting in more pulling force events per area. This impedes the centering effect of cortical pulling, unless the number of AMTs far exceeds the number of cortical pulling force complexes to balance pulling and pushing forces (Howard and Garzon-Coral 2017; Wu et al., 2017). Indeed, an elegant series of *in vitro* reconstitution experiments of centrosome positioning in metal chambers coated with (a limited amount of) yeast dynein demonstrated that cortical pulling can center an MTOC (Laan et al., 2012). However, *in vivo* experiments showed that spindle centering is not impaired upon depletion of the cortical force generator component *gpr-1/2* (Kimura and Kimura, 2011; Pécréaux et al., 2016; Simone et al., 2018). Taken together, cortical pulling forces may contribute to, but are not required for, spindle centering in the *C. elegans* zygote.

Magnetized worm embryos provide an attractive answer

In a recent landmark study, magnetic tweezers were used to directly quantify the forces that keep the spindle centered in the *C. elegans* early embryo (Garzon-Coral et al., 2016). The work put exact numbers on the best studied *in vivo* model for mitotic spindle positioning. This allowed the combination of all experimental and theoretical work in a model with unprecedented accuracy. As can be visualized by spindle ablation (Grill et al., 2001, 2003; Labbé et al., 2004) and was assumed in theoretical work (Kimura and Onami, 2005; Pecreaux et al., 2006), the mitotic spindle behaves like a spring under tension. *gpr-1/2* RNAi increased the measured centering stiffness of the metaphase spindle and identified cortical pulling as a net decentering force (Garzon-Coral et al., 2016). The centering stiffness of the metaphase and anaphase spindle in the *C. elegans* zygote was measured to be 16 pN/µm (Garzon-Coral et al., 2016). This implies a force of ~0.5 pN per pushing AMT (Howard and Garzon-Coral, 2017), which is considerably lower than the expected pushing force of ~5 pN (Dogterom and Yurke, 1997; Laan et al., 2012). On the contrary, these force and stiffness values are in the same order of magnitude as those measured and predicted for buckling microtubules (Garzon-Coral et al., 2016; Howard and Garzon-Coral, 2017; Pécréaux et al., 2016). Altogether, the centering of the mitotic spindle in the *C. elegans* zygote with the observed high positional stability, low stiffness, and low force is best described by a model that predominantly depends on pushing force of many AMTs that buckle when they reach the cell cortex (Howard and Garzon-Coral, 2017; Wu et al., 2017).

It's all about dynamics

All mentioned aspects of spindle force generation depend on microtubule dynamics: microtubule growth/shrinking rates affect the total number and length of AMTs, and the extent and duration of cortical pushing and pulling events. How and if cells regulate dynamic properties of AMTs for mitotic spindle positioning is only beginning to be understood. *In vivo* experiments have shown that reducing microtubule depolymerization by depletion of KLP-7^{MCAK} increased spindle centering by AMT pushing forces (Garzon-Coral et al., 2016). Likewise, the cortical protein EFA-6 enhances microtubule dynamics in the *C. elegans* early embryo: depletion of EFA-6 resulted in more and longer AMTs (O'Rourke et al., 2010). This possibly results in enhanced centering stiffness by increased AMT pushing and may explain the observed reduction in centrosome oscillations. In mammalian cells, the mitotic interactor and substrate of Plk1 (MISP) protein is an actin-binding protein that promotes AMT stability when phosphorylated by mitotic kinases Cdk1 and Plk1 (Zhu et al., 2013). Although this is required for correct spindle orientation, the exact mechanism was not unraveled in the study. Insightful work that combines *in vivo* quantifications and *in silico* 3D simulations of spindle positioning showed how altered microtubule dynamics may influence cortical pulling force generation (Kozlowski et al., 2007). As mentioned earlier, cortical dynein promotes catastrophe of captured AMTs and slows down their depolymerization. Doing so, the amount of (active) dynein also moderates the balance of cortical pushing and pulling force.

Cortical dynein pulls it of

After (pro)metaphase spindle centering, an asymmetric spindle position can be achieved by directed asymmetry in decentering cortical pulling forces (Grill et al., 2001, 2003; Labbé et al., 2004). Pulling force generation depends on dynamic AMTs that are captured by cortically anchored dynein. The interaction between anchored dynein and a dynamic microtubule plus-end promotes microtubule catastrophe. A depolymerizing microtubule anchored by dynein was shown to generate forces of up to 5 pN (Laan et al., 2012). The measured pulling force of 5

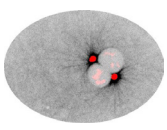

pN is similar to the force generated by dynein motor activity (Roberts et al., 2013). The fact that the maximum cortical pulling force equals dynein's stalling force could indicate that dynein processivity is limiting for cortical pulling force generation. Given the centering stiffness of the spindle of 16 pN/µm, the observed 2 µm posterior spindle displacement in the *C. elegans* zygote requires ~30 pN net pulling in the posterior direction (2 x 16 pN = 32 pN) (Garzon-Coral et al., 2016). The posterior displacement and transverse oscillations were estimated to arise from a difference of ~10 active force generators (Howard and Garzon-Coral, 2017; Pécréaux et al., 2016). The posterior spindle displacement in the *C. elegans* zygote thus results from a moderate asymmetry in the estimated total number of ~100 cortical force generators to be active simultaneously (Grill et al., 2001; Redemann et al., 2010).

Exactly how a cortically anchored depolymerizing microtubule results in pulling force generation is poorly understood, but it can be imagined as follows: if a mobile object (centrosome) is connected to an immobile object (cell cortex) by a cable (AMT), then shrinking of the AMT will pull the centrosome towards the cortex. It remains unresolved if the energy for pulling originates from microtubule depolymerization, from dynein motor activity, or from both. Pulling force generation by dynein was shown to require ATP and therefore likely dynein motor activity (Laan et al., 2012). If AMT depolymerization is the energy source, then dynein motor activity may still be required to anchor the shrinking MT to the cortex (Kozlowski et al., 2007). The energy may somehow be transduced by the cortical anchor in a manner similar to the Dam1/SKA1 ring complex in the kinetochore–microtubule anchoring network (Vleugel et al., 2016a). Important steps in solving these problems will come from uncovering how dynein interacts with microtubules in the cortical pulling force conformation: end-on or laterally, as a single motor or team wise.

Dynein's power button

For *in vitro* reconstitution experiments, researchers often use a constitutively active mutant form of yeast dynein. Activation of wild type metazoan dynein is rather intricate. The spatiotemporal activation of dynein *in vivo* is achieved by various regulators specific to different cellular processes but always involves the compulsory dynein activator complex dynactin (Carter et al., 2016; Raaijmakers and Medema, 2014). The joint assembly and activation of the large dynein/dynactin complex occurs through adaptors such as Bicaudal 2 (BICD2) (McKenney et al., 2014; Schlager et al., 2014). These adaptor proteins form homodimers through a long coiled-coil domain, which also mediates the dynein–dynactin assembly. Exactly how the coiled-coil domain interacts with dynactin determines if a single or double dynein is subsequently recruited. The dynein pair binds microtubules in parallel, enhancing the processive movement and stalling force of the complex (Grotjahn et al., 2018; Urnavicius et al., 2018). If and how cortical dynein is activated for pulling force generation is not clear, but the LIN-5^{NuMA} protein, containing a long coiled-coil domain required for homodimerization, is a good candidate promoter of cortical dynein/dynactin assembly (Fisk Green et al., 2004; Harborth et al., 1995; Lorson et al., 2000; Merdes et al., 1996). There is evidence that LIN-5 and NuMA interact with dynein/dynactin, although the exact nature of this interaction is unresolved (Kotak et al., 2012; Merdes et al., 2000, 1996; Nguyen-Ngoc et al., 2007). By adding a promiscuous biotin ligase (BioID) to seven members of the dynein complex, the human dynein interactome was identified by proximity labeling with biotin (Redwine et al., 2017). NuMA was not found to be among the dynein interacting proteins. However, the experiments were not performed with synchronized cells; hence, mitotic cells make up a small part of the data and a putative NuMA–dynein interaction could easily have been missed. Therefore, the question of whether and how LIN-5^{NuMA} activates dynein for cortical pulling force generation remains unanswered for now.

The anaphase cortex rallies the forces

If LIN-5^{NuMA} is a dynein adaptor/activator, then cortical LIN-5^{NuMA} recruitment is an important determinant of cortical pulling force generation. Recent work has uncovered additional NuMA cortical localization mechanisms that help explain the switch to decentering cortical pulling as the dominant force during anaphase. During early mitosis, NuMA localizes mainly to the centrosome and spindle where it is required for spindle pole focusing together with dynein/dynactin (Merdes et al., 2000, 1996). Mitotic kinases are key regulators for the spatiotemporal regulation of cortical NuMA. Aurora A kinase (AurA) localizes to spindle poles where it phosphorylates NuMA and promotes its translocation to the cortex (Gallini et al., 2016). Also at the spindle poles, Polo-like kinase 1 (Plk1) locally inhibits the interaction between NuMA and dynein/dynactin (Kiyomitsu and Cheeseman, 2012). Cortical NuMA levels progress during mitosis, with the strongest increase in anaphase (Kotak et al., 2013). Progression from metaphase to anaphase coincides with cyclin dependent kinase 1 (Cdk1) inactivation. Consequently, the phosphorylation/dephosphorylation balance of multiple NuMA target residues is shifted towards dephosphorylation after the metaphase-anaphase transition. Cdk1 directly phosphorylates NuMA on T2055, which is counteracted by the phosphatase PP2CA (Kotak et al., 2013); dephosphorylated NuMA T2055 promotes cortical NuMA localization during anaphase. In parallel, Cdk1 inactivation relieves the inhibition of protein phosphatase 1 (PP1) by p37, enhancing the mobility of the spindle pole population of NuMA and cortical enrichment during anaphase (Lee et al., 2018). Perturbations of these mitotic kinases and phosphatases results in aberrant cortical NuMA levels and exaggerated off-center spindle movements during metaphase (Kotak et al., 2014; Lee et al., 2018). This is indicative of an important role for cortical NuMA localization in pulling force generation. NuMA phosphorylation by AurA enables NuMA binding to cortical band 4.1 proteins (Kiyomitsu and Cheeseman, 2013), which is an additional NuMA anchor in addition to Gα–LGN. Recent work suggests that NuMA may also bind membrane phosphoinositides directly (Kotak et al., 2014). It has been proposed that the increase in cortical NuMA levels during anaphase is required for spindle pole separation and chromosome segregation but that this potential force of extra NuMA can only be unchained after the spindle has been carefully positioned (Seldin and Macara, 2017).

Where does dynein come from?

Cortical dynein binding is the ultimate step before AMT capture and pulling force generation. But how is dynein recruited to cortical NuMA? In budding yeast, dynein tracks microtubule plus-ends via kinesin Kip2-dependent movement through interaction with Pac1^{Lis1} and Bik1^{CLIP170} (Cianfrocco et al., 2015). When reaching the cortex, dynein is off-loaded from the MT plus-end to the cortical force generator anchor Num1 in a dynactin-dependent manner (Ananthanarayanan et al., 2013; Markus and Lee, 2011). The microtubule plus-end binding of dynein is conserved: human dynein tracks microtubule plus-ends together with dynactin, dependent on EB1 and CLIP170 (Cianfrocco et al., 2015). However, whether this plus-end bound dynein is off-loaded when the AMT reaches the cortex and whether this contributes to efficient pulling force generation is unknown. Alternatively, dynein is recruited to the cortex from the cytoplasmic pool. Unraveling how dynein is delivered to the cortex is complicated by the fact that the molecular details of the interaction between dynein/dynactin and LIN-5^{NuMA} remain unresolved.

Conserved complexity

In metazoans, cortical pulling force generators are multiprotein complexes. This increases the adaptability and complexity of regulation. The *C. elegans* Gα–GPR-1/2–LIN-5, *Drosophila* Gα–Pins–Mud, and vertebrate Gα–LGN–NuMA trimers represent the core components of mitotic

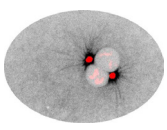

spindle positioning. The previous paragraphs focused on the basic principles of mitotic spindle positioning in cells that are not organized into tissues and in the absence of external guidance cues. The following section provides some examples of how combinations of the trimeric complex are regulated differently to position the spindle in different organisms, cell types, and developmental stages.

Cells round up during mitosis, a process which is regulated by Cdk1 kinase activity and mediated by actomyosin contractility (Ramanathan et al., 2015; Stewart et al., 2011). Mitotic rounding is not perfect, and cells maintain some elongation in the direction of tissue stretch. The Hertwig rule dictates that these cells divide along the mitotic long axis. However, in cultured epithelial cells under stretch, the interphase long axis better predicts division orientation than the mitotic long axis (Wyatt et al., 2015). The tensile stress is transduced by intercellular junctions and these are expected to play an instructive role in spindle orientation. For epithelial cells of the *Drosophila* notum, tricellular junctions containing discs large (Dlg) recruit Mud^{NuMA} as a memory of interphase cell geometry that persists in mitosis (Fig. 2) (Bosveld et al., 2016). The tricellular junction distribution is influenced by tissue stretch and thus instructs a division in the direction of tissue tension, regardless of mitotic cell shape. Such a division orientation relieves tissue stretch and has a morphogenetic result similar to convergent extension (Wyatt et al., 2015). For columnar epithelial cells, divisions along the interphase long axis would be out of the epithelial plane. These cells therefore depend on mitotic rounding to respond to polarity cues that instruct a planar spindle orientation and overrule the highly elongated interphase cell shape (Chanet et al., 2017). Hence, the cortical force generator complex can interpret polarity and mechanical stress-derived signals to correctly position the spindle.

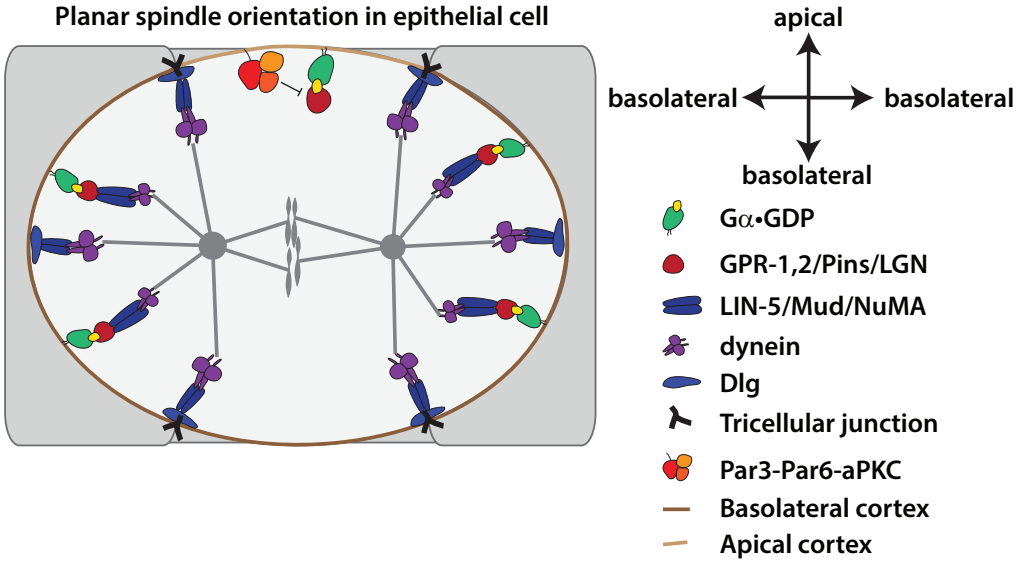

Figure 2 Schematic illustrations of mitotic spindle positioning in epithelial tissue cells. Epithelial cells that are to divide in the epithelial plane position force generators on the basolateral cortices. Apical aPKC phosphorylates and antagonizes Pins^{LGN} localization. Basolateral Pins^{LGN} localization is further promoted by the polarity protein discs large (Dlg). Dlg can also give a more specific positional cue when part of a tricellular junction (TCJ).

Signals that direct mitotic spindle positioning often attract or repel GPR-1/2$^{Pins/LGN}$. *Drosophila* neuroblast (NB) spindles align along the apicobasal axis. This is instructed by the apical Bazooka^{Par3}–Par6–aPKC complex and mediated by inscuteable (Insc), which links Pins^{LGN} to Bazooka^{Par3} and thus recruits it apically (Fig. 3) (Schaefer et al., 2000). Baz–Insc enriches Pins apically and does not constitute a cortical force generator because the Pins^{LGN}–Insc^{mInsc} and Pins^{LGN}–Mud^{NuMA} interactions are mutually exclusive (Culurgioni et al., 2011, 2018). Mouse inscuteable (mInsc) can also instruct an apicobasal spindle orientation. Such perpendicular instead of planar divisions contribute to indirect neurogenesis of radial glial cells in the developing neural cortex, stratification of epidermal basal progenitor cells of the embryonic skin, and mammary gland regeneration cycles at pregnancies (Culurgioni et al., 2018; Postiglione et al., 2011; Williams et al., 2014). These examples illustrate how the spindle orientation is regulated at multiple levels during development and contributes to cell type specification and tissue morphogenesis.

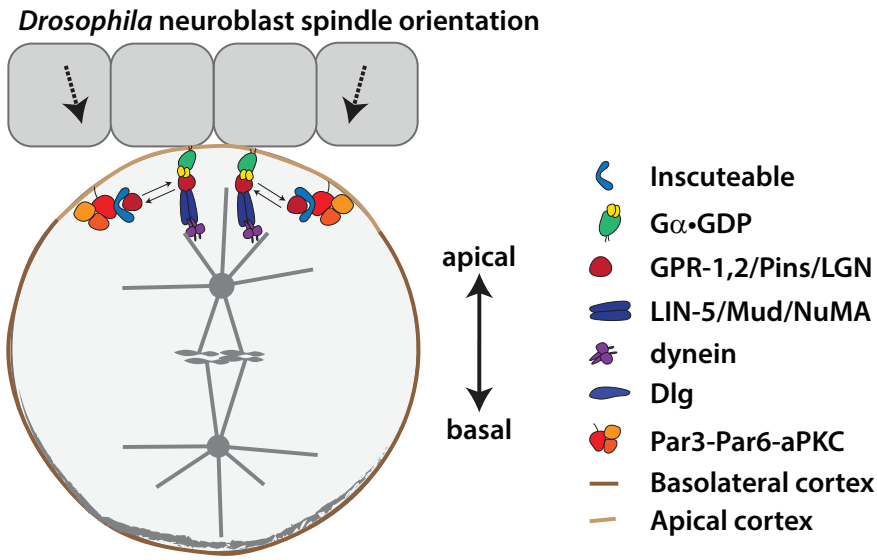

Figure 3 The Drosophila neuroblast (NB) as example of apicobasal spindle orientation. In response to signals from overlying neuroepithelial cells, the NB sets up an apical-basal polarity axis. Baz^{Par3}-Par6-aPKC marks the apical cortex and recruits Inscuteable (Insc). Insc enriches Pins^{LGN} at the apical cortex and thus promotes an apicobasal orientation of the mitotic spindle. Accumulation of actomyosin on the basal cortex contributes to size asymmetry and results in a smaller basal cell after division.

To assure planar division of epithelial cells, multiple mechanisms are employed. In 3D cysts of canine kidney (MDCK) cells, LGN is phosphorylated apically by aPKC. This prevents apical localization of LGN and assures a planar spindle orientation (Hao et al., 2010; Zheng et al., 2010). The polarity protein Dlg is also used as spindle orientation cue that recruits Pins^{LGN} to the basolateral cortex in several cell types (Fig 2). The interaction between Pins^{LGN} and Dlg requires Pins^{LGN} phosphorylation by AurA and was shown to be required for planar spindle orientation in *Drosophila* NBs and embryonic columnar epithelial cells, chick neuroepithelial cells, and cultured mammalian cells (Chanet et al., 2017; Johnston et al., 2009; Saadaoui et al., 2014; Siegrist and Doe, 2005). In *Drosophila* SOP cells, Dlg recruits Pins^{LGN} to the anterior cortex (Bellaïche et al., 2001). In the same cells, Mud^{NuMA} is recruited to the posterior apical cortex by the Wnt receptor frizzled

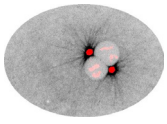

(Fz) and its effector disheveled (Dsh) in response to planar cell polarity cues (Fig. 4). A Fz–Dsh dependent localization of NuMA is conserved and also orients the mitotic spindle during zebrafish gastrulation and *C. elegans* endoderm specification (Bei et al., 2002; Ségalen et al., 2010). Thus, in addition to intracellular signals, intercellular signals can instruct spindle orientation in tissues.

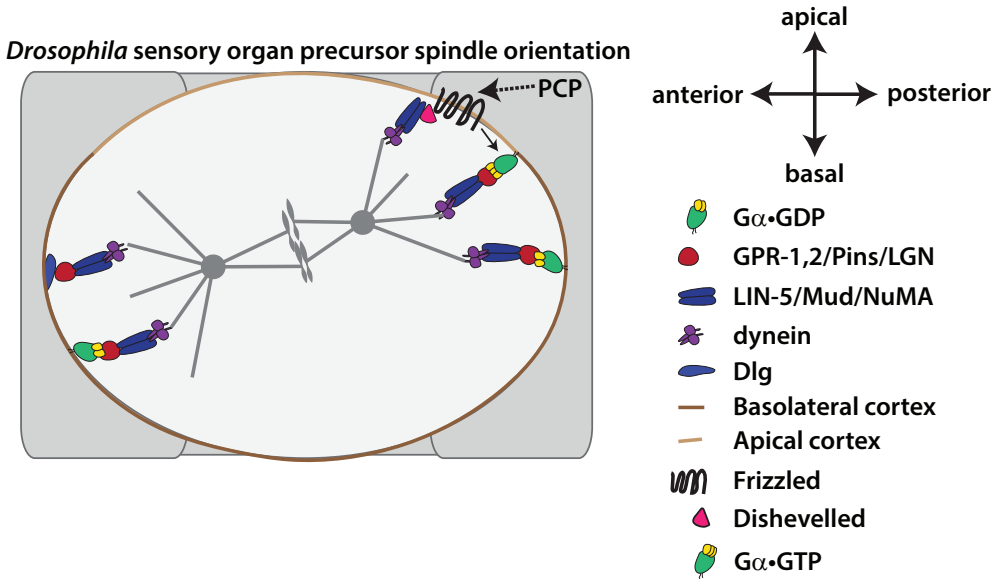

Figure 4 Model of spindle positioning in response to planar cell polarity signals, Drosophila SOP cell as example. To assure an anterior-posterior spindle orientation, Dlg anchors Pins at the anterior cortex. Furthermore, in response to Wnt PCP signaling, posterior apical Wnt receptor Frizzled is activated and recruits Mud^{NuMA} through its cofactor Dishevelled. Frizzled also promotes generation of Gαo·GTP which can recruit Pins.

In conclusion, Gα–GPR–LIN-5 and its functional homologs are involved in every metazoan cell division studied so far, albeit in varying compositions and with varying localization patterns. The processes they mediate are complex and regulated by myriad mechanisms and pathways: the examples mentioned in this chapter are far from complete. For example, cortical Myosin-10 can anchor AMTs and orient the spindle with respect to actin retraction fibers in cultured fibroblasts (Kwon et al., 2015). Another cytoskeletal motor, Kinesin-73 (Khc73), contributes to AMT anchoring and spindle orientation in *Drosophila* (Lu and Prehoda, 2013; Siegrist and Doe, 2005). Also, NuMA contains a MT-binding domain that was found to contribute to cortical AMT capture and spindle orientation in the mouse epidermis (Seldin et al., 2016). Nevertheless, dynein-dependent AMT anchoring is the central, conserved mechanism that is most generally required for pulling force generation and spindle positioning (Pietro et al., 2016). As the regulation of these processes is complex and only starts to be understood, further *in vitro*, *in vivo*, and *in silico* experiments will be needed to generate an integrated understanding of mitotic spindle positioning in homeostasis, development, and pathogenesis.

Instructing the cell cleavage plane

In animal cells, the mitotic spindle is an important source of guiding signals to position the cell cleavage plane. The spindle asters send a "polar relaxation" signal, and the midzone an "equatorial stimulation" signal to the actomyosin cortex to induce furrow ingression (Galli and van den Heuvel, 2008). The equatorial stimulating signal involves the centralspindlin components ZEN-4^{MKLP1} and CYK-4^{MgcRacGAP}, and ECT-2^{ECT2} (Galli and van den Heuvel, 2008; Roubinet and Cabernard, 2014). Centralspindlin may promote furrowing at the equatorial cortex by binding to antiparallel astral microtubules as well as midzone microtubules. In *C. elegans*, the astral pathway depends on Gα–GPR-1/2 as well as LET-99, which antagonizes GPR-1/2 localization at the site of furrow induction (Bringmann et al., 2007). The equatorial repulsion of GPR-1/2–LIN-5 is conserved in other animals: LGN–NuMA is repelled from the equatorial cortex by a chromosome-derived Ran·GTP gradient and centralspindlin components in mammalian cell culture (Kiyomitsu and Cheeseman, 2012; Kotak et al., 2014). Possibly, the thus generated local minimum in cortical force generation and anchored AMTs are part of the instructive cue for furrow formation (Dechant and Glotzer, 2003).

Spindle-independent furrow positioning mechanisms have also been described (Cabernard et al., 2010; Ou et al., 2010). These are regulated by PAR-polarity and rely on asymmetry and concerted flows of cortical actomyosin. Polarized actomyosin activity can 'squeeze' one future daughter cell to generate size asymmetry (Fig. 2 B). This has been described for *Drosophila* and *C. elegans* neuroblasts (Cabernard et al., 2010; Ou et al., 2010; Roubinet et al., 2017). The *C. elegans* zygote has a strong actomyosin asymmetry with higher levels at the anterior cortex. This would induce cell cleavage in the anterior half of P0 and result in an inversed AB:P1 ratio. To circumvent this, anterior actomyosin contractility is inhibited by PAR-4 and ANI-1^{Anillin} (Pacquelet et al., 2015). Thereby, spindle-independent cleavage furrow positioning is inactivated, and the cleavage plane follows the spindle-dependent instructions.

In summary, more than 130 years after Oscar Hertwig's seminal work, both the exploration of new models and detailed studies of established models continue to uncover mechanisms that position the mitotic spindle and cell cleavage plane. And even though the more complex systems are the ones that many aim to understand, the *C. elegans* zygote remains an attractive model to study asymmetric cell division: it employs all essential components in a system that is not influenced by most of the mentioned 'additional' input that may confound results. Many principles of mitotic spindle and cytokinetic furrow positioning were first described in the *C. elegans* zygote. It is not unthinkable that researchers will continue to be fascinated by this zygotic division for another 100 years, and that important aspects of the regulation of this division have yet to be discovered.

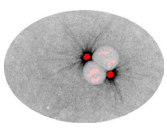

Scope of this thesis

Correct execution of asymmetric cell division requires precise positioning of the mitotic spindle. This is achieved by pulling forces, generated by cortical dynein–microtubule interactions. Cortical dynein is anchored by the conserved Gα—GPR-1/2—LIN-5 (*C. elegans*), Gα—Pins—Mud (*Drosophila*), and Gα–LGN–NuMA (vertebrates) protein complex. Regulation of this complex assures appropriate spindle positioning and thereby daughter cell size, content, and position during development and homeostasis. The core players in the regulation of spindle positioning have been recognized for about two decades, and their functions have been studied in a wide range of models and systems. This thesis describes new mechanisms that contribute to mitotic spindle positioning in the *C. elegans* zygote through regulation of the Gα–GPR-1/2–LIN-5–dynein force generator and microtubule dynamics.

Differential regulation of spindle positioning components in space and time partly results from posttranslational modifications such as protein phosphorylation. Cell polarity and cell-cycle signaling networks contain various kinases and are prominent cues in the regulation of mitotic spindle positioning. Our group previously described that phosphorylation of LIN-5 by the polarity regulator atypical protein kinase C (PKC-3) negatively regulates anterior pulling forces during asymmetric cell division of the *C. elegans* zygote (Galli et al., 2011a). In addition, many additional *in vivo* phosphorylated LIN-5 residues were identified (Galli et al., 2011a). Chapter 3 describes an investigation of the function of these additional LIN-5 phosphorylations and identification of possible cell-polarity-, cell-cycle-, and signal-transduction kinases involved. For several of the phosphorylated residues, we identified candidate kinases through RNAi knock-down experiments or *in vitro* kinase assays. To test the functional relevance, we mutated the phosphorylated residues to non-phosphorylatable or phosphorylation-mimicking residues by means of CRISPR/Cas9-mediated genome engineering. We found evidence to support that consecutive phosphorylation of LIN-5 S659 by glycogen synthase kinase 3 (GSK-3) and S662 by casein kinase 1 (CK1) promotes the GPR-1—LIN-5 interaction and cortical pulling force generation. The PAR-1 kinase appears to phosphorylate LIN-5 residue S397 *in vivo*, although we did not detect a contribution of this phosphorylation in spindle positioning in the early embryo. In contrast, our findings support that CDK-1 phosphorylation of LIN-5 T168 and T181 is essential for the LIN-5-mediated dynein recruitment and thereby cortical pulling force generation. This work increases our understanding of the regulation of asymmetric spindle positioning. It also provides a powerful approach for future studies that address phosphoregulation and protein-protein interactions in *C. elegans*.

In Chapter 4 of this thesis, we examine whether phosphorylation of LIN-5 by PKC-3^{aPKC} attenuates anterior pulling forces in parallel with reduced cortical microtubule dynamics by the adenomatous polyposis coli protein (APR-1). We found that cortical APR-1 levels are negatively regulated by MOM-5 (Frizzled) and DSH-2 (Disheveled). Dependent on the anterior-posterior PAR polarity axis, APR-1 becomes asymmetrically enriched at the anterior cortex, where it reduces cortical microtubule dynamics and pulling force generation. Using a previously described three-dimensional simulation of spindle positioning in the *C. elegans* zygote (Kimura and Onami, 2005, 2007, 2010), we show that the increased spindle pole movements upon *apr-1* RNAi can be explained by the stabilization of cortical astral microtubules by APR-1. This partly fills the gap in understanding the molecular mechanisms that connect anterior-posterior PAR-polarity and spindle positioning. Our results also provide more mechanistic insight in the previously described role of APC^{APR-1} in spindle positioning.

Cortical pulling force is generated when cortically anchored dynein associates with depolymerizing astral microtubules. Dynein was previously described to track microtubule plus-ends in yeast (Han et al., 2001; Lenz et al., 2006) and in mammalian cells in culture (Kobayashi and Murayama, 2009; Vaughan et al., 1999). This dynein plus-end tracking behavior is required for effective pulling force generation in budding- and fission yeast (Ananthanarayanan et al., 2013;

Markus and Lee, 2011). In Chapter 5, we describe the existence of two independent cortical populations of dynein in the *C. elegans* zygote. One of these dynein populations tracks microtubule plus-ends, which depends on end-binding protein 2 (EBP-2), and the other is recruited to the cortex by LIN-5 and is essential for pulling force generation. Under normal conditions, the plus-end tracking of dynein is not essential for pulling force generation, as CRISPR/Cas9-mediated knockout of all three *ebp* genes does not result in observable spindle positioning defects. However, this pool becomes important upon partial loss of dynein function, suggesting that it creates a buffer pool for robust pulling force generation. Using total internal reflection (TIRF) and fluorescence recovery after photobleaching (FRAP) microscopy, we found that dynein and LIN-5 have similar dynamics at the cortex. Furthermore, we describe differences in dynein immobility between the posterior and anterior cortex, which is regulated by PAR-polarity. This work thus provides a detailed analysis of protein dynamics and contributes to the understanding of how PAR-polarity regulates effectors of spindle positioning.

Although regulation of Gα–GPR-1/2–LIN-5–dynein and its homologs have been described in various contexts, little is known about the individual contributions of Gα, GPR-1/2, LIN-5, and dynein to cortical pulling force generation. In Chapter 6, we describe light-controlled localization of endogenous proteins in the *C. elegans* early embryo using the ePDZ–LOV heterodimerization system. Light-induced cortical localization of force generator components enabled control over pulling force generation, and thereby positioning of the spindle and cell cleavage plane. We show that direct cortical recruitment of dynein is insufficient for pulling force generation. In contrast, cortical dynein anchoring by LIN-5 is essential and sufficient for cortical pulling force generation. This provides evidence for LIN-5 as an activator of cortical dynein and possibly as an adapter for the dynein–dynactin complex. In contrast, Gα and GPR-1/2 are not required to generate pulling forces, although the wild type distribution of forces depends on anchoring through Gα. We also describe the inducible germline-specific knockout of endogenous genes and identify an essential, joint regulation of Gα by the GTPase activating protein RGS-7 and molecular chaperone/guanine nucleotide exchange factor RIC-8. This chapter thus deepens the understanding of Gα–GPR-1/2–LIN-5–dynein function through the implementation of novel methods.

We have extensively used recently developed CRISPR/Cas9 technologies, which was crucial to reach the conclusions in every chapter. This thesis therefore rides the early wave of CRISPR/Cas9 methods produced by the *C. elegans* community. Applications include the mutation of individual codons in the endogenous locus of LIN-5 (Chapters 3 and 4), fluorescent labeling of endogenous proteins to study their behavior at endogenous concentrations (Chapter 5), introduction of *lox* sites to conditionally knock-out endogenous genes (Chapter 6), and tagging of endogenous proteins with light-controlled interacting domains to manipulate all relevant proteins (Chapter 6). As CRISPR/Cas9-mediated genome engineering and tagging of endogenous proteins are gaining territory, germline silencing of transgenes will also pose challenges to researchers that do not study the germline or early embryo. After all, tagging of endogenous proteins for study in somatic tissues can provoke germline silencing responses and affect the development and viability of the animal. To overcome the germline silencing responses evoked by the expression of *cre*, *epdz*, and *lov* transgenes, we developed a method for optimization of transgene sequences (Chapter 6). Because of the methodological aspects, the work described in this thesis should be relevant not only for researchers in the spindle positioning field, but also for a broader *C. elegans* community.

As every answer raises new questions, the research described in this thesis has an open ending. Chapter 7 provides a more general discussion and makes suggestions for future research to follow up on these open endings. Some questions that were asked but not answered in the preceding chapters are addressed in this chapter. These questions are for instance the molecular function of RIC-8, the mechanism of cortical APR-1 localization, and the overall structure and strength of the Gα–GPR-1/2–LIN-5–dynein force generator.

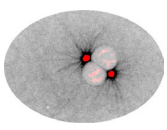

3

Multisite phosphorylation of NuMA-related LIN-5 controls mitotic spindle positioning in *C. elegans*

Vincent Portegijs[1], Lars-Eric Fielmich[1,*], Matilde Galli[1,a,*], Ruben Schmidt[1,2], Javier Muñoz[3,b], Tim van Mourik[1], Anna Akhmanova[2], Albert J. R. Heck[3], Mike Boxem[1] and Sander van den Heuvel[1]

[1] Developmental Biology, Faculty of Sciences, Department of Biology, Utrecht University, Padualaan 8, 3584 CH Utrecht, The Netherlands.

[2] Cell Biology, Faculty of Sciences, Department of Biology, Utrecht University, Padualaan 8, 3584 CH Utrecht, The Netherlands.

[3] Biomolecular Mass Spectrometry and Proteomics, Bijvoet Center for Biomolecular Research and Utrecht Institute for Pharmaceutical Sciences, Utrecht University, Padualaan 8, 3584 CH Utrecht, The Netherlands.

[a] Present address: Hubrecht Institute, Uppsalalaan 8, 3584 CT Utrecht, The Netherlands.

[b] Present address: Spanish National Cancer Research Centre (CNIO), ProteoRed-ISCIII, Melchor Férnandez Almagro, 3, 28029 Madrid, Spain.

* These authors contributed equally to this publication

An adapted version of this manuscript was published in *PLoS Genetics* in 2016

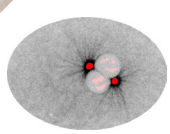

Abstract

During cell division, the mitotic spindle segregates replicated chromosomes to opposite poles of the cell, while the position of the spindle determines the plane of cleavage. Spindle positioning and chromosome segregation depend on pulling forces on microtubules extending from the centrosomes to the cell cortex. Critical in pulling force generation is the cortical anchoring of cytoplasmic dynein by a conserved ternary complex of Gα, GPR-1/2, and LIN-5 proteins in *C. elegans* (Gα–LGN–NuMA in mammals). Previously, we showed that the polarity kinase PKC-3 phosphorylates LIN-5 to control spindle positioning in early *C. elegans* embryos. Here, we investigate whether additional LIN-5 phosphorylations regulate cortical pulling forces, making use of targeted alteration of *in vivo* phosphorylated residues by CRISPR/Cas9-mediated genetic engineering. Four distinct *in vivo* phosphorylated LIN-5 residues were found to have critical functions in spindle positioning. Two of these residues form part of a 30 amino acid binding site for GPR-1, which we identified by reverse two-hybrid screening. We provide evidence for a dual-kinase mechanism, involving GSK3 phosphorylation of S659 followed by phosphorylation of S662 by casein kinase 1. These LIN-5 phosphorylations promote LIN-5–GPR-1/2 interaction and contribute to cortical pulling forces. The other two critical residues, T168 and T181, form part of a cyclin-dependent kinase consensus site and are phosphorylated by CDK1-Cyclin B *in vitro*. We applied a novel strategy to characterize early embryonic defects in lethal T168/T181 knockin substitution mutants, and provide evidence for sequential LIN-5 N-terminal phosphorylation and dephosphorylation in dynein recruitment. Our data support that phosphorylation of multiple LIN-5 domains by different kinases contributes to a mechanism for spatiotemporal control of spindle positioning and chromosome segregation.

Introduction

Animal development and tissue homeostasis depend critically on cell divisions that create cells with specific shapes and functions, in the right numbers and at the proper positions. The spindle apparatus plays a central role in the cell division process, as it segregates the chromosomes in mitosis and determines the plane of cell cleavage during cytokinesis (Galli and van den Heuvel, 2008; McNally, 2013; Morin and Bellaïche, 2011). Placement of the spindle in the cell center during division results in the formation of daughter cells of equal size, whereas off-center migration and spindle rotation allows the creation of differently sized daughter cells at specific locations. Moreover, the plane of cell cleavage determines whether polarized cells undergo symmetric or asymmetric cell division. Asymmetric cell divisions create cell diversity and allow maintenance of tissue-specific stem cells, by combining self-renewal with the generation of differentiating daughter cells (Reviews: (Gönczy, 2008; Knoblich, 2010)). Thus, tight control of the spindle function and position is needed to coordinate chromosome segregation with cleavage plane determination, which is essential for genetic stability, tissue integrity and stem cell maintenance in a wide variety of evolutionary contexts.

Pioneering studies in *Caenorhabditis elegans* and *Drosophila melanogaster* revealed that the position of the spindle responds to polarity cues during asymmetric cell division (Galli and van den Heuvel, 2008; Gönczy, 2008; Knoblich, 2010; Morin and Bellaïche, 2011). In *C. elegans,* anterior-posterior (A-P) polarity is established after fertilization of the oocyte. This involves re-distribution of specific partitioning-defective (PAR) proteins into two opposing domains of the cell cortex. The PDZ-domain proteins PAR-3 and PAR-6 form a complex with the PKC-3 aPKC polarity kinase and become restricted to the anterior half of the zygote, while the PAR-2 ring-finger protein and PAR-1 kinase occupy the posterior domain (Rose and Gönczy, 2014). This A-P polarity guides the asymmetric localization of cytoplasmic determinants as well as the position of the mitotic spindle. During the first mitotic division, the spindle is positioned off-center, to instruct

an asymmetric cell division that creates a larger anterior blastomere (AB) and smaller germline precursor cell (P1). Next, the spindle rotates by 90 degrees in P1, to instruct another asymmetric division with a cleavage plane perpendicular to the one of AB. These early divisions of the *C. elegans* embryo have served as an important model for studies of the coordinated regulation of cell polarity, fate determinant localization, and spindle positioning during asymmetric cell division.

In addition, studies in *C. elegans* and *Drosophila* uncovered an evolutionarily conserved protein complex that mediates spindle positioning. This complex consists of the alpha subunit of a heterotrimeric G protein in association with the TPR/GoLoco protein GPR-1/2 and coiled-coil protein LIN-5 in *C. elegans* (Gα–Pins–Mud in *Drosophila*, Gα–LGN–NuMA in mammals) (Reviews: (Galli and van den Heuvel, 2008; Gönczy, 2008; Knoblich, 2010; McNally, 2013; Morin and Bellaïche, 2011; Rose and Gönczy, 2014)). The GPR-1/2 GoLoco motifs interact with Gα-GDP (Kimple et al., 2002), while the tetratricopeptide repeats (TPR) associate with the C-terminus of LIN-5 (Fig 1A). The ternary protein complex acts at the cell cortex in conjunction with cytoplasmic dynein and microtubule plus ends to generate microtubule pulling forces that promote chromosome segregation and position the spindle (Couwenbergs et al., 2007; Kotak et al., 2012; Kozlowski et al., 2007; Laan et al., 2012; Nguyen-Ngoc et al., 2007). Based on results obtained for NuMA, an extended N-terminal domain of LIN-5 likely mediates interaction with the dynein motor complex (Kotak et al., 2012). It remains unclear how Gα–GPR-1/2–LIN-5 engages dynein and microtubule depolymerization in the generation of cortical pulling forces, and how pulling forces are temporally and spatially restricted.

Asymmetric positioning and rotation of the spindle result from imbalance in the pulling forces. It has long been known that the cortical polarity of the *C. elegans* zygote is fundamental for the spatial organization of pulling forces, creating a higher net force in the posterior than the anterior, which causes the spindle to move off center (Grill et al., 2001, 2003). This is in part achieved through PKC-3 mediated phosphorylation of LIN-5, which inhibits anteriorly directed pulling forces (Galli et al., 2011a). Phosphorylation also appears to regulate cortical pulling forces in other systems. For example, phosphorylation by aPKC inhibits Pins/LGN localization to the apical cell membrane and promotes planar cell division of MDCK canine kidney cells during cyst formation (Du and Macara, 2004). Moreover, phosphorylation of NuMA by Plk1 and Cdk1 has been implicated in the timing of chromosome segregation and positioning of the mitotic spindle in human cells (Kiyomitsu and Cheeseman, 2012; Kotak et al., 2013). In addition to spindle positioning, the Gα–GPR-1/2–LIN-5 complex is essential for chromosome segregation, in all cell divisions except for the first few embryonic divisions in *C. elegans* (Albertson et al., 1978; Lorson et al., 2000; Srinivasan et al., 2003). Phosphorylation is likely to play a key role in coordinating chromosome segregation and spindle positioning through spatiotemporal regulation of Gα–GPR-1/2–LIN-5 function.

Our previous studies identified extensive *in vivo* phosphorylation of LIN-5 in *C. elegans* embryos (Galli et al., 2011a). The function of the majority of these phosphorylations remained unknown. Here we apply a combination of techniques to determine which phosphorylations are critical for LIN-5 function. CRISPR/Cas9-mediated genetic engineering allowed us to introduce single codon alterations in the *C. elegans* genome, and to compare non-phosphorylatable, and potentially phosphomimetic LIN-5 mutants. In addition to PKC-3, we found that the PAR-1 polarity kinase likely phosphorylates LIN-5 *in vivo*, but physiological consequences of this phosphorylation were not detected. Alanine substitution mutagenesis of *lin-5* transgenes pointed to four phosphorylated residues with critical functional contributions. Two of these residues form part of a 30 amino-acid domain of LIN-5 required for binding GPR-1/2. Phosphorylation of these residues promotes cortical pulling forces and GPR-1/2 localization *in vivo*, and appears to occur sequentially by GSK3 and casein kinase 1 (CK1). Moreover, we identified essential residues in the LIN-5 N-terminus that are phosphorylated by CDK1. Our data from extensive knockin

replacement mutants are consistent with a mechanism involving sequential phosphorylation and dephosphorylation of the LIN-5 N-terminus in dynein recruitment to the meiotic spindle and cell cortex. Thus, a combination of phosphorylations by cell-cycle and polarity associated kinases likely underlies the spatiotemporal control of pulling forces in chromosome segregation and asymmetric cell division.

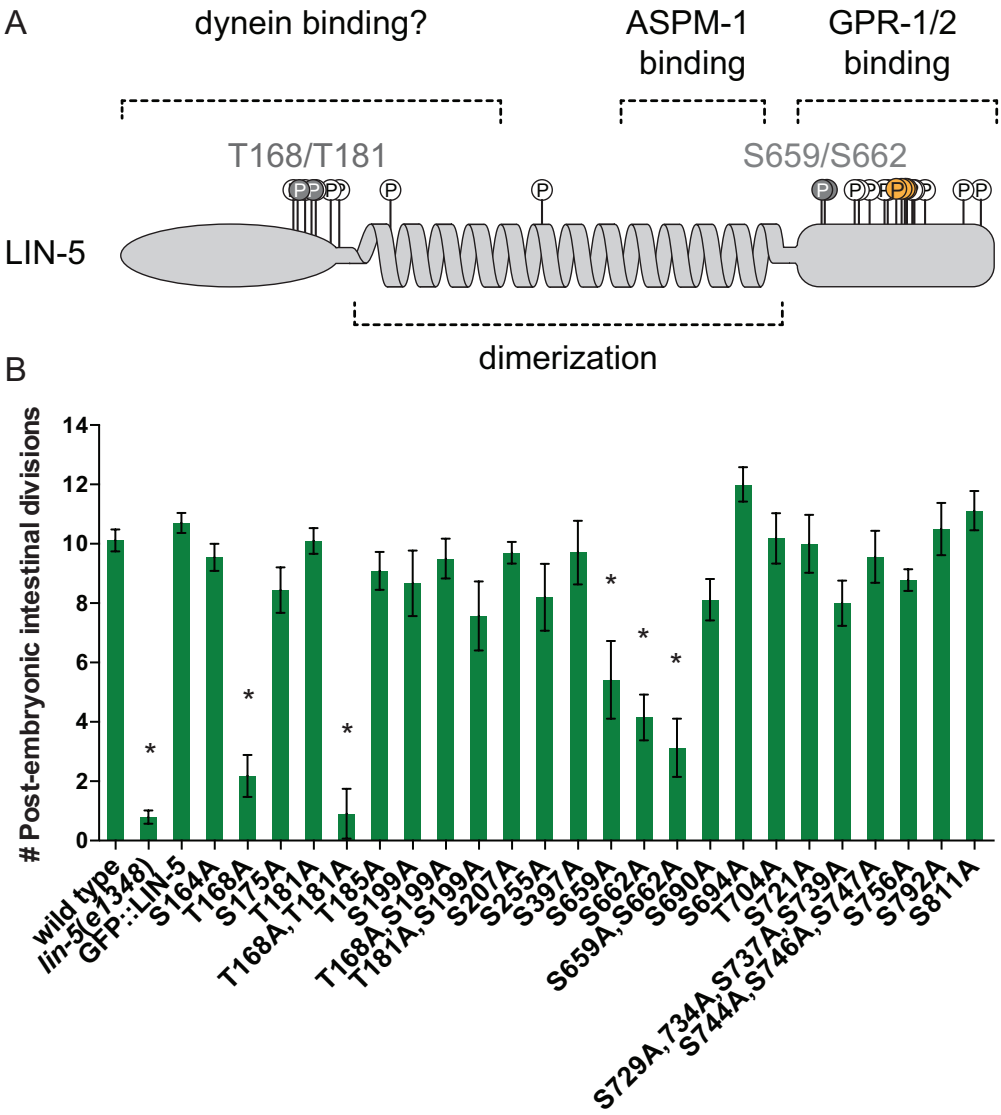

Figure 1 Phosphorylation of LIN-5 controls post-embryonic divisions in the intestine. **(A)** Overview of LIN-5 structure and binding domains. *In vivo* phosphorylated residues are indicated by open circles. Grey circles and numbers represent the phosphorylated amino acids essential for LIN-5 function. Yellow circles indicate previously identified residues phosphorylated by PKC-3 **(B)** Quantification of post-embryonic intestinal divisions in heterozygous *lin-5(e1348) / mIn1* (wild type), homozygous *lin-5(e1348)* animals and homozygous lin-5(e1348) animals expressing GFP-LIN-5 transgenes with alterations of the indicated phospho-site(s). n=7-22 (average: 15). Error bars, s.e.m. * P < 0.01 compared to wild type, Unpaired Students T-test.

Results

Multiple *in vivo* phosphorylated residues are critical for LIN-5 function

Previously, we described that at least 25 residues of LIN-5 are phosphorylated *in vivo* (Fig 1A) (Galli et al., 2011a). To acquire insight in which phosphorylations are functionally relevant, we replaced each phosphorylated serine or threonine with an alanine residue that cannot be phosphorylated. The relevant codon alterations were introduced in a cloned genomic *lin-5* DNA fragment and subsequently tested for functionally complementing the *lin-5*(*e1348*) null mutation *in vivo* (Lorson et al., 2000). In the presence of maternal product, *lin-5*(*e1348*) mutants fail to undergo chromosome segregation during postembryonic divisions and continue abortive mitoses (Albertson et al., 1978; Lorson et al., 2000; Srinivasan et al., 2003). Transgenes containing wild-type *lin-5* or *gfp*::*lin-5* coding sequences restored post-embryonic cell divisions in *lin-5*(*e1348*) null mutants (Fig 1B). However, these *lin-5* transgenes appeared susceptible to germline and somatic silencing, as reliable rescue and GFP-LIN-5 expression was observed only in the F1 generation. Hence, we examined transgenic F1 animals, focusing on vulval development and nuclear divisions in the intestine as a quantitative measure for LIN-5 function (Fig 1B).

Alanine substitutions of threonine 168, serine 659, and serine 662 were the only single amino acid changes that significantly compromised LIN-5 function *in vivo*. The T168A mutation had the strongest effect and almost completely eliminated the ability to restore intestinal divisions in *lin-5*(*e1348*) null mutants (Fig 1B). Interestingly, this strong effect was specific for the intestine: LIN-5^{T168A} expression allowed *lin-5* mutants to develop a normal vulva (S1 Fig). T168 forms part of an ideal consensus phosphorylation site (S/T*-P-x-K/R) for the mitotic cyclin-dependent kinase 1 (CDK-1) (Errico et al., 2010). CDK-1 is likely to regulate LIN-5, as multiple CDK-1 consensus sites are present in the LIN-5 N- and C-terminus, and CDK1 phospho-regulation of the NuMA C-terminus has been reported (Kotak et al., 2013; Seldin et al., 2013). We generated double alanine substitutions of T168 in combination with T181 or S199, two nearby candidate residues for CDK-1 phosphorylation. Strikingly, the transgene encoding LIN-5[T168A,T181A], but not LIN-5[T168A,S199A], completely failed to rescue intestinal mitoses and vulva formation in *lin-5*(*e1348*) mutants (Fig 1B and S1 Fig). Because phosphorylation of T181 by itself was not essential for post-embryonic divisions, T168 and T181 phosphorylations likely cooperate to control LIN-5 function.

The individual and combined S659A and S662A substitutions (LIN-5[S659A,S662A]) also reduced *lin-5*(*e1348*) complementation. By contrast, simultaneous alanine substitutions of serines 729, 734, 737, and 739 did not prevent LIN-5 function (Fig 1B and S1 Fig). In agreement with the latter result, PKC-3 (aPKC) phosphorylation of these residues inhibits LIN-5 function and is not required for cell division (Galli et al., 2011a). Our alanine-substitution experiments indicate that in addition to spatiotemporal regulation of LIN-5 by PKC-3, phosphorylation of LIN-5 residues in the dynein-interacting N-terminus and GPR-1/2 binding C-terminus may contribute to LIN-5 regulation *in vivo*.

In vitro kinase assays reveal candidate LIN-5 kinases

To determine whether CDK1 is indeed able to phosphorylate T168 and T181 of LIN-5, we performed *in vitro* kinase assays with recombinant GST-LIN-5 expressed in *E. coli* as a substrate. Indeed, immunopurified human CDK1-cyclin B phosphorylated GST-LIN-5, but not GST alone (S2A and S2B Fig). Analysis of *in vitro* phosphorylated GST-LIN-5 by mass spectrometry revealed extensive phosphorylation of T168, T181, and S744 of LIN-5 (S2B Fig). Additionally, peptides containing phosphorylated T704 and S756 were also found, and some other phosphopeptides less frequently. Taken together, CDK1-cyclin B phosphorylates LIN-5 *in vitro* at multiple sites including T168 and T181, and phosphorylation of T168 and T181 *in vivo* appears to be required for LIN-5 function.

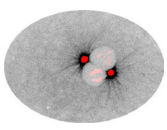

In contrast to T168 and T181, residues S659 and S662 are not part of apparent consensus phosphorylation sites. In our previous *in vivo* mass-spec data, the S659/S662 double phosphorylated peptides were abundant, while the corresponding unphosphorylated peptides were not detected (Galli et al., 2011a). This may indicate that S659 and S662 are constitutively phosphorylated in early embryos. To gain insight in which kinases may be involved, we examined LIN-5 phosphorylation *in vitro* with a series of polarity and cell cycle kinases, followed by mass spectrometry analyses. This revealed several residues that were phosphorylated by multiple kinases *in vitro* (Fig 2A). In striking contrast, S659 was only phosphorylated by GSK3, and none of the tested kinases phosphorylated S662 (Fig 2A). We considered several potential explanations for this lack of phosphorylation: the responsible kinase(s) may not have been included in the assays, residue S662 may not be accessible in the recombinant protein, or S662 phosphorylation may require a priming event. To test the latter possibility, we performed *in vitro* kinase assays with synthetic peptides that contain the S659 and S662 residues, either unphosphorylated or phosphorylated at one of the positions. Testing several kinases, we found that casein kinase 1 (CK1) efficiently phosphorylates S662, but only when the peptide contained a phosphorylated S659 residue (Fig 2B). As for the full length protein, only GSK3 phosphorylated S659 in the unphosphorylated peptide. Based on the combined *in vitro* data, we propose that GSK3 phosphorylation of residue S659 is a priming reaction for CK1 phosphorylation of S662. Highly similar phosphorylation has been reported for the Wnt/Frizzled co-receptor LRP6, with GSK3 priming for CK1 phosphorylation at similar sites (Niehrs and Shen, 2010; Zeng et al., 2005).

In addition to CDK1, GSK3 and CK1 phosphorylation, our analyses revealed phosphorylation of LIN-5 by the polarity kinase PAR-1. While several phosphopeptides were detected, some were rare and the quantitative software program MaxQuant only recognized the S397 and S739 LIN-5 residues as *in vitro* phosphorylated by PAR-1 (Fig 2A). S397 is located in the LIN-5 coiled coil region and its phosphorylation was previously observed in embryos (Fig 2A) (Galli et al., 2011a). However, our previous *in vivo* analysis failed to identify LIN-5 phosphorylations that were diminished after *par-1* RNAi (Galli et al., 2011a). Re-evaluation of the quantitative mass spectrometry data revealed that, although masked by an abundant unrelated peptide, the ratio between the phosphorylated and unphosphorylated S397 peptide was severely reduced in *par-1(RNAi)* embryos compared to control RNAi embryos (S3 Fig). In contrast, S739 phosphorylation was not significantly affected by *par-1* knockdown *in vivo* (Galli et al., 2011a). Taken together, we identified multiple phosphorylated LIN-5 residues as well as candidate kinases that could be important in the regulation of LIN-5 function. In addition to four adjoining residues phosphorylated by PKC-3 in the C-terminus, T168 and T181 may be phosphorylated by CDK-1, S397 by PAR-1, and S659 by GSK-3, to prime phosphorylation of S662 by CK1.

A 30 amino acid LIN-5 domain that includes S659/S662 mediates GPR-1/2 interaction

Both S659/S662 and the four residues phosphorylated by PKC-3 are located in the LIN-5 C-terminus which mediates GPR-1/2 binding (Fisk Green et al., 2004; Galli et al., 2011a). As phosphorylation could affect GPR-1/2 association, we wanted to define which LIN-5 residues are critical for GPR-1/2 binding. Testing deletion constructs in yeast two-hybrid assays confirmed that the LIN-5 C-terminal region is sufficient for GPR-1 association. GPR-1 interaction was observed for all truncated LIN-5 proteins except for those with deletions in the 609-671 amino acid region (Fig 3A). At the same time, including only the 609-671 LIN-5 fragment did not allow growth in this assay, possibly due to an inability of this short fragment to fold properly in yeast (Fig 3A). The essential 609-671 region does not contain serine 729, 734, 737, and 739 phosphorylated by PKC-3 *in vivo*, in agreement with our previous conclusion that PKC-3 phosphorylation of LIN-5 does not prevent interaction with GPR-1/2 (Galli et al., 2011a).

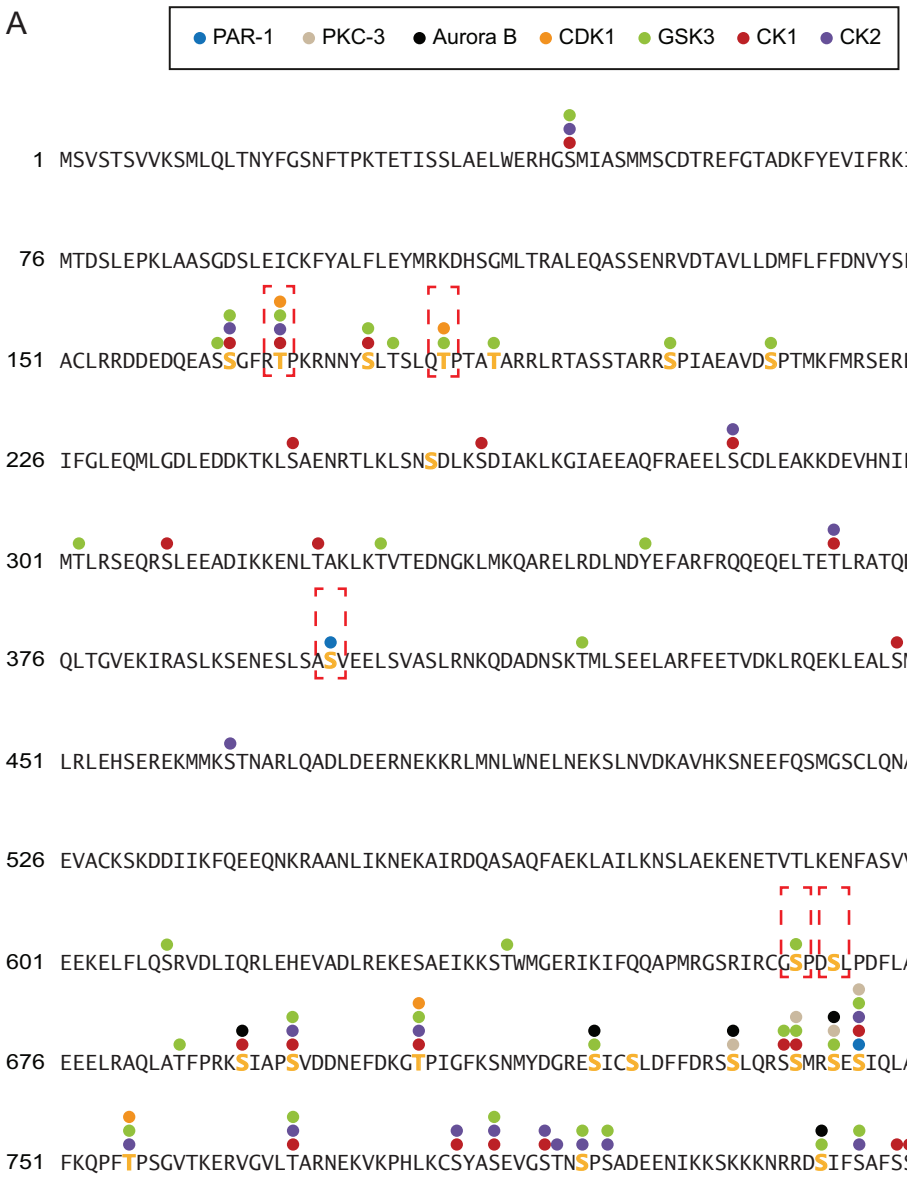

Figure 2 LIN-5 phosphorylation by cell cycle and polarity kinases in vitro. **(A)** Graphic overview of mass spectrometry analysis of *in vitro* kinase assays, revealing multiple target residues in LIN-5 phosphorylated by PAR-1, PKC-3, CK1, CK2, GSK3, CDK1 and Aurora kinases. Yellow residues indicate *in vivo* phosphorylated residues, brackets indicate essential residues identified in complementation assay. **(B)** Radioactive counts (CPM) of *in vitro* kinase assays with CK1 and GSK3 on a synthetic LIN-5 peptide 654-670 with or without synthetic incorporation of phosphorylated amino acids S659 or S662.

To identify specific LIN-5 amino acids required for GPR-1/2 interaction, we performed "reverse yeast two-hybrid screening". This method selects mutations that disrupt bait-prey protein interactions, making use of *URA3*-mediated conversion of 5-fluoroorotic acid (5-FOA) to a toxic product (Vidal et al., 1996a). The normal interaction between LIN-5 and GPR-1 leads to GAL4-controlled *URA3* expression in yeast two-hybrid assays, and causes cell death in the presence of 5-FOA. Thus, following mutagenesis of one of the binding partners, interaction-deficient alleles can be recovered from 5-FOA-resistant colonies (Vidal et al., 1996b). We used PCR-based random mutagenesis of LIN-5 prey fragments (amino acids 609-821), and isolated 163 5-FOA resistant yeast colonies in a reverse yeast two-hybrid screen (for details see Methods and Materials, S4A Fig). 89 colonies contained a single missense mutation in the LIN-5 coding sequences, together changing 15 different amino acids. Substitutions of 12 of these 15 individual amino acids caused loss of GPR-1 interaction again in the re-test (Fig 3B and 3C). The 12 affected residues were all located between amino acids 638-667 of LIN-5. Importantly, the interaction-defective alleles included missense mutations of the phosphorylated residues S659 and S662. In fact, S662 was found altered to glycine, cysteine and asparagine (S4B Fig). These data indicate that a 30 amino acid stretch in the LIN-5 C-terminal region, which includes the *in vivo* phosphorylated S659 and S662 residues, mediates the interaction with GPR-1.

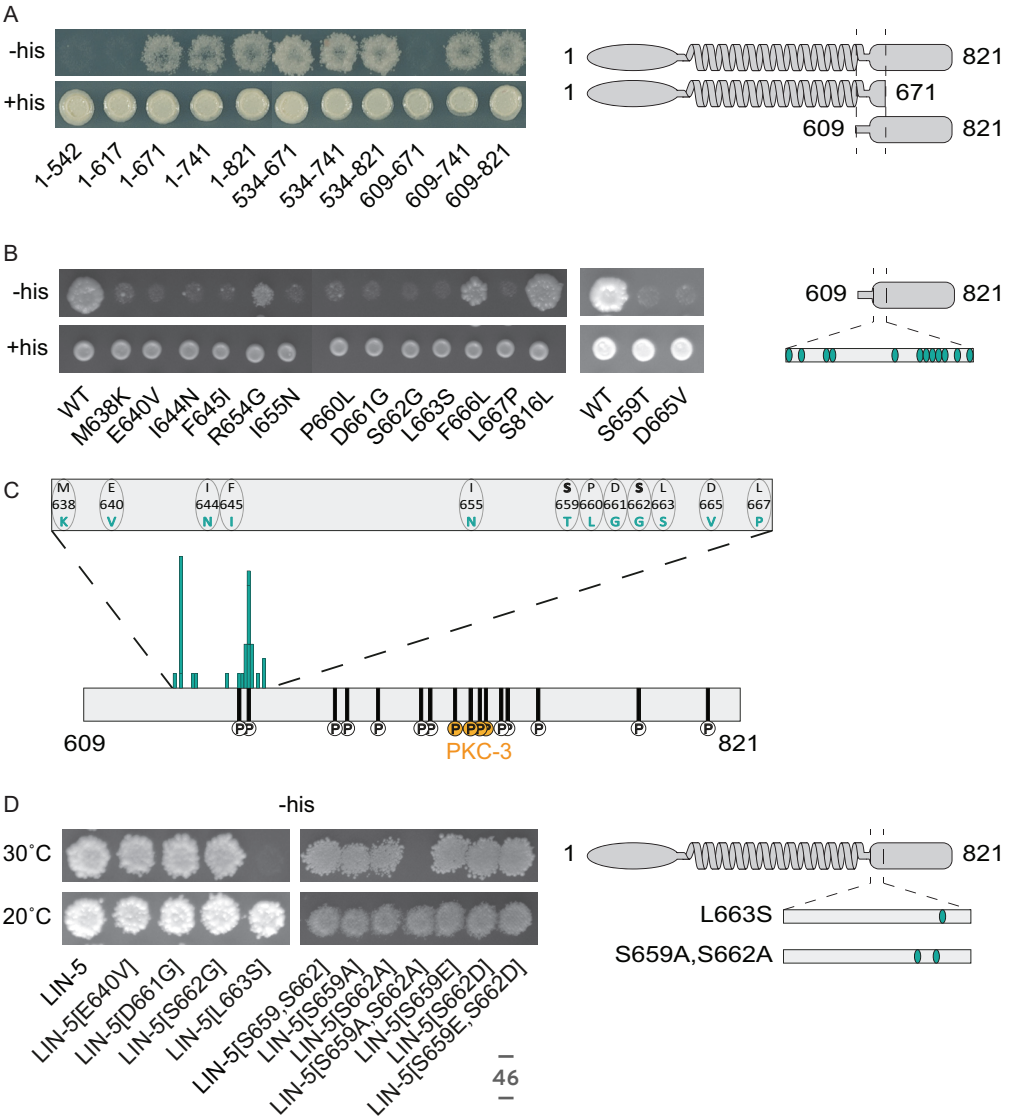

Following up on the interaction defective alleles, we noticed that the effect of missense mutations was substantially reduced when tested in the context of full length LIN-5, compared to the C-terminus only. Western blot analysis did not reveal substantial differences in protein levels compared to wild type (S5A Fig). The LIN-5 coiled-coil region promotes dimerization and is thereby expected to increase GPR-1 binding avidity. Only one of the four most frequently identified mutations, L663S, also interfered with full length LIN-5 binding to GPR-1 (Fig 3D, left panel). However, at a reduced temperature (20°C), this leucine 663 to serine (LIN-5[L663S]) mutation still allowed growth on selective media, indicating that GPR-1 interaction is not completely abolished. We also tested S659 and S662 phosphorylation-site mutants in the context of full length LIN-5. While the single mutations had little effect on GPR-1 binding, replacement of both serine 659 and 662 by alanine reduced GPR-1 interaction in yeast, as detected by lack of growth on -His plates at 30°C (Fig 3D, right panel). Phosphomimetic substitutions (S to D or E) of S659, S662, or both, did not reduce interaction (Fig 3D, right panel). These results are consistent with phosphorylation of S659 and S662 contributing to GPR-1/2 binding, and taking place in yeast as well as *C. elegans*. Taken together, our forward and reverse yeast two-hybrid assays identified LIN-5 residues that appear to mediate interaction with GPR-1/2, which are located within a 30 amino acid C-terminal domain. This includes S659 and S662, of which the phosphorylation *in vivo* likely contributes to GPR-1/2 binding.

Examining LIN-5 phosphoregulation *in vivo* by CRISPR/Cas9-mediated genome engineering

We used CRISPR/Cas9-mediated gene targeting to engineer *lin-5* alleles and examine the effects of amino acid substitutions *in vivo* (Chen et al., 2013; Dickinson et al., 2013; Kim et al., 2014; Waaijers et al., 2013). First, we created the *lin-5*[L663S] mutation by introducing a single nucleotide alteration in the endogenous *lin-5* locus. This resulted in a typical *lin-5* loss-of-function phenotype, with homozygous sterile, thin and uncoordinated larvae that fail to undergo chromosome segregation but continue abortive mitoses (Albertson et al., 1978; Lorson et al., 2000). We determined the number of nuclei in the intestine and ventral cord, following fixation and staining of DNA. In *lin-5*[L663S] mutants, both tissues contained severely reduced numbers of nuclei compared to the wild type, consistent with a failure to undergo chromosome segregation in most post-embryonic divisions (Fig 4A-4B, S6A Fig). Thus, a single change of amino acid L663 in the GPR-1-binding motif of LIN-5 results in strong loss-of-*lin-5* function. This result confirms the power of reverse yeast two-hybrid screening in identifying amino acids that affect protein-protein interactions *in vivo* (Vidal et al., 1996a).

Next, we used genome engineering to alter the *in vivo* phosphorylated residues T168, T181, S397, S659 and S662. For each residue, we created a non-phosphorylatable alanine substitution allele, as well as one or more potentially phosphomimetic alleles that contain aspartic acid or glutamic acid at the relevant positions. Alteration of the PAR-1 phosphorylated S397 residue had no apparent effect. Homozygous S397A and S397E animals were viable and showed normal development. Even close examination of LIN-5-mediated processes did not reveal abnormalities (See below; Fig 4C and Fig 4D, S6A and S6B Fig and S1 Video). Thus, although this phosphorylation occurs *in vivo*, it is by itself not a major determinant of LIN-5 function.

Figure 3 Yeast two-hybrid assays identify critical residues in LIN-5 for GPR-1 interaction. (A) Yeast two-hybrid analysis of DB::GPR-1 (bait) interaction with AD::LIN-5 (prey) fragments of varying sizes on Sc (synthetic complete) −Leu−Trp (+His, control) and Sc −Leu−Trp−His + 3-AT (-His, selection) plates. (B) Yeast two-hybrid analysis of DB::GPR-1 (bait) interaction with AD::LIN-5 (prey) fragments containing single amino acid changes on Sc −Leu−Trp and Sc −Leu−Trp−His + 3-AT plates. (C) Graphical representation of LIN-5 residues required for GPR-1 binding. Size of bars indicates frequency of found mutations, with every bar presenting a different amino acid change. (D) Yeast two-hybrid analysis of DB::GPR-1 (bait) interaction with AD::LIN-5 (prey) full length containing single amino acid changes on Sc −Leu−Trp−His + 3-AT plates at 20°C and 30°C.

Compared to our transgene rescue experiments (Fig 1B and S1 Fig), the effect of S659 and S662 alanine-substitution mutations in endogenous *lin-5* was quite mild. The *lin-5*[S659A,S662A] double mutant animals were viable, with only a slight reduction in intestinal nuclei number (S6A Fig), but displayed a significant increase in embryonic lethality (3.6±1.0% at 25°C, wild type 0.9±0.4%). The phosphomimetic *lin-5*[S659E,S662D] mutation did not cause embryonic lethality or larval defects, consistent with constitutive phosphorylation of these residues in early embryos (S6A Fig).

In stark contrast, alteration of the candidate CDK-1 phosphorylated residues in the N-terminus, T168 and T181 to alanine (*lin-5*[T168A,T181A]), aspartic acid (*lin-5*[T168D,T181D]) or glutamic acid (*lin-5*[T168E,T181E]), all resulted in typical *lin-5* mutant offspring. Regardless of the mutant combination, homozygous animals derived from heterozygous parents developed into sterile, thin and uncoordinated larvae, and showed severely impaired cell division during larval development (Fig 4A and Fig 4B). Importantly, substitution of threonine 168 and 181 with serine residues (*lin-5*[T168S, T181S]) did not lead to any detectable phenotype or defects in cell division (Fig 4A and Fig 4B). These observations and the *in vivo* phosphorylation of T168 and T181 indicates that phospho-regulation of T168 and T181 is critical for LIN-5 function, in agreement with the results of the transgene rescue experiments (Fig 1B and S1 Fig). Together, our targeted genome alterations identified several individual amino acids that are required for the *in vivo* function of LIN-5, including phosphorylated residues in the N-terminus and residues in the GPR-1 binding domain.

Figure 4 *In vivo* phenotypical analysis shows developmental defects in LIN-5 phosphomutants. **(A)** Quantification of intestinal nuclei following propidium iodide staining in homozygous LIN-5 phosphorylation mutants compared to wild type and *lin-5(e1348)* null animals. Null mutants are expected to contain 20 nuclei, wild type animals 32-34 nuclei. Individual values are plotted, n>11. **(B)** Quantification of P-cells and juvenile motor neurons in the ventral cord region P2-P10 in propidium iodide stained homozygous LIN-5 phosphorylation mutants compared to wild type and *lin-5(e1348)* null animals. Nuclei were counted in late larval stages of asynchronous populations of worms, with null mutants expected to have 24 nuclei (9 P cells and 15 juvenile motor neurons) and wild-type animals 65 nuclei. Individual values are plotted, n>11. **(C)** Analysis of hallmarks of the first 2 embryonic divisions in LIN-5 phosphorylation mutant, based on time-lapse DIC microscopy. Oscillations are plotted in percentage of embryo height, elongation and AB size as a percentage of embryo width, flattening and rotation as a total fraction of analyzed embryos. **(D, E)** Mean peak velocities (μm s−1) of anterior and posterior spindle poles measured in a 12.5 s time frame after spindle severing in one-cell embryos of the indicated genotypes, cultured at 25°C (D) or 20°C (E). Error bars: s.e.m. Statistical analyses: Unpaired Welch Students T-test, *P < 0.01 compared to wild type, ** P < 0.001 compared to wild type, *** P < 0.0001 compared to wild type, ns not significant.

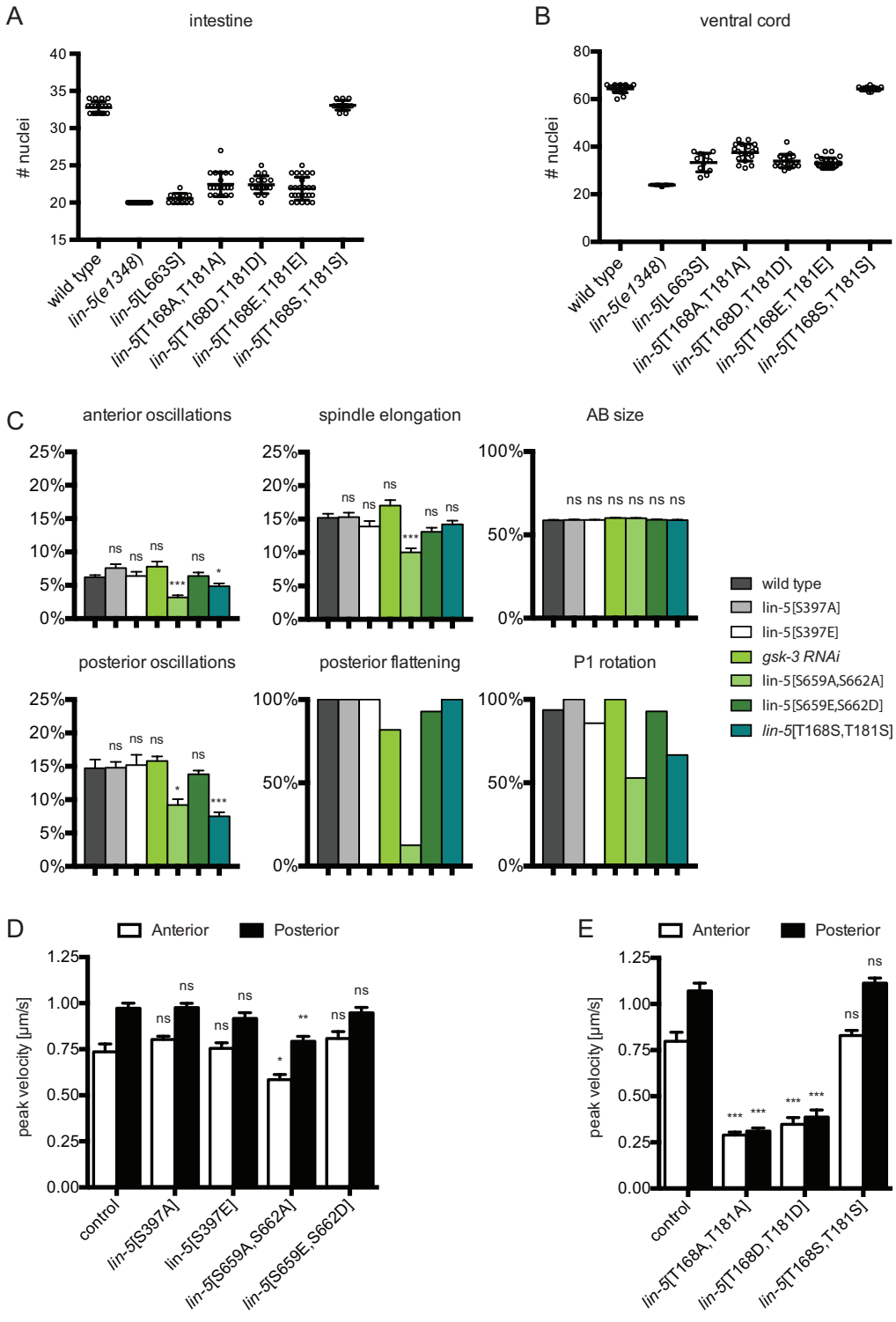
A
intestine
nuclei
wild type
lin-5(e1348)
lin-5[L663S]
lin-5[T168A,T181A]
lin-5[T168D,T181D]
lin-5[T168E,T181E]
lin-5[T168S,T181S]
B
ventral cord
nuclei
C
anterior oscillations
spindle elongation
AB size
posterior oscillations
posterior flattening
P1 rotation
wild type
lin-5[S397A]
lin-5[S397E]
gsk-3 RNAi
lin-5[S659A,S662A]
lin-5[S659E,S662D]
lin-5[T168S,T181S]
D
Anterior
Posterior
peak velocity [µm/s]
control
lin-5[S397A]
lin-5[S397E]
lin-5[S659A,S662A]
lin-5[S659E,S662D]
E
Anterior
Posterior
peak velocity [µm/s]
control
lin-5[T168A,T181A]
lin-5[T168D,T181D]
lin-5[T168S,T181S]

LIN-5 S659/S662 phosphorylation contributes to cortical pulling forces

Additional characterizations of the non-phosphorylatable and phosphomimetic mutants revealed insight in the functional contribution of LIN-5 phosphorylation. As the contribution of S659 and S662 phosphorylation appeared quite subtle, we examined the spindle in early embryos with substitutions of these residues in detail. In the wild type, meiosis completes after fertilization and results in the formation of a haploid maternal pronucleus, which migrates to meet the paternal pronucleus in the posterior, after which the adjoined pronuclei and centrosomes migrate to the center, rotate and form a spindle along the long axis of the zygote (Galli and van den Heuvel, 2008; Rose and Gönczy, 2014) (S1 Video). Observations with differential interference contrast (DIC) microscopy showed that these events all occur normally in *lin-5*[S659A,S662A] and *lin-5*[S659E,S662D] mutants. Subsequently, in wild-type embryos, the chromosomes become aligned at the metaphase plate and are segregated to opposite poles during anaphase. During spindle elongation, the posterior spindle pole oscillates extensively, while the anterior pole remains relatively steady. This coincides with spindle movement towards the posterior, and is followed by flattening of the posterior pole (S1 Video). Starting in anaphase, mutant embryos with non-phosphorylatable *lin-5*[S659A,S662A] deviated from the wild-type, while *lin-5*[S659E,S662D] mutants showed no phenotype. Specifically, *lin-5*[S659A,S662A] mutants showed significantly dampened oscillation of both the anterior and posterior pole, reduced spindle elongation, and nearly absent flattening of the posterior spindle pole (Fig 4C and S6B Fig). Nevertheless, both non-phosphorylatable and phosphomimetic S659/S662 mutants underwent asymmetric division of the zygote as normal, which resulted in the formation of a larger anterior blastomere (AB) and smaller germline precursor cell (P1). The spindle normally rotates by 90 degrees prior to division of the P1 blastomere (S1 Video). This failed to occur or was incomplete in 47.1% of the *lin-5*[S659A,S662A] two-cell embryos, compared to 6.3% and 7.3% incomplete rotation scored in wild type and *lin-5*[S659E,S662D] mutant embryos, respectively (Fig 4C and S6B Fig). As protein levels were comparable to wild type (S5B Fig), these results suggest that cortical pulling forces are reduced in *lin-5*[S659A,S662A] mutants. Interestingly, this does not disrupt the asymmetry of the first division and has only a small effect on viability.

To determine cortical pulling forces more directly, we performed spindle severing assays with a UV laser beam (Grill et al., 2001). Confirming our DIC analyses, the peak velocities of spindle pole movements were significantly reduced in *lin-5*[S659A,S662A] embryos (anterior pole 20.5%, posterior pole 18.4% reduced compared to wild type) (Fig 4D, S2 Video and S5 Video). Similar experiments performed with *lin-5*[S659E,S662D] mutant embryos and PAR-1 phosphorylation site mutants (S397A and S397E) did not reveal significant divergence from the wild type (Fig 4D, S3 Video, S4 Video and S6 Video). These data support the conclusion that phosphorylation of S659 and S662 contributes to cortical pulling forces, both in the anterior and posterior, and thereby to spindle pole oscillation, spindle elongation, posterior pole flattening and spindle rotation in P1. Moreover, the finding that pulling forces, albeit reduced, remained asymmetric in *lin-5*[S659A, S662A] mutants explains why these mutants show normal asymmetry of the first division, and normal sizes of the AB and P1 blastomeres.

We wondered whether Wnt-signaling could locally control GSK-3 kinase activity to affect LIN-5 S659, S662 phosphorylation and asymmetric cell division. In the EMS blastomere of the 4-cell embryo, the spindle rotates from a left/right to anterior/posterior position to correctly specify and position the E and MS daughter cells (Sulston et al., 1983). This rotation is redundantly controlled by MES-1/SRC-1 and MOM-2/MOM-5 Wnt/Frizzled signaling pathways (Bei et al., 2002). We examined whether the Wnt pathway contributes to EMS spindle rotation through phosphorylation of LIN-5[S659,S662]. Making use of a *mes-1*(*bn74*ts) mutant strain expressing GFP-b-tubulin, we observed normal spindle rotation in *lin-5*[S659A,S662A] mutant embryos, with only one of 13 embryos showing a tilted spindle angle in the EMS blastomere (S6C Fig). *mes-1*(*bn74*ts) ; *lin-5*[S659E,S662D] mutant embryos showed an occasional failed rotation or tilted spindle

angle. In control *mes-1*(*bn74*ts) ; *gsk-3(RNAi)* mutants, the EMS spindle failed to rotate in 9/11 embryos (S6C Fig). This clear difference in phenotype shows that LIN-5 S659 phosphorylation is not the major contribution of GSK-3 in EMS spindle rotation. Asymmetric divisions of epithelial seam cells in the *C. elegans* epidermis also depend on a Wnt/b-catenin asymmetry pathway (Takeshita and Sawa, 2005; Wildwater et al., 2011), and remained normal in *lin-5*[S659A,S662A] and *lin-5*[S659E,S662D] mutants. Thus, evidence for developmental regulation of LIN-5–GPR-1/2 interaction through Wnt-signaling was not obtained. Instead, absence of unphosphorylated S659/S662 peptides in our mass spectrometry analyses, and the wild-type appearance of phosphomimetic mutants point to constitutive phosphorylation of the S659/S662 residues.

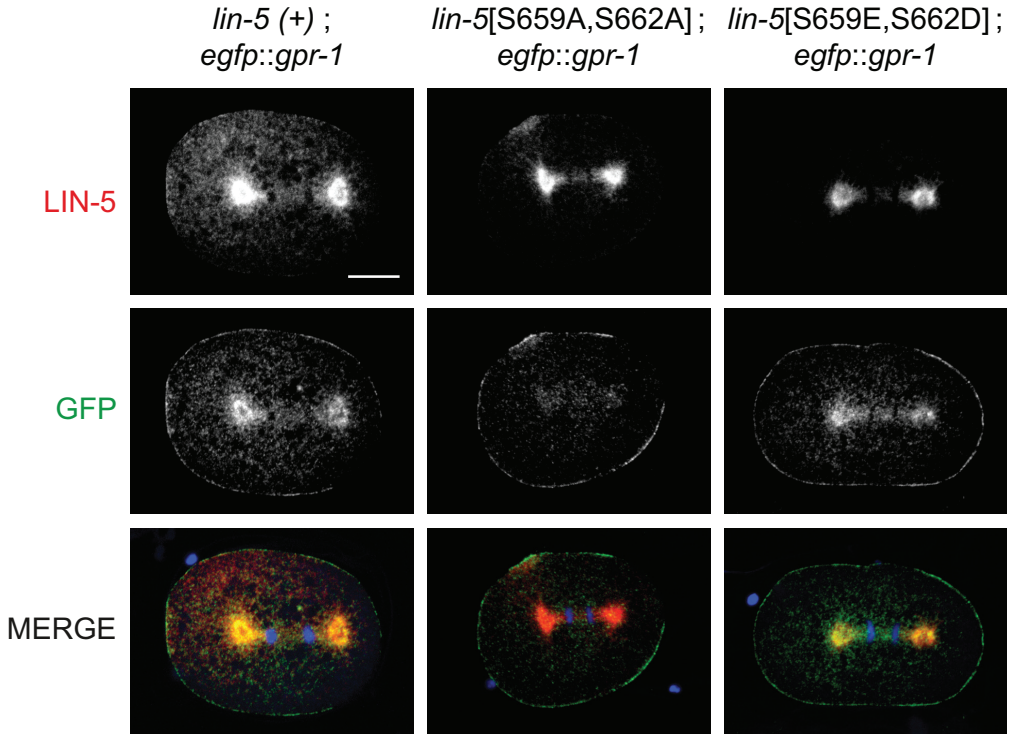

Figure 5 Localization of LIN-5 and GPR-1 in phosphorylation mutants. Immunohistochemistry staining of embryos expressing wild-type or phosphomutant *lin-5* and endogenously tagged *egfp::gpr-1*. Representative images of one-cell embryos in anaphase, stained with anti-LIN-5 (red) and anti-eGFP (green) antibodies, and DAPI to visualize DNA. All images taken with same exposure time, objective and magnification. Anterior to the left, scale bars 10 µm.

GPR-1 fails to localize to the centrosome in LIN-5[S659A,S662A] mutants

Our yeast two-hybrid data showed reduced interaction between LIN-5[S659A,S662A] and GPR-1 compared to wild type, which likely explains the reduced pulling forces observed *in vivo*. We examined whether the colocalization between LIN-5 and GPR-1 *in vivo* depends on LIN-5 phosphorylation. Hereto, we generated strains with *lin-5*[S659,S662] double phosphorylation-site alterations in combination with *egfp::gpr-1*, a CRISPR/Cas9-mediated knockin allele of the endogenous *gpr-1* locus. Immunohistochemical detection of eGFP and LIN-5 showed

normal colocalization of LIN-5 and GPR-1 in phosphomimetic *lin-5*[S659E,S662D] mutants at the centrosomes and cell cortex (Fig 5, S7 Fig; note that LIN-5 becomes clearly visible at the cortex only after the one-cell stage). In contrast, in *lin-5*[S659A,S662A] mutant embryos, GPR-1 localized to the cortex but no longer accumulated at the centrosomes (Fig 5). Notably, GPR-1/2 localization at the cortex primarily depends on association with the GOA-1 and GPA-16 Gα proteins and is required for pulling forces, whereas ASPM-1–LIN-5 anchors GPR-1/2 at the centrosome without early embryonic requirement (Srinivasan et al., 2003; van der Voet et al., 2009). Thus, while the loss of centrosomal GPR-1 appears to confirm a reduced binding affinity for LIN-5[S659A,S662A] compared to wild-type LIN-5, the reduced pulling forces likely result from a similarly reduced affinity between these proteins at the cortex. Nevertheless, LIN-5 still localized to the cortex in *lin-5*[S659A,S662A] mutants (S7 Fig). This likely reflects different dynamics of the two complexes; with rapid exchange of LIN-5 at the cortex while centrosomal GPR-1/2 accumulation likely depends on prolonged LIN-5 association. The combined observations in yeast two-hybrid assays, phenotypic analyses, and protein localization studies strongly indicate that phosphorylation of LIN-5 residues S659 and S662 contributes to the affinity of the LIN-5/GPR-1/2 interaction *in vivo*.

A potential LIN-5 phosphorylation-dephosphorylation cycle in dynein recruitment

Characterization of the CDK-1 phosphorylation site mutants required a different strategy, as homozygous *lin-5*[T168A,T181A] and *lin-5*[T168D,T181D] mutants are fully sterile. To be able to examine the effects of these mutations in early embryos, we created trans-heterozygotes carrying these mutations and *egfp*::*lin-5*, a functional CRISPR/Cas9-generated knockin allele of endogenous *lin-5*. The *egfp*::*lin-5* allele served both as a visible balancer for the *lin-5* phosphorylation site mutations, and allowed selective knockdown of functional *lin-5* by RNAi against *egfp*. This strategy allowed us to obtain and characterize early embryos with CDK1-phosphorylation site alterations in LIN-5.

Control immunohistochemical staining experiments confirmed that *egfp* RNAi treatment of homozygous *egfp*::*lin-5* adults completely removed LIN-5 and eGFP from the offspring (S8 Fig). Following *egfp* RNAi treatment of heterozygous animals with wild type *lin-5 (lin-5(+) / egfp::lin-5)*, LIN-5 localized normally, but the eGFP staining was lost (Fig 6). These results demonstrate that the RNAi effect remains specific for *egfp::lin-5* and does not carry over to the untagged *lin-5* allele. Testing balanced *lin-5*[T168A,T181A] and *lin-5*[T168D,T181D] animals the same way, we observed that the mutant LIN-5 proteins are expressed and localize as normal to the cortex and centrosomes, while the early embryonic divisions were clearly defective (Fig 6 and S5C Fig). Interestingly, *lin-5*[T168A,T181A] and *lin-5*[T168D,T181D] showed similar abnormalities, emphasizing the critical role for the *in vivo* phosphorylated threonine residues at these positions.

Using the above-described method, we also performed live imaging by time-lapse DIC microscopy and spindle severing experiments with *lin-5*[T168A,T181A] and *lin-5*[T168D,T181D] mutant embryos. Again, the defects observed in both mutants resembled *lin-5* strong loss-of-function (Fisk Green et al., 2004; Lorson et al., 2000), and cortical pulling forces were greatly reduced in both mutants (Fig 4E, S7 Video and S8 Video). In contrast, homozygous *lin-5*[T168S,T181S] mutants showed normal spindle pulling forces (Fig 4E and S9 Video). This indicates that the two threonine residues are not essential per se, but phosphorylation and de-phosphorylation at these sites is likely critical. The *lin-5*[T168S,T181S] mutants did show dampened spindle oscillation, which might result from somewhat different kinetics of threonine versus serine phosphorylation and dephosphorylation in CDK1 substrates (Suzuki et al., 2015).

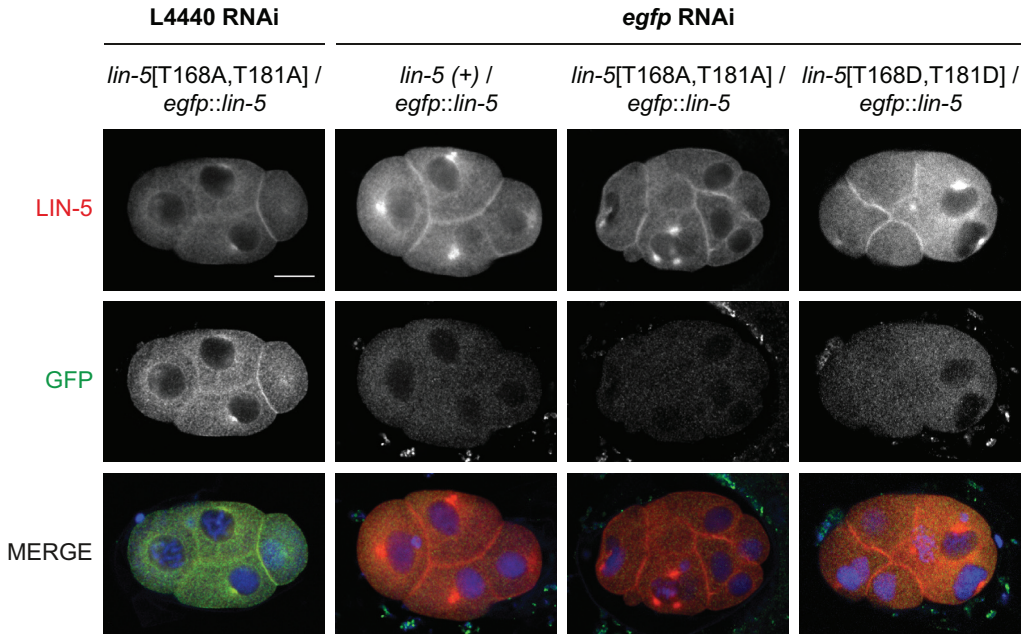

Figure 6 T168 and T181 mutants show normal subcellular LIN-5 localization. Immunohistochemistry staining of embryos heterozygous for *egfp::lin-5* and wild-type or phosphomutant *lin-5* as indicated. L4 animals were treated with feeding RNAi against control or *egfp* RNAi to specifically remove *egfp::lin-5* function, 48 hours before fixation of their embryos. Representative fluorescence microscopy images of embryos stained with anti-LIN-5 (red) and anti-GFP (green) antibodies, and DAPI to visualize DNA. All images taken with same exposure time, objective and magnification. Anterior to the left, scale bars 10 μm.

Because the N-terminus of LIN-5 is implicated in the recruitment of dynein (Kotak et al., 2012), we crossed both mutants with an *mCherry*::*dhc-1* strain, in which the mCherry tag was introduced into the endogenous dynein heavy chain gene by CRISPR/Cas9-mediated knockin. This homozygous *mCherry*::*dhc-1* strain is viable and develops as normal. mCherry::DHC-1 was diffusely detected in the cytoplasm, and distinctly localized at the nuclear envelope, kinetochores, astral microtubules, spindle poles and cell cortex. Localization of dynein was dynamic during all stages of mitosis, but cortical dynein was barely detectable at the one-cell stage. However, following treatment of permeabilized embryos with nocodazole to depolymerize microtubules, mCherry::DHC-1 accumulated on the cell cortex of one-cell embryos in metaphase and anaphase (Fig 7A and S9 Fig). Strikingly, this cortical dynein localization was abolished by *lin-5* RNAi, and did not occur in *lin-5*[T168A,T181A] and *lin-5*[T168D,T181D] mutant embryos (Fig 7A). Since these mutant LIN-5 forms localize to the cell cortex, T168 and T181 are critical for the function of LIN-5 as a cortical dynein anchor.

In addition to cortical localization of dynein in mitosis, LIN-5 is also required for dynein recruitment to the poles of the meiotic spindle (van der Voet et al., 2009). Accumulation of dynein at the spindle poles, as well as the cell cortex, occurs coincident with anaphase onset of meiosis I and II, and is needed for spindle rotation and expulsion of chromosomes into a polar body (Crowder et al., 2015; Ellefson and McNally, 2011; van der Voet et al., 2009). While homozygous *lin-5*[T168S,T181S] mutants showed normal meiosis, we observed polar body absence and abnormally large polar bodies in eGFP::LIN-5-depleted *lin-5*[T168A,T181A] and *lin-5*[T168D,T181A]

embryos, consistent with *lin-5* loss of function. To examine meiotic spindle rotation and dynein localization in such embryos, we combined the *lin-5* mutations, balanced by *egfp::lin-5*, with homozygous *gfp::tbb-2* βtubulin and mCherry::DHC-1 dynein reporters (Fig 7B, S10 Video, S11 Video, S12 Video, S13 Video, S14 Video, S15 Video, S16 Video, S17 Video, S18 Video, S19 Video, S20 Video and S21 Video). In a control strain with wild-type LIN-5, spindle rotation and dynein accumulation occurred in 10 of 11 embryos (the one exception showed rotation but only weak mCherry::DHC-1 accumulation) (Fig 7B left, S10 Video, S11 Video and S12 Video). Examination of *egfp* RNAi treated *egfp::lin-5* embryos with combined DIC and fluorescence microscopy revealed normal diffuse association of DHC-1 with the meiotic spindle in meiotic prophase, followed by gradual loss of mCherry::DHC-1 from the anaphase spindle, rather than accumulation of dynein at the poles. The failure in dynein localization coincided with failure to rotate the meiotic spindle (Fig 7B). These results agree with our previously reported meiotic *lin-5* RNAi phenotype (Srinivasan et al., 2003; van der Voet et al., 2009), although this time we also observed abnormally elongated meiotic spindles in meiosis II in a subset of the embryos, as has been reported for dynein complex subunits (Crowder et al., 2015). eGFP::LIN-5-depleted *lin-5*[T168A,T181A] and *lin-5*[T168D,T181D] embryos were indistinguishable from *lin-5* knockdown mutants (Fig 7 B, S13 Video, S14 Video, S15 Video, S16 Video, S17 Video, S18 Video, S19 Video, S20 Video and S21 Video).

In conclusion, substitution of LIN-5 T168 and T181 with non-phosphorylatable alanine or phosphomimetic aspartic acid residues creates a severe defect in LIN-5-mediated dynein recruitment. In contrast, replacement of the same residues with phosphorylatable serine residues did not compromise LIN-5 function (Fig 4A, 4B, 4E). Combined with the available literature (Ellefson and McNally, 2011; McCarthy Campbell et al., 2009; van der Voet et al., 2009), these data point to CDK-1-mediated phosphorylation and subsequent dephosphorylation of the LIN-5 N-terminus as a critical step in dynein recruitment to the meiotic spindle and cell cortex (see below).

Discussion

In this study, we investigated whether the extensive *in vivo* phosphorylation of the LIN-5^{NuMA} protein is important for chromosome segregation and cell cleavage plane determination. We combined *in vivo* and *in vitro* phosphorylation analysis, identified critical phosphorylated LIN-5 residues by complementation, and defined the LIN-5–GPR-1 interaction domain by reverse yeast two-hybrid screening. Using this information, we created phosphosite mutants and tagged alleles by genetic engineering, and determined the *in vivo* contribution of individual phosphorylated residues by protein localization studies, time-lapse microscopy and spindle severing experiments. The combined data indicate that a variety of cell cycle and polarity kinases phosphorylate LIN-5, with specific phosphorylations promoting pulling force generation while others inhibit LIN-5 function. The combined phosphorylations of the LIN-5 N-terminus and C-terminus are critical in the spatiotemporal control of cortical pulling forces, and thereby for correct chromosome segregation, and spindle positioning (Fig 8).

A

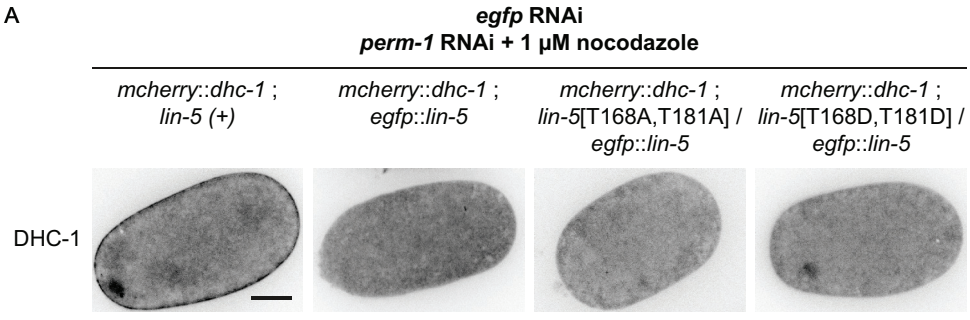

cortical DHC-1	8/10 embryos	0/15 embryos	0/14 embryos	0/15 embryos
parents	N/A	N/A	6	6

B

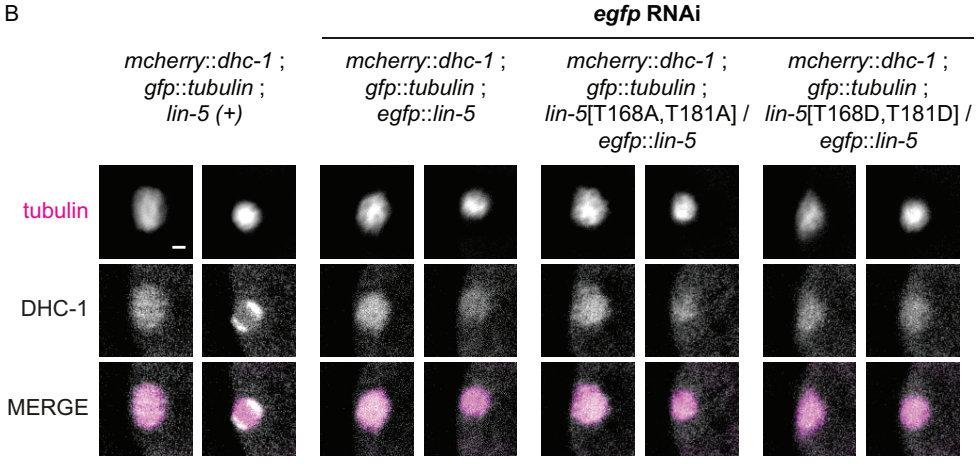

focus DHC-1	10/11 embryos	0/10 embryos	0/17 embryos	0/16 embryos

Figure 7 DHC-1 fails to accumulate at meiotic spindle poles in LIN-5 T168, T181 phosphosite mutants. **(A)** Representative still images of *mcherry::dhc-1; lin-5*[T168,T181] variant one-cell embryos treated with *perm-1* RNAi, *egfp* RNAi and 1 µM nocodazole, and imaged by spinning disk confocal microscopy. The number of embryos with cortical mCherry::DHC-1 is indicated, with "parents" indicating the number of animals from which embryos were analyzed. All images were taken with the same objective, magnification, and exposure time. Anterior to the left, scale bars 10 µm. **(B)** Representative snapshots of live imaging of *mcherry::dhc-1 ; tubulin::gfp ; lin-5*[T168,T181] meiotic embryos treated with *egfp* RNAi, and imaged by wide field microscopy. Time interval between prophase and anaphase is 100 seconds. All images were taken with same exposure time, objective and magnification. Anterior to the left, scale bars 2 µm.

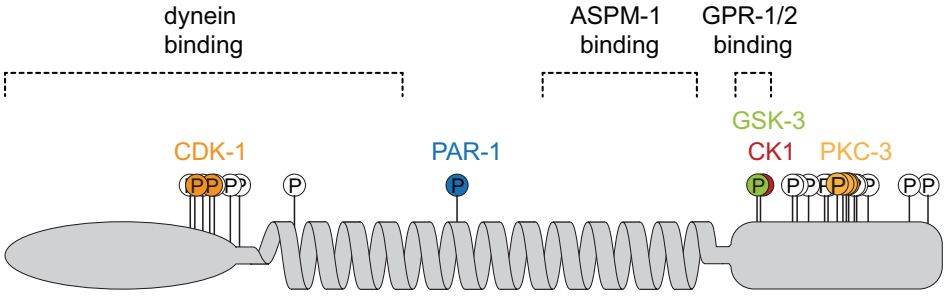

phosphorylated sites	kinase	phenotype
T168, T181	CDK-1	loss of cortical dynein and strong loss of pulling forces
S397	PAR-1	none observed
S659, S662	GSK-3, CK1	reduced GPR-1 binding and reduced pulling forces
S729, S734, S737, S739	PKC-3	increased anterior pulling forces

Figure 8 Summary of the proposed critical phosphorylations of LIN-5 by CDK-1, PAR-1, GSK3, CK1 and PKC-3. Overview of how phosphorylation-site mutations affect LIN-5 function *in vivo* in regulating cortical pulling forces that position the mitotic spindle and contribute to chromosome segregation.

CRISPR/Cas9-mediated genomic engineering has added an important tool to a powerful genetic system, and more efficient procedures are continuously developed (Arribere et al., 2014; Dickinson et al., 2015; Kim et al., 2014; Paix et al., 2015; Waaijers and Boxem, 2014; Ward, 2014). The use of CRISPR/Cas9 allowed us to precisely alter one or two codons of specific serine/threonine residues within the normal genetic background. Using knockin alleles eliminates unwanted effects of transgene overexpression or silencing. In particular transgene silencing has long hampered *lin-5* studies and was also observed in our complementation studies. Transgene expression levels that are close to a threshold level may explain why the *lin-5*[S659A,S662A] mutation showed a strong loss-of-function phenotype, while the effect of the same mutations introduced in the endogenous locus was less severe. In addition to phospho-site mutations, we also created tagged endogenous alleles of *lin-5*, *gpr-1* and *dhc-1* for fluorescent fusion protein expression. This allowed the development of a novel method for analysis of early lethal mutations. This method makes use of a functional eGFP-tagged allele, which acts as a visible balancer and allows the specific removal of wild-type function by *egfp* RNAi.

In a previous study, we revealed *in vivo* kinase activity through differential labeling of *C. elegans* cultures with stable nitrogen isotopes, followed by kinase knockdown and quantitative analysis of phosphopeptides by mass spectrometry (Galli et al., 2011a). This strategy worked well for PKC-3, but various limitations can prevent detection of kinase-substrate relations *in vivo*. The phosphorylation of LIN-5 by PAR-1 was missed in our previous analysis, because of overlap between the relevant LIN-5 phosphopeptides and unrelated peptides. Identification of mitotic substrates of CDK-1 is difficult *in vivo*, because CDK-1 knockdown results in complete sterility and arrest of fertilized oocytes before completion of meiosis (Boxem et al., 1999). Casein kinase I, in turn, is represented by 87 family members in *C. elegans* (Plowman et al., 1999), making it less likely that knockdown experiments will reveal a quantitative difference in substrate phosphorylation. The *in vitro* kinase assays in the current study revealed candidate kinases that were otherwise difficult to detect. The PAR-1 *in vitro* kinase assays pointed to a specific LIN-5

phosphorylation that was subsequently confirmed by our *in vivo* data. The *in vitro* phosphorylation of peptides with single phosphorylated residues was instrumental in detecting a probable two-step mechanism for S662 phosphorylation by CKI, following a priming phosphorylation by GSK3. Thus, while detecting direct phosphorylation *in vivo* remains the ultimate goal, *in vitro* assays continue to provide meaningful insight.

The combined *in vitro* and *in vivo* kinase analyses strongly suggest that PAR-1 phosphorylates LIN-5 at serine 397. Replacing this serine with non-phosphorylatable alanine or phosphomimetic glutamic acid apparently did not affect viability, development, cell division, chromosome segregation or spindle pulling forces. In fact, many phosphorylations that occur *in vivo* may be bystander rather than regulatory events, and determining which phosphorylations are critical *in vivo* has received great attention in the current study. The first selection came from alanine substitution mutagenesis combined with complementation of a *lin-5* null mutation. This revealed that 4 of the 25 phosphorylated residues are critical for LIN-5 function. As we could only score larval divisions in this assay, we cannot exclude that additional phosphorylations may be critical during embryogenesis. Remarkably, 2 of the 4 critical residues form part of a probable GPR-1/2 binding domain, while the other 2 appear to mediate contact with dynein at the cortex.

We defined the GPR-1/2 binding domain through screening for LIN-5 residues that are essential for GPR-1/2 interaction in yeast two-hybrid assays. The strong clustering of missense mutations in this screen combined with results from deletion analyses suggests a short linear GPR-interaction epitope. This is in full agreement with results from crystal structure studies of the related NuMA-LGN complex. The TPR repeats in the N-terminal half of LGN form helix-turn-helix repeats that together organize into a superhelical bundle (Culurgioni et al., 2011; Zhu et al., 2011). The inner surface of this bundle forms a binding channel for an extended NuMA peptide of 28 amino acids (Zhu et al., 2011). Many electrostatic and hydrogen interactions between side chains of the NuMA peptide and TPR motifs together provide a high affinity binding site.

The TPR-repeat interaction site in LIN-5 resembles that of NuMA in size, position, and overall amino-acid composition. The exact residues are not well-conserved, however, probably because the many amino acids that contribute weak interactions provide a limited biological constraint for the conservation of individual amino acids. Notably, the core of the binding site contains EPEQLDDW in human NuMA and SPDSLPDF in LIN-5, sharing three identical and two similar residues as well as negative charge. The NuMA peptide contains four acidic residues (D, E), while two D residues and two phosphorylated serines are negatively charged in the LIN-5 peptide.

Phosphorylation offers the opportunity to regulate LIN-5–GPR-1/2 binding. In fact, dual GSK3 and CK1 phosphorylation of the LRP6 Wnt-co-receptor regulates the interaction of LRP6 with axin (Wu et al., 2009; Zeng et al., 2005). We did not obtain evidence to support developmentally regulated LIN-5–GPR-1 binding. Alanine substitution of S659 and S662 significantly reduced spindle pulling forces, but division of the zygote, EMS blastomere and seam cells continued to be asymmetric. The latter types of divisions depend on the Wnt/β-catenin asymmetry pathway, which in EMS positions the spindle redundantly with *mes-1/src-1* signaling (Bei et al., 2002). Even the combined *lin-5*[S659A,S662A] mutation and *mes-1* knockdown did not interfere with A-P positioning of the spindle in EMS. Moreover, we could functionally replace serine 659 and 662 with glutamic and aspartic acid, suggesting that charge, rather than phospho-regulation, is critical for GPR-1/2 interaction.

A contribution of CDK-1 phosphorylation in LIN-5 regulation was expected. CDK1/cyclin B kinases are the master regulators of mitosis that phosphorylate hundreds of substrate proteins (Errico et al., 2010; Holt et al., 2009; Olsen et al., 2010). The LIN-5 N- and C-terminus and corresponding domains in NuMA contain multiple CDK1 consensus sites. CDK1/cyclin B has been shown to regulate Xenopus and human NuMA through phosphorylation of the C-terminus

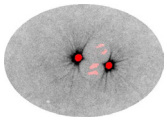

(Gehmlich et al., 2004; Kotak et al., 2013). Specifically, phosphorylation at T2055 interferes with the cortical localization of NuMA, thereby inhibiting dynein recruitment until CDK1/cyclin B is inactivated at the metaphase/anaphase transition (Kotak et al., 2013). Our results indicate that this temporal regulation may also involve critical phosphorylation of the dynein-interacting N-terminus of NuMA by CDK1/Cyclin B.

In *C. elegans*, dynein recruitment to the meiotic spindle and cell cortex, as well as mitotic pulling forces, depend on activation of the anaphase promoting complex/cyclosome (APC/C), and inactivation of CDK-1/Cyclin B (Ellefson and McNally, 2011; McCarthy Campbell et al., 2009; van der Voet et al., 2009). Thus, phosphorylation of specific mitotic substrates by CDK-1/Cyclin B is likely to inhibit dynein recruitment and pulling force generation. A recent study identified the p150 dynactin subunit as a likely candidate for inhibition by CDK-1/cyclin B phosphorylation (Crowder et al., 2015). Our results point to the LIN-5 N-terminus as another critical target for CDK-1 regulation. Supporting this conclusion, T168, T181 are part of CDK consensus sites, are phosphorylated *in vivo*, and are efficiently phosphorylated by CDK1/Cyclin B *in vitro*. Substitution of LIN-5 T168 and T181 with phosphomimetic glutamic acid or aspartic acid residues resulted in strong loss of LIN-5 function, supporting that CDK-1 phosphorylation normally inhibits LIN-5. More surprising, an indistinguishable phenotype was observed following T168 and T181 replacement with non-phosphorylatable alanine. This could indicate that the threonine residues are critical for LIN-5 folding, or that phosphorylation of these threonines in the N-terminus also contributes to dynein recruitment. In stark contrast to alanine substitution, replacement of the same residues with phosphorylatable serine had no detectable effect on pulling forces, meiotic and mitotic cell divisions, viability and fertility. While other explanations are possible, these data are consistent with a required sequential CDK-1 phosphorylation and dephosphorylation of LIN-5 T168 and T181. Therefore, we propose a two-step model, in which CDK-1/cyclin B induces the assembly of a LIN-5 pre-force generating complex in prometaphase. Subsequent removal of the phosphates, which follows CDK inactivation by the APC/C at anaphase onset, promotes interaction of this complex with dynein.

Many of the lessons learned from studies in worms and flies have subsequently been found to apply broadly to the animal kingdom. The initial discovery of LIN-5 requirement in spindle positioning in *C. elegans* (Lorson et al., 2000) has contributed to identifying similar functions for NuMA in mammalian systems (Lechler and Fuchs, 2005). It will be intriguing to find out to what extent the phospho-regulation of pulling forces translates from *C. elegans* to mammalian systems, and specifically whether reversible CDK1 phosphorylation of the NuMA N-terminus controls dynein interaction and spindle positioning.

Materials and methods

C. elegans strains

Strains were cultured on nematode growth medium plates, seeded with *Escherichia coli* OP50 as previously described (Brenner, 1974). Animals were maintained at 20°C, unless stated otherwise. All strains used in this study are found in Table S1. Genome modifications in strains SV1568, SV1569, SV1586, SV1588, SV1589, SV1590, SV1600, SV1619, SV1621, SV1622, SV1695 and SV1901 were introduced by making use of CRISPR/Cas9 genome editing as described below.

Post-embryonic analysis of LIN-5 phosphomutants

For functional analysis of wild type and phosphomutant LIN-5, 5 ng/µl *Plin-5*::*gfp*::*lin-5* DNA, together with 5 ng/µl *Psur-5*::*dsRed* and 25 ng/µl Lambda DNA (Fermentas), was injected into

the gonad of SV918 young adults. *Psur-5::dsRed* positive F1 progeny were selected making use of a fluorescence stereo microscope (Leica, MZ16F). After this, *lin-5*(*e1348*) homozygous animals were selected based on absence of pharyngeal *Pmyo-2*::*gfp*, expressed from the *mIn1* balancer chromosome. Rescue analysis of *lin-5* null animals was performed by Differential Interference Contrast and fluorescence microscopy, using a Zeiss Axioplan microscope. Intestinal nuclei were counted only in animals expressing *Psur-5*::*dsRed* in all intestinal nuclei. Vulva development was assayed for all animals L4 and older.

For quantification of cell numbers in CRISPR/Cas9 knockin mutants, asynchronous populations of animals were fixed, DNA stained with propidium iodide and intestinal and ventral cord nuclei were counted using a Zeiss Axioplan fluorescence microscope. Cells were counted at late larval stages. For the ventral cord, all nuclei of the P2-to-P10 daughter cells and juvenile motor neurons in the region between these cells were counted.

In vitro and *in vivo* kinase assays

For *in vitro* CDK1 kinase assays, immunoprecipitations were performed from mitotic lysates of HeLa cells using mouse monoclonal anti cyclin B1 (GNS1) or beads alone as negative control. Immunoprecipitations were incubated for 30 min at 30°C with either Histone H1, bacterially produced GST or GST–LIN-5 in kinase buffer containing 50 mM HEPES at pH 7.5, 5 mM $MgCl_2$, 2.5 mM $MnCl_2$, 1 mM dithiothreitol, 50 µM ATP and 2.5 µCi [γ-^{32}P] ATP. Reactions were terminated by the addition of SDS (5x sample buffer). For mass spectrometry analysis, no [γ-^{32}P] ATP was added to the kinase assays and incubation time was prolonged to 2 hours at 30°C.

For *in vitro* GSK3 and CK1 kinase assays, peptides (RRRIRCGSPDSLPDFLADN) containing either unphosphorylated, phosphorylated S659 or phosphorylated S662 were used. Kinases were incubated for 30 min at 25 °C with synthetic peptide in kinase buffer containing 200 µM ATP, 50 mM HEPES at pH 7.5, 10 mM $MgCl_2$, 1 mM EGTA, 2 mM dithiothreitol, supplemented with 20 µCi [γ-^{32}P] ATP for radioactive kinase assays. Reactions were terminated by the addition of SDS (4*x* sample buffer).

All other *in vitro* kinase assays were performed as previously described (Galli et al., 2011a).

In short, kinases were incubated for 30 min at 25 °C with bacterially produced GST or GST–LIN-5 in kinase buffer containing 200 µM ATP, 50 mM HEPES at pH 7.5, 10 mM $MgCl_2$, 1 mM EGTA, 2 mM dithiothreitol, supplemented with 20 µCi [γ-^{32}P] ATP for radioactive kinase assays. Reactions were terminated by the addition of SDS (4*x* sample buffer). For mass spectrometry analysis, no [γ-^{32}P] ATP was added to the kinase assays and incubation time was prolonged to 2 hours at 25°C. Kinases used in this study were: recombinant *C. elegans* PAR-1 (a kind gift from Erik Griffin and Geraldine Seydoux), and mammalian Aurora B (a kind gift from Susanne Lens), CK1 (New England Biolabs), CK2 (New England Biolabs), and GSK3 (New England Biolabs).

In-gel digestion and phosphopeptide enrichment

Gel bands were cut and processed for protein in-gel digestion as described elsewhere (Galli et al., 2011a). Briefly, proteins were reduced with dithiothreitol and then alkylated with iodoacetamide. Trypsin was added at a concentration of 10 ng/µl and the mixture was digested overnight at 37°C. Subsequently, peptides were collected from the supernatants and a second extraction using 10% formic acid was performed. Phosphopeptides from LIN-5 were enriched using TiO_2 chromatography (Pinkse et al., 2008). Basically, home-made GELoader tips (Eppendorf, Hamburg, Germany) were packed with TiO2 beads (5 µm, INERTSIL). Peptides were loaded in 10% formic acid and subsequently washed with 20 µl of 80% acetonitrile, 0.1% trifluoroacetic

acid (Fluka, Sigma-Aldrich). Phosphopeptides were then eluted twice with 20 µl of 1.25% ammonia solution (Merck, Germany), pH 10.5, and 3 µl of 100% formic acid was finally added to acidify the samples.

Mass spectrometric analysis

Nanoflow LC-MS/MS was carried out by coupling an Agilent 1100 HPLC system (Agilent Technologies, Waldbronn, Germany) to an LTQ-Orbitrap XL mass spectrometer (Thermo Electron, Bremen, Germany). Peptide samples were delivered to a trap column (AquaTM C18, 5 µm (Phenomenex, Torrance, CA); 20 mm x 100-µm inner diameter, packed in house) at 5 µl/min in 100% solvent A (0.1 M acetic acid in water). Next, peptides eluted from the trap column onto an analytical column (ReproSil-Pur C18-AQ, 3µm (Dr. Maisch GmbH, Ammerbuch, Germany); 40 cm x 50-µm inner diameter, packed in house) at ~100 nl/min in a 90 min or 3 h gradient from 0 to 40% solvent B (0.1 M acetic acid in 8:2 (v/v) acetonitrile/water). The eluent was sprayed via distal coated emitter tips butt-connected to the analytical column. The mass spectrometer was operated in data-dependent mode, automatically switching between MS and MS/MS. Full-scan MS spectra (from m/z 300 to 1500) were acquired in the Orbitrap with a resolution of 60,000 at m/z 400 after accumulation to target value of 500,000 in the linear ion trap. The five most intense ions at a threshold above 5000 were selected for collision-induced fragmentation in the linear ion trap at a normalized collision energy of 35% after accumulation to a target value of 10,000. Peak lists were created from raw files with MaxQuant[43]. Peptide identification was carried out with Mascot (Matrix Science) against a *Caenorhabditis elegans* protein database (http://www.wormbase.org) supplemented with all the frequently observed contaminants in MS (23,502 protein sequences in total). The following parameters were used: 10 ppm precursor mass tolerance, 0.6 Da fragment ion tolerance, up to 3 missed cleavages, carbamidomethyl cysteine as fixed modification, oxidized methionine, phosphorylated serine, threonine and tyrosine as variable modifications. Alternatively, MaxQuant and its search engine Andromeda was also employed for peptide identification and quantification.

Yeast two-hybrid fragment analysis

Full length *gpr-1* was PCR amplified from the ORFeome library (kind gift from Marc Vidal) using KOD polymerase (Novagen) and cloned into bait vector pPC97. Fragments of *lin-5* were PCR amplified from the ORFeome library with KOD polymerase (Novagen) and cloned into prey vector pPC86-AN (Boxem et al., 2008). DB::GPR-1- and AD::LIN-5-encoding plasmids were transformed sequentially into yeast strain Y8930 (Boxem et al., 2008). Positive interactions were identified on the basis of the activation of the HIS3 and ADE2 reporter genes, indicated by growth on synthetic complete –leucine –tryptophan –histidine + 2 mM 3-Amino-1,2,4-triazole (Sc –leu–trp–his + 3-AT) and synthetic complete –leucine –tryptophan –adenine (Sc –leu–trp–ade) plates.

Generation and verification of yeast two-hybrid *lin-5* mutants

To generate mutant clones, PCR was performed on pVP054 (pPC86-AN containing nucleotides 1821-2466 encoding amino acid 609-821 of *lin-5*) with increased $MgCl_2$ concentration of 7 mM. PCR products were cloned into pPC86-AN and transformed to DH5α competent cells. Bacterial colonies were collected and the DNA was isolated using a Nucleobond Xtra DNA purification kit (Macherey-Nagel). Bacterial clones were transformed into MB004 (Y8930 in which ADE2 is replaced by URA3 by homologous recombination) containing DB::GPR-1 and plated on synthetic complete –leucine –tryptophan + 2 g/l 5-fluoroacetic acid (Sc –leu–trp + FOA). Colonies were picked and spotted to synthetic complete –leucine –tryptophan (Sc –leu–trp) plates for validation, PCR and sequencing. Clones with single amino acid changes were re-tested by PCR amplification of the fragment and re-cloning into pPC86-AN. Interaction deficient alleles were

identified on the basis of no activation of the HIS3 or URA3 reporter gene, indicated by absence of growth on Sc −leu−trp−his + 3-AT plates and synthetic complete –leucine −tryptophan –uracil (Sc −leu−trp−ura) plates.

Validation of yeast two-hybrid full-length mutants

For generation of full length mutant clones, plasmids containing fragment clones with selected point mutations were digested and cloned into pVP055 (pPC86-AN containing nucleotides 1-2466 encoding amino acid 1-821 of *lin-5*). Phospho-mutants were generated by either site-directed mutagenesis of pVP055 or Gibson assembly into pVP055 of short regions of *lin-5* with point mutations carried in the overlapping region. DB::GPR-1 and AD::LIN-5-encoding plasmids were transformed sequentially into yeast strain MB004. Interaction deficient alleles were identified on the basis of no activation of the HIS3 or URA3 reporter gene, indicated by absence of growth on Sc −leu−trp−his + 3-AT plates and Sc −leu−trp−ura plates.

Generation of CRISPR/Cas9 repair templates

CRISPR repair constructs were inserted into the pBSK vector using Gibson Assembly (New England Biolabs). Homologous arms of at least 1500 bp upstream and downstream of the CRISPR/Cas9 cleavage site were amplified from either cosmid C03G3 (for *lin-5* constructs) or *C. elegans* genomic DNA using KOD Polymerase (Novagen). Linkers containing the altered cleavage sites and point mutations were synthesized (Integrated DNA technologies). For *fkbp*::*egfp*::*gpr-1*, codon-optimized *fkbp* was synthesized (Integrated DNA technologies) and codon-optimized *egfp* was amplified from pMA-*egfp* (a kind gift from Anthony Hyman). For *egfp*::*lin-5*, codon-optimized *egfp* was amplified from pMA-*egfp*. For *mcherry*::*dhc-1*, codon-optimized *mcherry* was amplified from TH0563-PAZ-*mCherry* (a kind gift from Anthony Hyman). Mismatches were introduced in the sgRNA target site to prevent cleavage of knockin alleles. All plasmids and primers used for cloning are available upon request.

CRISPR/Cas9 genome editing

Young adults were injected with a solution containing the following injection mix: 30-50 ng/µl *Peft-3*::Cas9 (Addgene 46168; (Friedland et al., 2013), 30-100 ng/µl u6::sgRNA with appropriate target for *dhc-1*, *gpr-1* and *lin-5*, 30-50 ng/µl repair template and 2.5 ng/µl *pmyo-2::tdTomato*. Progeny of animals that express tdTomato were picked to new plates 3–4 days post injection. PCRs with primers diagnostic for homologous recombination at the endogenous locus were performed on F2-F3 populations, where one primer targeted the altered basepairs in the sgRNA site, point mutation or fluorescent tag and the other targeted a region just outside the homology arm. All primers used for genome editing are available upon request.

Preparation of protein lysates for Western blot analysis

For yeast protein lysates, cultures were grown overnight at 30°C. Yeast cells corresponding to 4 OD of culture were harvested, treated with Sodium hydroxide and resuspended in 100 2X sample buffer containing β-mercaptoethanol (Kushnirov, 2000).

For *C. elegans* protein lysates, strains SV1569, SV1663 and SV1664 were grown at 20°C one generation on NGM plates seeded with HB101, followed by a second generation in S-Medium with HB101 bacteria. Gravid adults were harvested and embryos were isolated by hypochlorite treatment. Embryo pellets were snap frozen in liquid nitrogen, grinded using mortar and pestle and resuspended in 5 ml fresh lysis buffer (containing 20 mM Tris-HCl pH 7.8, 250 mM NaCl, 15% glycerol, 0.5% IGEPAL, 0.5 mM EDTA, 50 mM Sodium fluoride, 1 mM β-mercaptoethanol

and protease inhibitors (Roche complete, Mini, EDTA-free)). The suspension was passed through a French press 3 times, and the lysate was cleared at 13,000 rpm for 15 min at 4°C.

Western blot Analysis

Protein samples were separated on gradient acrylamide gels and subjected to western blotting on polyvinylidene difluoride membrane (Immobilon-P, Millipore). Membranes were blocked with 5% skim milk in PBST for 1 hour at room temperature, or overnight at 4°C for stripped blots. For protein detection, primary antibodies used in this study were: mouse anti—LIN-5 (1:1000) (Lorson et al., 2000) and rabbit anti-Tubulin (1:1000, Abcam) for stripped blots. Secondary antibodies used were: donkey anti-mouse HRP (1:5000, Abcam), and goat anti-rabbit HRP (1:5000, Jackson Immunoresearch). Proteins were dectected with Signalfire Plus chemiluminescent detection (Cell Signaling Technologies) and a Chemidoc MP Imager (Bio-Rad).

Time-lapse imaging and live-cell imaging

DIC time-lapse imaging was performed on strains N2, SV1568, SV1588, SV1590 and SV1600. Animals were grown overnight at 25°C. RNAi feeding of N2 against *gsk-3* was performed with the bacterial clone from the Orfeome-based RNAi Library (Rual et al., 2004; Timmons and Fire, 1998). L4 animals were grown for approximately 32 hours at 15°C before shifting overnight to 25°C for imaging, except SV1901 which was kept at 20°C. Embryos were dissected from adults in a solution of 0.8x egg salt (containing 94 mM NaCl, 32 mM KCl, 2.7 mM $CaCl_2$, 2.7 mM $MgCl_2$, 4 mM HEPES, pH 7.5; (Tagawa et al., 2001)) on coverslips and mounted on slides with 3% agarose prepared with egg salt. Embryos were imaged with 5s time intervals with a 100x/1.4 NA lens on a Zeiss microscope at 20°C. Relative positions of the spindle and furrow were analyzed manually using ImageJ.

Live-cell imaging of EMS rotation was performed on strains SV1783, SV1784 and SV1785. L4 animals were grown overnight at 20°C. Embryos were dissected from young adults as above and imaged with a 100x/1.4 NA lens on a Zeiss microscope at 20°C. Spindle rotation in EMS was followed over time with images taken at several time points.

Live-cell imaging of microtubule depolymerization upon nocodazole treatment was performed on strain AZ244. Young adult animals were injected with dsRNA (Fire et al., 1998) against *perm-1* and grown for 20 hours at 15°C. Embryos were dissected from young adults in a solution of 0.8x egg salt containing 1 µM nocodazole on coverslips and mounted on concave slides. Embryos were imaged with a 60x/1.4 NA lens on a Nikon Eclipse Ti microscope with Perfect Focus System and Yokogawa CSU-X1-A1 spinning disk confocal head at room temperature.

Live-cell imaging of mitotic DHC-1 localization was performed on strains SV1619, SV1635, SV1638 and SV1639. Young adult animals were injected with dsRNA (Fire et al., 1998) against *perm-1* and *egfp* and grown for 20 hours at 15°C. Embryos were dissected from young adults in a solution of 0.8x egg salt containing 1 µM nocodazole on coverslips and mounted on concave slides. Still images of mitotic embryos in metaphase were taken within minutes after nocodazole addition. Eliminating nonspecific toxic effects, embryos on the same slide at the same time continued nuclear envelope degradation, and *perm-1(RNAi)* embryos continued embryonic development in the absence of nocodazole.

Embryos were imaged with a 60x/1.4 NA lens on a Nikon Eclipse Ti microscope with Perfect Focus System and Yokogawa CSU-X1-A1 spinning disk confocal head at room temperature. mCherry::DHC-1 localization was analyzed in mitotic one-cell embryos after nuclear envelope breakdown. Mitotic embryos were also identified based on presence of a polar body, enlarged centrosomes and remnant of the mitotic spindle.

Live-cell imaging of meiotic DHC-1 localization was performed on strains SV1702, SV1898, SV1899 and SV1902. For RNAi treated animals, young adult animals were injected with dsRNA (Fire et al., 1998) against *egfp* and grown for 24 hours at 15°C. Embryos were dissected from young adults as above and imaged with 10s time intervals with a 100x/1.4 NA lens on a Zeiss microscope at 20°C. For images presented in Fig 7B and S12 Video, S15 Video, S18 Video and S21 Video, images were processed by subtracting a Gaussian-blur filtered image (Sigma(Radius): 20) using ImageJ. S10 Video, S11 Video, S13 Video, S14 Video, S16 Video, S17 Video, S19 Video and S20 Video represent the unprocessed files.

UV laser spindle ablation

Spindle severing with a UV laser microbeam was performed on strains SV1585, SV1594, SV1596, SV1618, SV1700 and SV1701 essentially as previously described (Grill et al., 2001). RNAi feeding of SV1700 and SV1701 against *egfp* was performed with a bacterial clone containing full-length *egfp* in the L4440 double T7 plasmid (Timmons and Fire, 1998). L4 animals were grown on RNAi for approximately 48 hours. For analysis of spindle pulling forces, animals were kept at 25°C for 24 h before ablations. Spindle ablations were carried out at 25°C (Fig 4D) or 20°C (Fig 4E) on a spinning-disc confocal microscope. The spindle midzones were severed at anaphase onset and images of GFP-b-tubulin were taken at 0.5 s intervals. For analysis, the position of the spindle poles was automatically tracked using the MTrack2 plugin in ImageJ. Peak velocities of the anterior and posterior spindle poles were determined within a 12.5 s time frame after ablation. Representative videos for every strains are shown in S2-9 Video.

Microscope setup: Nikon Eclipse Ti microscope with Perfect Focus System, Yokogawa CSU-X1-A1 spinning disk confocal head, S Fluor 100x N.A. 0.5-1.3 objective (at 1.3), Photometrics Evolve 512 EMCCD camera, Cobolt Calypso 491 nm (100 mW) and Teem Photonics 355 nm Q-switched pulsed lasers, ILas system (Roper Scientific France/ PICT-IBiSA, Institut Curie) to control the UV-laser, ET-GFP (49002) filter, ASI motorized stage MS-2000-XYZ with Piezo Top Plate with Tokai Hit INUBG2E-ZILCS Stage Top Incubator (controlled at 25 °C), controlled by MetaMorph 7.7 software.

Antibodies and immunohistochemistry

For immunostaining, embryos were dissected from adults in 8 µl of water on poly-L-lysine–coated slides. Embryos were freeze-cracked and fixed for 5 min in methanol at −20°C and then for 20 min in acetone at −20°C. After fixation, embryos were rehydrated in phosphate-buffered saline (PBS) containing 0.05% Tween-20 (PBST) and blocked with blocking solution (PBST containing 1% bovine serum albumin and 1% goat serum [Sigma-Aldrich]) for 1 h. Embryos were stained with primary and secondary antibodies for 1 h and washed after each incubation with PBST four times, 15 min each time. Finally, the embryos were embedded in ProLong Gold Antifade containing 4′,6-diamidino-2-phenylindole (DAPI). Primary antibodies used in this study were: mouse anti–LIN-5 (1:10; (Lorson et al., 2000) and rabbit anti-GFP (1:500, Life Technologies). Secondary antibodies were used at a concentration of 1:500. Secondary antibodies used were: goat anti-rabbit Alexa Fluor 488, and goat anti-mouse Alexa Fluor 568 (Invitrogen). Images were taken with a 63x/1.4 NA lens on a Zeiss confocal microscope.

Immunohistochemistry quantification of LIN-5 levels

Embryos were dissected and stained with antibodies as described above. Images were taken with a 63x/1.4 NA lens on a Zeiss confocal microscope using identical microscope setting for all images taken for every secondary antibody. Mean intensity of LIN-5 was measured using ImageJ by selecting fixed size regions that depended on the developmental stage. For every embryo 2 centrosomes and cytoplasmic regions were quantified.

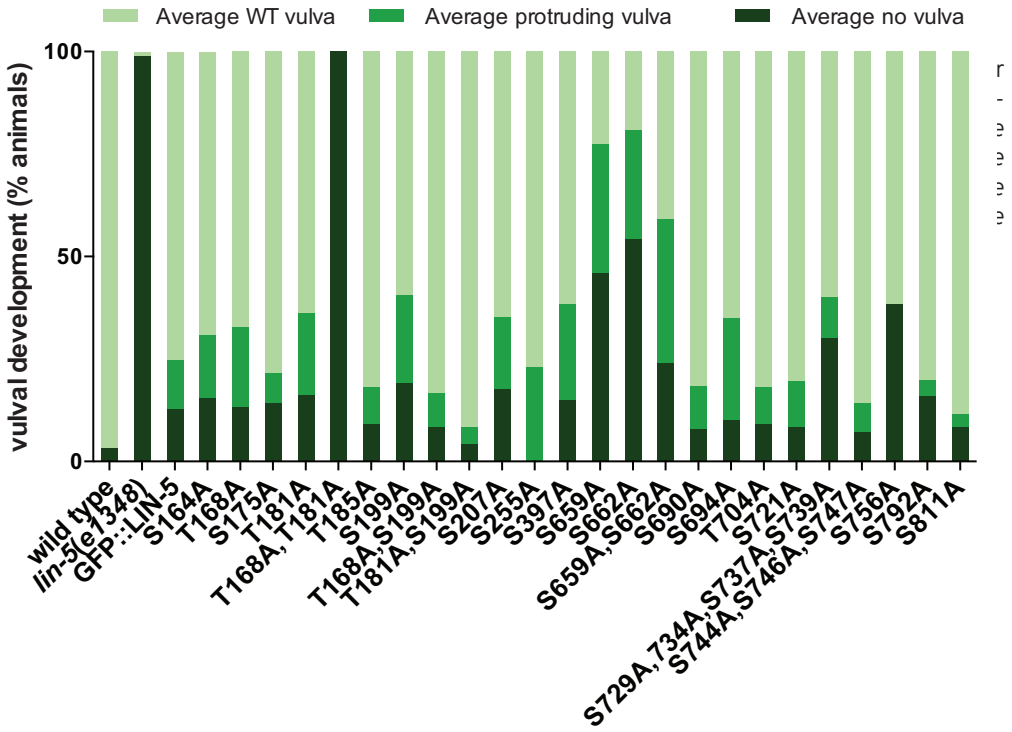

Supplementary figure 1 Phosphorylation of LIN-5 controls post-embryonic divisions in the vulva. Quantification of vulval development in heterozygous *lin-5(e1348) / mIn1* (Wild type), homozygous *lin-5(e1348)* animals, and homozygous *lin-5(e1348)* animals expressing *gfp::lin-5* transgenes.

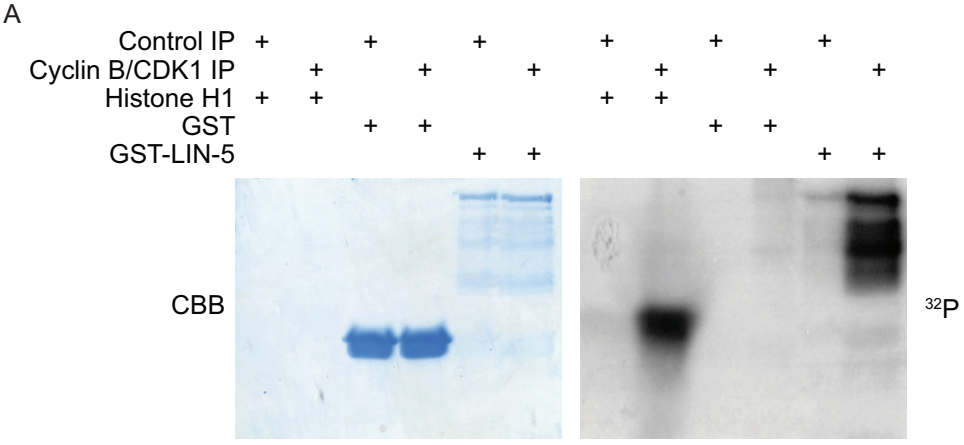

B

residue	peptide sequence	peptide mascot scores						
		CDK1 kinase assay						
T168	RDDEDQEASSGFRTPK	47.4	47.2	32.6	41.8	27.2		
	DDEDQEASSGFRTPK	24.8						
T181	RNNYSLTSLQTPTATAR	42.4						
	NNYSLTSLQTPTATAR	82.0	81.9	26.0	40.3			
T704	KSIAPSVDDNEFDKGTPIGFK	46.6	32.4					
S744	SESIQLASPSSAGEFK	53.3	40.3	84.3	32.4	95.0	26.5	37.3
S756	QPFTPSGVTK	21.0						

Supplementary figure 2 Cdk1 phosphorylates LIN-5 *in vitro*. **(A)** In vitro Cdk1 kinase assay with recombinant GST-LIN-5, GST alone, or Histone H1. Left; Coomassie brilliant blue (CBB)-stained gel. Right; autoradiogram. **(B)** List of LIN-5 phosphopeptides identified by mass spectrometry analysis of Cdk1 *in vitro* kinase assay with GST-LIN-5. Phosphopeptides are shown with individual Mascot Scores. Only Mascot Scores above 20 were accepted as reliable peptide identifications.

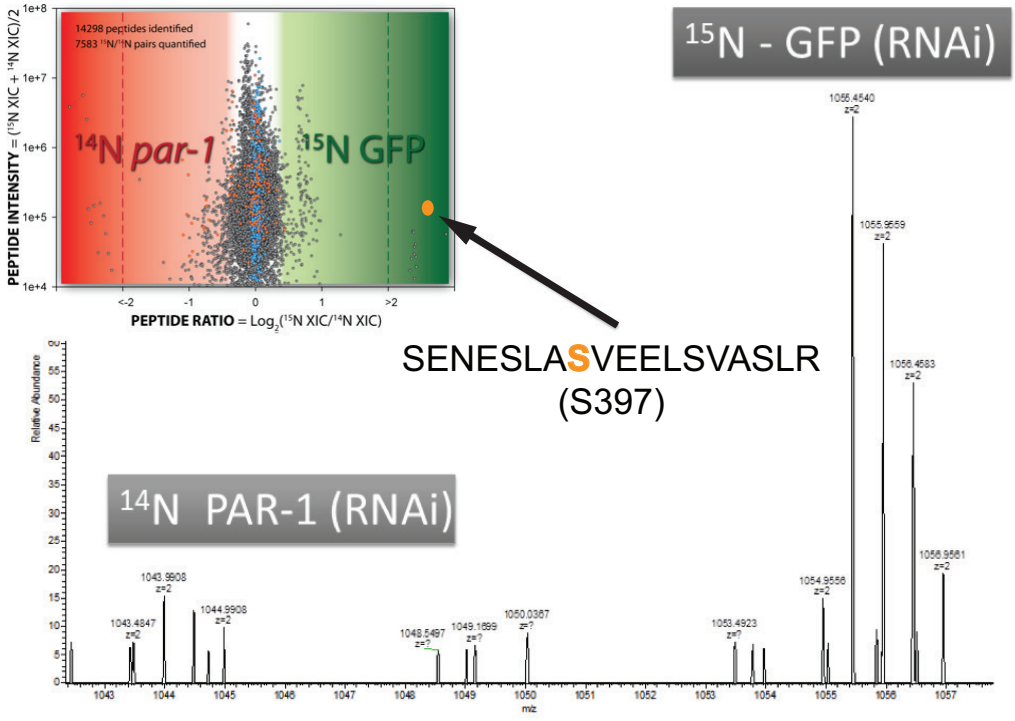

Supplementary figure 3 PAR-1 phosphorylates LIN-5 *in vivo*. Log_2 ratios for all of the quantified $^{15}N/^{14}N$ peptide pairs as a function of their mass spectrometry intensities in the three LIN-5 immunoprecipitates. LIN-5 phospho-peptides are represented in red, and LIN-5 regular peptides are represented in blue. Peptides belonging to other proteins are shown in grey. Peptide intensities were calculated using the average of the ^{14}N and ^{15}N extracted ion chromatograms.

A

summary	mutations identified	possible total
unique nucleotides mutated	184	642 nucleotides
unique amino acids changed	111	213 amino acids
single amino acid changes (not stop)	15	213 amino acids
amino acids changed to early stops	31	213 amino acids
DNA changes	clones identified	possible total
clones without nucleotide changes	2	163 clones
clones with 1 nucleotide changed	89	163 clones
clones with 2 nucleotides changed	31	163 clones
clones with 3 nucleotides changed	25	163 clones
clones with >3 nucleotides changed	16	163 clones
clones with nucleotide deletion	38	163 clones
clones with nucleotide insertion	1	163 clones
amino acid changes	clones identified	possible total
clones without amino acid changes	4	163 clones
clones with 1 amino acid change (excluding frame shift)	77	163 clones
clones with 1 amino change leading to an early stop	49	163 clones
clones with 2 amino acid changes (excluding frame shift)	31	163 clones
clones with 2 amino changes leading to an early stop	7	163 clones
clones with 3 amino acid changes (excluding frame shift)	12	163 clones
clones with 3 amino changes leading to an early stop	4	163 clones
clones with >3 amino acid changes	3	163 clones
clones containing frame shifts	36	163 clones

B

residue	changed to	times found	validated mutation	interaction deficient
M638	K	2	YES	YES
	T	1	NO	n/a
E640	K	1	NO	n/a
	V	8	YES	YES
I644	N	1	YES	YES
F645	I	1	YES	YES
R654	G	2	YES	NO
I655	N	1	YES	YES
S659	T	1	YES	YES
P660	L	1	YES	YES
D661	G	1	YES	YES
S662	C	3	NO	n/a
	G	4	YES	YES
	N	1	NO	n/a
L663	S	3	YES	YES
D665	V	3	YES	YES
F666	L	2	YES	NO
L667	P	2	YES	YES
S816	L	1	YES	NO

Supplementary figure 4 Summary of GPR-1 interaction-deficient LIN-5 alleles. **(A)** Summary of sequencing results of all interaction-deficient alleles of LIN-5 identified in the reverse yeast two-hybrid assay before further validation. **(B)** Overview of all interaction deficient alleles of LIN-5 containing a single amino acid change identified in the reverse yeast two-hybrid assay before further validation. Validation is shown in figure 3B.

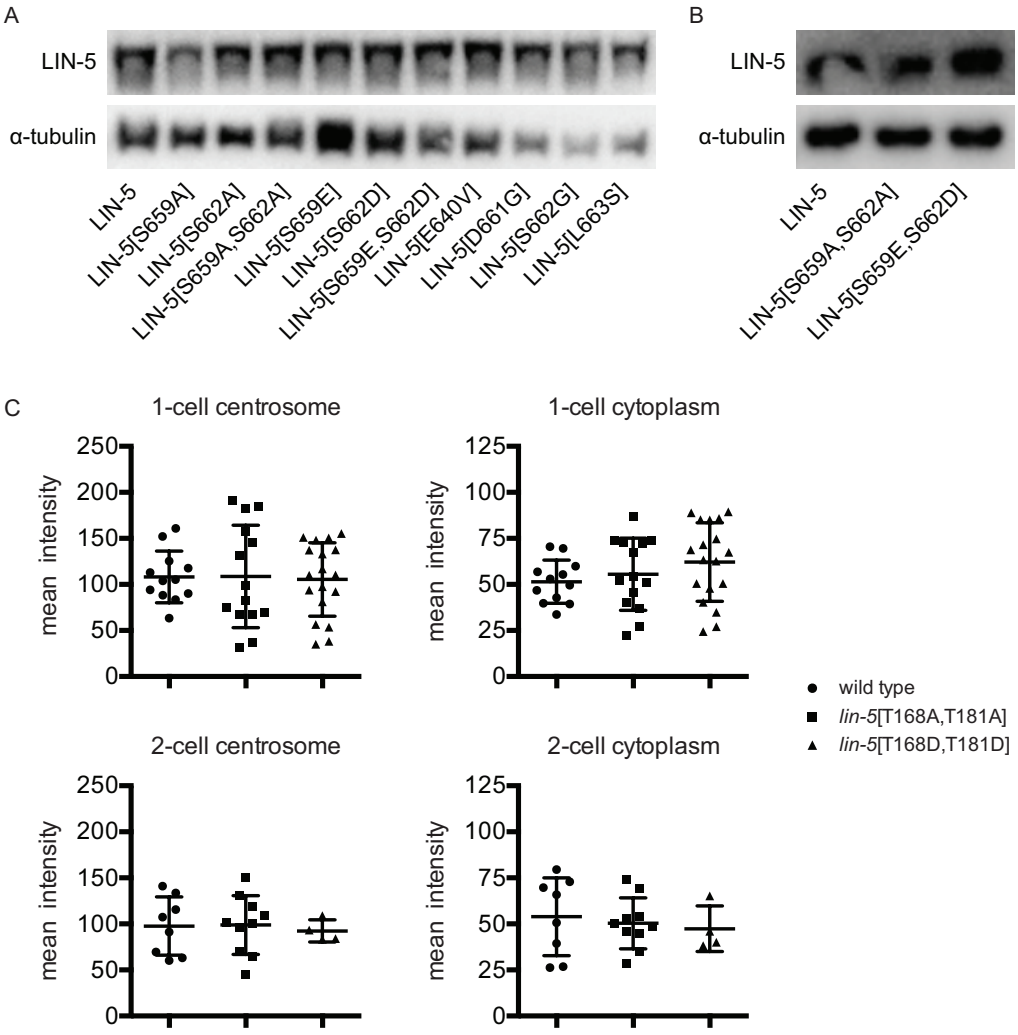

Supplementary figure 5 Detection of protein levels in LIN-5 mutants. **(A)** Western blots of lysates of yeast clones containing the indicated LIN-5 expression constructs, probed for LIN-5 and tubulin (loading control) levels. **(B)** Western blots of *C. elegans* lysates with detection of LIN-5 and tubulin (loading control). **(C)** Quantification of mean intensity of immunostainings of *lin-5*[mutant T168,T181] / *egfp::lin-5* embryos treated with *egfp* RNAi and stained with LIN-5 antibodies. Graphs indicate single values for centrosomes and cytoplasm in 1- and 2-cell embryos.

A

mutation	intestinal nuclei	ventral cord nuclei	n
wild type	32.8±0.2	64.4±0.4	18
lin-5(*e1348*)	20.0±0.0	23.9±0.1	20
lin-5[L663S]	20.6±0.2	33.4±1.2	11
lin-5[T168A,T181A]	22.5±0.4	37.6±0.8	19
lin-5[T168D,T181D]	22.4±0.3	33.9±0.7	17
lin-5[T168E,T181E]	21.9±0.3	33.1±0.4	24
lin-5[T168S,T181S]	33.1±0.2	64.3±0.2	13
lin-5[S397A]	32.5±0.3	64.0±0.3	13
lin-5[S397E]	32.3±0.3	63.4±0.4	13
lin-5[S659A,S662A]	32.0±0.3	64.0±0.3	10
lin-5[S659E,S662D]	32.9±0.3	63.9±0.5	11

B

	anterior oscillations	posterior oscillations	spindle elongation	posterior flattening	AB size	P1 rotation
wild type	6.2±1.0% (n=10)	14.7±4.1% (n=10)	15.2±1.8% (n=9)	100.0% (n=13)	58.7±1.7% (n=24)	93.7% (n=16)
lin-5[S397A]	7.6±1.8% (n=10)	14.8±2.7% (n=10)	15.3±2.1% (n=10)	100.0% (n=12)	59.0±1.1% (n=17)	100.0% (n=12)
lin-5[S397E]	6.4±1.9% (n=9)	15.2±4.6% (n=9)	13.9±2.4% (n=9)	100.0% (n=13)	58.9±1.3% (n=17)	85.7% (n=14)
gsk-3 RNAi	7.8±2.4% (n=10)	15.8±2.2% (n=10)	17.0±2.4% (n=9)	81.8% (n=11)	60.1±0.9% (n=12)	100.0% (n=10)
lin-5 [S659A,S662A]	3.2±1.1% (n=13)	9.2±3.2% (n=13)	10.0±2.3% (n=15)	12.5% (n=8)	60.0±1.4% (n=27)	52.9% (n=17)
lin-5 [S659E,S662D]	6.4±1.8% (n=12)	13.8±2.0% (n=12)	13.1±2.0% (n=11)	92.9% (n=14)	59.1±1.2% (n=20)	92.9% (n=14)
lin-5 [T168S,T181S]	4.9±1.5% (n=12)	7.5±2.2% (n=12)	14.2±1.9% (n=12)	100.0% (n=12)	58.8±1.1% (n=13)	66.7% (n=12)

C

	wt	A-P	L-R	n	defective A-P	defective L-R
mes-1(*bn74 ts*) ; *lin-5*[S659A,S662A]	12	1	0	13	7,7%	0%
mes-1(*bn74 ts*) ; *lin-5*[S659E,S662D]	14	3	1	18	16,7%	5,6%
mes-1(*bn74 ts*) ; *gsk-3 (RNAi)*	1	1	9	11	9,1%	81,8%

Supplementary figure 6 Phenotypical analysis shows developmental defects in LIN-5 phosphomutants. **(A)** Averages of quantification of intestinal nuclei and P-cells plus juvenile motor neurons (P2-P10 region) by propidium iodide staining in wild type, homozygous LIN-5 phosphorylation mutants, and homozygous *lin-5(e1348)* null animals. Statistical analysis in s.e.m., analyzed by Graphpad PRISM. **(B)** Statistical averages of DIC microscopy imaging of hallmarks of the first 2 embryonic divisions in LIN-5 phosphorylation mutants. Oscillations are plotted in percentage of embryo height, elongation and AB size as a percentage of embryo width, flattening and rotation as a total fraction of analyzed embryos. Statistical analysis in s.e.m., analyzed by Graphpad PRISM. **(C)** Quantification of EMS spindle rotation in *mes-1(bn74 ts) ; lin-5[S659,S662]* phosphorylation mutant and *mes-1(bn74 ts)* ; *gsk-3(RNAi)* embryos. Spindle rotation was quantified by live-imaging of the *gfp*::tubulin marker. Wt indicates number of embryos with wild type rotation, defective A-P indicates number of embryos with a failure to fully align in the anterior-posterior direction, defective L-R indicates number of embryos with a failure to rotate in the left-right direction.

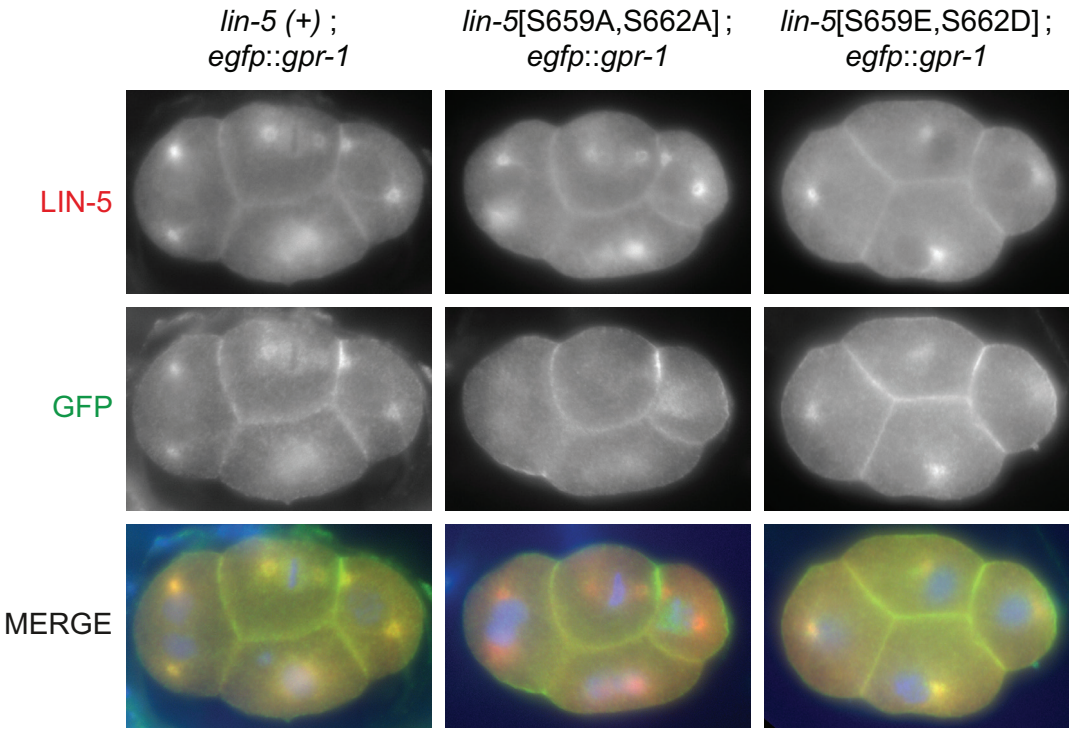

Supplementary figure 7 Localization of LIN-5 and GPR-1 in phosphorylation mutants. Immunohistochemistry staining of embryos expressing wild-type or phosphomutant *lin-5* and endogenously tagged *egfp::gpr-1*. Representative images of four-cell embryos, stained with anti-LIN-5 (red) and anti-eGFP (green) antibodies, and DAPI to visualize DNA. All images taken with same exposure time, objective and magnification. Anterior to the left, ventral up.

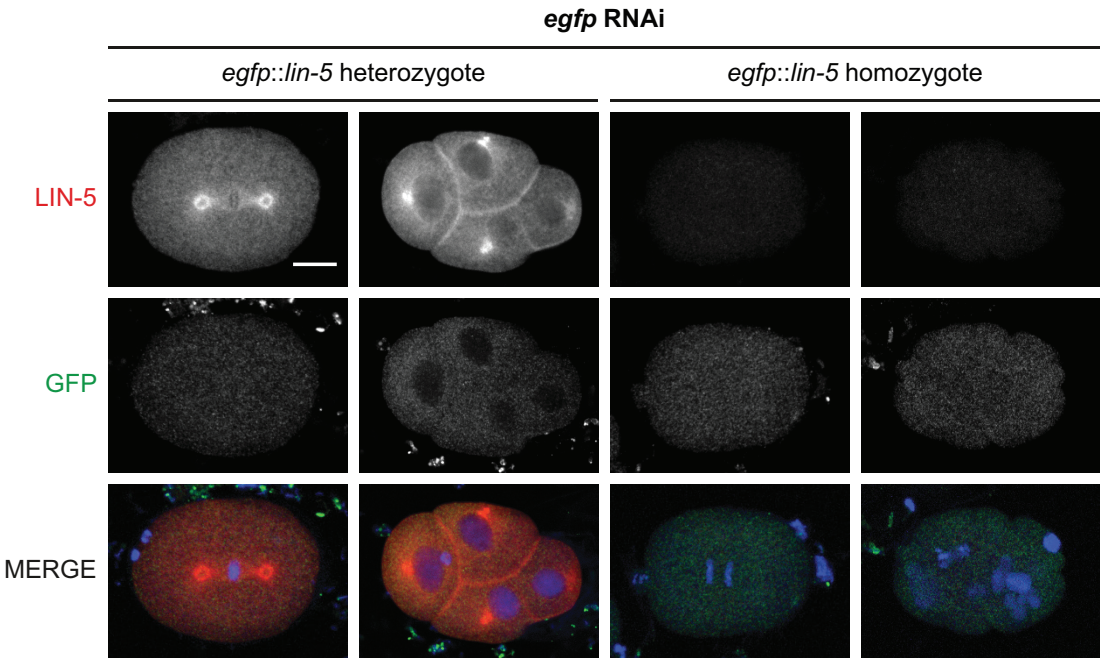

Supplementary figure 8 Specific knockdown of eGFP::LIN-5 upon *egfp* RNAi. Immunohistochemistry staining of heterozygous and homozygous *egfp::lin-5 C. elegans* embryos with anti-LIN-5 (red) and anti-GFP (green) antibodies, DNA stained with DAPI. Two representative embryos are shown for every condition. All images same objective and magnification, anterior to the left, scale bars 10 µm.

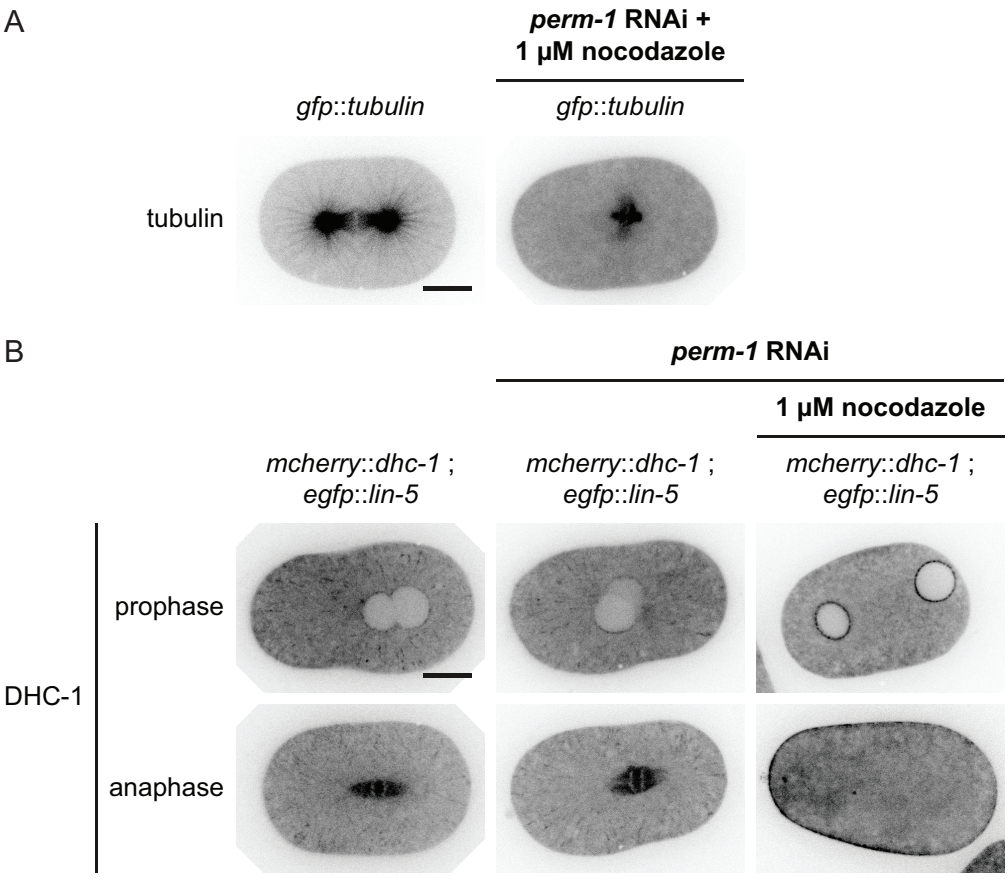

Supplementary figure 9 Cortical localization of mCherry::DHC-1 after nocodazole treatment. **(A)** Representative snapshots of live imaging of GFP::tubulin in *gfp::tubulin* one-cell embryos treated with or without *perm-1* RNAi + 1 µM nocodazole, and imaged by spinning disk confocal microscopy. Scale bars, 10 µm, all images with same objective and magnification. **(B)** Representative snapshots of live imaging of mCherry::DHC-1 in *mcherry::dhc-1* ; *egfp::lin-5* one-cell embryos in prophase and metaphase treated with or without *perm-1* RNAi in the presence or absence of 1 µM nocodazole, and imaged by spinning disk confocal microscopy. All images taken with same objective and magnification, anterior to the left, scale bars 10 µm.

Strain	genotype	comment
N2	wild type	Fig. 4A-C, S6A-B
SV13	lin-5(e1348) / mnC1 dpy-10(e128) unc-52(e444)	Fig. 4A-B, S6A
SV918	lin-5(e1348) / mln1	Fig. 1, S1
SV1568	lin-5(he237[S659A,S662A])	Fig. 4A, S6A-B, CRISPR allele
SV1569	gpr-1(he238[fkbp:: egfp::gpr-1])	Fig. 5, CRISPR allele
SV1585	lin-5(he237[S659A,S662A]) ; ruIs57 [unc-119(+) ; ppie-1::gfp::β-tubulin]	Fig. 4D
SV1586	lin-5(he240[L663S])	Fig. 4A, S6A, CRISPR allele
SV1587	lin-5(he241[T168A,T181A]) / +	CRISPR allele
SV1588	lin-5(he242[S397E])	Fig. 4A, S6A-B, CRISPR allele
SV1589	lin-5(he244[egfp::lin-5])	Fig. S7, CRISPR allele
SV1590	lin-5(he243[S397A])	Fig. 4A, S6A-B, CRISPR allele
SV1594	lin-5(he242[S397E]) ; ruIs57[unc-119(+) ; ppie-1::gfp::β-tubulin]	Fig. 4D
SV1596	lin-5(he243[S397A]) ; ruIs57[unc-119(+) ; ppie-1::gfp::β-tubulin]	Fig. 4D
SV1600	lin-5(he249[S659E,S662D])	Fig. 4A, S6A-B, CRISPR allele
SV1618	lin-5(he249[S659E,S662D]) ; ruIs57[unc-119(+) ; ppie-1::gfp::β-tubulin]	Fig. 4D
SV1619	dhc-1(he250[mcherry::dhc-1])	Fig. 7A, S8B, CRISPR allele
SV1620	lin-5(he251[T168D,T181D]) / +	CRISPR allele
SV1621	lin-5(he251[T168D,T181D]) / lin-5(he244[egfp::lin-5])	Fig. 4A, 6, S6A
SV1622	lin-5(he241[T168A,T181A]) / lin-5(he244[egfp::lin-5])	Fig. 4A, 6,S6A
SV1635	dhc-1(he250[mcherry::dhc-1]) ; lin-5(he244[egfp::lin-5])	Fig. 7A
SV1638	dhc-1(he250[mcherry::dhc-1]) ; lin-5(he251[T168D,T181D]) / lin-5(he244[egfp::lin-5])	Fig. 7A

SV1639	dhc-1(he250[mcherry::dhc-1]) ; lin-5(he241[T168A,T181A]) / lin-5(he244[egfp::lin-5])	Fig. 7A
SV1663	lin-5(he237[S659A,S662A]) ; gpr-1(he238[fkbp::egfp::gpr-1])	Fig. 5
SV1664	lin-5(he249[S659E,S662D]) ; gpr-1(he238[fkbp:: egfp::gpr-1])	Fig. 5
SV1695	lin-5(he261[T168E,T181E]) / +	Fig. 4A, S6A, CRISPR allele
SV1700	lin-5(he241[T168A,T181A]) / lin-5(he244[egfp::lin-5]) ; ruIs57[unc-119(+) ; ppie-1::gfp::β-tubulin]	Fig. 4E
SV1701	lin-5(he251[T168D,T181D]) / lin-5(he244[egfp::lin-5]) ; ruIs57[unc-119(+) ; ppie-1::gfp::β-tubulin]	Fig. 4E
SV1702	dhc-1(he250[mcherry::dhc-1]) ; ruIs57[unc-119(+)ppie-1::gfp::β-tubulin]	Fig. 7B
SV1783	lin-5(he237[S659A,S662A]) ; ruIs57[unc-119(+) ; ppie-1::gfp::β-tubulin] ; mes-1(bn74)	Fig. S6C, maintained at 15°C
SV1784	lin-5(he249[S659E,S662D]) ; ruIs57[unc-119(+) ; ppie-1::gfp::β-tubulin] ; mes-1(bn74)	Fig. S6C, maintained at 15°C
SV1785	ruIs57[unc-119(+) ; ppie-1::β-tubulin::GFP] ; mes-1(bn74)	Fig. S6C, maintained at 15°C
SV1898	dhc-1(he250[mcherry::dhc-1]) ; lin-5(he241[T168A,T181A]) / lin-5(he244[egfp::lin-5]) ; ruIs57[unc-119(+) ; ppie-1::gfp::β-tubulin]	Fig. 7B
SV1899	dhc-1(he250[mcherry::dhc-1]) ; lin-5(he251[T168D,T181D]) / lin-5(he244[egfp::lin-5]) ; ruIs57[unc-119(+) ; ppie-1::gfp::β-tubulin]	Fig. 7B
SV1901	lin-5 (he281[T168S,T18S])	Fig. 4A, S6A
SV1902	dhc-1(he250[mcherry::dhc-1]) ; lin-5(he244[egfp::lin-5]) ; ruIs57[unc-119(+) ; ppie-1::gfp::β-tubulin]	Fig. 7B, CRISPR allele
SV1911	lin-5 (he281[T168S,T18S]) ; ruIs57[unc-119(+) ; ppie-1::gfp::β-tubulin]	Fig. 4E
AZ244	unc-119 (ed3) ; ruIs57[unc-119(+) ; ppie-1::gfp::β-tubulin]	Fig. 4D-E, S8A
SS392	mes-1(bn74)	maintained at 15°C

Table S1 Overview of all strains used in this study, including the corresponding figure. CRISPR/Cas9 genome engineered strains are indicated in the comment section.

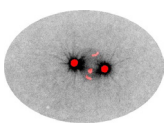

4

The tumor suppressor APC is an attenuator of spindle-pulling forces during *C. elegans* asymmetric cell division

Kenji Sugioka[1,2,3], Lars-Eric Fielmich[4], Kota Mizumoto[2], Bruce Bowerman[3], Sander van den Heuvel[4], Akatsuki Kimura[5,6] and Hitoshi Sawa[1,2,6]

[1]Multicellular Organization Laboratory, National Institute of Genetics, 1111 Yata, Mishima, 411-8540 Japan

[2]RIKEN Center for Developmental Biology, 2-2-3 Minatojima-minamimachi, Chuo-ku, Kobe 650-0047 Japan

[3]Institute of Molecular Biology, University of Oregon, Eugene, OR 97403 USA

[4]Developmental Biology, Biology Department, Science 4 Life, Utrecht University, Padualaan 8, 3584 CH, Utrecht, Netherlands

[5]Cell Architecture Laboratory, National Institute of Genetics, 1111 Yata, Mishima, 411-8540 Japan

[6]Department of Genetics, School of Life Science, Sokendai, 1111 Yata, Mishima, 411-8540 Japan

An adapted version of this manuscript was published in *Proceedings of the National Acadamy of Sciences of the USA* in 2018

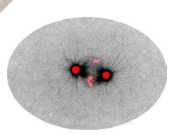

Abstract

the adenomatous polyposis coli (APC) tumor suppressor has dual functions in Wnt/β-catenin signaling and accurate chromosome segregation, and is frequently mutated in colorectal cancers. Although APC contributes to proper cell division, the underlying mechanisms remain poorly understood. Here we show that *C. elegans* APR-1/APC is an attenuator of the pulling forces acting on the mitotic spindle. During asymmetric cell division of the *C. elegans* zygote, a LIN-5/NuMA protein complex localizes dynein to the cell cortex to generate pulling forces on astral microtubules that position the mitotic spindle. We found that APR-1 localizes to the anterior cell cortex in a Par-aPKC polarity-dependent manner and suppresses anterior centrosome movements. Our combined cell biological and mathematical analyses support the conclusion that cortical APR-1 reduces force generation by stabilizing microtubule plus ends at the cell cortex. Furthermore, APR-1 functions in coordination with LIN-5 phosphorylation to attenuate spindle pulling forces. Our results document a physical basis for spindle-pulling force attenuation, which may be generally used in asymmetric cell division, and when disrupted potentially contributes to division defects in cancer.

Introduction

The mitotic spindle segregates chromosomes and determines the plane of cell cleavage during animal cell division. Forces that act on the mitotic spindle regulate its position to produce daughter cells of the proper size, fate and arrangement, thereby playing a significant role in asymmetric cell division, tissue integrity and organogenesis. In various organisms, cells regulate spindle positioning through cortical force generators that pull on astral microtubules (Knoblich, 2010; Pietro et al., 2016; Rose and Gönczy, 2014; Siller and Doe, 2009; Williams and Fuchs, 2013). An evolutionarily conserved force generator complex, consisting of LIN-5/NuMA, GPR-1,2/LGN and Gα interacts with dynein and dynamic astral microtubules to position the mitotic spindle during the asymmetric divisions of the *C. elegans* early embryo (Rose and Gönczy, 2014), *Drosophila* and mammalian neuroblasts (Knoblich, 2010; Siller and Doe, 2009), and skin stem cells (Williams and Fuchs, 2013). Although Par-aPKC polarity and cell cycle regulators are known to control spindle positioning (Portegijs et al., 2016; Rose and Gönczy, 2014), how the forces are regulated spatiotemporally to position the spindle in various cell types during development remains poorly understood.

The tumor suppressor adenomatous polyposis coli (APC) is a widely conserved multifunctional protein with two major roles. First, APC functions as part of a degradation complex to down-regulate β-catenin-TCF dependent transcription, thereby controlling cell fate and proliferation in various cell types (Clevers and Nusse, 2012). Second, APC functions as a microtubule-associated protein to stabilize MTs. It has been suggested that this function of APC regulates cell migration (Barth et al., 2008; Etienne-Manneville, 2009), spindle orientation (Pereira and Yamashita, 2011; Yamashita et al., 2003), and chromosome segregation (Bahmanyar et al., 2009; Rusan and Peifer, 2008). In mammals, loss of the former function is closely associated with colon cancer (Moser et al., 1992; Su et al., 1992). Loss of the latter function causes spindle positioning defects (Beamish et al., 2009; Green et al., 2005) and chromosome instability (CIN) (Fodde et al., 2001; Green and Kaplan, 2003; Kaplan et al., 2001), a hallmark of metastatic tumors (Hanahan and Weinberg, 2011), suggesting that the cytoskeletal roles of APC during mitosis are also relevant for oncogenesis. How APC regulates the mitotic spindle remains poorly understood and is complicated by its multiple functions, binding-partners and cellular locations (Bahmanyar et al., 2009; Klotz et al., 2012).

Yeast and fly studies have suggested that APC at the cell cortex contributes to mitotic spindle positioning. Kar9, a yeast protein with limited homology to APC, localizes asymmetrically to the cell cortex of budding daughter cells through type V myosin-dependent transport of growing microtubule ends (Hwang et al., 2003; Korinek et al., 2000; Lee et al., 2000). Cortical Kar9 captures microtubules (MTs) by binding yeast EB1, and promotes alignment of the spindle along the mother-bud axis (Korinek et al., 2000; Lee et al., 2000; Miller and Rose, 1998; Siller et al., 2006). *Drosophila* APC2 predominantly localizes to the cell cortex in syncytial embryos. APC2 mutants show a CIN phenotype, presumably because APC2 is required for proper centrosome separation (Poulton et al., 2013). The forces that mediate centrosome separation have been proposed to depend on APC2 connecting astral MTs to cortical actin(Poulton et al., 2013). However, the mechanism by which cortical APC regulates spindle-pulling forces has not been directly addressed in any organism.

We report here that loss of cortical APR-1/APC disrupts asymmetries in spindle movements during mitotic division of the *C. elegans* zygote. In wild-type embryos, the net pulling forces acting on the mitotic spindle become higher in the posterior compared to the anterior, causing the spindle to move posteriorly during metaphase and anaphase (spindle displacement) (Galli and van den Heuvel, 2008; Gönczy, 2008). In anaphase, the posterior spindle pole swings along the transverse axis (spindle oscillation), while the anterior pole remains relatively stable. We found APR-1 to be enriched at the anterior cortex in a PAR-polarity dependent manner. Depletion of APR-1 resulted in anterior pole oscillations that resemble those of the posterior pole. Moreover, laser-mediated spindle severing showed that the spindle-pulling forces acting on the anterior spindle pole are increased in *apr-1(RNAi)* embryos. Using live imaging and numerical simulation, we found that the APR-1 dependent stabilization of MT-cortex interactions negatively regulates the pulling forces acting on the anterior centrosome in wild-type zygotes. Our study identifies APR-1 as an attenuator of spindle-pulling forces, and improves our understanding of how cortical polarity precisely regulates spindle positioning during asymmetric cell division.

Results and discussion

APR-1/APC localizes asymmetrically to the cell cortex in a PAR and Frizzled protein dependent manner

We have previously shown that APR-1 localizes asymmetrically to the anterior cortex in the EMS blastomere at the six-cell stage and in post-embryonic seam cells, in response to Wnt signals that regulate the asymmetry of these divisions (Mizumoto and Sawa, 2007; Sugioka et al., 2011). While analyzing GFP::APR-1 localization in early embryos, we noticed that APR-1 is also asymmetrically localized in the zygote, called P0, where roles for Wnt signaling have not been reported. APR-1 formed dot-like particles that were enriched within the anterior cortex throughout P0 cell division (APR-1 asymmetry) (Figure 1A). We quantified the number of APR-1 dots by counting the fluorescent foci with a signal above a threshold (see Materials and methods). The foci numbers changed from prophase to metaphase, and from anaphase to telophase. Nevertheless, we observed anterior enrichment of APR-1 foci throughout mitosis (Figure 1A and 1D).

It is well-established that the Par-aPKC system generates anterior-posterior (A-P) cell polarity to regulate the asymmetric division of P0, through interactions between anterior (PAR-3, PAR-6, PKC-3) and posterior (PAR-2, PAR-1) *partitioning defective* (PAR) proteins at the cell cortex (Figure 1B; (Munro and Bowerman, 2009)). We found that APR-1 asymmetry in P0 was disrupted after RNAi knockdown of *par-3*, *pkc-3* or *par-2* (Figure 1C, 1E, and Figure S1), suggesting that its asymmetry is established through the Par-aPKC system.

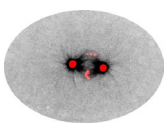

In EMS and seam cells, the establishment of APR-1 asymmetry depends on Wnt proteins (Mizumoto and Sawa, 2007; Sugioka et al., 2011). In P0, MOM-2 is the only Wnt protein that is maternally provided as mRNA (Harterink et al., 2011), although the mRNA appears not to be translated until the 4-cell stage (Oldenbroek et al., 2013). As expected, we found that APR-1 localization was not affected in *mom-2(or309)* null mutants, suggesting that the APR-1 asymmetry in P0 does not require Wnt ligands (Figure 1C, 1E, and Figure S1).

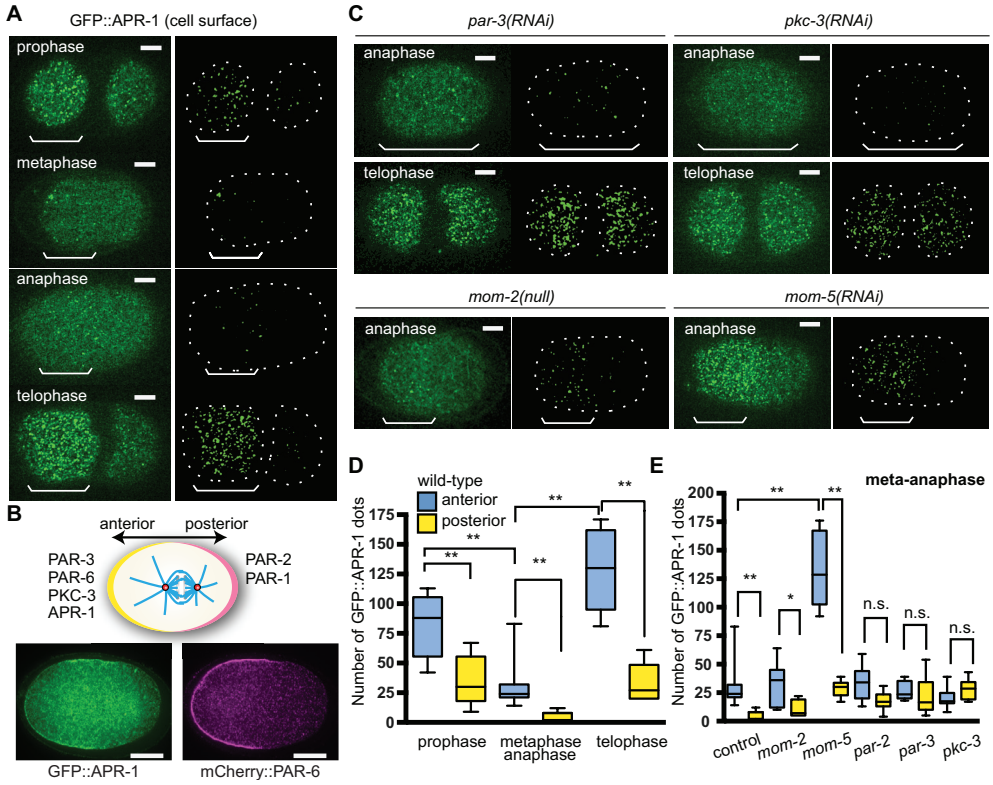

Figure 1 The Par-aPKC system and Frizzled signaling regulate APR-1 asymmetric localization during zygote division. **(A)** GFP::APR-1 signals on the cell surface in different mitotic stages. In the right panels, computationally detected APR-1 dots are shown (see Material and Methods). **(B)** GFP::APR-1 and mCherry::PAR-6 localizations in the cell midplane during asymmetric cell division. GFP signal was amplified by the anti-GFP immunostaining. Schematic drawing shows polarized protein localizations. **(C)** GFP::APR-1 signals on the cell surface in *mom-2(null)* mutants and *mom-5*, *par-2* or *par-3* RNAi embryos. **(D)** Quantified numbers of GFP::APR-1 dots on the anterior and posterior cell cortex of wild-type embryos in different mitotic stages. n = 5, 10, 5 from left to right. **(E)** Quantified numbers of GFP::APR-1 dots at metaphase or anaphase in RNAi embryos. n = 10, 7, 10, 9, 10, 10, from left to right. Ends of whiskers indicate minimum or maximum values. Double asterisk, asterisk and n.s. indicates: $p < 0.01$, $p < 0.05$ and $p > 0.05$ (One-way ANOVA with Holm-Sidak's multiple comparison test). Scale bars are 10 μm.

Despite the lack of a requirement for MOM-2/Wnt, we observed altered APR-1 localization after RNAi knockdown of downstream Wnt signaling components. Specifically, knockdown of the Frizzled receptor MOM-5 or simultaneous inhibition of the Dishevelled homologs, DSH-2 and MIG-5, increased the numbers of APR-1 foci at metaphase/anaphase in both the anterior and posterior cortex without altering APR-1 expression levels (Figure 1C, 1E, Figure S1, and Figure S2A). Inhibition of WRM-1/β-catenin did not affect APR-1 localization, and *mom-5(RNAi)* as well

as *dsh-2;mig-5(RNAi)* embryos still showed APR-1 asymmetry (Figure 1C, 1E, and Figure S1). DSH-2 localizes to the posterior cell cortex during Wnt-dependent asymmetric cell divisions later in development (Mizumoto and Sawa, 2007; Walston et al., 2004). In contrast, DSH-2 localization in P0 was not asymmetric (Figure S2B), consistent with the lack of Dishevelled requirement in APR-1 asymmetry. Interestingly, inhibition of the Axin homolog PRY-1 and Casein kinase homolog KIN-19 resulted in loss of APR-1 asymmetry only during meta-anaphase, suggesting their partial requirement in the establishment or maintenance of APR-1 asymmetry (Figure S1B and S1C).These results are consistent with observations at a later developmental stage (Baldwin and Phillips, 2014). We conclude that APR-1 asymmetry in P0 is established by the Par-aPKC system with partial involvement of Axin and Casein kinase, while Frizzled and Dishevelled negatively regulate the levels of cortical APR-1.

APR-1 asymmetrically suppresses centrosome movements during P0 cell division

The Par-aPKC system independently regulates two P0 asymmetries: the segregation of cell fate determinants (e.g. PIE-1 and PGL-1) and posterior mitotic spindle displacement and thereby asymmetric cell cleavage. In *apr-1(RNAi)* embryos, GFP::PIE-1 segregated into the posterior daughter cell as in wild-type embryos, indicating that APR-1 is not involved in cytoplasmic determinant localization (Figure S2C). In contrast, *apr-1(RNAi)* embryos showed abnormal spindle oscillations. In wild type P0, posterior spindle displacement (represented by centrosome movements along the A-P axis) starts during metaphase and continues during anaphase when it coincides with transverse oscillations (represented by centrosome movements along the transverse axis) of the two spindle poles (Figure 2A, 2B, 2D, 2E). The posterior spindle pole oscillates more vigorously than the anterior pole (Figure 2B, 2E and Video 1), as a result of higher posterior than anterior cortical pulling forces (Pecreaux et al., 2006). In *apr-1(RNAi)* embryos, spindle movements were exaggerated: in some embryos, the mitotic spindle moved back and forth along the A-P axis (Figure 2C, 2D, and Video 2), and in some cases, the anterior spindle pole exhibited excessive transverse oscillations, visible by the increased frequency and amplitude of the spindle pole tracks (Figure 2C, 2E and Video 2). As a result, the total distance traveled by the anterior centrosome significantly increased compared to that in control embryos (Figure 2F). These data indicate that APR-1 suppresses anterior spindle pole movements and thereby control spindle positioning during anaphase.

In *mom-5(ne12)* null mutant embryos, in which APR-1 levels were increased at both the anterior and posterior cortex, we observed reduced posterior spindle pole oscillations (Figure S3A and S3B). However, spindle pole oscillations were not restored in *apr-1(RNAi); mom-5(null)* embryos (Figure S3B). These results suggest APR-1-independent functions of MOM-5 that influence spindle movements. Because of this, we could not determine the effects of excess cortical APR-1 on spindle pole movements in the *mom-5(null)* background. However, in other aspects of spindle dynamics described below, elevated cortical APR-1 localization potentiated APR-1 function.

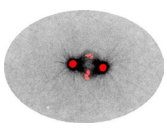

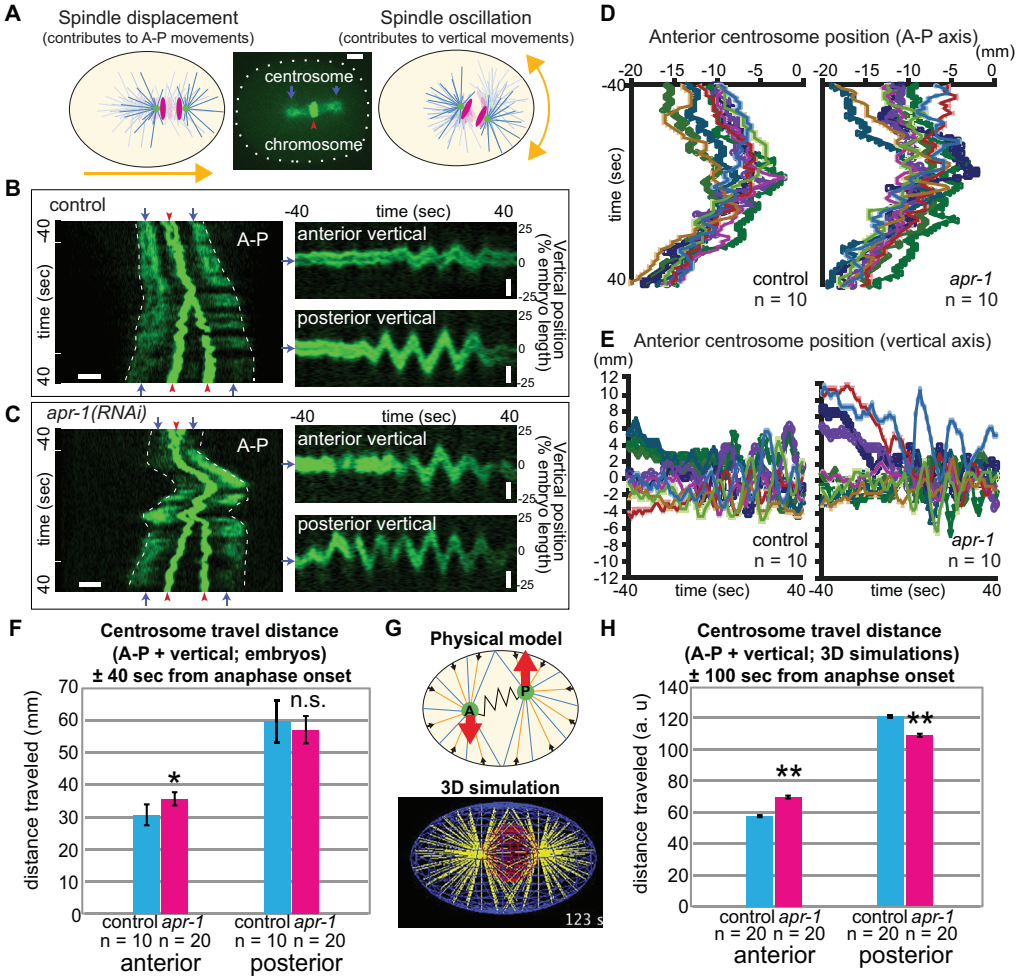

Figure 2 APR-1 asymmetrically suppresses centrosome movements during the P0 cell division. **(A)** Schematic drawings of spindle movements along the A-P and transverse axes. Spindle displacement and oscillations contribute mainly to the movements along the A-P and transverse axes, respectively. Blue arrows and red arrowhead indicate centrosomes (gamma-tubulin) and chromosomes (Histone H2B), respectively. **(B, C)** Centrosome movements in A-P (left panels) and transverse (right panels) axes in control **(B)** and *apr-1(RNAi)* ± 40 second around anaphase onset **(C)**. Kymographs (stack of line images of each time point) were made to show centrosome movements along the A-P and transverse axes separately. **(D, E)** Anterior centrosome position during cell division along the A-P **(D)** and vertical axes **(E)**. Cell centers are position zero. (F, H) Total distances for movements of the anterior and posterior poles in living embryos **(F)** and in 3D simulations (H). **(G)** Physical model used for 3D simulations. A and P indicate the anterior and posterior spindle poles harboring shrinking MTs (orange) and elongating MTs (blue). Red and black arrows indicate centrosome movements and cortical force generation. For each MT catastrophe at the cortex, the average pulling forces acting on a single MT at the posterior are stronger than those at the anterior, due to the different probabilities of MT-force generator interactions (see Materials and methods). Error bars show 95% CI. Double asterisk and n.s. indicates: $p < 0.01$ and $p > 0.05$ compared to control (Kruskal-Wallis test followed by Dunn's multiple comparison test). Scale bars indicate 5 µm.

APR-1 asymmetrically stabilizes microtubule-cortex interactions

As mammalian APC and *C. elegans* APR-1 in the EMS cell can stabilize MTs (Sugioka et al., 2011; Zumbrunn et al., 2001), we hypothesized that anteriorly enriched APR-1 in the P0 cell may also increase MT stability at the cell cortex to regulate asymmetric spindle movements. To assess this possibility, we analyzed the MT-cortex interactions using live imaging of GFP::β-tubulin expressing embryos. In kymographs of midplane images, astral microtubules appear to persist longer on the anterior cell cortex than on the posterior, consistent with previous observations (Figure 3A; (Labbé et al., 2003)). To precisely quantify MT-plus end residence time at the cortex, we measured the duration of GFP::β-tubulin foci on the flattened cell surface (Figure 3B). Most of the GFP::β-tubulin foci initially co-localized with the EB1-related plus-end binding protein EBP-2 (96.1%; n = 255), confirming that the foci represent MT plus-ends. Shortly after the cortical attachment, EB1 dissociates from MT plus-ends, while some MTs remained at the cortex after the release of EB1 (Fig. 3B and 3D). The numbers of such long-lived microtubule plus-ends were higher anteriorly, accounting for the asymmetry in cortical MT residence time in wild-type zygotes (Figure 3B-3D; red arrows in 3C, Video 3 and Video 4).

Notably, the MT residence time at the anterior cortex was significantly lower in *apr-1(RNAi)* embryos than in the wild type (Figure 3C, 3E and Video 5). In contrast, *mom-5* mutants with excess cortical APR-1 showed an increased MT residence time at both the anterior and posterior cell cortex (Figure 3C, 3E and Video 6). RNAi knockdown of *apr-1* overcame this *mom-5* phenotype, reducing MT cortical residence throughout the cortex (Figure 3C, 3E and Video 7). Thus, APR-1 stabilizes microtubule-cortex interactions and acts downstream of MOM-5 (Figure 4D).

The exaggerated anterior spindle pole movements in *apr-1(RNAi)* embryos implicate APR-1 in spindle-pulling force regulation. We investigated this possibility using spindle severing assays (Figure 4A; (Grill et al., 2001)). After cutting the spindle midzone with a UV laser, the average peak velocities of the anterior and posterior spindle poles moving toward the cell cortex were calculated (Figure 4A). In control embryos, the posterior spindle pole moved faster than the anterior pole, as expected (Figure 4A, 4B, and Video 8). In *apr-1(RNAi)* embryos, we observed an increased average peak velocity specifically for the anterior spindle pole (Figure 4A, 4B, and Video 8). In *mom-5(null)* embryos with excess cortical APR-1, both the anterior and posterior spindle poles showed reduced average peak velocities (Figure 4B and Video 8). Combined *apr-1(RNAi);mom-5(null)* embryos showed increased average peak velocities and resembled *apr-1(RNAi)* embryos (Figure 4B and Video 8). These results indicate that the cortical levels of APR-1 inversely correlate with spindle-pulling forces and suggest a role for APR-1 as cortical pulling force attenuator (Figure 4D).

APR-1-dependent stabilization of MTs accounts for reduced pulling forces on the anterior spindle pole

We have shown that APR-1 is enriched at the anterior cell cortex, promotes cortical MT residence times anteriorly, and suppresses both spindle-pulling forces and anterior spindle pole oscillations, raising the possibility that these processes are mechanistically linked. It has been shown that cortical pulling forces are generated when MTs reaching the cortex meet dynein and undergo catastrophe (transition from MT plus end growth to rapid shrinkage) (Laan et al., 2012). Therefore, we hypothesized that cortical APR-1 reduces the MT catastrophe frequency and thereby attenuates force generation and spindle movement. However, it is not clear whether the magnitude of APR-1-dependent cortical MT stabilization is sufficient to suppress spindle movement.

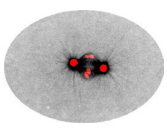

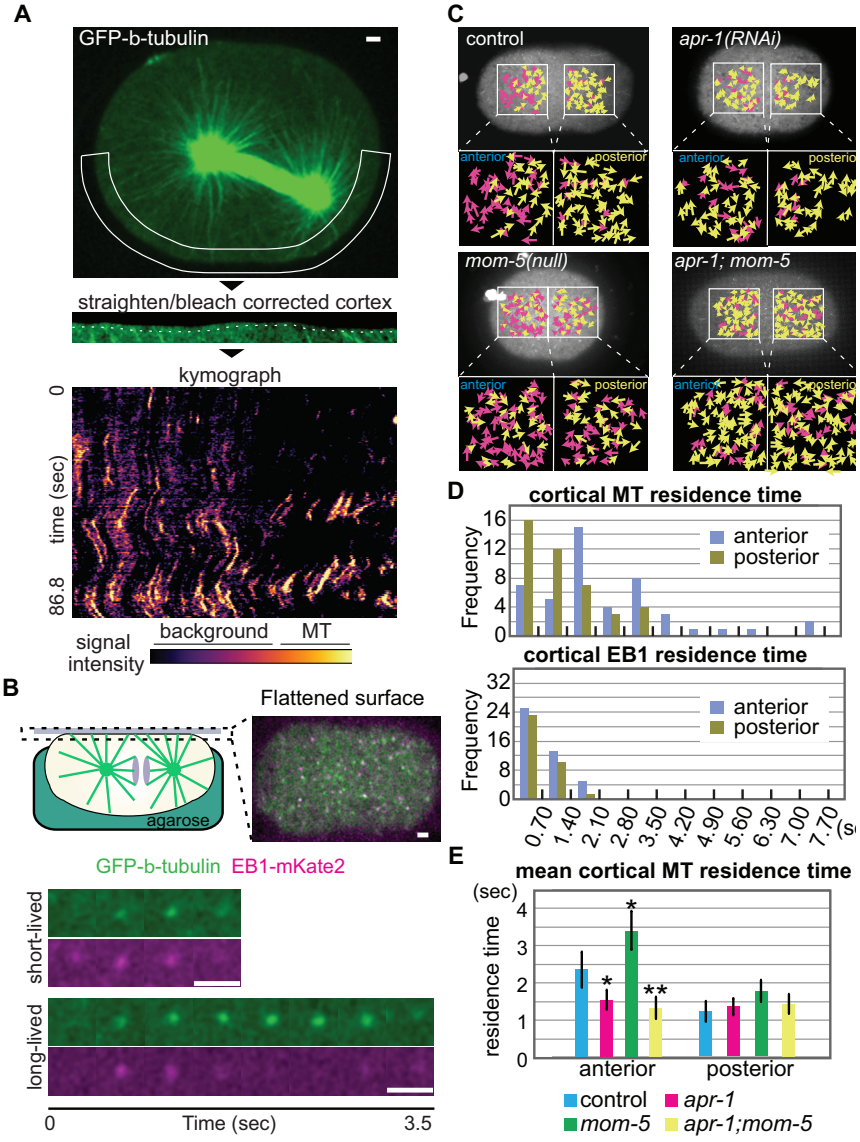

Figure 3 APR-1 asymmetrically stabilizes microtubule-cortex interactions. **(A)** Cortical MT dynamics. Cortical area outlined by the solid line in top figure was extracted, straightened, and corrected for photobleaching. This cortical area, depicted by the dotted line (middle), was used to generate a kymograph (bottom). Color code of the kymograph was changed to highlight MTs. **(B)** Measurement of cortical MT residence. The embryos were mounted on agarose pads and flattened by coverslips to visualize cortical microtubule ends in a single focal plane. Examples of short and long-lived foci were shown below with simultaneous imaging of GFP::β-tubulin and EB1::mKate2. **(C)** Cortical microtubule dots in the indicated genotypes during metaphase-anaphase. Images are max projection of cortical GFP::β-tubulin for 60 frames (42 sec). Yellow and Magenta arrows indicate the MT dots whose residence time was shorter and longer than 2.1 sec, respectively. See also Video 3, 5-7. **(D)** Distribution of quantified cortical MT or EB1 residence time in wild-type animals. **(E)** Mean cortical MT residence time of indicated genotypes. n = 47, 42, 77, 67, 64, 61, 37, 44, from left to right. Error bars show 95% CI. Double asterisk and asterisk indicate: $p < 0.01$ and $p < 0.05$ compared to control (Kruskal-Wallis test followed by Dunn's multiple comparison test). Scale bars indicate 2.5 μm.

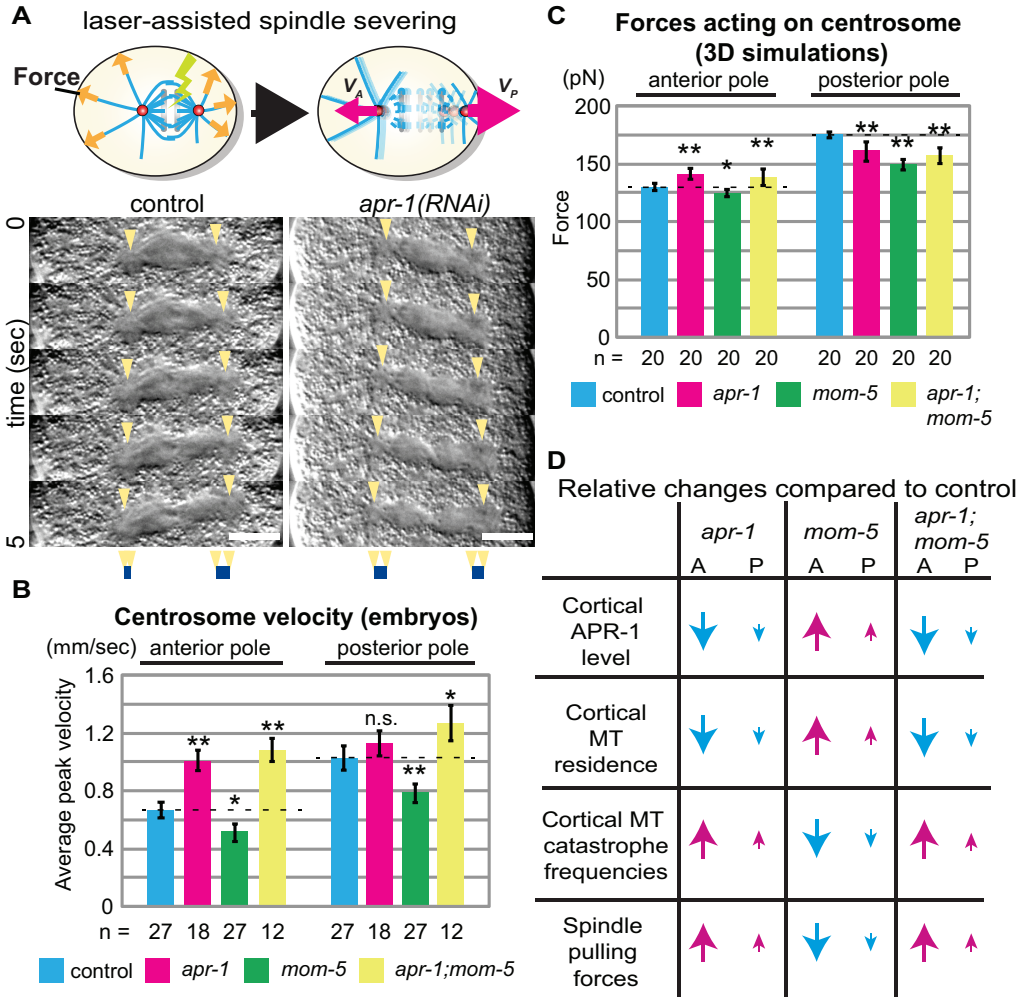

Figure 4 APR-1 asymmetrically attenuates pulling forces acting on the mitotic spindle. **(A)** Spindle severing experiments. The midzones of mitotic spindles were severed by laser irradiation around anaphase onset (upper left panel). Upon spindle severing, spindle remnants moved at different velocities depending on the net strength of pulling forces (upper right panel). Montages of dissected spindle dynamics were shown in the bottom panels as DIC images; spindle poles devoid of yolk granules were indicated by arrowheads. **(B)** Average peak velocity of spindle poles after spindle severing. **(C)** The average of outward pulling forces over 5 sec from anaphase onset (t = 100 s) for 20 independent simulations. Error bars show 95% CI. Double asterisk and asterisk indicate: $p < 0.01$ and $p < 0.05$ compared to control (one-way ANOVA with Holm-Sidak's method). **(D)** Summary of relationships between cortical APR-1 level, cortical MT residence, cortical MT catastrophe frequencies, and spindle pulling forces. Scale bars indicate 10 µm.APR-1 asymmetrically attenuates pulling forces acting on the mitotic spindle.

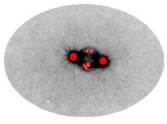

We decided to examine this issue using numerical simulation. First, we estimated MT catastrophe frequencies from their cortical residence time (Supplementary Table 1, Figure S4). In control embryos, the estimated catastrophe frequency at the anterior cortex was about half of that at the posterior cortex. Such a reduced catastrophe frequency was not detected at the anterior cortex of *apr-1(RNAi)* embryos, indicating that in wild type embryos the catastrophe frequency is suppressed by APR-1.

We set the rescue frequency of all MTs high, so that soon after the MTs start to shorten, they regrow to reach the cortex (Supplemental Table 2). This assumption was introduced to make the number of MTs reaching the cortex almost constant regardless of the differences in catastrophe frequencies between anterior and posterior, which is the case in living embryos (Video 3). Without this assumption, the number of MTs reaching the cortex should be ~2-fold higher at the anterior because the catastrophe frequency is about half of the posterior catastrophe frequency. The mechanistic basis of this assumption is provided by the *in vivo* observation that individual microtubules appear to form bundles, and multiple EB1 tracks move along a bundled fiber toward the cell cortex, making rescue frequency of the fiber higher than individual MTs (Video 4), which is consistent to the previous observation (Kozlowski et al., 2007).

We conducted 3-dimensional simulations of spindle movements. As in previous simulations (Hara and Kimura, 2009; Kimura and Onami, 2005, 2007, 2010), the spindle moves as a result of three kinds of forces acting on astral MTs that radiate from each spindle pole (Figure 2G). First, all MTs generate pulling forces proportional to their length ("cytoplasmic pulling force"). This force is important for positioning of the spindle in the cell center during mitotic prophase (Hamaguchi and Hiramoto, 1986; Kimura and Kimura, 2011; Kimura and Onami, 2005), and is also critical for oscillation (Pecreaux et al., 2006). Second, MTs that reach the cell cortex generate the pulling force at their plus ends only when they undergo catastrophe ("cortical pulling force"). The current theory for the basis of oscillation is that when the spindle poles move toward one side, the pulling force from that side becomes stronger ("positive feedback" or "negative friction"), while the opposing centering force also increases (Grill et al., 2005; Pecreaux et al., 2006; Vogel et al., 2009). With this mechanism, the spindle is not stabilized at the center but oscillates. In our model, the frequency of the force generation depends on the number of active cortical force generators and the MT residence time controlled by APR-1, both of which have A-P asymmetry. The third force connects the anterior and posterior spindle poles. We assumed a spring-like connection between the poles that was weakened after anaphase onset to mimic the spindle elongation.

Numerical simulations were conducted for control, *apr-1(RNAi),* and *mom-5(null)* situations (Figure S5), by setting the catastrophe frequency to values estimated from experimental data (e.g. 0.31 /s for the anterior and 0.72 /s for the posterior, see Supplementary Table 1). The simulation results indicated that the APR-1-dependent stabilization of MTs is sufficient to suppress oscillation of the anterior pole (Figure 2H). In wild-type simulations, the spindle moved toward the posterior and elongated upon anaphase onset (Figure S5A and Video 9). The oscillations perpendicular to the A-P axis were also reproduced for both spindle poles (Figure S5B). In *apr-1(RNAi)* simulations, in which the catastrophe frequency at the anterior cortex was increased, the amplitude of the anterior spindle pole oscillations was increased (Figure 2H, Figure S5 and Video 9). Furthermore, the average peak velocities of anterior poles in the severing experiments were also consistent with the forces acting on anterior spindle poles in our simulations (Figure 4C). Overall, the numerical simulations supported the hypothesis that the APR-1-dependent stabilization of MTs at the cortex can suppress spindle pole oscillations through the reduction of force generation.

Anterior APR-1 and LIN-5 phosphorylation together attenuate spindle pulling forces

We investigated the significance of spindle pulling force attenuators in asymmetric cell division. Along with APR-1, we focused on the LIN-5 protein. LIN-5 interacts with cortical GPR-1/2 and dynein in cortical force generation (Nguyen-Ngoc et al., 2007). We have previously reported that anteriorly-localized PKC-3/aPKC phosphorylates LIN-5 to attenuate cortical-pulling forces (Galli et al., 2011a). We edited the *lin-5* genomic locus to substitute four aPKC phosphorylated serine residues with alanine by CRISPR/Cas9-mediated homologous recombination (*lin-5 4A* mutation). In spindle severing experiments, combining *apr-1(RNAi)* and the *lin-5 4A* mutation caused significantly enhanced average peak velocities of the anterior poles as compared to *apr-1(RNAi)* embryos (Figure 5A). Compared to *lin-5 4A* embryos, the increase in anterior peak velocity was not significant (p= 0.07; Figure 5A). However, in contrast to the single mutants, the ratio of anterior to posterior centrosome peak velocities in *apr-1(RNAi)*; *lin-5 4A* double mutants was significantly reduced compared to wild-type controls (Figure 5B). These data suggest that the Par-aPKC-dependent asymmetric localization of APR-1 and phosphorylation of LIN-5 together attenuate cortical pulling forces to generate pulling force asymmetry that positions the mitotic spindle (Figure 5C-5E).

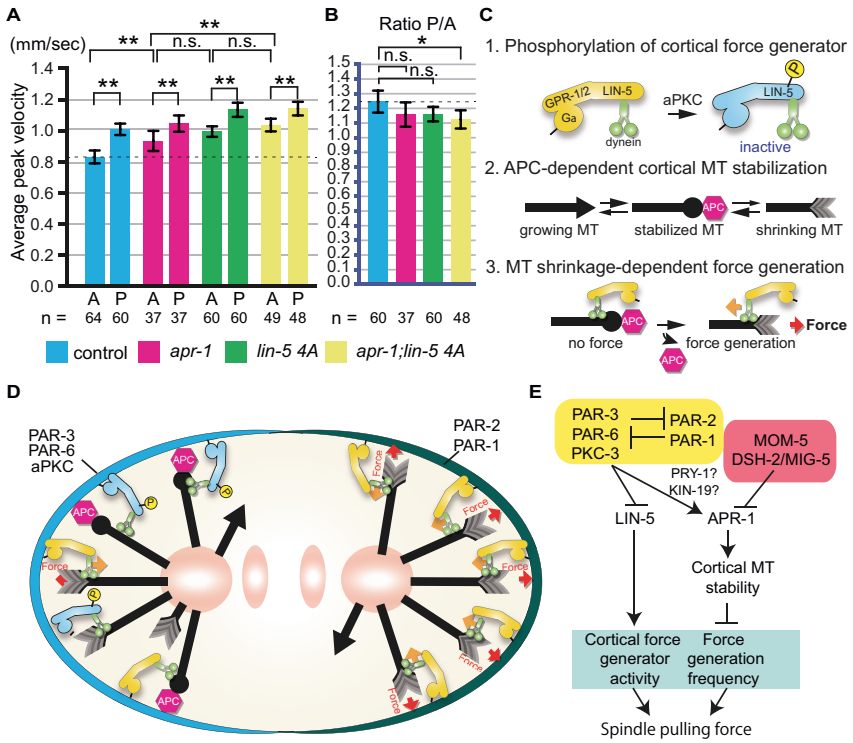

Figure 5 Anterior APR-1 enrichment and LIN-5 phosphorylation together attenuate spindle pulling forces to generate pulling force asymmetry. **(A, B)** Average peak velocity of spindle poles **(A)** and their posterior/anterior ratio **(B)** after spindle severing. Error bars show 95% CI. Double asterisk and asterisk indicate: $p < 0.01$ and $p < 0.05$ compared to control (one-way ANOVA with Holm-Sidak's method). **(C)** Three elementary processes used in the model described in the panel C. (1) aPKC-dependent LIN-5 phosphorylation results in the inhibition of force generation, (2) Cortical MT stabilization by APC reduces the MT catastrophe frequency and (3) MT shrinkage-dependent force generation is suppressed by step (2). **(D)** A schematic model of asymmetric spindle force regulation in P0 cell (see text). (E) A diagram of spindle pulling force regulation pathways at the anterior cell cortex.

Conclusion

In this study, we investigated how the APR-1/APC protein regulates mitotic spindle movements in the *C. elegans* one-cell embryo, a well-established model for asymmetric cell division. We observed that APR-1/APC becomes asymmetrically enriched at the anterior cell cortex, dependent on the Par-PKC-3 polarity pathway. We found that APR-1 attenuates spindle pulling forces, most likely though stabilization of MTs at the anterior cell cortex. In concert, Wnt signaling components MOM-5/Frizzled and Disheveled proteins suppressed cortical accumulation of APR-1, thereby contributing to the correct levels of pulling forces. To test these assumptions, we performed numerical simulations, which closely mimicked the spindle movements in wild-type and mutant embryos. These combined data strongly support the conclusion that MT stabilization by APR-1 contributes to correct spindle positioning. Finally, we provide evidence to suggest that asymmetric APR-1 enrichment and PKC-3 phosphorylation of LIN-5 act in parallel to regulate asymmetric cell division. These conclusions are likely to apply broadly and improve our understanding of the microtubule-associated functions of APC.

Although APC is a component of Wnt signaling, its localization has been reported to be regulated by the Par-aPKC polarity pathway in migrating mammalian astrocytes (Etienne-Manneville and Hall, 2003), and during axonal differentiation of developing hippocampal neurons (Shi et al., 2004), as we observed in the *C. elegans* one-cell embryo. Scratching of astrocyte monolayers in wound-healing assays triggers APC localization to the cell cortex at the leading edge, in response to CDC42-induced Par-aPKC polarity and Wnt5a signaling (Schlessinger et al., 2007). Interestingly, polarity establishment in this system is followed by centrosome re-orientation through APC-microtubule interactions (Etienne-Manneville and Hall, 2003). Thus, the mechanisms that control centrosome positioning through interactions between Par polarity, Wnt signaling, and APC may be conserved across species. The dynamic change in cortical APR-1 levels during P0 cell division is intriguing: this may reflect cell cycle dependent activation of the Wnt signaling pathway as reported in fly and mammalian cultured cells (Davidson et al., 2009).

While the roles of cortical APC have been unclear, it was previously proposed that APC stabilizes microtubules through microtubule plus-end binding protein EB1 (Etienne-Manneville and Hall, 2003; Gundersen et al., 2004). Consistently, in the *C. elegans* EMS blastomere, cortical APC stabilizes MT ends coated with EB1 (Sugioka et al., 2011). However, a few examples including the present study indicate that cortical APC can stabilize microtubules independently of EB1. First, truncated mammalian APC that lacks the EB1 interaction domain has been shown to localize to the cell cortex and to MTs in epithelial cells (Reilein and Nelson, 2005). In addition, *Drosophila* APC2, which lacks the C-terminal EB1 binding domain, interacts with microtubule plus ends at the cortex and contributes to centrosome segregation (Poulton et al., 2013). In our study, APR-1 at the anterior cortex stabilizes MTs but the mean cortical residence time of EBP-2/EB1 was symmetric. We also observed that the cortical residence time of EB1 is much shorter than that of MTs in P0, as reported previously (Kozlowski et al., 2007). Therefore, APR-1 at the anterior cortex of P0 likely stabilizes MTs independently of EB1 binding. We observed recently that deleting all EB family members has limited effects on spindle behavior and viability in *C. elegans* (Schmidt et al., 2017). Therefore, the microtubule stabilizing effects of cortical APC probably do not depend on EB1 protein interactions.

Mitotic spindle positioning is tightly controlled during embryogenesis, in various adult stem cell divisions, and in symmetric divisions (Kiyomitsu and Cheeseman, 2012; Siller and Doe, 2009; Williams and Fuchs, 2013). While many studies have focused on the localization of cortical force generators that pull on microtubule plus ends, attenuators of spindle pulling forces may be just as important in creating asymmetry. In fact, a variety of molecular mechanisms appear to suppress spindle pulling forces in the one-cell embryo, including PKC-3-mediated LIN-5

phosphorylation (Galli et al., 2011a), cortical actin (Berends et al., 2013), and posterior-lateral LET-99 localization (Krueger et al., 2010). This study provides insight into and a physical basis of spindle pulling force attenuation: we found that APC acts as an attenuator of spindle pulling forces, through stabilization of microtubule plus ends at the cortex. Importantly, a similar force attenuator function of APC is potentially used in oriented divisions of *Drosophila* germline stem cells (Yamashita et al., 2003), as well as mouse embryonic stem cells (ES cells) attached to Wnt-immobilized beads (Habib et al., 2013), as these systems exhibit asymmetric APC localizations similar to what we have observed in the *C. elegans* zygote. Our study also implies that not only APC but also other proteins involved in MT stabilization are potential cortical spindle pulling force attenuators.

The observed pulling force attenuation function may be relevant for the chromosomal instability (CIN) phenotype associated with APC loss in human colon cancer (Fodde et al., 2001; Kaplan et al., 2001). Initial studies of cultured mammalian cells associated APC loss and CIN with defective kinetochore-microtubule attachments, although abnormal spindle structures were also observed in APC defective cells (Fodde et al., 2001; Kaplan et al., 2001). In *Drosophila* embryos, APC2 was found to localize predominantly to the cell cortex (McCartney et al., 2001). Chromosome missegregation associated with APC2 loss in such embryos was linked to a cytoskeletal function of APC in centrosome segregation (Poulton et al., 2013). In our study, we found that *C. elegans* APC localizes to the cell cortex where it negatively regulates spindle-pulling forces. Consequently, the absence of APC results in increased pulling forces exerted on the spindle poles. Interestingly, defective kinetochore attachments have been shown to cause chromosome segregation defects in *C. elegans*, in a manner dependent on cortical pulling forces (Cheeseman et al., 2005). Thus, combining these data with our results raises a new and testable hypothesis that increased cortical-pulling forces and abnormal MT-kinetochore interactions synergistically elevate the risk of CIN in developing tumors with APC mutations.

Materials and methods

C. elegans culture and strains

All strains used in this study were cultured by standard methods (Brenner, 1974). Most worms were grown at 20 °C or 22.5 °C and then incubated at 25 °C overnight before the analysis. Worms used for anti-DSH-2 staining were grown at 22.5 °C. Worms carrying PIE-1::GFP were grown at 15°C and incubated at 25°C overnight before the analysis. The following alleles were used: *mom-2(or309), mom-5(ne12), par-2(it51)*. We used *mom-5(ne12)* null mutants for all *mom-5* experiments except those in Figure 1. The following integrated transgenic lines were used: *oslS15* (32) for GFP::APR-1; *ruIS32* (Praitis et al., 2001) for GFP::H2B; *ojIS1* (Strome et al., 2001) for GFP::β-tubulin; *axIS1462* (Merritt et al., 2008) for GFP::PIE-1; *axIS1720* (Merritt et al., 2008) for GFP::PGL-1; *tjIS8* for GFP::EBP-1; *ruIS57* for GFP::tubulin; *ax1928* for mCherry::PAR-6 (Zonies et al., 2010);. We also generated EBP-2::mKate2 fusion strain *ebp-2*(*or1954*[*ebp-2*::mKate2]) and *lin-5 (he260[S729A,S734A,S737A,S739A])*strain by CRISPR/Cas9 genome editing as described below.

Generation of CRISPR repair templates

For the generation of the *ebp-2*::mKate2 strain, CRISPR repair constructs containing 700 bp homologous arms were synthesized as gBlock fragments (Integrated DNA Technologies, Coralville, IA) and assembled into pJET2.1 vector using in-house Gibson Assembly reaction mix (Gibson et al., 2009). For the generation of the *lin-5 4A* strain, CRISPR repair constructs were inserted into the pBSK vector using Gibson Assembly (New England Biolabs, Ipswich, MA). Homologous arms

of at least 1500 bp upstream and downstream of the CRISPR/Cas9 cleavage site were amplified from cosmid C03G3 using KOD Polymerase (Novagen (Merck) Darmstadt, Germany). Linkers containing the point mutations were synthesized (Integrated DNA technologies, Coraville, IA). Mismatches were introduced in the sgRNA target site to prevent cleavage of the repair template and knock-in alleles. All plasmids and primers used for this study are available upon request.

CRISPR/ Cas9 genome editing

Young adults were injected with solutions containing the following injection mix. For *ebp-2*::mKate2, 10 ng/µl pDD162 P*eft-3*::Cas9 with sgRNA targeting C-terminus of *ebp-2* locus (Addgene 47549; (Dickinson et al., 2013)), 10 ng/µl repair template, and 65 ng/µl selection marker pRF4 were used. For *lin-5* 4A, 50 ng/µl P*eft-3*::Cas9 (Addgene 46168; (Friedland et al., 2013)), 50 ng/µl of two PU6::sgRNAs targeting the region of the four serine residues to be mutated to alanine, 50 ng/µl repair template and 2.5 ng/µl selection marker P*myo-2*::tdTomato were used. Progeny of animals that carry selection markers were transferred to new plates 3–4 days post injection. For *ebp-2*::mKate2, GFP positive animals were crossed with a strain carrying GFP::tubulin to obtain *ebp-2*::mKate2 with GFP::tubulin (EU3068; *ebp-2*(*or1954*[*ebp-2*::mKate2] II). For *lin-5* 4A, PCRs with primers diagnostic for recombination products at the endogenous locus were performed on F2-F3 populations, where one primer targeted the altered base pairs in the sgRNA site and point mutations and the other just outside the homology arm. The resulting strain (SV1689; *lin-5* (*he260*[S729A/S734A/S737A/S739A]) II) was crossed with AZ244 (*unc-119(ed3)* III; *ruIs57*) to obtain the *lin-5* 4A strain with GFP::tubulin (SV1690; *lin-5(he260); ruIs57*).

RNAi

DNA fragments corresponding to nucleotide 848-1547 of the *apr-1* cDNA were amplified and used for the production of the dsRNA and feeding RNAi. For the experiments in Figure 5, we injected the dsRNA into the gonad and worms were subsequently cultured under feeding RNAi at 25 °C for over 16 hrs before dissecting embryos. For the rest of experiments, after injection of the dsRNA into the gonad, worms were incubated at 25 °C without feeding RNAi for over 30 hrs before dissecting embryos.

Microscopy and analysis of living embryos

All embryos were dissected in an egg salt buffer from gravid hermaphrodites (Edgar, 1995). For live imaging except for the experiments in Figure 5, the embryos were mounted on 4 % agar pads under a coverslip and sealed with petroleum jelly. For most of the experiments embryos were observed at room temperature by a CSU10 spinning-disc confocal system (Yokogawa Electric, Musashino, Japan) mounted on an AxioPlan 2 microscope (Carl Zeiss, Oberkochen, Germany) with a Plan-Apochromat 100X 1.4 NA oil immersion lens. The specimens were illuminated with a diode-pumped solid-state 488 nm laser (HPU50100, 20mW; Furukawa Electric, Tokyo, Japan). Images were acquired with an Orca ER12-bit cooled CCD camera (Hamamatsu Photonics, Hamamatsu, Japan), and the acquisition system was controlled by IP lab software (2 X 2 binning; Milwaukee, WI). Acquired images were processed with the Image J (Eliceiri et al., 2012) and Adobe Photoshop (Adobe Systems, San Jose, CA). For the experiments in Figure 3B, images were captured with a confocal unit CSU-W with Borealis (Andor Technology, Belfast,

Northern Ireland) and dual EMCCD cameras iXon Ultra 897 (Andor Technology) mounted on an inverted microscope Leica DMi8 (Leica Microsystems, Wetzlar, Germany) controlled by Metamorph (Molecular Devices, Sunnyvale, CA). Spindle severing experiments were performed with a Micropoint system (Photonic instruments, St Charles, IL) equipped with a 2 mW pulsed nitrogen laser (model VL-337; Laser Science Inc., Franklin, MA) exciting Coumarin 440 dye. For the experiments in Figure 5, embryos were mounted on 4 % agarose pad dissolved in egg salts buffer and observed by a Nikon Eclipse Ti microscope with Perfect Focus System (Nikon, Tokyo, Japan) equipped with CSU-X1-A1 spinning disk confocal head (Yokogawa Electric) and S Flour 100X 1.3 NA objectives. The specimens were illuminated with Cobolt Calypso 491 nm laser (Cobolt, Solna, Sweden). Spindle severing experiments were performed with 355 nm Q-switched pulsed lasers (Teem Photonics, Meylan, France) with ILas system (Roper Scientific France, Lisses, France/ PICT-IBiSA, Institut Curie). Temperature was maintained at 25°C by INUBG2E-ZILCS Stage Top Incubator (Tokai Hit, Fujinomiya, Japan) on the motorized stage MS-2000-XYZ with Piezo Top plate (ASI, Eugene, OR). Images were acquired with an Evolve 512 EMCCD camera (Photometrics, Tucson, AZ), and the acquisition system was controlled by MetaMorph (Molecular Devices).

Immunostaining

For the analysis of GFP::APR-1 and mCherry::PAR-6 colocalization, we performed the freeze-crack method to permeabilize embryos and fixed them in methanol at -20°C for 5 min followed by acetone at -20°C for 5 min. After washing three times with PBS supplemented with 1% tween-20, the embryos were incubated with rabbit polyclonal anti-GFP antibody (1:1000, invitrogen) overnight. After incubation with goat anti-rabbit Fluorescein (1:1000, Invitrogen), embryos were imaged for Fluorescein and mCherry signal. Embryos were fixed and stained with rabbit anti-DSH-2 antibody as described (Hawkins et al., 2005).

Measurement of embryo volumes

The volumes (V) of embryos were estimated from the measured embryo length (X) and width (Y). When three semi-axes of ellipsoid (embryo) in the x, y and z axes are defined as a, b and c, volume of ellipsoid $V = 4/3\pi abc$. With the assumption of equal embryo width in the y and z axes, we estimated a, b and c as 0.5X, 0.5Y and 0.5Y and calculated V.

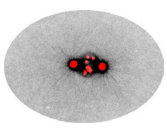

Statistical analysis

For multiple comparisons, one-way ANOVA with Holm-Sidak's method and Kruskal-Wallis test followed by Dunn's multiple comparison test were performed for the data with normal distribution and skewed distribution (judged by F-test), respectively. No statistical method was used to predetermine sample size. The experiments were not randomized. The investigators were not blinded.

Quantification of the data from fluorescence images

For the quantification of the number of dots formed by GFP::APR-1, 8 bit images were processed with Gaussian blur and segmented with the threshold that covers all the visible dots using Fiji. Then number of segments were counted by the Image J plug-in Analyze Particles. For the quantification of total APR-1 level in Figure S2A, 4 successive focal planes including cell center and cell surfaces (corresponding to the upper half of the cell) were combined by the sum projection and average signal intensity of cell region was subtracted by that in the area devoid of embryos. For the generation of kymographs that show the centrosome movements along the anterior-posterior axis, (Figure 2B and 2C, left panels), we drew lines passing through both centrosomes (some centers are missing due to the transverse movements) and generated kymographs using Image J function Multi Kymograph. For the generation of kymographs that show centrosome movements along the transverse axis (Figure 2B and 2C, right panels), we first adjusted the center of the centrosome manually and drew a line that passes through the center of the anterior or posterior centrosome and performed the same procedures. Note that kymographs are composed of linear pixels of each frame for all time points that together show the centrosome trajectory over time. For the quantification of spindle movements, the coordinates of the center of the centrosomes were analyzed with the Image J plug-in Manual Tracking. For the generation of kymographs of cortical microtubules, (Figure 3A), we extracted and straightened cortical regions and performed photo-bleach corrections (exponential fit method) by Image-J. The image color map was changed to mpi-inferno with Image-J. For the quantification of cortical residence times of GFP::EB1 and GFP::β-tubulin, the number of frames from appearance to disappearance of each dot were counted manually. Note that some MT dots whose start and end of cortical localization were unclear were not counted. The average peak velocity after spindle severing was calculated from the distance traveled by the centrosome center.

3-dimensional simulation of spindle movement

Overview. The simulations included 2 spindle poles connected by a spring with dynamic astral MTs inside a cell. The cell was simulated as an oval with a long axis of 50 μm and two short axes of 30 μm. The initial position of the spindle poles was set in the center of the cell and aligned along the long axis with the distance of 10μm, which corresponds to the size of the spindle. The MTs grow and shrink from the spindle poles stochastically according to the dynamic instability. Depending on the length and configuration of the MTs, 3 kinds of forces act on spindle poles to move them as explained below. From an initial configuration, the configuration of the MTs and the spindle poles was calculated at successive time steps as conducted in previous simulations (Hara and Kimura, 2009; Kimura and Onami, 2005, 2007, 2010). The parameters used are listed in Table S2.

Force 1, cytoplasmic pulling forces. All MTs generate pulling force proportional to their length. This force is important to bring the spindle at the cell center (Hamaguchi and Hiramoto, 1986; Kimura and Kimura, 2011; Kimura and Onami, 2005), and is also critical for oscillation (Pecreaux et al., 2006). The cytoplasmic pulling force generated for an i-th MT was modeled as $Fcytoplasm(i) = D \times L(i) \times FFG(i)$, where D is the density of active force generators in the cytoplasm and $L(i)$ is the length of the MT. $FFG(i)$ is same as in the cortical pulling force. The direction of the force is the same as the direction of the MT. We note that the centering force required for oscillation can also

be provided by a force that microtubules produce when they push against the cortex (Garzon-Coral et al., 2016) instead of the cytoplasmic pulling force. The detailed mechanisms (i.e. pulling or pushing) of the centering force do not affect the overall behavior of our model.

Force 2, cortical pulling forces. MTs that reached the cell cortex generate pulling forces toward their direction only when they start to shrink. The cortical pulling force generated for an *i*-th MT was modeled as $Fcortex(i) = Npotential(i) \times Pactive(i) \times FFG(i)$. *Npotential* is the number of force generators that can potentially interact with the MT. We set this value at 30 for the posterior cortex and 15 for the anterior cortex. The experimental value of this parameter has not been investigated, but this number is consistent with a previous study estimating that the total number of force generators is less than 50 and the density is double at the posterior cortex compared to anterior cortex (Grill et al., 2003). *Pactive* is the probability that the potentially interacting force generators are active. A critical assumption to generate robust oscillation here is to model this value high when the spindle pole is approaching the site of the force generator, and low when the spindle pole is leaving (Grill et al., 2005; Pecreaux et al., 2006). In the previous study (Pecreaux et al., 2006), *Pactive* was defined as $Pactive = pmean + (f'/fc) \times pmean \times (1-pmean) \times v - \tau \times (f'/fc) \times pmean \times (1-pmean) \times a$. For simplicity, we neglected the acceleration term (*a*) and fixed the *pmean* parameter to 0.5 to see the extensive oscillation (Pecreaux et al., 2006). We set $f'/fc = 4.0/ Vmax$, and thus used $Pactive = 0.5 + v/Vmax$. Here *v* is the velocity of the spindle pole toward the direction of the force generator on the cortex. When $v<0$, we set $Pactive = 0$. *FFG* is formulated as $FFG = Fstall (1-v/Vmax)$ (Kimura and Onami, 2005; Pecreaux et al., 2006). When $v>Vmax$, we set $FFG = 0$. In the simulation, force generation for shrinking MTs lasts for 100 steps (1 s).

Force 3, forces connecting the two poles. To connect the anterior and posterior spindle poles, which is done by spindle MTs *in vivo*, we treated the spindle as a Hookean spring. The natural length increases proportionally from 10 μm at time zero to 12 μm at $t = 100$ s, which is the onset of anaphase in the simulation. After the onset of anaphase, the natural length increases proportionally to 22 μm at $t = 200$ s. The spring constant is high (1 pN/μm) so that the length of spindle is almost maintained to the natural length.

Acknowledgements

We thank Nancy Hawkins for the anti-DSH-2 antibody, the *Caenorhabditis* Genetics Center (funded by the NIH Office of Research Infrastructure Programs; P40 OD010440) for strains. This work was supported by the Netherlands Organization for Scientific Research (NWO) research program 821.02.001 to SvdH, NIH grant R01GM049869 to B.B., by the Human Frontier Science Program and NIG-JOINT (2013-A60) to K.S., by the Uehara Memorial Foundation to H.S., and Grants-in-Aid for Scientific Research from the Ministry of Education, Culture, Sports, Science, and Technology of Japan to H.S (JP22127005) and A.K. (JP15H04732 and JP15KT0083).

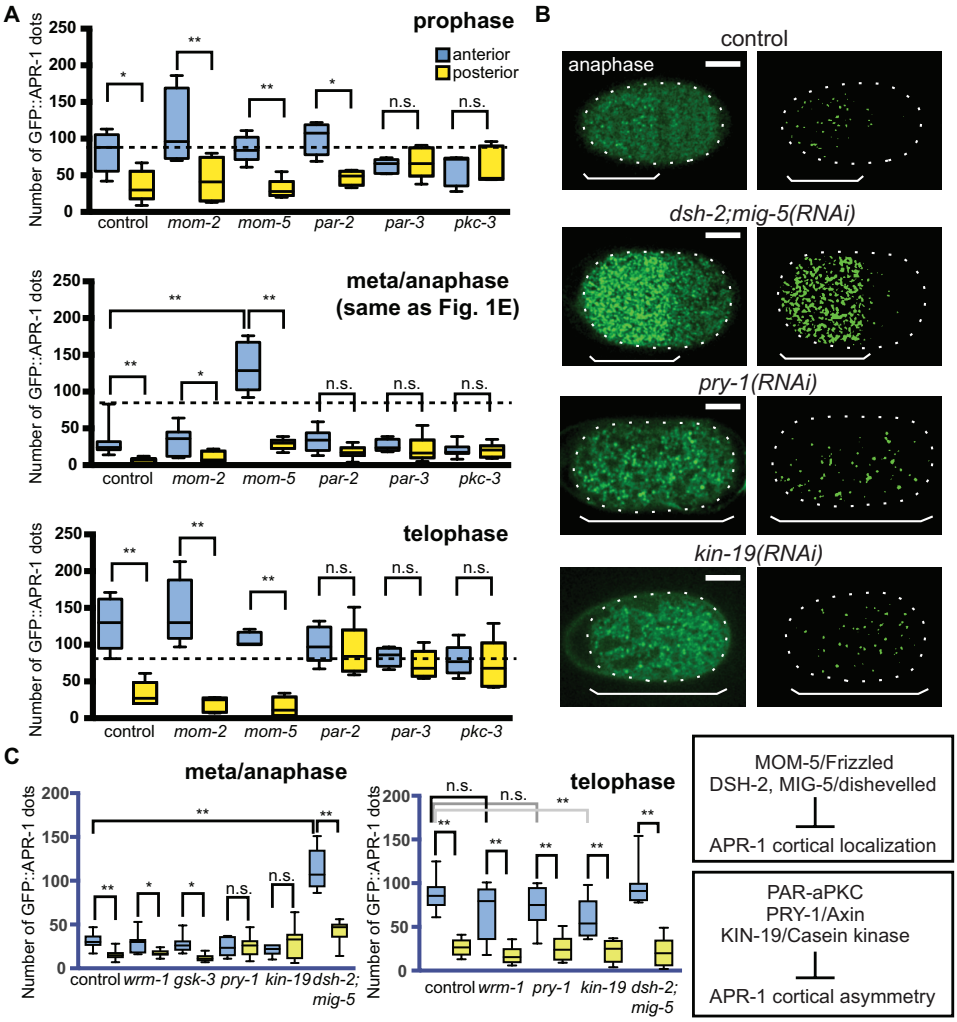

Supplementary figure 1 Temporal and genetic regulation of cortical GFP::APR-1 localization. **(A, C)** Quantified numbers of GFP::APR-1 dots on the anterior and posterior cell cortex are shown for prophase, metaphase, anaphase and telophase of control and RNAi embryos. **(B)** APR-1 dots in the in the indicated RNAi experiments. Left and right panels are original and computationally segmented binary images, respectively. Ends of whiskers indicate minimum to maximum values. Double asterisk, asterisk and n.s. indicates: $p < 0.01$, $p < 0.05$ and $p > 0.05$ (One-way ANOVA with Holm-Sidak's multiple comparison test). Scale bars indicate 10 µm.

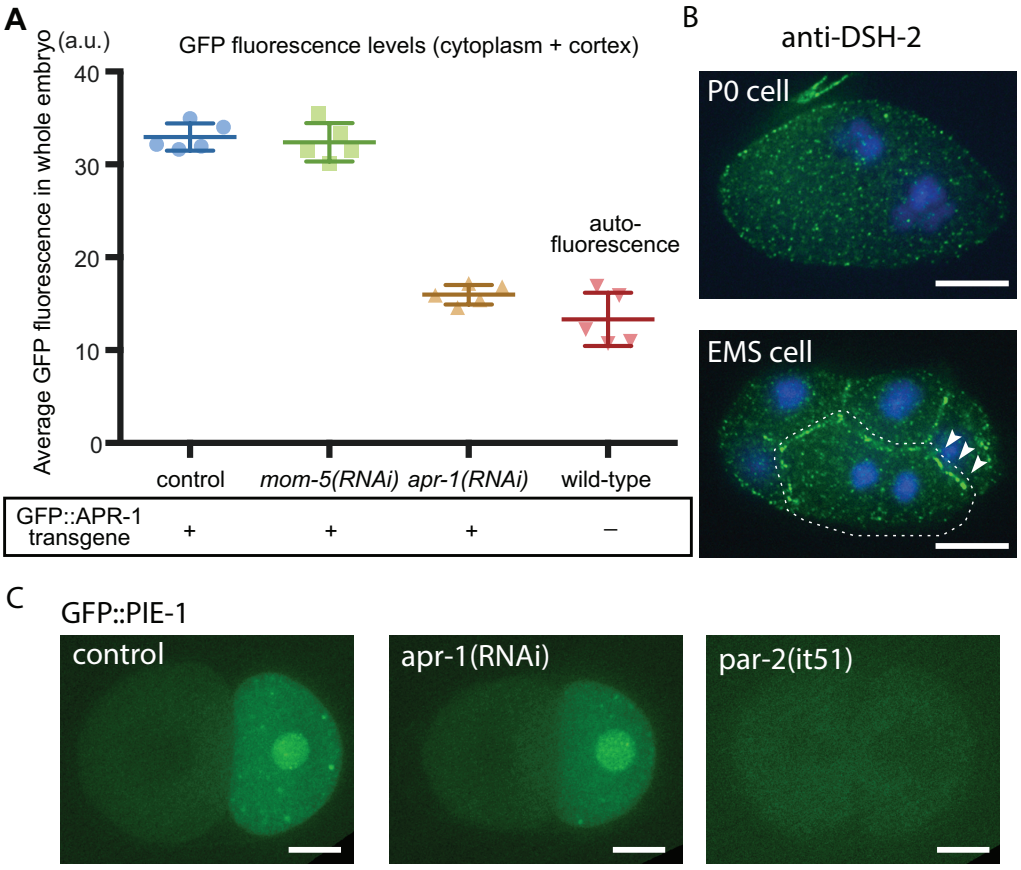

Supplementary figure 2 Roles of Wnt signaling in P0 cell division. **(A)** APR-1 level after RNAi experiments. GFP fluorescence signal intensity per area of the whole embryo including the cell cortex and cytoplasm were measured and shown. Signal in wild-type indicates autofluorescence. **(B)** Immunofluorescence images of the DSH-2 protein during P0 and EMS cell division. Blue is DAPI staining. In EMS, the DSH-2 protein is enriched at the cell boundary between EMS and P2 (arrowheads) while no asymmetry was observed in P0. **(C)** Localization of the cell fate determinant GFP::PIE-1 in the indicated genotypes. Control and *apr-1(RNAi)* shows PIE-1 enrichment in the posterior blastomere P1. In the *par-2* mutant, PIE-1 asymmetry was lost. Scale bars indicate 10 µm.

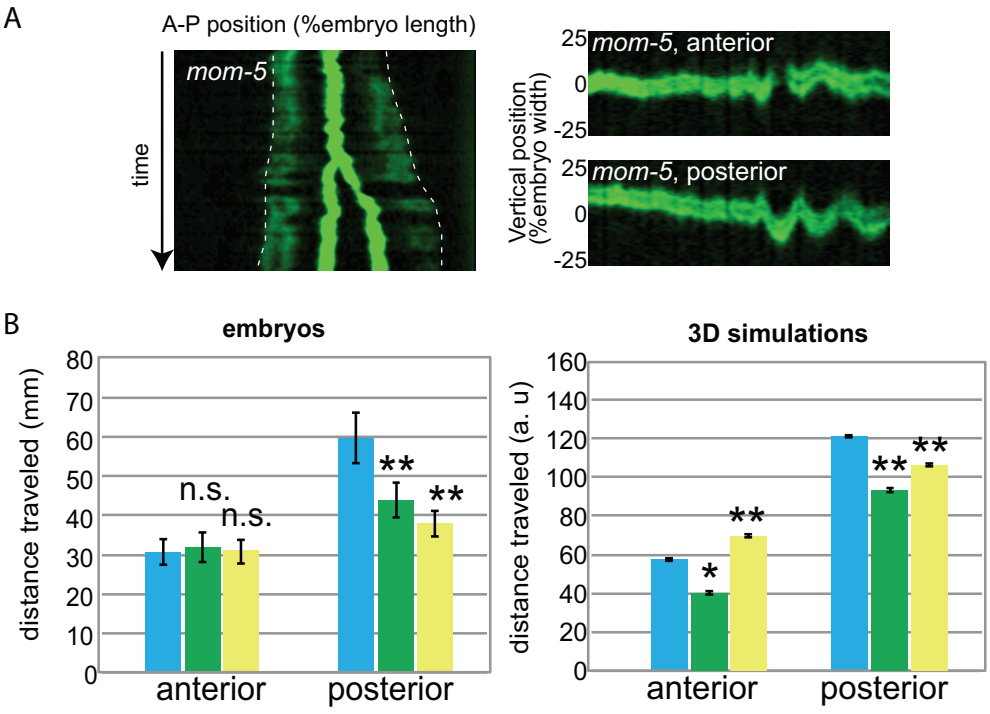

Supplementary figure 3 Effects of *mom-5(RNAi)* on spindle pole movements and embryo sizes. **(**A) Kymographs of the spindle movements in *mom-5(RNAi)*. Kymographs were generated as in Figure 2. **(B)** Distance traveled by the anterior or posterior spindle pole. Total distance centrosome traveled for ± 40 sec and ± 100 sec from anaphase onset were shown for *in vivo* measurements (left) and 3D simulations (right). Error bars show 95% CI. Asterisk indicate $p < 0.05$ compared to control (Kruskal-Wallis test followed by Dunn's multiple comparison test).

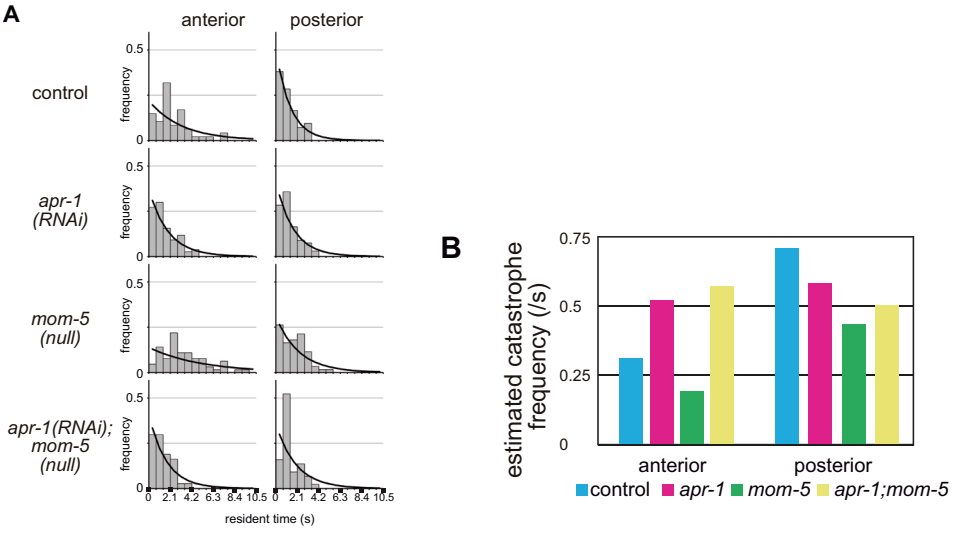

Supplementary figure 4 Estimation of microtubule catastrophe frequencies at the cortex. **(A)** Frequencies of MT residence times at the cell cortex observed experimentally (histograms) and predicted from the estimated catastrophe frequencies (black lines). **(B)** Estimated catastrophe frequencies for indicated genotypes. The data is the same as in Supplementary Table 1.

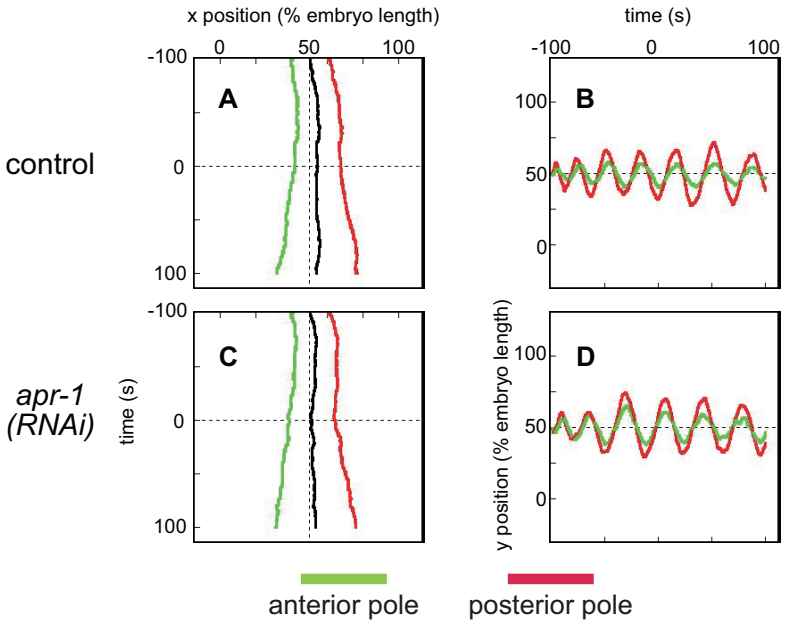

Supplementary figure 5 Numerical simulation of spindle movements. **(A-D)** Representative trajectories of the spindle poles in the simulation. The trajectories of the anterior (green) and posterior (red) poles are shown. Their midpoint (black) is also shown in **(A and D)**. **(A, B)** Control condition. **(C, D)** *apr-1(RNAi)* condition. **(A and D)** Trajectories along A-P axis (x axis). **(C and E)** and those along an axis perpendicular to the x axis (y axis) are shown.

	anterior cortex	posterior cortex
control (N2)	0.31 (/s)	0.72 (/s)
apr-1	0.53 (/s)	0.59 (/s)
mom-5	0.20 (/s)	0.44 (/s)
apr-1;mom-5	0.58 (/s)	0.51 (/s)

Table 1 Estimated catastrophe frequencies of the microtubules at the cortex. When catastrophe occurs stochastically with the frequency of λ, the probability distribution of the cortical residency time will be $P(t) = \lambda\exp(-\lambda t)$. Therefore, the probability of observing cortical residency time between t1 and t2 will be $P(t1 \sim t2) = \exp(-\lambda t1) - \exp(-\lambda t2)$. We fitted the experimentally obtained probability distribution of the cortical MT residency time to this equation to estimate the catastrophe frequencies of the MTs at the cortex.

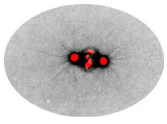

		References
Microtubule (MT) dynamics		
Growth velocity (Vg) [mm/s]	0.328	(Srayko et al., 2005)
Shrinkage velocity (Vs) [mm/s]	0.537	(Kozlowski et al., 2007)
Catastrophe frequency (Fcat) at cytoplasm [/s][a]	0.046	(Kozlowski et al., 2007)
Rescue frequency (Fres) [/s][b]	1	
Number of fibers per pole	296	(Srayko et al., 2005)
Pulling force, motor mediated		
Stall force of motor (F_{stall}) [pN]	1.1	(Gross et al., 2000)
Maximum velocity of motor (V_{max}) [mm/s]	2	(Gross et al., 2000)
Pulling force, attachment of FG (cytoplasmic length dependent)		
Density of motors (D) [/mm]	0.2	
Pulling force, attachment of FG (cortical)		
Potential number of force generators at the cortex ($N_{potential}$, anterior, PAR-3 dependent)	15	
Potential number of force generators at the cortex ($N_{potential}$, posterior, PAR-2 dependent)	30	
The mean probability of the activation of the force generators (p_{mean}) [/s]	0.5	(Pecreaux et al., 2006)

Spindle as a spring	
Natural length [mm]	10-22
Spring constant [pN/mm]	1
Size of the cell	
Long axis [mm]	50
Short axis [mm]	30
Drag force of nucleus/spindle pole	
Drag coefficient, for translational movement (G_{trans}) [pN s/mm][c]	190
Drag coefficient, for rotational movement (G_{rot}) [pN s mm][c]	25,000
Model-specific parameter	
Time step [s]	0.01

Table 2 Parameter values used in the simulation.

[a] See Table 1 for catastrophe frequency at the cortex

[b] A high frequency was used in this study. See text for a detailed explanation.

[c] $6\pi r\eta$ for translational movement and $8\pi r^3\eta$ for rotational movement.
Here, we set r (Stokes' radius) to 10 μm and η (viscosity of the cytosol) to 1.0 pNs/ μm².

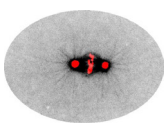

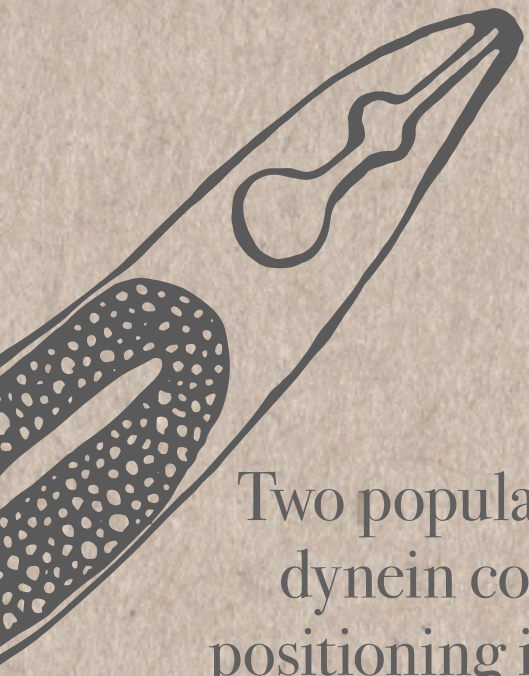

5

Two populations of cytoplasmic dynein contribute to spindle positioning in *C. elegans* embryos

Ruben Schmidt[1,2], Lars-Eric Fielmich[1], Ilya Grigoriev[2], Eugene A. Katrukha[2], Anna Akhmanova[2] and Sander van den Heuvel[1*]

[1]Developmental Biology, Department of Biology, Faculty of Sciences, Utrecht University, Padualaan 8, 3584 CH Utrecht, The Netherlands.

[2]Cell Biology, Department of Biology, Faculty of Sciences, Utrecht University, Padualaan 8, 3584 CH Utrecht, The Netherlands.

An adapted version of this manuscript was published in *Journal of Cell Biology* in 2017

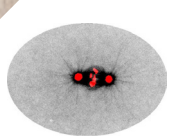

Abstract

The position of the mitotic spindle is tightly controlled in animal cells, as it determines the plane and orientation of cell division. Contacts between cytoplasmic dynein and astral microtubules at the cell cortex generate pulling forces that position the spindle. An evolutionarily conserved Gα-GPR-1/2$^{Pins/LGN}$–LIN-5$^{Mud/NuMA}$ cortical complex interacts with dynein and is required for pulling force generation, but the dynamics of this process remain unclear. Here, by fluorescently labeling endogenous proteins in *C. elegans* embryos, we show that dynein exists in two distinct cortical populations. One population directly depends on LIN-5, while the other is concentrated at microtubule plus ends and depends on End Binding proteins (EBs). Knockout mutants lacking all EBs are viable and fertile and display normal pulling forces and spindle positioning. However, EB protein-dependent dynein plus-end tracking was found to contribute to force generation in embryos with a partially perturbed dynein function, indicating the existence of two mechanisms that together create a highly robust force-generating system.

Introduction

The mitotic spindle dictates the plane of cell cleavage through its position and interactions with the cell cortex (reviewed in Galli and van den Heuvel, 2008; Morin and Bellaïche, 2011). Thereby, the position of the spindle determines the relative size and location of daughter cells, and controls whether polarized cells divide symmetrically or asymmetrically. Thus, accurate positioning of the spindle is critical for a wide range of processes that include maintenance of tissue integrity, creation of different cell types, and coordination of stem cell proliferation and differentiation.

The *C. elegans* early embryo provides an important *in vivo* model for studies of spindle position regulation. The one-cell embryo divides asymmetrically based on an anterior-posterior (A-P) polarity axis established after fertilization (Rose and Gönczy, 2014). Spindle severing experiments revealed that pulling forces acting from the cell cortex on astral microtubules (MTs) position the spindle, and are higher in the posterior than in the anterior (Grill et al., 2001). This pulling force asymmetry leads to posterior displacement of the spindle, and allows cell cleavage to create two blastomeres of unequal size and developmental fate.

Genetic screens and biochemical experiments have revealed a variety of factors that control cortical pulling forces. Among these are the evolutionarily conserved proteins Ga, GPR-1/2$^{Pins/LGN}$ and LIN-5$^{Mud/NuMA}$ (Colombo et al., 2003; Gotta and Ahringer, 2001; Gotta et al., 2003; Lorson et al., 2000; Srinivasan et al., 2003). These proteins are needed to form the force generator complex (FGC), which also includes cytoplasmic dynein (Nguyen-Ngoc et al., 2007). This large multi-subunit protein complex is the major minus-end directed motor in cells and is essential for a large variety of cellular processes (reviewed in Kardon and Vale, 2009). In the current model, dynein is recruited to the cell cortex either directly or indirectly via an extended N-terminal region of LIN-5 (Kotak et al., 2012). Dynein then associates with astral MTs in an end-on configuration, inducing pulling forces via both MT depolymerization and minus-end directed movement. Both *in vivo* and in *vitro* studies support this model (Gusnowski and Srayko, 2011; Hendricks et al., 2012; Laan et al., 2012; Nguyen-Ngoc et al., 2007).

It remains unclear, however, how dynein is recruited to the cortex and how MT dynamics are coupled to force generation and mitotic spindle positioning. MT growth and shrinkage are spatiotemporally modulated by a large variety of MT-associated proteins (MAPs), a subset of which concentrates at the growing MT plus-end (Akhmanova and Steinmetz, 2015). These MT plus-end-tracking proteins (+TIPs) form a highly interconnected and dynamic network, which is regulated in a cell cycle and position-dependent manner to fine-tune MT dynamics (Ferreira et

al., 2013; Honnappa et al., 2006; Tamura et al., 2015; Zimniak et al., 2009). Members of the end-binding (EB) protein family are seen as master regulators of the +TIP network, as they bind autonomously to the growing MT end and recruit multiple other +TIPs (Akhmanova and Steinmetz, 2015; Bieling et al., 2007; Honnappa et al., 2006; Maurer et al., 2012; Zhang et al., 2015b).

Dynein is known to behave as a +TIP in a variety of cellular contexts (Han et al., 2001; Kobayashi and Murayama, 2009; Lenz et al., 2006; Vaughan et al., 1999). In mammals this is classically regarded as part of a 'search-and-capture' mechanism, by which the complex finds cargo molecules via the MT plus-end before initiating transport (Kirschner and Mitchison, 1986; Vaughan et al., 2002). Interactions between EB1, CLIP-170, and the dynactin protein p150Glued recruit the human dynein complex to the MT plus-end (Berrueta et al., 1999; Duellberg et al., 2014; Lansbergen et al., 2004). In the budding yeast *S. cerevisiae*, dynein plus-end tracking is coupled to off-loading at the cortex and association of dynein with its cortical anchor Num1 (Lee et al., 2003; Markus and Lee, 2011; Sheeman et al., 2003). Disruption of dynein plus-end recruitment is thus associated with spindle positioning defects in yeast, but whether this applies to animals remains to be determined.

In this study, we explore the localization of dynein during mitotic pulling force generation in the one-cell *C. elegans* embryo. Fluorescent protein tagging of endogenous dynein helped reveal two cortical populations, one enriched at MT plus-ends depending on end-binding protein-2 (EBP-2), and a MT-independent population recruited by LIN-5. The LIN-5–dependent dynein population exhibited significant asymmetry in cortical retention, governed by PAR polarity. This indicates that a subpopulation of LIN-5 is dynein associated and differentially regulated. We created single, double and triple deletion mutants of EB family genes, and found that spindle positioning and embryonic development can proceed as normal in the absence of dynein plus-end tracking. However, plus-end tracking appeared to provide a back-up mechanism to ensure robust force generation when dynein function is partially perturbed.

Results

Visualization of the endogenous dynein complex

We applied a CRISPR/Cas9-assisted knock-in strategy to visualize the dynamics of cytoplasmic dynein in the early *C. elegans* embryo. To label all possible compositions of the dynein complex, we added a fluorescent protein (FP) to the dynein heavy chain, encoded by *dhc-1* in *C. elegans* (Fig. 1A). To allow for functional comparison, we inserted *mcherry* directly upstream of the *dhc-1* stop codon, and *mcherry* or *egfp* directly upstream of the *dhc-1* start codon. A glycine linker was inserted between FPs and *dhc-1* to preserve independent protein folding (Fig. 1A).

Multiple homozygous viable knock-in strains were obtained with N- or C-terminal DHC-1 protein fusions. However, C-terminal tagging of *dhc-1* caused severe embryonic lethality and a reduced brood size (Fig. 1B). Differential interference contrast (DIC) microscopy revealed spindle positioning and cell division defects from the one-cell stage onward, in two independent strains. These defects are in accordance with perturbed dynein function (Schmidt et al., 2005). We concluded that C-terminal tagging of endogenous DHC-1 causes partial loss of function and did not further study dynein in these strains. Homozygous larvae with N-terminally tagged DHC-1 were fully viable, produced a normal brood size (Fig. 1B) and appeared healthy during all stages of development. Thus, N-terminal tagging of DHC-1 with mCherry or eGFP does not perturb dynein function.

Epifluorescence microscopy revealed that mCherry::DHC-1 and eGFP::DHC-1 are expressed in all somatic tissues and in the germline (Fig. 1C, blow-up). Following early embryos by spinning disc confocal fluorescence microscopy (SDCM), DHC-1 was detected in the cytoplasm during all stages

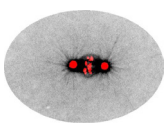

of the cell cycle, and localized specifically to the nuclear envelope, centrosomes, kinetochores, kinetochore MTs, central spindle, astral MTs and the cell cortex during mitosis (Fig. 1D). This localization pattern is in accordance with previous immunohistochemistry and overexpression studies (Gassmann et al., 2008; Kimura and Kimura, 2011; Nguyen-Ngoc et al., 2007; Schmidt et al., 2005). In addition, we noticed comet-like accumulations of dynein radiating from the centrosomes to the cell periphery in a pattern that appeared to follow the mitotic astral MT network.

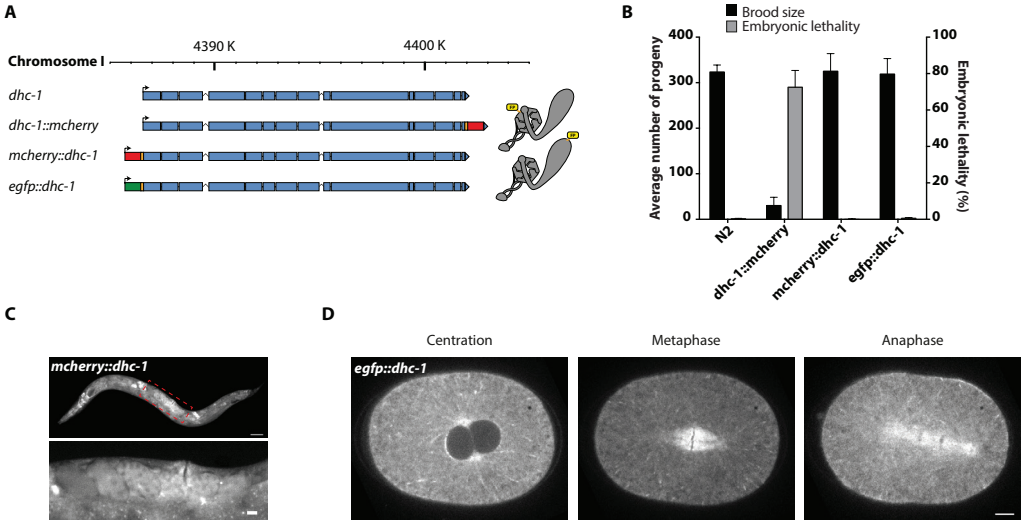

Figure 1 Endogenous tagging of *dhc-1*. **(A)** Dynein tagging strategies. Colors indicate *dhc-1* exons (blue), *mcherry* (red), *egfp* (green) and linkers (orange). Cartoons illustrate dynein heavy chain with FP fused to C- (top) or N-terminus (bottom). **(B)** Brood size and embryonic lethality of *dhc-1* knockin strains, shown as means ± SD, N=4 animals each. **(C)** Wide-field image showing mCherry::DHC-1 expression in adult, with blow-up of germline. Scale bars, 50 µm (top) and 10 µm (bottom). **(D)** SDCM images of eGFP::DHC-1 localization in the one-cell embryo. Scale bar, 5 µm.

Dynein tracks MT plus-ends during mitosis

To further explore the dynein localization pattern, *Ppie-1*::*gfp::tbb-2β-tubulin* (Praitis et al., 2001) was co-expressed with *mcherry::dhc-1* and imaged in embryos. Dynein comets were clearly MT-associated (Fig. 2A, arrow, Video 1). Since dynein is a minus-end directed motor protein, cortex-directed dynein comets may represent a plus-end tracking population. To examine this possibility, we co-expressed *mcherry::dhc-1* with *ebp-2::gfp* (Kozlowski et al., 2007; Srayko et al., 2005). This revealed a strong overlap between dynein and EBP-2::GFP comets (Fig. 2B, C, Video 2). Moreover, the velocities of mCherry::DHC-1 and EBP-2::GFP comets were almost identical (Fig. 2D), and agree with previous measurements of MT growth speeds during metaphase (0.72 ± 0.02 µm/s (Srayko et al., 2005)). Dynein accumulation at MT plus-ends appears a general feature of mitotic animal cells, as we also observed this in HeLa cells stably expressing labeled dynein intermediate chain 2 (DIC2-GFP) (Splinter et al., 2012; Poser et al., 2008). Moreover, we observed MT plus-end tracking of dynein in later stages of *C. elegans* embryos (Fig. S1A, B), and overlap between dynactin components GFP::DNC-1^{p150Glued} and GFP::DNC-2$^{p50/dynamitin}$ and mCherry::DHC-1 comets (Fig. S2A). Together, our data show that the endogenous dynein complex tracks MT plus ends.

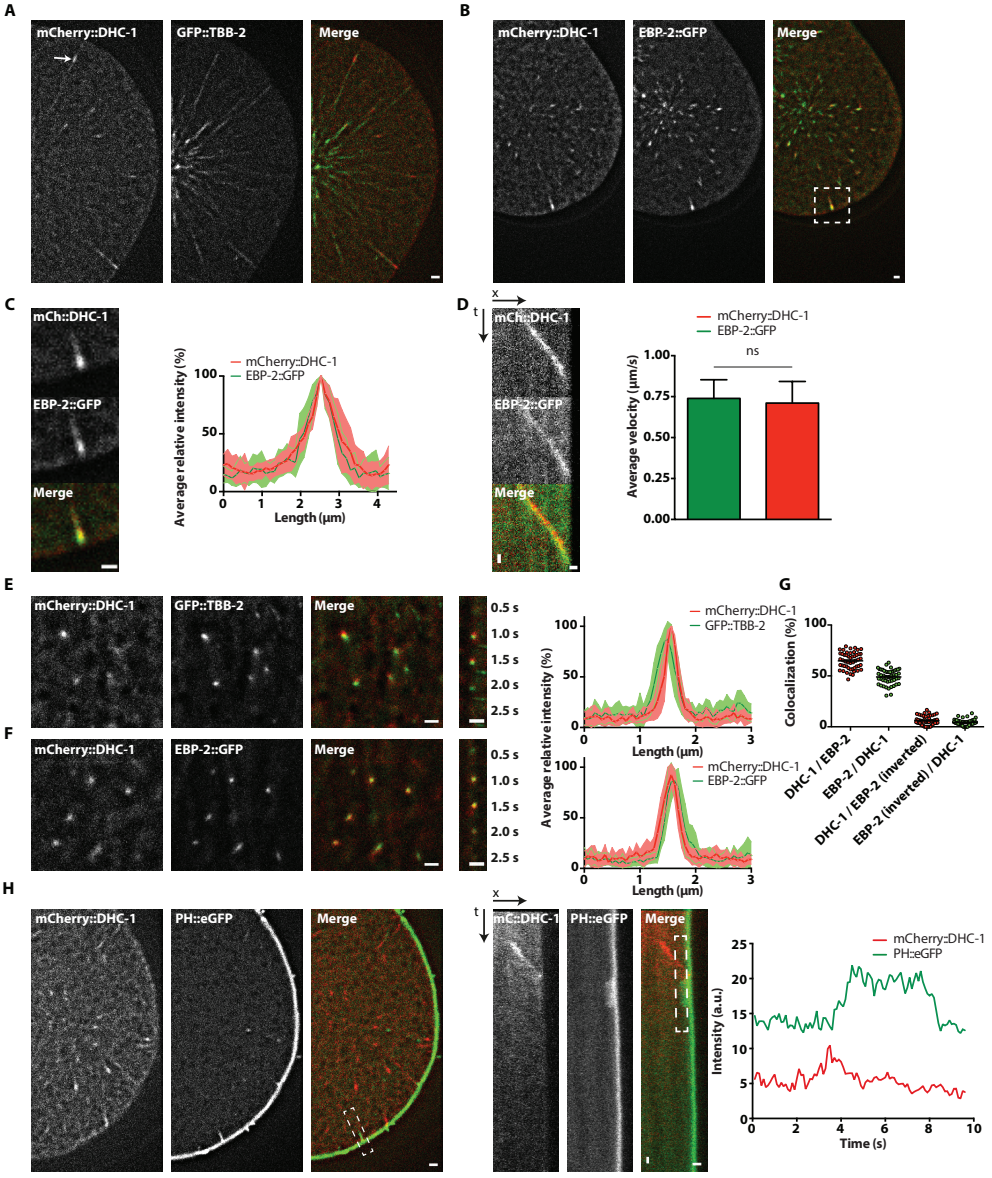

Figure 2 Dynein tracks MT plus-ends during mitosis. **(A, B)** SDCM images of embryos expressing mCherry::DHC-1 and GFP::TBB-2 **(A)**, or EBP-2::GFP **(B)**. Arrow: dynein at the plus-end. White box: blow-up shown in **(C)**. **(C)** Intensity profiles of mCherry::DHC-1 and EBP-2::GFP comets, shown as percentage of maximum, mean ± SD (N=10). (D) Kymographs (left) and average velocities (right) of metaphase comets; mCherry::DHC-1 (N=57) and EBP-2::GFP (N=116) means ± SD. Unpaired Welch Student's t-test; ns not significant. **(E, F)** TIRF images of early anaphase mCherry::DHC-1 and GFP::TBB-2 **(E)** or EBP-2::GFP **(F)** localization. Graphs show intensity profiles as mean (N=10 E, F) percentage of maximum ± SD. **(G)** Quantification of EBP-2::GFP and mCherry::DHC-1 colocalization as in **(F)**, shown as means ± SEM of per-frame percentage colocalization of 2351 mCherry::DHC-1 and 3178 EBP-2::GFP particles from 3 embryos. **(H)** SDCM images of anaphase mCherry::DHC-1 and PH::eGFP localization. Panels 4-6 are kymographs of the invagination indicated in panel 3 (white box). Graph shows intensity profiles as measured along the box in panel 6, representative of N=25 events. Scale bars, 1 µm (horizontal) and 1 s (vertical).

Next, we addressed whether MT plus-end tracking of the dynein complex relates to pulling force generation. Using dual-color total internal reflection fluorescence (TIRF) microscopy, we observed simultaneous appearance and strong colocalization of dynein comets with end-on MT plus end-cortex contacts in mitosis (Fig. 2E-G, Video 3, 4). Interestingly, the concentrated mCherry::DHC-1 signal dissipated when MTs stopped growing, as judged by the loss of EBP-2::GFP signal, suggesting that the majority of dynein molecules are released.

To image dynein comets during cortical force generation, we focused on invaginations of the plasma membrane, which appear to visualize individual force generation events (Redemann et al., 2010). To readily detect such invaginations, we created a reporter strain with single copy integrated PH::eGFP expressed from the general *eft-3* promoter. Dual-color imaging of PH::eGFP and mCherry::DHC-1 revealed frequent co-occurrence of dynein comets reaching the cortex and emergence of membrane invaginations (13/25 events; Fig. 2H, Video 5). However, there was no enrichment of dynein after the initiation of invaginations. This confirms that a significant part of the dynein population present at the MT plus-end dissipates upon membrane contact, and likely does not contribute to pulling forces.

EBs and dynein plus-end tracking are not required for development and spindle positioning

To examine the contribution in cortical pulling forces, we decided to disrupt dynein plus-end accumulation by removing EBs. Two homologs of mammalian EBs, EBP-1 and EBP-2, exhibit plus-end tracking activity when overexpressed in the embryo (Srayko et al., 2005). An annotated third homolog, *ebp-3*, has likely arisen by duplication of the genomic region containing the *ebp-1* gene, and their nearly identical DNA sequences suggest that this was a recent event. However, the predicted EBP-3 protein lacks the calponin homology (CH) domain, which is required for recognition of the MT plus-end (Maurer et al., 2012; Slep and Vale, 2007). Although we suspect that e*bp-3* is a pseudogene, we will refer to the *ebp-1* and *ebp-3* genes collectively as *ebp-1/3*.

Knockdown of *ebp-1/3* by RNAi did not appear to affect eGFP::DHC-1 plus-end tracking. In contrast, loss of *ebp-2* expression abolished the appearance of dynein comets (Fig. 3A). Interestingly, this did not result in obvious spindle positioning or cell division defects. As RNAi knockdown probably is incomplete, we used CRISPR/Cas9 to create knockout alleles for both *ebp-2* and *ebp-1/3* (Fig. 3B). The *ebp-1* and *ebp-3* genes were removed together by excision of a ~17 kb region. For *ebp-2,* the coding region and ~1 kb upstream of the start codon was deleted. Both the Δ*ebp-1/3* and Δ*ebp-2* strains could be stably maintained as homozygotes, indicating that neither *ebp-1/3* nor *ebp-2* are required for normal development and reproduction.

The *ebp* deletion mutants closely resembled the RNAi embryos in dynein localization. In Δ*ebp-1/3* embryos, dynein still localized to the MT plus-ends, while this localization was completely absent in Δ*ebp-2* embryos (Fig. 3C, Video 6). In contrast, dynein localization to the nuclear envelope, spindle midzone and poles did not appear to be affected in either case, which indicates that dynein depends on EBP-2 specifically for recruitment to MT plus-ends (Fig. S2C-E).

While general development was normal, Δ*ebp-1/3* caused a slight reduction in brood size and a slight increase in embryonic lethality (Fig. 3D). Surprisingly, Δ*ebp-1/2/3* animals were viable and could be maintained as triple homozygous mutants, showing that development and reproduction can proceed in the absence of EBs. Triple mutants showed a stronger reduction in brood size than Δ*ebp-1/3* animals, which indicated some redundancy amongst the EBs. Embryonic lethality remained low, which is remarkable given the expected profound disruption of the +TIP network. While Δ*ebp-1/2/3* larvae generally did not show developmental defects, we observed

a low penetrant pleiotropic phenotype amongst adults. This included a low frequency of dumpy, sterile, and/or uncoordinated animals, as well as non-viable larvae that exploded through the vulva. In addition, some triple mutant adults developed irregularities that seemed epidermal bulges. Because of the very low penetrance, we did not further examine these abnormalities.

Next, we assessed whether spindle positioning was affected in *ebp* deletion mutants. Importantly, asymmetric positioning of the spindle and subsequent asymmetric division of the one-cell embryo was not affected in any of the mutants (Fig. S3A). Δ*ebp-1/2/3* embryos exhibited a slightly rounder shape compared to wild type embryos (Fig. S3B). The position of pronuclear meeting did not change significantly (Fig. S3C), while centration of the nucleocentrosomal complex occurred slightly more posterior in each mutant (Fig. S3D). Spindles formed along the long axis as normal (Fig. S3E), while their elongation during anaphase was slightly increased in Δ*ebp-1/2/3* embryos (Fig. S3F). Regardless of these small deviations, the outcome of mitosis was not affected. However, all Δ*ebp* strains showed accelerated progression through mitosis (Fig. 3E and Fig. S3G, Video 7). This was observed in Δ*ebp-1/3* and Δ*ebp-2* embryos, but was most dramatic in Δ*ebp-1/2/3* mutants. Both progression from pronuclear meeting to nuclear envelope breakdown (NEBD), and the time between the start of chromosome segregation and cytokinesis were significantly faster than normal (Fig. S3G-J). However, there was no significant reduction in the time between NEBD and anaphase onset (Fig. S3I), indicating that the accelerated mitosis does not result from bypassing or premature satisfaction of the spindle assembly checkpoint.

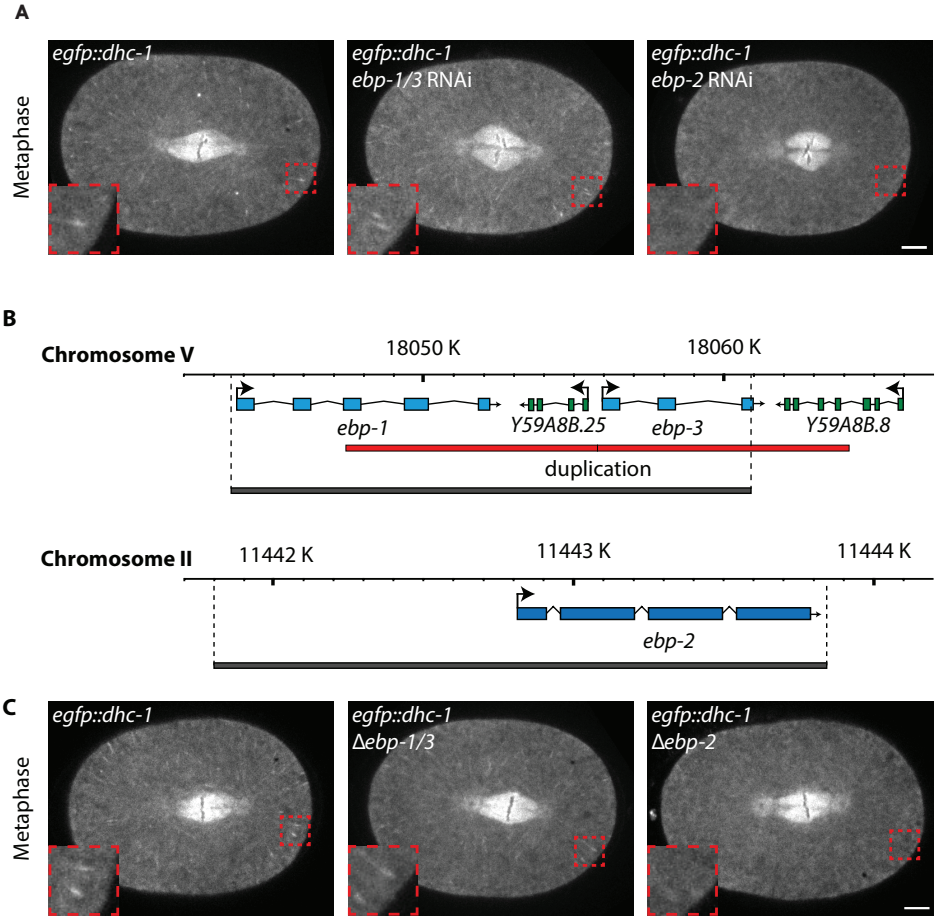

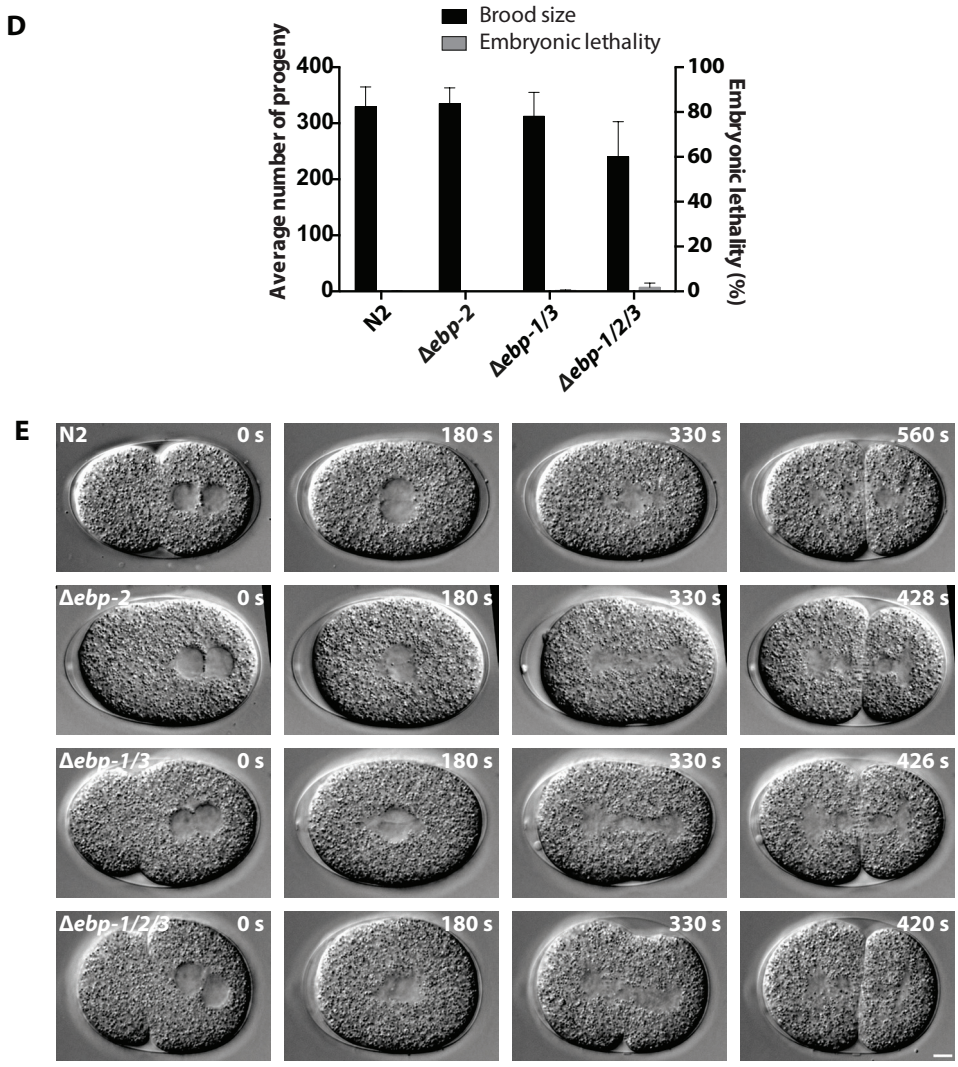

Figure 3 Analysis of dynein plus-end tracking and development of *Δebp* mutants. **(A)** SDCM images illustrating eGFP::DHC-1 localization in wild type, *ebp-2(RNAi)* and *ebp-1/3(RNAi)* embryos. Blow-ups highlight the presence or absence of dynein comets. **(B)** *ebp-1/3* and *ebp-2* knockout strategies. Relevant genes shown in blue and green, genetic duplication in red, and genetic deletions in grey. **(C)** SDCM images illustrating eGFP::DHC-1 localization in wild type, *Δebp-2* and *Δebp-1/3* embryos. Blow-ups highlight the presence or absence of dynein comets. **(D)** Embryonic lethality and brood size of *Δebp* mutants shown as means ± SD, N= 4 animals each. **(E)** DIC images of N2, *Δebp-2*, *Δebp-1/3* and *Δebp-1/2/3* one-cell embryos. Time past pronuclear meeting (t=0) is indicated in seconds. Scale bar, 5 µm.

EBs and dynein plus-end tracking are not required for cortical pulling forces

We quantified the amplitudes of spindle pole movements during anaphase as a first read-out for cortical force generation (Pecreaux et al., 2006). Interestingly, spindle rocking was generally not affected by the removal of EBs. The posterior pole showed a slight but significant increase in maximum amplitude in the Δ*ebp-1/3* background, but this was not observed in Δ*ebp-1/2/3* mutants (Fig. 4A).

To more directly quantify cortical pulling forces during spindle displacement, we performed spindle severing assays with a focused UV laser beam (Grill et al., 2001). Upon severing the spindle during anaphase onset, the centrosomes separate with a velocity proportional to the net forces acting on their astral MTs (Grill et al., 2001) (Fig. 4B, Video 9). Remarkably, all Δ*ebp* mutants assembled apparently normal mitotic spindles and showed normal spindle pole peak velocities (Fig. 4C). Thus, cortical pulling force generation during spindle positioning is largely unaltered in the absence of EB proteins.

In addition to recruiting proteins to the MT plus-end, EB proteins affect MT dynamics (Komarova et al., 2009; Maurer et al., 2014; Zanic et al., 2013; Zhang et al., 2015b). However, the effect of complete loss of EB family members on MT dynamics has not been reported *in vivo*. A hurdle for studying MT dynamics in the one-cell worm embryo is the extremely dense MT network (Kozlowski et al., 2007). Therefore, we imaged labeled MTs at the cortex by TIRF microscopy and quantified the duration of end-on MT-cortex contacts during spindle displacement (Fig. 4D). This revealed a slight increase in average residence time in all Δ*ebp* mutants, of which only Δ*ebp-2* was significantly different from wild type, while the average density of cortical MT contacts remained constant (Fig. 4E, Video 10). This indicates that loss of EBP-2 either reduces MT growth rate, catastrophe frequency or both, thereby allowing prolonged contact with the cell cortex. Interestingly, Δ*ebp-2* and Δ*ebp-1/2/3* embryos also exhibited reduced midzone MT densities (Fig. S4A-C), which led to full or partial bisection of spindles during anaphase and could be caused by altered MT dynamics. This phenotype is reminiscent of *spd-1PRC1* loss of function, which diminishes the mechanical strength of the midzone by loss of MT bundling (Verbrugghe and White, 2004). In addition, the intensity profile of the metaphase astral MT network was slightly steeper in Δ*ebp-2* and Δ*ebp-1/2/3* mutants compared to controls (Fig. 4F), indicating that the distribution of MT length was mildly altered. Collectively, these results indicate that complete loss of EBs has a mild effect on MT organization and dynamics *in vivo*, but does not significantly change spindle assembly and positioning.

LIN-5 recruits dynein to the cell cortex independent of MT plus-end tracking

If dynein plus-end tracking is not required for spindle positioning, then how does dynein reach the cortex? Previous studies have visualized cortical dynein localization by immunohistochemistry (Kotak et al., 2012; Nguyen-Ngoc et al., 2007). While cortical dynein could be observed in two-cell embryos, staining of one-cell embryos did not show clear cortical localization. Time-lapse SDCM of eGFP::DHC-1 zygotes revealed no measurable enrichment of dynein at the cortex over cytoplasmic values during metaphase spindle displacement, similar to *lin-5(RNAi)* embryos (Fig. 5A). However, we observed transient regions of DHC-1 enrichment in cortical patches during late anaphase (Fig. 5B). These patches were most pronounced at the posterior cortex during spindle rocking, and often followed the oscillatory behavior of the spindle poles (Fig. S4D, E). This indicates that spindle pole proximity and cortical dynein recruitment could be coupled

like they are in mammalian cells (Kiyomitsu and Cheeseman, 2012). The cortical enrichment of dynein was not perturbed in Δ*ebp-1/3* or Δ*ebp-2* mutant embryos. In contrast, *lin-5(RNAi)* abolished cortical dynein localization but did not affect its plus-end tracking (Fig. 5B). Thus, EBP-2 and EBP-1/3 are not required for the cortical localization of dynein during anaphase, which fully depends on LIN-5.

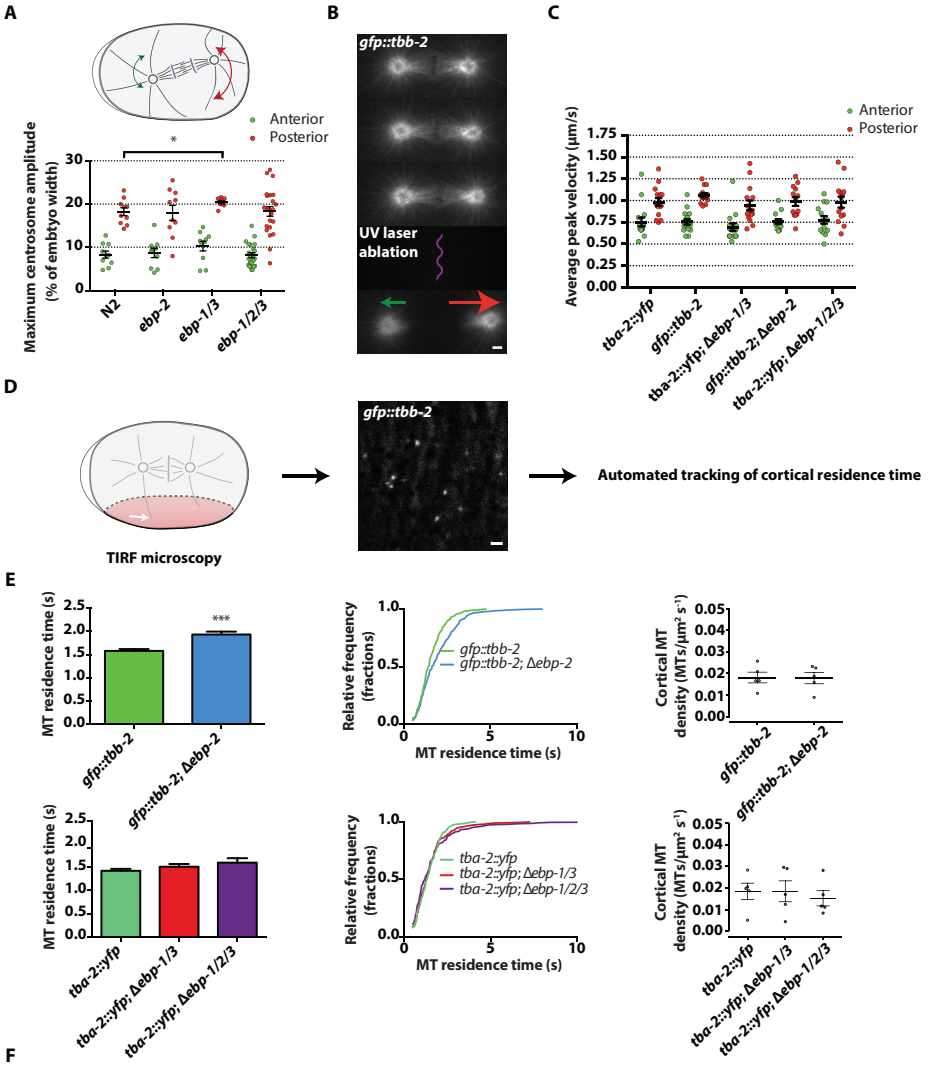

To explore the relative cortical localization patterns of LIN-5 and dynein, *egfp::lin-5; mcherry::dhc-1* embryos were imaged by SDCM (Fig. 5C). In late metaphase, eGFP::LIN-5 became modestly enriched at the cortex as compared to the adjacent cytoplasm, both in the anterior and posterior. While this was not observed for dynein (Fig. 5A, C) both LIN-5 and dynein showed higher cytoplasmic levels in the anterior compared to the posterior during all mitotic stages (Fig. S5A). This gradient affects the relative cortex to cytoplasm ratios calculated for the anterior and posterior, and causes the increase of cortical levels observed in the posterior, which is not observed when a mean cytoplasmic value is used for normalization of all points instead (Fig. S5A).

During anaphase, cortical enrichment of eGFP::LIN-5 increased substantially, most noticeably in the posterior. When averaging fluorescence intensities from multiple embryos, mCherry::DHC-1 did not show clear enrichment at the cortex above local cytoplasmic levels during anaphase. This reflects the patchy appearance of cortical dynein enrichment along the A-P axis (Fig. 5C, and above). Importantly, side-by-side comparison of non-normalized cortical line scans revealed a strong cross-correlation between cortical eGFP::LIN-5 and mCherry::DHC-1 (Fig. 5C; examples in Fig. S5B). This indicates that both proteins follow a similar cortical distribution, in agreement with LIN-5-dependent dynein localization. These protein localization patterns can account for force asymmetries in anaphase, but not during metaphase spindle displacement.

In a previous study, we observed cortical dynein localization in the absence of astral MTs (Portegijs et al., 2016). We repeated this experiment for *egfp::dhc-1* and *mcherry::dhc-1*; *egfp::lin-5* embryos permeabilized by *perm-1* RNAi treatment and exposed to 1 µM nocodazole (Berends et al., 2013; Carvalho et al., 2011). The use of tubulin and EBP-2 markers confirmed the absence of astral MTs, while the presence of a spindle remnant revealed cells in mitosis (Fig. 5D, arrow). Dynein still localized to the cortex during mitosis in these embryos, and this localization strongly overlapped with and depended on LIN-5 (Fig. 5D). Thus, LIN-5 recruits dynein to the cell cortex during mitosis, which can occur directly from the cytoplasm and in the absence of astral MTs.

Figure 4 Loss of EBP-1/2/3 mildly affects MT dynamics and does not perturb normal mitotic pulling force generation. **(A)** Quantification of anaphase centrosome rocking in wild type and *Δebp* embryos. Maximum amplitudes are shown as means ± SEM, unpaired Welch Student's *t*-test; * $P < 0.05$, N=10-23. **(B)** Example of spindle severing with a UV laser (purple) in a GFP::TBB-2 embryo. Arrows indicate the direction and relative speed of centrosome displacement upon bisection. **(C)** Quantification of centrosome velocities upon spindle severing in wild type and *Δebp* embryos, shown as means ± SEM, unpaired Welch Student's *t*-test, N=13-15. **(D)** Method for quantification of cortical MT residence time by TIRF microscopy of embryos expressing fluorescent tubulin. **(E)** Quantifications as illustrated in **(D)** for control and *Δebp* embryos. Bars represent mean ± SEM, Mann-Whitney U test; *** $P < 0.001$. $233 \leq N \leq 343$ events from 5 embryos for each condition. Graphs show cumulative relative fractions of residence time distributions. Right graphs show density of cortical MT contacts as average MTs/µm^2 s^{-1} per embryo, bars are means ± SEM. **(F)** Quantification of astral MT densities in metaphase control and *Δebp* mutant embryos as measured by radial intensity plots (first panel). Plots were aligned and normalized to maximum values at the centrosome. N=20 asters from 10 embryos per condition. Scale bar, 1 µm.

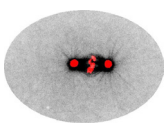

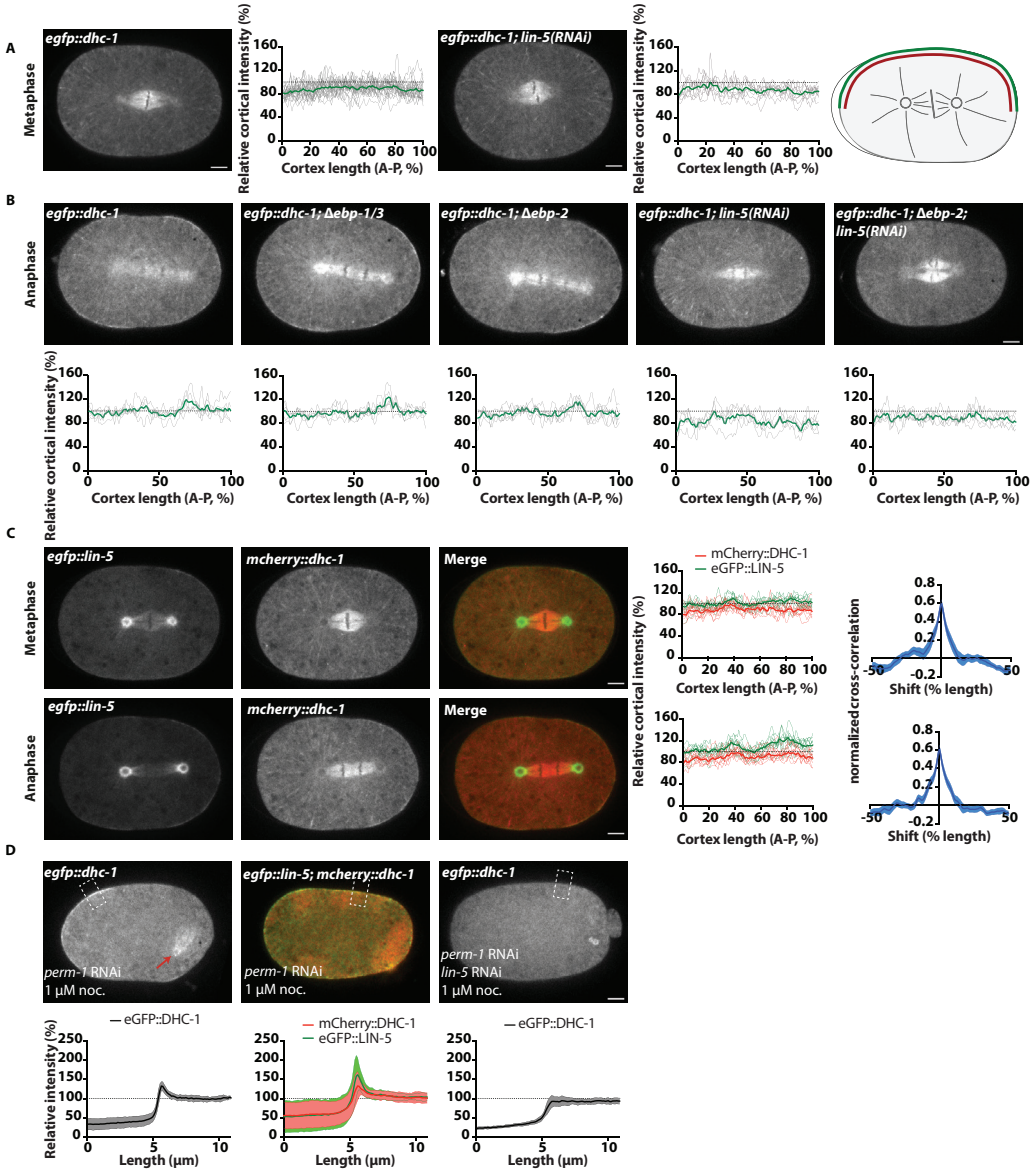

Figure 5 Cortical dynein depends on recruitment from the cytoplasm by LIN-5, but not on EBP-2-mediated plus-end tracking. **(A)** SDCM images showing eGFP::DHC-1 localization in control and *lin-5(RNAi)* metaphase embryos. Graphs show relative cortical over cytoplasmic eGFP::DHC-1 intensities as measured along the cortex (last panel, green line) and normalized to a cytoplasmic line (red). Dotted lines at Y=100% indicate a 1:1 cortex to cytoplasm ratio. Mean (green) and individual (grey) traces are shown. N=12 embryos, 24 cortexes for control and N=5 embryos, 10 cortexes for *lin-5(RNAi)*. **(B)** SDCM images of anaphase embryos of indicated genotypes. Graphs show relative cortical over cytoplasmic eGFP::DHC-1 intensities, quantified and shown as described in **(A).** N=6 embryos per condition. **(C)** SDCM images show mCherry::DHC-1 and eGFP::LIN-5 localization. Mean (thick lines) and individual (thin lines) intensity plots shown in left graphs. Right graphs show cross-correlation between cortical LIN-5 and DHC-1 plots, expressed as means ± SEM, N=10 embryos, 20 cortexes. **(D)** SDCM images showing dynein or LIN-5 localization in *perm-1(RNAi)* or *perm-1(RNAi)*; *lin-5(RNAi)* embryos treated with 1 µM nocodazole. Graphs indicate fluorescence intensity profiles as measured in boxes shown in superimposed panels. Red arrow points to mitotic spindle remnant. Plots are mean (N=10) intensities relative to cytoplasmic values ± SD. Scale bars, 5 µm.

As SDCM did not reliably detect dynein at the cortex during metaphase, we visualized cortical eGFP::DHC-1 more selectively at this stage by TIRF microscopy. Notably, this revealed two cortical populations of dynein that could be genetically separated. One population was detected as bright fluorescent spots that were absent in the Δ*ebp-2* background, and thus represented dynein comets at the cell cortex (Fig. 6A, 4th panel, arrow). A second population consisted of relatively dim spots that were absent in *lin-5(RNAi)* embryos (Fig. 6A, 3rd panel, arrowhead). Most notably, *Δebp-2; lin-5(RNAi)* embryos showed almost complete loss of detectable cortical dynein (Fig. 6A, Video 8). Furthermore, the increase in dynein levels associated with MT plus-ends at the cortex in *lin-5(RNAi)* embryos may indicate that the cortex and MT plus-end compete for dynein binding or that LIN-5 suppresses dynein plus-end accumulation (relative cumulative distribution in Fig. 6B, and sum of intensities in Fig. 6C). Thus, two populations of dynein are present at the cortex in metaphase: an EBP-2-dependent plus-end tracking population and a LIN-5-dependent cortical population. As shown in Fig. 5D, LIN-5 can most likely recruit dynein directly from the cytoplasm to the cortex, which would explain why plus-end tracking of dynein is not required for its cortical localization during mitosis.

To investigate whether the cortical populations of dynein and LIN-5 show asymmetries that relate to asymmetric spindle positioning, we examined their dynamics by time-lapse TIRF microscopy combined with fluorescence recovery after photobleaching (FRAP) analysis. To this end, eGFP::DHC-1 and eGFP::LIN-5 embryos were photobleached in regions in the anterior and posterior, after which recovery of fluorescence was recorded during a 30 s timespan relevant for spindle positioning (Fig. 6D). Overall, LIN-5 recovered more quickly than dynein, in wild type as well as in Δ*ebp-2* embryos (Fig. 6E-G; Supplementary Table II). As dissociation of LIN-5 also removes dynein, more stable cortical retention of dynein compared to LIN-5 would not be expected. However, statistical analyses indicated that the averaged eGFP::LIN-5 and eGFP::DHC-1 fluorescence recovery curves are most reliably fit by two-phase nonlinear regression analysis (Extra sum-of-squares F test one- vs. two-phase fit ****P<0,0001). The half-lives of the fast phases of cortical eGFP::LIN-5 and eGFP::DHC-1 recovery were similar to the recovery half-life of the corresponding proteins in the cytoplasm (Fig. 6F and Fig. S5D). This probably reflects that our FRAP measurements include a cytoplasmic protein fraction, or alternatively, that part of the cortical population exchanges at a speed similar to cytoplasmic diffusion. The contribution of the fast phase was larger for LIN-5 recovery compared to DHC-1, which contributes to the faster overall recovery of LIN-5 (Fig. 6G).

Importantly, the half-lives for the slow phase of recovery were similar for LIN-5 and dynein (Fig. 6F, colored bars). Thus, this phase likely reflects the dynamics of a LIN-5–bound dynein population at the cortex. In addition to a fast and slow recovering phase, a small protein fraction remained immobile within the 30 seconds interval. Interestingly, individual fits revealed a statistically larger immobile fraction of eGFP::DHC-1 in the posterior compared to the anterior (Fig. 6GH). This difference also appeared detectable for eGFP::LIN-5 but was not significant (Fig. 6GH). FRAP analysis of eGPF::DHC-1 in Δ*ebp-2* embryos also showed asymmetry in dynein dynamics, indicating that the asymmetry resides in the LIN-5-dependent cortical dynein population, as detected in Fig. 6A-C. Notably, the FRAP curves of Δ*ebp-2* embryos showed higher recovery than wild type (Fig. 6E), even extending beyond 100% (Fig. 6H). This may be attributed to the faster progression through mitosis in Δ*ebp-2* embryos (Fig. S3G-J), in combination with an increase in cortical dynein during mitosis from metaphase onwards. Nevertheless, extrapolation of the curves confirmed a higher percentage recovery in the anterior compared to posterior of Δ*ebp-2* embryos, similar to wild type eGFP::DHC-1 embryos (Fig. 6H). Disruption of polarity by knockdown of *par-2* or *par-3* abolished the observed asymmetry in cortical eGFP::DHC-1 recovery (Fig. 6E and H).

In summary, the obtained FRAP curves probably result from combined measurements of dynein in the cytoplasm and LIN-5–associated dynein at the cortex. The LIN-5-associated cortical dynein includes a relatively stable population, which depending on PAR polarity is enriched in the posterior, and thus may be critical for pulling forces.

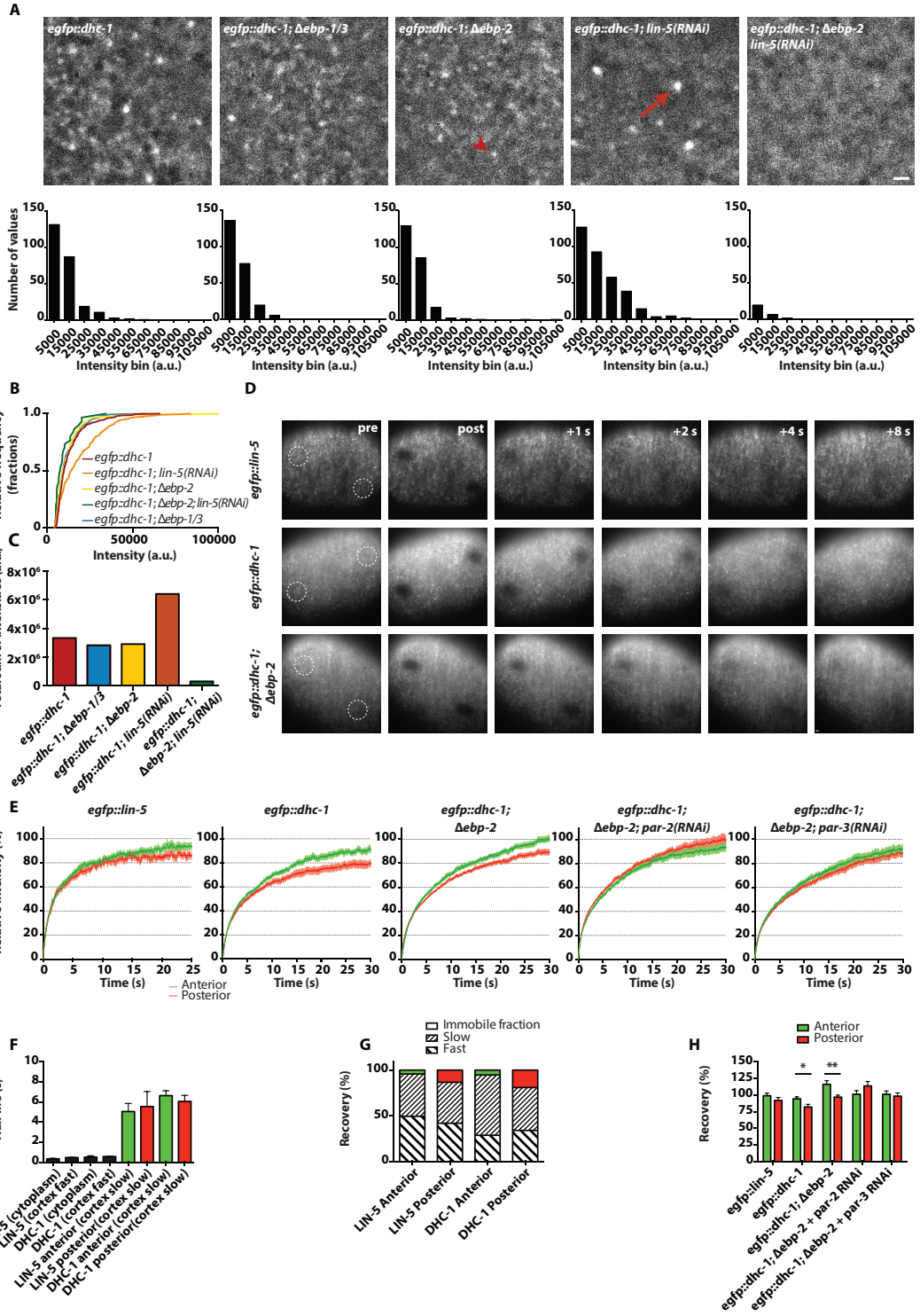
A
egfp::dhc-1
egfp::dhc-1; Δebp-1/3
egfp::dhc-1; Δebp-2
egfp::dhc-1; lin-5(RNAi)
egfp::dhc-1; Δebp-2 lin-5(RNAi)
Number of values
Intensity bin (a.u.)
B
Relative frequency (fractions)
Intensity (a.u.)
egfp::dhc-1
egfp::dhc-1; lin-5(RNAi)
egfp::dhc-1; Δebp-2
egfp::dhc-1; Δebp-2; lin-5(RNAi)
egfp::dhc-1; Δebp-1/3
C
Total sum of intensities (a.u.)
egfp::dhc-1
egfp::dhc-1; Δebp-1/3
egfp::dhc-1; Δebp-2
egfp::dhc-1; lin-5(RNAi)
egfp::dhc-1; Δebp-2; lin-5(RNAi)
D
pre
post
+1 s
+2 s
+4 s
+8 s
egfp::lin-5
egfp::dhc-1
egfp::dhc-1; Δebp-2
E
egfp::lin-5
egfp::dhc-1
egfp::dhc-1; Δebp-2
egfp::dhc-1; Δebp-2; par-2(RNAi)
egfp::dhc-1; Δebp-2; par-3(RNAi)
Relative intensity (%)
Time (s)
Anterior
Posterior
F
Half life (s)
LIN-5 (cytoplasm)
LIN-5 (cortex fast)
DHC-1 (cytoplasm)
DHC-1 (cortex fast)
LIN-5 anterior (cortex slow)
LIN-5 posterior(cortex slow)
DHC-1 anterior (cortex slow)
DHC-1 posterior(cortex slow)
G
Immobile fraction
Slow
Fast
Recovery (%)
LIN-5 Anterior
LIN-5 Posterior
DHC-1 Anterior
DHC-1 Posterior
H
Anterior
Posterior
Recovery (%)
egfp::lin-5
egfp::dhc-1
egfp::dhc-1; Δebp-2
egfp::dhc-1; Δebp-2 + par-2 RNAi
egfp::dhc-1; Δebp-2 + par-3 RNAi

Partial dynein perturbation reveals a contribution of dynein plus-end tracking

While dynein plus-end tracking is not required for force generation and spindle positioning in wild type conditions, it might function as a back-up mechanism to ensure robust force generation. If so, a contribution of dynein plus-end tracking may become detectable in certain stress conditions, for example when dynein function is partially compromised. To examine this possibility, we used the temperature-sensitive (ts) allele *dhc-1(or195)*, which causes severe perturbation of DHC-1 function and 100% embryonic lethality at non-permissive temperatures (Schmidt et al., 2005). We aimed to partially interfere with DHC-1 function at semi-permissive temperatures, to be able to examine whether *ebp-2* loss causes an enhanced or synthetic phenotype. Exposure of *dhc-1(or195)* mutants to temperatures ranging from 15 to 25°C revealed progressively more severe defects at higher temperatures (Fig. 7A). The reduction in brood size and increase in embryonic lethality were strongly enhanced by the simultaneous presence of the Δ*ebp-2* allele at temperatures below 25°C (Fig. 7A). To assess whether this synergistic effect is related to spindle positioning, we performed spindle severing experiments with *dhc-1(or195)* and *dhc-1(or195); ebp-2(RNAi)* embryos, as homozygous *gfp::tbb-2; dhc-1(or195); Δebp-2* mutants were not viable. Most *dhc-1(or195); ebp-2(RNAi)* embryos could assemble functional mitotic spindles (100% for *gfp::tbb-2* and *gfp::tbb-2; ebp-2(RNAi)*, 87,5% for *gfp::tbb-2; dhc-1(or195)* and 73,3% for *gfp::tbb-2; dhc-1(or195); ebp-2(RNAi)* at 20°C). Interestingly, *ebp-2* RNAi strongly reduced pulling forces at the semi-permissive temperature of 20°C (Fig. 7B). This reduction did not result from an indirect effect on MT dynamics, as the *dhc-1(or195)* mutation itself did not significantly affect cortical MT residence time at 20°C, or perturb the prolonged cortical contact caused by *ebp-2* RNAi (Fig. 7C). Furthermore, while the density of astral MTs was reduced in metaphase spindles of *dhc-1(or195)* embryos compared to wild type, this mild effect was not further exacerbated by the knockdown of *ebp-2* (Fig. 7CD). Based on these results, we conclude that EBP-2-dependent plus-end tracking of dynein contributes to robust spindle positioning and can serve as a backup mechanism that ensures efficient force generation when dynein function is partially perturbed.

Figure 6 Cortical dynein shows PAR polarity-dependent asymmetric dynamics in metaphase. **(A)** TIRF images of early anaphase cortical eGFP::DHC-1 in different genetic backgrounds, showing plus-end-associated (arrow) and cortical dynein dots (arrowhead). Bar graphs show frequency distributions of particle intensities from N=6 embryos per condition during 10 seconds starting at posterior spindle displacement. Scale bar, 1 µm. **(B)** Cumulative frequency distribution of the data shown in (A). **(C)** Comparison of total particle intensity sums (N=30-344 particles) for each condition shown in (A). **(D)** TIRF microscopy and FRAP of cortical eGFP::LIN-5 and eGFP::DHC-1 in anterior and posterior regions during metaphase. **(E)** Quantification of FRAP as shown in **(D)**. Curves show means ± SEM. *egfp::lin-5*: N=28 anterior, 22 posterior. *egfp::dhc-1*: control N=19, *Δebp-2* N=35, *Δebp-2; par-2(RNAi)* N=24, *Δebp-2; par-3(RNAi)* N=21. **(F)** Half-lives for cytoplasmic (one-phase) and cortical (two phases- fast and slow) recovery curves. Bars represent means ± SEM. *egfp::lin-5* (cytoplasm) N=7, *egfp::dhc-1* (cytoplasm) N=30. N values for cortical FRAP curves as in **(E)**. Unpaired Welch Student's t-test. **(G)** Quantification of the contribution of fast and slow phases of eGFP::LIN-5 and eGFP::DHC-1 to FRAP. N-values as in **(E)**. **(H)** Recovery of curves shown in **(E)**. *egfp::lin-5*, *egfp::dhc-1; Δebp-2*, *egfp::dhc-1; Δebp-2; par-2(RNAi)* A vs. P, Wilcoxon matched-pairs signed rank test. *egfp::dhc-1; egfp::dhc-1;Δebp-2; par-3(RNAi)* A vs. P, Paired Student's t-test. *P<0,05 **P<0,01. N-values as in **(E)**.

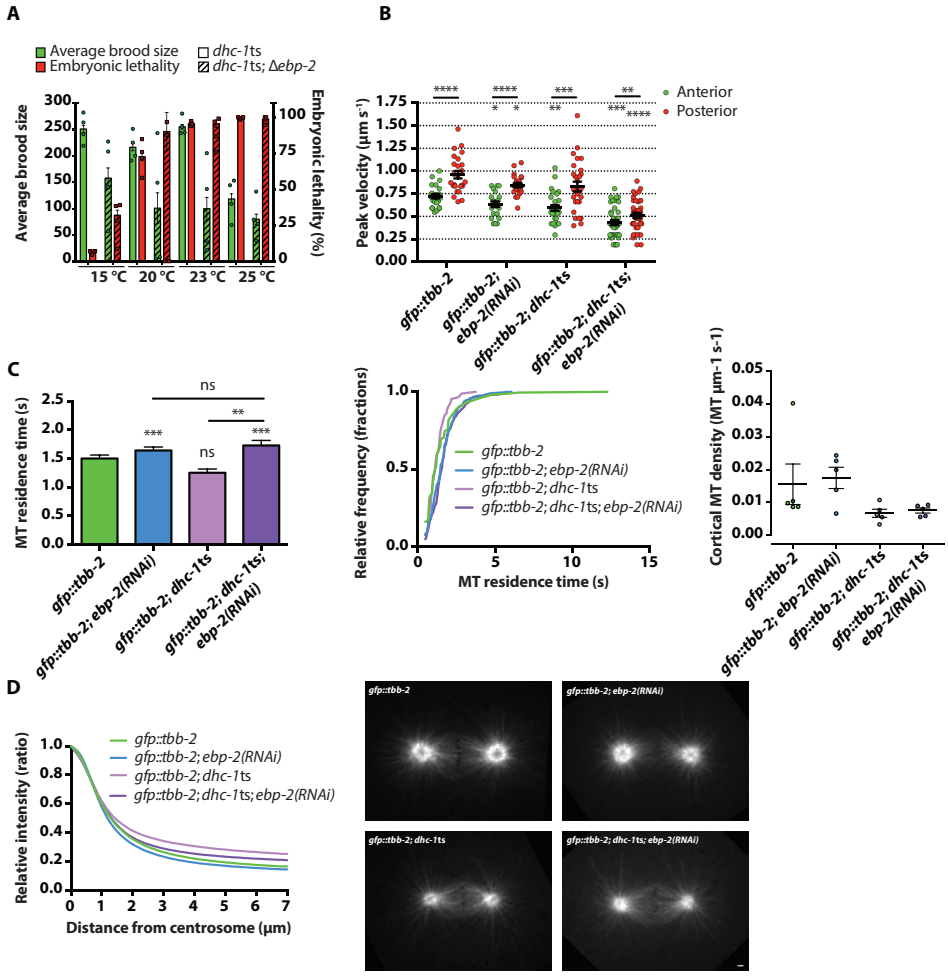

Figure 7 EBP-2 is required for efficient force generation when dynein function is partially perturbed. **(A)** Embryonic lethality and brood size of *dhc-1(or195ts)* and *dhc-1(or195ts); Δebp-2* strains at different temperatures shown as means ± SD, n=4 animals each. (B) Quantification of centrosome velocities upon spindle severing. Bars show mean ± SEM; unpaired (between genotypes) and paired (within embryos) Student's t-tests, ** P<0.01, *** P<0.001, **** P<0.0001. *gfp::tbb-2:* control N=25, *ebp-2(RNAi)* N=21, dhc-1ts N=28, dhc-1ts; ebp-2(RNAi) N=38. **(C)** Quantification of cortical MT residence time as described in Fig. 4D. Bars are means ± SEM, Mann-Whitney U test; **P<0.01, *** P < 0.001. N=87-410 events from 5 embryos for each condition. Graphs show cumulative fractions of residence time distributions. Right graphs show density of cortical MT contacts as average MTs/µm2 s-1 per embryo, bars are means ± SEM. **(D)** Quantification of astral MT densities in metaphase embryos, measured as shown in Fig. 4F. Plots were aligned and normalized to maximum values at the centrosome. N=20 asters from 10 embryos per condition. Scale bar, 1 µm.

Discussion

In this study, we investigated the localization and dynamics of the dynein complex during asymmetric spindle positioning in a well-established *in vivo* model, the *C. elegans* one-cell embryo. By tagging endogenous dynein and live imaging, we revealed two populations of dynein that together ensure robust cortical pulling force generation. To critically examine the importance of the MT plus-end bound dynein population, we generated a complete knockout of all *ebp* family members and demonstrated that these genes are not essential, but contribute to the control of microtubule dynamics and spindle formation. Finally, we provide a detailed analysis of the asymmetries and dynamics of the major FGC components, dynein and LIN-5, at the cortex of one-cell embryos.

While C-terminal tagging of the *dhc-1* dynein heavy chain was recently used (Zhang et al., 2015a), we observed that this creates partial loss of function. It is currently unclear whether this translates to dynein in other organisms. N-terminally and C-terminally tagged yeast Dyn1 appear functional (Reck-Peterson et al., 2006). However, Dyn1 lacks the C-terminal regulatory extension present in the cytoplasmic dynein heavy chain of *C. elegans* and other organisms (Nicholas et al., 2015). A BAC transgene with a C-terminally GFP-tagged mouse dynein heavy chain is commonly used in mammalian studies (Poser et al., 2008). However, cells in culture with normal endogenous DHC do not depend on the tagged protein. Therefore, tagging the N-terminal DHC tail region instead of the C-terminal motor domain seems the best option for future *in vivo* studies.

Dynein plus-end tracking was previously described for other organisms (Han et al., 2001; Kobayashi and Murayama, 2009; Lenz et al., 2006; Vaughan et al., 1999). In budding yeast, dynein is actively delivered to the cortex by a plus-end tracking complex that also contains a kinesin (Lee et al., 2003; Markus and Lee, 2011; Sheeman et al., 2003). In animal cells, MT plus-end bound dynein is not transported by kinesins but is merely concentrated by binding to +TIPs, which are organized by EB proteins (Akhmanova and Steinmetz, 2015). Indeed, we found that loss of EBs completely abolished dynein plus-end tracking. Strikingly, this mechanism, and in fact the whole EB protein family, turned out to be dispensable for *C. elegans* development and viability.

It is surprising that EBs are not essential in worms, since significant defects in microtubule dynamics, and spindle formation or positioning have been reported in mammalian cells (Ban et al., 2009; Draviam et al., 2006; Ferreira et al., 2013; Green et al., 2005; Komarova et al., 2009; Toyoshima and Nishida, 2007; Xia et al., 2012). These studies did not report a block of cell division upon EB loss, and in fact the phenotypes associated with EB knockouts in yeast and plants are relatively mild (Berlin et al., 1990; Bisgrove et al., 2008). Several considerations may explain the weak phenotypes. First, EB-dependent plus-end tracking does not mediate transport and delivery of +TIPs, but just promotes their transient concentration from the surrounding cytoplasm. This probably provides a limited gain over diffusion. Moreover, EB loss removes plus-end recruitment of both positive and negative MT regulators. In addition, the phenotypes of constitutive knockouts might be milder than acute protein depletions due to compensatory mechanisms.

In contrast to EB-dependent plus-end tracking, LIN-5 is essential for asymmetric spindle positioning. Using endogenously tagged LIN-5 and dynein, we observed that both proteins display a shallow cytoplasmic gradient throughout mitosis, reminiscent of the pattern described for GPR-1/2 and LIN-5 in fixed embryos (Park and Rose, 2008). While the biological cause and function of this cytoplasmic asymmetry remains unknown, it indicates that cortical enrichment as judged by eye or cytoplasm-normalized plots can lead to its over- or underestimation. Thus, we compared non-normalized cortical traces instead and found a strong correlation between LIN-5 and dynein cortical intensity patterns. Interestingly, our analysis did not reveal a clear A-P asymmetry in cortical localization for either protein at the time of initial spindle displacement in late metaphase. However, FRAP analysis combined with TIRF microscopy revealed an asymmetric

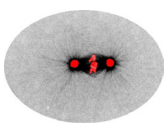

and PAR-dependent stable population of dynein in the posterior. This subpopulation of LIN-5–bound dynein may be critical in force generation, as the number of active force generators has been reported to be higher in the posterior (Grill et al., 2003). LIN-5 showed only a small stable fraction at the cortex, which was non-significantly enriched in the posterior. We assume that not all cortical LIN-5 is dynein associated. Hence, the relevant population might be somewhat obscured in the total pool of cortical LIN-5. Together, our observations indicate that asymmetries in dynein behavior during initial spindle displacement probably do not result from asymmetric enrichment of LIN-5. Instead, other levels of control, such as protein phosphorylation and the G√ GTPase cycle may determine LIN-5–dynein retention and pulling force asymmetry (Galli et al., 2011a; Portegijs et al., 2016).

Dynein still localized to the cortex in embryos that lack EBs, or were treated with nocodazole. This strongly suggests that LIN-5 can recruit dynein directly from the cytoplasm, as opposed to a MT-mediated delivery mechanism. MT-independent dynein recruitment has also been observed in nocodazole-treated mammalian cells, however, the correct cortical distribution of human dynein appears to depend on a dynamic astral MT network (Tame et al., 2014). Similarly, the localization of cortical dynein seemed randomized following nocodazole treatment of *C. elegans* embryos. Thus, in *C. elegans* and mammalian cells, MT-mediated delivery does not appear necessary for dynein localization to the cortex, but dynamic MTs appear required for the proper levels and distribution of dynein at the cortex.

We propose that dynein plus-end tracking functions as a local enrichment mechanism (Fig. 8). By concentrating dynein at the plus-end, MTs could promote local interaction of dynein with Gα–GPR-1/2–LIN-5 complexes at the cortex (Fig. 8, arrow 1). This hypothesis is supported by our finding that knockdown of EBP-2 enhances the reduction in forces caused by partial loss of DHC-1 function. In this context, enrichment of dynein at the plus-end appears needed for efficient force generation. In the absence of EBs and thus dynein plus-end tracking, FGCs would need to form through contacts between astral MTs and dynein-containing cortical complexes (Fig. 8, arrow 2). While this single mechanism was thought to be less efficient (Ananthanarayanan et al., 2013), the prolonged cortical residence of MTs in the absence of EBP-2 might allow for successful probing of the cortex, which could explain why Δ*ebp-2* does not solely lead to reduced force generation. In wild type cells, +TIPs form a protein-dense network, and the number of available binding sites in the vicinity of a MT plus end is limited (Duellberg et al., 2014). In EB-depleted cells, MT plus ends are probably less crowded, and cortical FGCs may associate with MTs more efficiently. Taken together, our work illustrates the complexity and robustness of the molecular mechanisms controlling the critical process of spindle positioning.

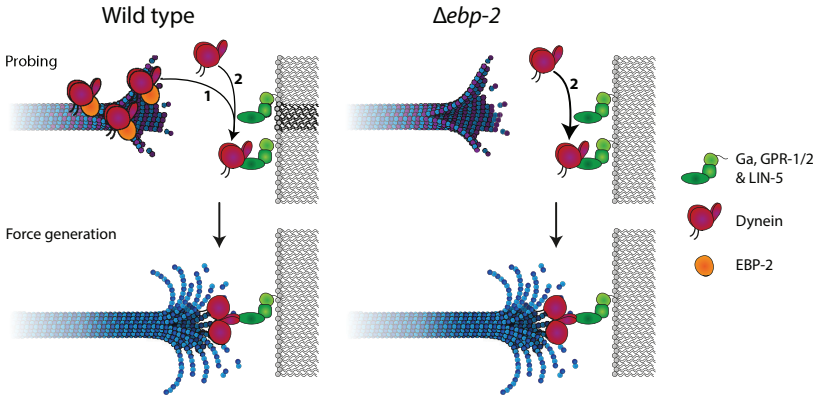

Figure 8 Model. Model of force generation in wild type (left) and *Δebp-2* (right) situations as explained in the text.

Materials and Methods

C. elegans strains

A summary of the strains used in this study is included in Supplementary Table I. All strains were maintained at 20 °C as described previously (Brenner, 1974), unless stated otherwise. Animals were grown on plates containing nematode growth medium (NGM) seeded with OP50 *Escherichia coli* bacteria.

Generation of CRISPR/Cas9 repair templates and gRNAs

Homology arms of at least 1500 bp flanking the CRISPR/Cas9 cleavage site were generated by PCR amplification from purified *C. elegans* genomic DNA using the KOD polymerase (Novagen). PCR products were inserted into the pBSK backbone by Gibson assembly (New England Biolabs). For the generation of *ph::egfp::lov* and *egfp::dhc-1*, *egfp* was amplified from pMA-*egfp*, *ph* from *Pwrt-2::gfp::ph* (Wildwater et al., 2011) and *lov* from *gfp::LOVpep::unc-54UTR* (Harterink et al., 2016). For *mcherry::dhc-1* and *dhc-1::mcherry*, codon-optimized *mcherry* was amplified from TH0563-PAZ-*mCherry* (a kind gift from A. Hyman). Primers containing overlaps between PCR fragments, linker sequences encoding 4 glycine residues and mutated gRNA sites were synthesized (Integrated DNA technologies) and are listed in Supplementary Table III. For the generation of gRNA vectors, oligonucleotides were annealed and inserted into pJJR50 using T4 ligation (New England Biolabs). Vectors were used to transform and purified from DH5α competent cells (Qiagen).

CRISPR/Cas9-mediated genome editing

Injection of *C. elegans* adults in the germline was carried out using an inverted microscope micro-injection setup. Injection mixes contained a combination of 30-50 ng/µl P*eft-3::cas9* (Addgene ID #46168(Friedland et al., 2013), 50-100 ng/µl u6::sgRNA with sequences targeted against either *cxTi10816*, *dhc-1*, *ebp-1*, *ebp-2* or *ebp-3*, 30-50 ng/µl of the repair template, 50 ng/µl PAGE-purified *pha-1* repair oligonucleotide (Integrated DNA technologies), 60 ng/µl pJW1285 (Addgene ID #61252 (Ward, 2014)), and 2.5 ng/µl P*myo-2::tdtomato* as a co-injection marker. Animals were grown for 3-5 days at either 20 or 25 °C after injection, and transgenic progeny was selected based on either expression of tdTomato in the pharynx or survival at the non-permissive temperature (25 °C). Subsequent assessment of genome editing events was carried out by either visual inspection using a wide-field fluorescence microscope and/or PCR amplification using primers targeting the inserted FP and a genomic region situated outside of the range of homology arms in case of *dhc-1*, or sequences flanking the predicted cut sites as well as an internal control in case of the Δ*ebp-1/2/3* knock-out mutants. The contexts of PCR-confirmed edited genomic loci were further inspected by sequencing (Macrogen Europe).

Quantification of embryonic lethality and total brood size

In three separate experiments, N2, SV1598, SV1619 and SV1803; N2, SV1868, SV1872, SV1877 and SV1882 or EU828 and SV1956 single L4-stage hermaphrodites were placed on OP50 feeding plates and kept at 15, 20, 23 and/or 25 °C, depending on the experiment. Animals were transferred to a new plate every day. On each plate, embryonic lethality was scored after 24 hours, and brood size 48 hours after removal of the parent. Experiments were executed in quadruplicate.

Microscopy

For time-lapse imaging embryos were dissected from *C. elegans* adults on coverslips in 0.8x egg salts buffer (94 mM NaCl, 32 mM KCl, 2.7 mM CaCl2, 2.7 mM MgCl2, 4 mM HEPES, pH 7.5) (Tagawa et al., 2001), and subsequently mounted on 4% agarose pads.

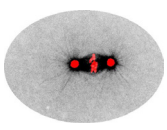

Live-cell SDCM imaging of one-cell embryos and HeLa cells was performed on a Nikon Eclipse Ti with Perfect Focus System, Yokogawa CSU-X1-A1 spinning disc confocal head, Plan Apo VC 60x N.A. 1.40 oil and S Fluor 100x N.A. 0.5-1.3 (at 1.3, for photo-ablation) objectives, Photometrics Evolve 512 EMCCD camera, DV2 two-channel beam-splitter for simultaneous dual-color imaging, Cobolt Calypso 491 nm (100 mW), Cobolt Jive 561 nm (100 mW) and Teem Photonics 355 nm Q-switched pulsed laser controlled with the ILas system (Roper Scientific France/ PICT-IBiSA, Institut Curie, used for photo-ablation), ET-GFP (49002), ET-mCherry (49008) and ET-GFPmCherry (49022) filters, ASI motorized stage MS-2000-XYZ with Piezo Top Plate, and Sutter LB10-3 filter wheel. The microscope was controlled with MetaMorph 7.7 software and situated in a temperature-controlled room at 20 °C.

HeLa cells were cultured as described previously (Splinter et al., 2012). For imaging of the dynein complex during mitosis, HeLa cells stably expressing DIC2-GFP were used. This cell line was generated and described previously in a BAC TransgeneOmics project (Poser et al., 2008). Imaging of mitotic cells was performed using the spinning disc setup described above, where the temperature was controlled at 37 °C with a Tokai Hit INUBG2E-ZILCS Stage Top Incubator during experiments.

For regular single- and dual-color channel imaging experiments, images were acquired in either streaming mode with 50, 100, 250, 500 or 1000 ms exposure, or time-lapse mode with 500 ms exposure and 5 second intervals. Laser power was kept constant within experiments. For spindle bisection assays, spindles were imaged after photo-ablation in streaming mode with 500 ms exposure time.

Simultaneous dual-color TIRF imaging of embryos was performed on a Nikon Eclipse Ti with Perfect Focus System, Nikon Apo TIRF 100x N.A. 1.49 oil objective, Photometrics Evolve 512 EMCCD camera, Optosplit III beam-splitter for simultaneous dual-color imaging, 488 nm (150 mW) and Cobolt Jive 561 nm (100 mW) lasers, ET-GFP (49002), ET-mCherry (49008) and ET-GFPmCherry (49022) filters, ASI motorized stage MS-2000-XY System for Inversted Microscope Nikon Te/Ti 2000, and Sutter LB10-3 filter wheel. Acquisition was controlled with MetaMorph 7.7 software and the setup was situated in a temperature-controlled room at 20 °C.

Single-color TIRF imaging of embryos was performed on either above-mentioned TIRF setup, or on an identical TIRF setup in which lasers were controlled by the Ilas-2 system (Roper Scientific France / PICT-IBiSA, Institut Curie), and image acquisition was controlled with MetaMorph 7.8 software.

Live-cell wide-field time-lapse differential interference contrast (DIC) microscopy imaging of embryos was performed on a Zeiss Axioplan upright microscope, with a 100x N.A. 1.4 PlanApochroma objective, controlled by AxioVision Rel 4.7 software, at an acquisition rate of 1 image per 2 seconds with constant exposure time and light intensity. Embryos were followed from pronuclear meeting until completion of the first cell division.

Images acquired by SDCM and TIRF microscopy were prepared for publication in ImageJ by linear adjustment of brightness and contrast, subtraction of background intensity as measured in images outside cells, and frame averaging. For images in Fig. 2, 4D, 6A and S2AB, a Gaussian blur filter was applied for background subtraction using ImageJ. Fluorophores used in this study to visualize proteins of interest include eGFP, mCherry and YFP.

RNA-mediated interference

For feeding RNAi experiments (Timmons and Fire, 1998), L4 animals were grown on seeded RNAi plates for 24 hours at 20 °C or 48 hours at 15 °C prior to imaging sessions (*lin-5*, *ebp-1/3*, *ebp-2*, *gpr-1*). Alternatively, the gonads of young adults were injected with double-stranded RNA (dsRNA) targeting RNA molecules of interest (*perm-1* and *perm-1* + *lin-5*) and grown for 20 hours at 15 °C (Fire et al., 1998). For these experiments, the products of T7 PCRs on RNAi clones were used as templates for *in vitro* dsRNA synthesis using the MEGAscript T7 transcription kit (ThermoFisher Scientific). Clones from both the Vidal and Ahringer RNAi libraries were used (Kamath et al., 2003; Rual et al., 2004).

UV laser spindle midzone severing

Severing of the mitotic spindle was performed in essence as described previously (Grill et al., 2001; Portegijs et al., 2016). AZ224, TH65, SV893, SV1874, SV1879 and SV1900 one-cell embryos were imaged during mitosis at 20 °C using a spinning disc confocal microscope equipped with a Teem Photonics 355 nm Q-switched pulsed laser controlled with the ILas system (Roper Scientific France/ PICT-IBiSA, Institut Curie). At anaphase onset, as judged by spindle morphology visualized with GFP::TBB-2 or TBA-2::YFP, embryos were subjected to spindle bisection as shown in Fig. 4B and Video 9. Subsequent displacement of centrosomes was followed by stream acquisition with 500 ms exposure time. Centrosome peak velocities after spindle severing were subsequently tracked automatically using the FIJI TrackMate plugin.

Fluorescence recovery after photobleaching (FRAP)

Local photobleaching of eGFP::LIN-5 and eGFP::DHC-1 fluorescence signal was performed during metaphase in a circular region with a diameter of 45 pixels (~2,8 µm) in both the anterior and posterior cortex (except for cytoplasmic LIN-5 FRAP experiments which were performed only in the anterior), and recovery was followed for up to 30 s afterwards. Intensities within the photobleached regions and a background area outside the signal of the embryo cortex were measured using a circular region with a diameter of 54 pixels (~3,38 µm), and a bleaching control was taken between but not overlapping the anterior and posterior photobleached regions. Recovery of the fluorescent signals was set to 100% based on the average intensity from 20 frames (1 s) before bleaching in the same region, and set to 0% directly after. All values were normalized to account for camera background and acquisition photobleaching, as described previously (Phair et al., 2003). Recovery curves of cortical FRAP experiments were aligned at their minimum value and fitted using one- and two-phase nonlinear regression analysis in Prism 6 (GraphPad software, inc.). For unpaired statistical comparison with initial phase parameters of cortical FRAP fits, individual cytoplasmic recovery parameters were approached by one-phase nonlinear regression analysis and subsequently averaged and tested for significance. For paired statistical testing of plateau values from cortical FRAP curves, individual curves were fit by one-phase nonlinear regression analysis, and anterior and posterior parameters were subsequently compared within samples.

Drug treatment of early embryos

To allow for small molecule drugs to enter the early *C. elegans* embryo, L4 animals were treated with *perm-1* RNAi for 20 hours prior to experiments (Carvalho et al., 2011). Egg-laying SV1803 or SV1635 adults were then splayed onto coverslips in 0.8x egg salts buffer with 1 µM nocodazole and mounted on slides with a concave indentation which prevents compression of the embryos. Metaphase one-cell embryos were identified by the presence of polar bodies, enlarged centrosomes and a spindle remnant and absence of a nuclear envelope and imaged by SDCM (Portegijs et al., 2016).

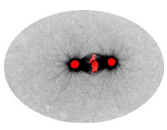

Data analysis

All intensity profile measurements of SDCM and TIRF microscopy data were generated using ImageJ and FIJI.

For cortical intensity profiles of strains SV1589, SV1619, SV1635 and SV1803, both halves of each embryo were traced with a 5 px wide freehand line from the anterior to the posterior pole with 5 replicates, and 5 matching traces were generated below each cortex in the cytoplasm. Intensity profiles were background corrected and each group of 5 traces was then averaged and subsequently divided into 100 bins to correct for varying lengths of the plots. Cortical plots were then plotted either with or without normalization over corresponding cytoplasmic measurements or the average thereof.

Analysis of the timing of key mitotic events and position of the nucleocentrosomal complex and centrosomes from DIC movies of N2, SV1868, SV1872, SV1877 and SV1882 strains was performed by hand using ImageJ.

Quantifications of cortical MT residence time were performed automatically by use of the FIJI plugin Trackmate v3.4.2 at 6 px estimated blob diameter and a threshold value of 1500. TIRF microscopy movies from strains AZ244, SV1874, TH65, SV1879, SV1900 and SV893 starting at posterior spindle displacement with 20 s total duration were background corrected by application of a Gaussian blur filter prior to analysis. Detected spots were then filtered to contain only those with <10 px displacement, which excludes any laterally growing MTs from the analysis.

Speeds of EBP-2::GFP and mCherry::DHC-1 comets in strain SV1857 as imaged by SDCM during metaphase were calculated based on angles made by tracks in kymograph images generated in ImageJ with the KymoResliceWide plugin. Kymograph locations were manually selected between the centrosome and cell cortex.

Quantification of the colocalization between EBP-2::GFP and mCherry::DHC-1 comets in strain SV1857 as imaged by simultaneous dual-color TIRF microscopy was executed using the ComDet plugin v0.3.6, and the same dual-color images with one channel inverted horizontally were used as an internal control. Particles were detected in both green and red channels independently, at approximated particle sizes of 4 (red) and 4,5 (green) pixels with sensitivities of SNR=4 and SNR=5 respectively. Colocalization was determined based on a maximum distance of 8.00 px.

Automatic tracking of particle intensities in TIRF movies of SV1803, SV1874 and SV1879 was executed using the ImageJ Analyze Particles plugin with parameter size = 10-Infinity pixels, circularity = 0.10-1.00 and with exclusion of particles on edges, after background-subtraction and manual image thresholding.

Radial intensity profiles of astral MT networks were generated using the Radial Profile Angle plugin for ImageJ, set to measure intensities in a 180° angle around each of two centrosomes with a radius of 150 px in metaphase embryos. Intensity profiles were then aligned at their maximum value corresponding to the outer rim of the centrosome, and normalized to their maximum values.

Cross-correlation analysis was performed on averaged non-normalized cortical intensity profiles of strain SV1635 using a custom MatLab (The MathWorks) script and the following equation which calculates the normalized cross-correlation for each Δx shift of one channel with respect to another:

$$\gamma(\Delta x) = \frac{\sum_x [I_1(x) - \langle I_1 \rangle][I_2(x - \Delta x) - \langle I_2 \rangle]}{\sqrt{\sum_x [I_1(x) - \langle I_1 \rangle]^2 \sum_x [I_2(x - \Delta x) - \langle I_2 \rangle]^2}}$$

All numerical data processing and graph generation was performed using Excel 2011 (Microsoft) and Prism 6 (GraphPad software, inc.).

Statistical analysis

All data are expressed as means with either SD or SEM, as indicated in the legends of each figure. Statistical differences were determined using two-tailed paired and unpaired Student's t-tests, Mann-Whitney U tests and the Wilcoxon matched-pairs signed rank test. Prior to selection of appropriate statistical analyses, data sets were tested for a Gaussian distribution using the D'Agostino-Pearson omnibus K2 normality test. A p-value of <0.05 was considered to be significant. *, P<0.05; **, P<0.01; ***, P<0.001; ****, P<0.0001. All statistical analyses were performed using Prism 6 (GraphPad software, inc.).

Online supplemental material

Figure S1 shows dynein plus-end tracking in cell types other than the one-cell *C. elegans* embryo. Figure S2 shows the localization of dynein at the mitotic spindle and its colocalization with dynactin at the MT plus-end. Figure S3 contains quantifications of various mitotic events and their timing as visualized by DIC microscopy as in Fig. 3E. Figure S4 shows that EBP-2 is required for assembly of the spindle midzone, and that cortical dynein patches follow the oscillatory behavior of the anaphase spindle. Figure S5 contains extended analyses of the subcellular localization patterns of LIN-5 and DHC-1 shown in Figure 5C, as well as recovery curves for the cytoplasmic FRAP experiments quantified in in Figures 6F and H. Table S1 contains parameters from nonlinear regression curve fits of eGFP::LIN-5 and eGFP::DHC-1 FRAP experiments. Table S2 contains a list of the *C. elegans* strains used in this study. Table S3 contains a list of the primers used in this study for CRISPR/Cas9-assisted genome engineering. Video S1 shows overlap of mCherry::DHC-1 with GFP::TBB-2 as in Fig. 2A. Video S2 shows colocalization of mCherry::DHC-1 with EBP-2::GFP as in Fig. 2B. Video S3 shows cortical overlap of mCherry::DHC-1 with GFP::TBB-2 as in Fig. 2E. Video S4 shows cortical overlap of mCherry::DHC-1 with EBP-2::GFP as in Fig. 2F. Video S5 shows co-occurrence of dynein comets reaching the cortex and the formation of membrane invaginations as in Figure 2H. Video S6 shows the localization of eGFP::DHC-1 in Δ*ebp* mutants as in Figure 3C. Video S7 shows DIC movies of mitotic wild type and Δ*ebp* one-cell embryos as in Figure 3E. Video S8 shows the genetic dissection of two cortical dynein populations as in Figure 6A. Video S9 shows an example of UV laser-mediated spindle severing as in Figure 4B. Video S10 shows end-on MT-cortex contacts as visualized by TIRF microscopy as shown in Figure 4D.

Acknowledgements

We thank all members of the van den Heuvel, Akhmanova and Boxem groups for helpful discussions and support. We acknowledge Wormbase and the Biology Imaging Center at the Faculty of Sciences, Department of Biology, Utrecht University. Some strains were provided by the *Caenorhabditis* Genetics Center (CGC), funded by NIH Office of Research Infrastructure Programs (P40 OD010440). This work was supported by a European Research Council (ERC) Synergy grant 609822 to A.A., and is part of program CW711.011.01 (SvdH) financed by the Netherlands Organization for Scientific Research (NWO).

Author contributions

AA, RS and SvdH designed the study, analyzed the data and wrote the paper. RS carried out most experiments, LEF performed the LIN-5 knockin and FRAP studies, IG was responsible for the analysis of HeLa cells and, with EK, provided technical support of microscopy, EK supported data analysis.

Competing financial interests statement

The authors declare no competing financial interests.

Supplementary figures and tables

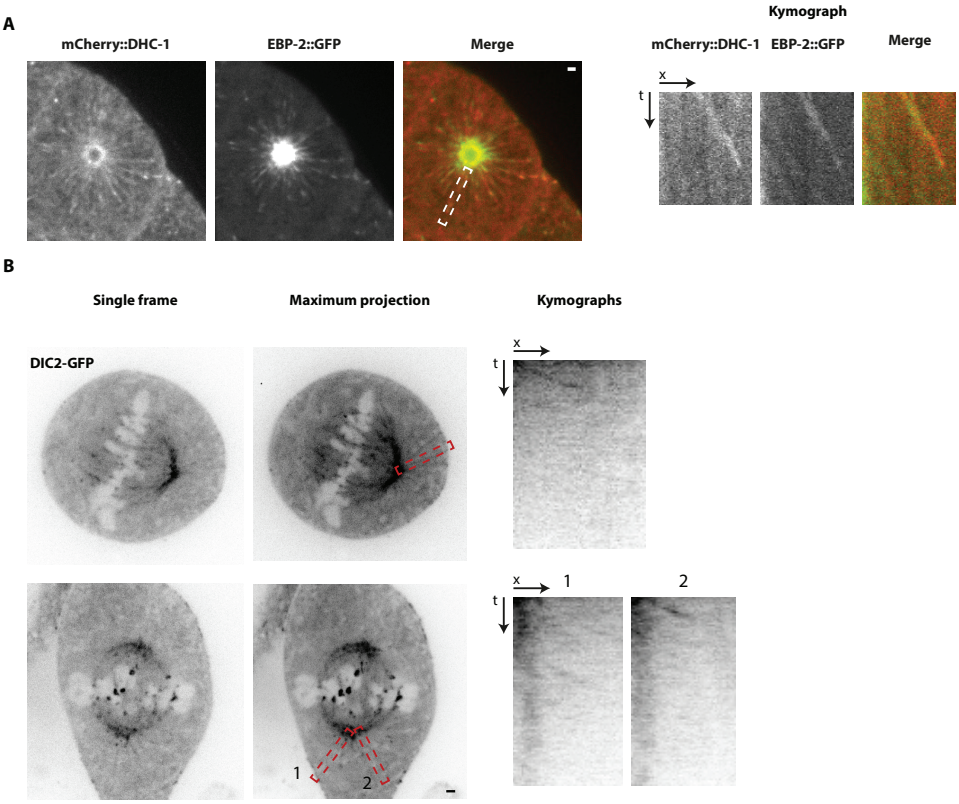

Supplementary figure 1 Dynein tracks plus-ends of astral MTs in cell types other than the *C. elegans* zygote. **(A)** Representative images of mCherry::DHC-1 (red) and EBP-2::GFP (green) localization in a 4-cell embryo. Images are averages of 10 consecutive frames taken from 100 ms stream-lapse movies. Kymograph position is indicated with the dashed line box. Scale bar, 1 µm.
(B) Representative single frames (left), maximum projections (middle) and kymographs (right) of DIC2-GFP localization in metaphase HeLa cells. Images taken from 500 ms ms stream-lapse movies. Kymograph positions are indicated with dashed line boxes. Scale bar, 1 µm.

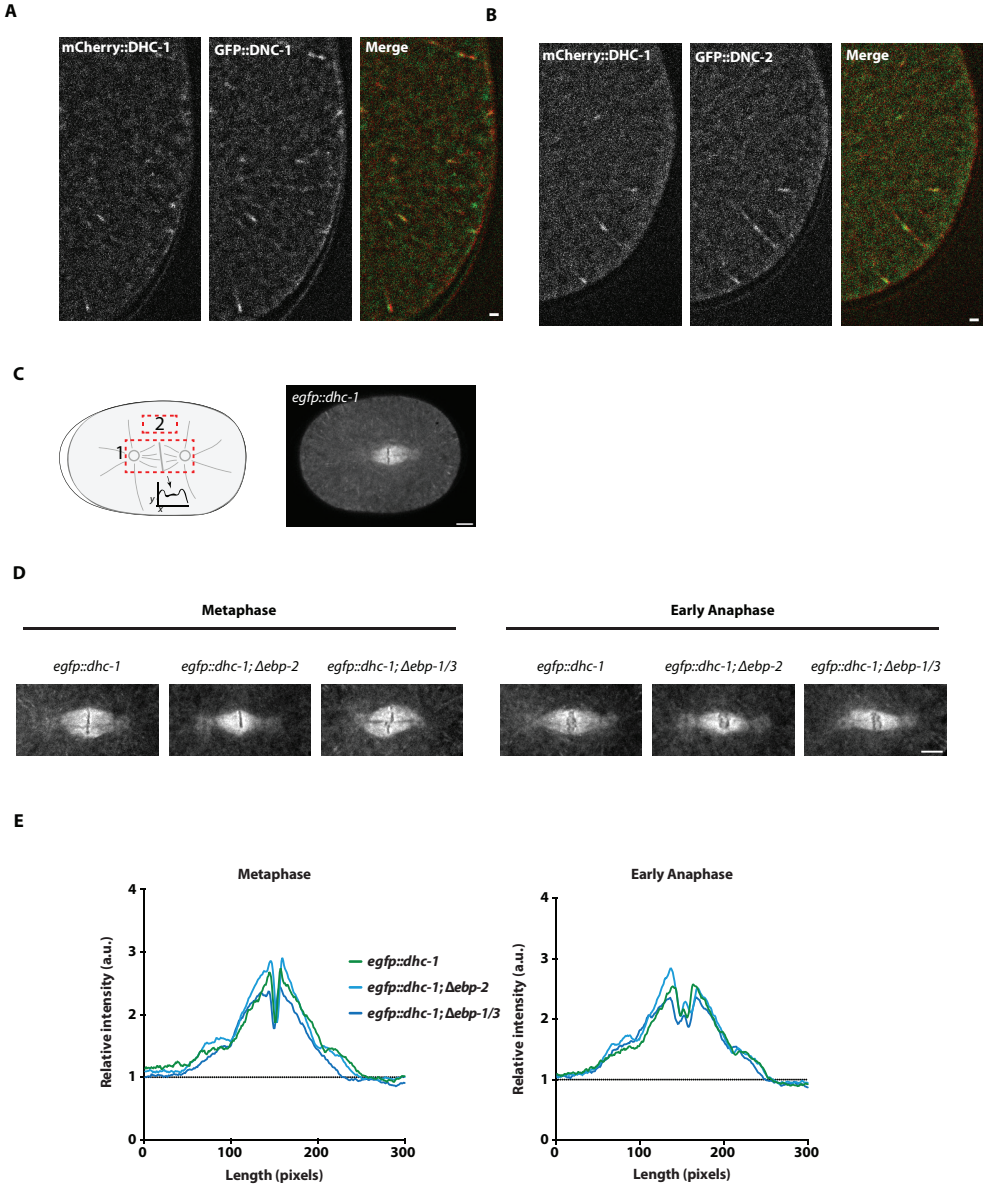

Supplementary figure 2 Dynactin components track MT plus-ends together with DHC-1, and dynein localization to the spindle midzone, kinetochores, kinetochore MTs and poles is not altered upon loss of EBP-1/2/3. **(A, B)** Representative simultaneous dual-color SDCLM images of mCherry::DHC-1 (red) and either GFP::DNC-1(A) or GFP::DNC-2 (B) localization during mitosis. Images are averages of 5 consecutive frames taken from 100 ms stream-lapse movies, after background subtraction by a gaussian blur filter. Scale bars, 1 µm. **(C)** Schematic representation (left) of approach to measure eGFP::DHC-1 (right) intensity along the mitotic spindle. Scale bar, 5 µm. **(D)** Representative SDCLM images of eGFP::DHC-1 localization in different wt or Δ*ebp* mutant backgrounds as indicated in each image, both during metaphase and early anaphase. Scale bar, 5 µm. **(E)** Quantification of dynein distribution along the horizontal axis of the spindle in different genetic backgrounds as indicated in the graph, represented as average (N=4) intensity normalized to average cytoplasmic values (measured in box in (A)). Spindle length in pixels.

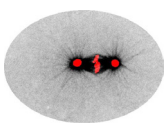

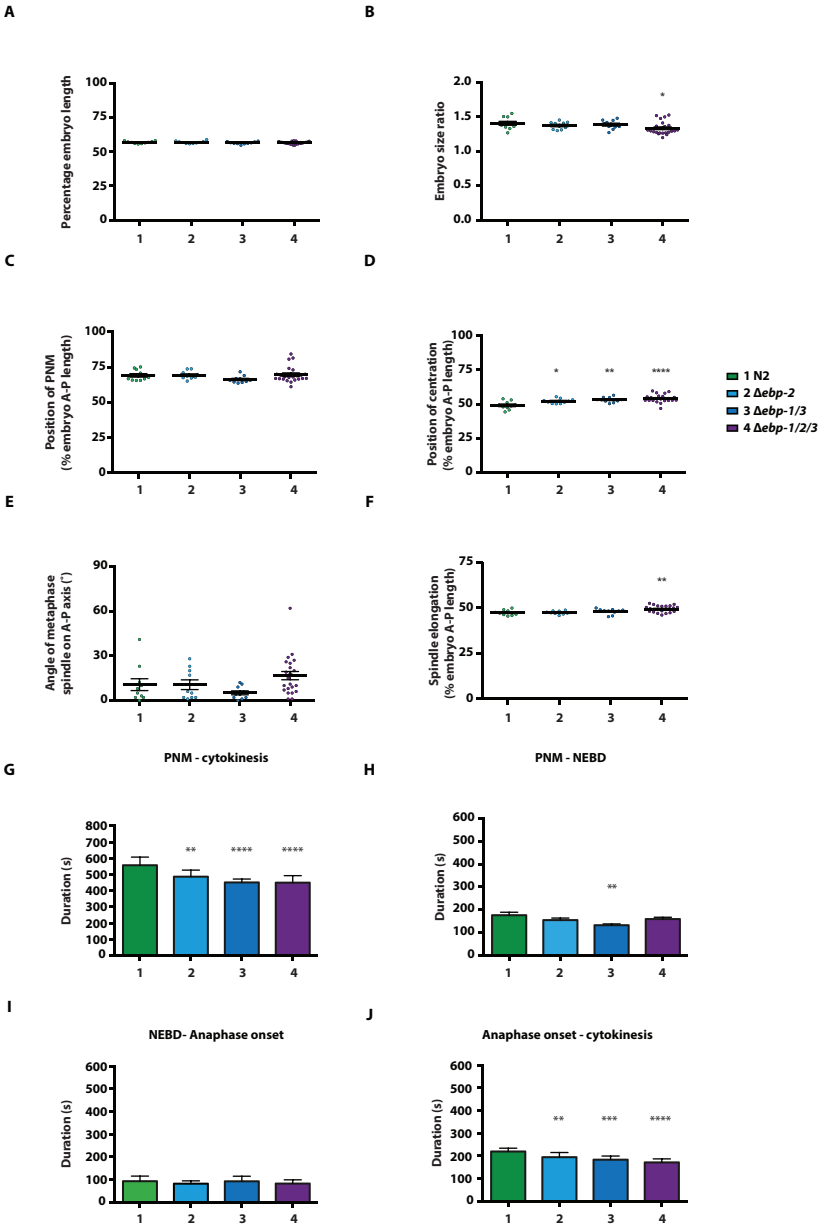

Supplementary figure 3 Characterization of key mitotic events and their timing in Δ*ebp* mutant embryos. Quantification of key mitotic events from DIC time-lapse movies of N2 (green), Δ*ebp-2* (light blue), Δ*ebp-1/3* (dark blue) and Δ*ebp-1/2/3* (purple) embryos during the first division. Asymmetry **(A)**, position of pronuclear meeting (PNM, **C**) and centration **(D)** and spindle elongation **(F)** are plotted as a percentage of total embryo length, embryo size **(B)** as the ratio of embryo length over embryo height, and metaphase spindle angle as the angle relative to the embryo A-P axis. Errors are mean (N≥10) + SEM, unpaired Welch Student's *t*-test (A-D and F) or Mann-Whitney U-test (E); * P < 0.05, ** P < 0.01, **** P < 0.0001 compared to wt, no indication means no significant difference from wt. **(G-J)** Quantification of duration of mitotic events from DIC time-lapse movies of N2 (green), Δ*ebp-2* (light blue), Δ*ebp-1/3* (dark blue) and Δ*ebp-1/2/3* (purple) embryos during the first division. Duration in seconds, errors are mean (N≥9) + SEM. unpaired Welch Student's *t*-test; * P < 0.05, ** P < 0.01, *** P < 0.001, **** P < 0.0001 compared to wt, no indication means no significant difference from wt.

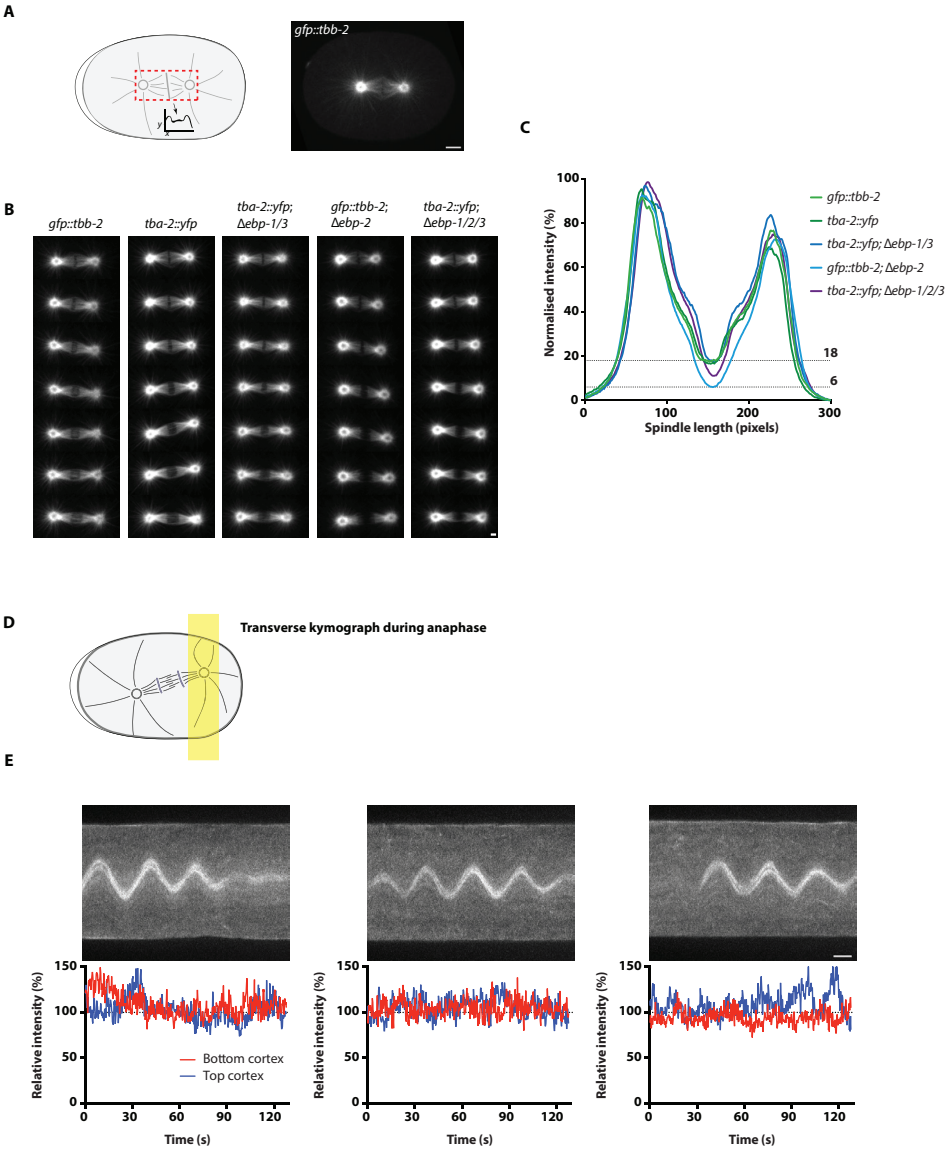

Supplementary figure 4 EBP-2 is required for proper spindle midzone establishment, and cortical dynein patches follow oscillatory spindle movements. **(A)** Schematic representation (left) of approach to measure MT (right) density along the mitotic spindle. **(B)** Montages of representative SDCLM movies of one-cell embryos expressing either GFP::TBB-2 or TBA-2::YFP (MTs), in different wt or Δ*ebp* mutant backgrounds as indicated in each image. Montages are generated from seven consecutive frames from time-lapse movies acquired at a rate of 1 frame per 5 seconds, all acquired with the same laser power and exposure time of 500 ms. Scale bar, 1 µm. **(C)** Quantification of MT abundance along the horizontal axis of the spindle in different genetic backgrounds during early anaphase as indicated in the graph, represented as average (N=7) intensity relative to the maximum value of all data sets. Spindle length in pixels. **(D)** Schematic representation of *C. elegans* embryo during anaphase spindle pole rocking, indicating where kymographs are positioned in the embryo. **(E)** Representative kymographs of eGFP::DHC-1 localization at the posterior pole and cortex during anaphase spindle rocking. Graphs show relative cortical eGFP::DHC-1 intensity, as quantified by generating linescans of both upper and lower cortex intensities and subsequent normalization over adjacent cytoplasmic values. Scale bar, 5 µm.

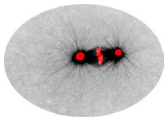

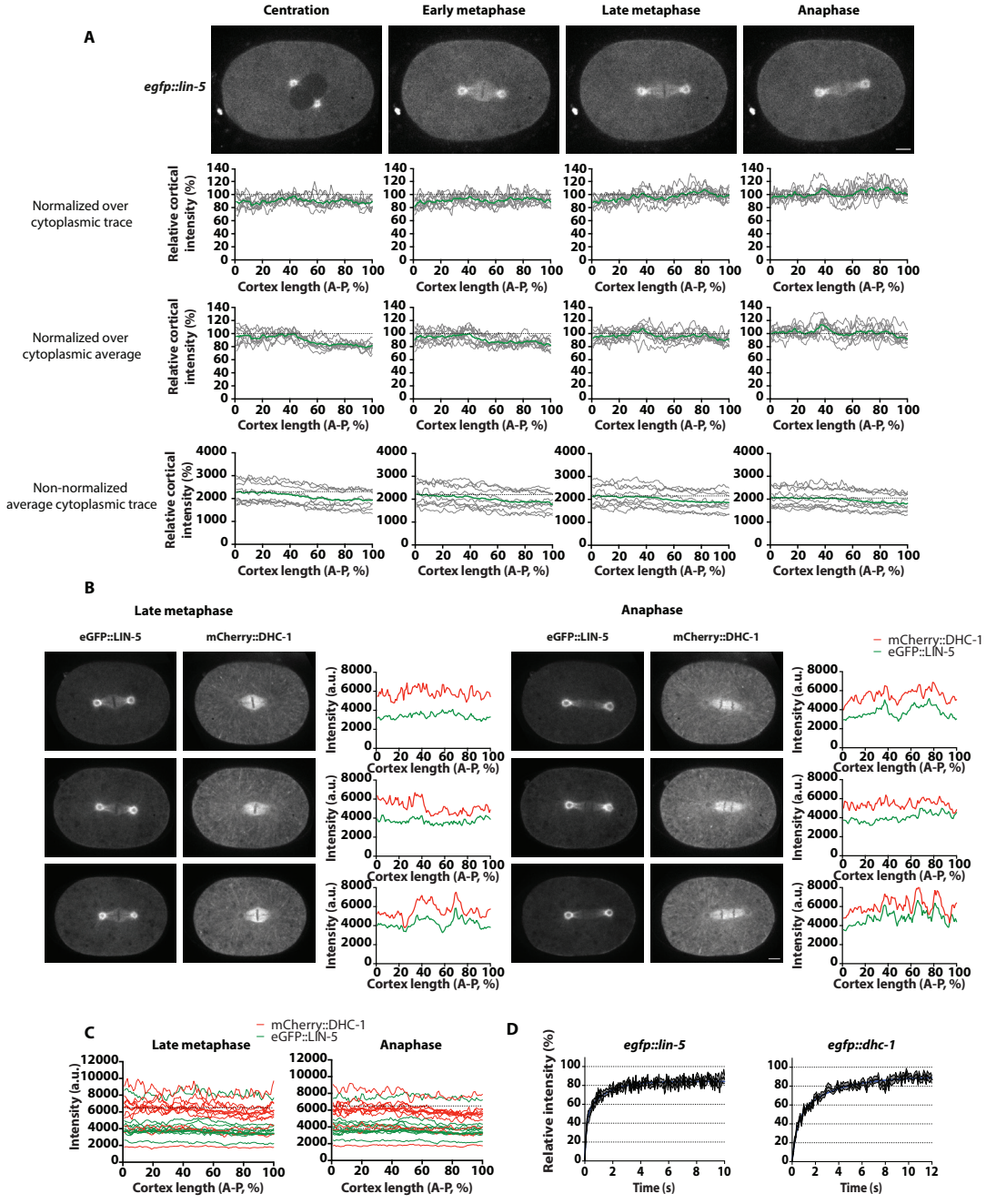
A
Centration
Early metaphase
Late metaphase
Anaphase
egfp::lin-5
Normalized over cytoplasmic trace
Normalized over cytoplasmic average
Non-normalized average cytoplasmic trace
Relative cortical intensity (%)
Cortex length (A-P, %)
B
Late metaphase
Anaphase
eGFP::LIN-5
mCherry::DHC-1
Intensity (a.u.)
Cortex length (A-P, %)
C
mCherry::DHC-1
eGFP::LIN-5
Late metaphase
Anaphase
D
egfp::lin-5
egfp::dhc-1
Relative intensity (%)
Time (s)

Supplementary figure 5 Extended analysis of cortical LIN-5 and dynein localization during mitosis. **(A)** Quantification of cortical eGFP::LIN-5 during centration, early metaphase, late metaphase and anaphase as shown in representative images in upper panels. Cortical intensity values are normalized over either cytoplasmic traces from below the cortex (first row of graphs) or over a single average cytoplasmic value (second row). Dotted lines at Y=100% indicate a 1:1 cortex to cytoplasm ratio. Non-normalized cytoplasmic intensities indicating a gradient of eGFP::LIN-5 during all mitotic stages are also shown (third row). Scale bar, 5 µm. **(B)** Individual non-normalized cortical traces of embryos expressing eGFP::LIN-5 and mCherry::DHC-1 during late metaphase and anaphase. Three representative embryos from the dataset used to quantify cortical enrichment and the cross-correlation index in Fig. 5C are shown in both stages. Scale bar, 5 µm. **(C)** Quantification of cortical eGFP::LIN-5 and mCherry::DHC-1 during late metaphase and anaphase as shown in representative images in (B). Non-normalized cytoplasmic intensities are plotted as individual (thin) and average (thick) plots. **(D)** Quantification of cytoplasmic eGFP::LIN-5 and eGFP::DHC-1 FRAP. Curves are expressed as mean + SEM; *egfp::lin-5* (N=7), *egfp::dhc-1* (N=30).

Strain	Genotype
N2	Wild type
SV893	dhc-1(or195ts) I; unc-119(ed3) III; ruIs57[unc-119(+) pie-1-GFP–α-tubulin]
SV1589	he244 [egfp::lin-5] II
SV1598	he248[dhc-1::mcherry] I
SV1619	he250[mcherry::dhc-1] I
SV1635	he244 [egfp::lin-5] II; he250[mcherry::dhc-1] I
EU828	dhc-1(or195ts) I
TH65	ddIs15 [unc-119(+) + C47B2.3(genomic)::YFP]]
AZ224	RuIs57[Ppie-1::gfp::tbb-2] V
SV1702	RuIs57[Ppie-1::gfp::tbb-2] V; he250[mcherry::dhc-1] I
SV1703	he258[Peft-3::ph::egfp::lov::tbb-2-3'UTR] IV; he250[mcherry::dhc-1] I
SV1803	he264[egfp::dhc-1] I
SV1840	ojIs5[pie-1::GFP::dnc-1 + unc-119(+)]; he250[mcherry::dhc-1] I
SV1841	ojIs57[Ppie-1::gfp::dnc-2 unc-119(+)]; he250[mcherry::dhc-1] I
SV1857	abcIs3[Ppie-1::ebp-2::gfp; unc-119(+)]; he250[mcherry::dhc-1] I
SV1868	he278[Δebp-2] II
SV1872	he279[Δebp-1, ΔY59A8B.25, Δebp-3]
SV1873	he278[Δebp-2]; he263[egfp::dhc-1] V
SV1874	he278[Δebp-2] II; RuIs57[Ppie-1::gfp::tbb-2] V
SV1877	he278[Δebp-2] II; he279[Δebp-1, ΔY59A8B.25, Δebp-3] V
SV1878	he279[Δebp-1, ΔY59A8B.25, Δebp-3] V; he263[egfp::dhc-1] I
SV1879	he279[Δebp-1, ΔY59A8B.25, Δebp-3] V; ddIs15 [[unc-119(+) + C47B2.3(genomic)::YFP]]
SV1900	unc-119(+) + C47B2.3(genomic)::YFP; he278[Δebp-2] II; he279[Δebp-1, ΔY59A8B.25, Δebp-3] V
SV1956	dhc-1(or195ts) I; unc-119(ed3) III; he278[Δebp-2]

Supplementary Table I List of *C. elegans* strains used in this study. This table shows a summary of the *C. elegans* strains including their corresponding genotypes as used in this study.

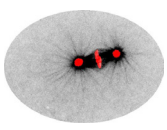

	eGFP::LIN-5			eGFP::DHC-1		
	Cortex anterior	Cortex posterior	Cytoplasm	Cortex anterior	Cortex posterior	Cytoplasm
N	28	22	7	19	19	15
One component fit						
Plateau (%)	89,31	83,74	81,98	87,61	75,71	85,21
95% CI	88,82 to 89,80	83,33 to 84,15	81,35 to 82,61	87,04 to 88,18	75,28 to 76,14	84,12 to 86,29
Half-life (s)	1,94	1,75	0,32	3,86	3,19	0,86
95% CI	1,88 to 1,20	1,70 to 1,80	0,230 to 0,34	3,768 to 3,966	3,11 to 3,28	0,80 to 0,92
Degrees of freedom	518	518	1357	599	599	119
R square	0,93	0,94	0,51	0,96	0,95	0,92
Two components fit						
Plateau (%)	94,49	86,73	84,27	94,69	80,89	90,02
95% CI	94,09 to 94,89	86,45 to 87,01	83,40 to 85,15	94,31 to 95,08	80,63 to 81,15	87,90 to 92,13
Percent fast (%)	46,36	42,6	57,51	28,56	33,86	51,81
Slow half-life (s)	4,73	3,58	0,99	7,11	6,25	2,26
95% CI	4,53 to 4,94	3,44 to 3,74	0,82 to 1,24	6,96 to 7,28	6,12 to 6,39	1,77 to 3,13
Fast half-life (s)	0,53	0,43	0,086	0,55	0,59	0,31
95% CI	0,50 to 0,57	0,40 to 0,47	0,066 to 0,12	0,52 to 0,59	0,56 to 0,62	0,24 to 0,43
Degrees of freedom	516	516	1355	597	597	117
R square	0,9937	0,9913	0,57	0,9973	0,9974	0,9656
Individual one-component fit	Slow phase	Slow phase		Slow phase	Slow phase	
Average plateau (%)	99,07	91,99	82,15	94,46	82,09	84,75
95% CI	90,97 to 107,2	82,79 to 101,2	76,60 to 87,69	88,13 to 100,8	73,83 to 90,35	79,84 to 89,75
Average half-life (s)	5,06	5,54	0,34	6,64	6,05	0,51

Supplementary Table II Parameters from eGFP::LIN-5 and eGFP::DHC-1 FRAP data nonlinear regression curve fits. This table shows the parameters acquired from nonlinear regression curve fitting of the FRAP data described in Fig. 6 D, E, F, G and H. Genotypes are indicated above columns, parameter types and their respective units of measurement are indicated to the left for each row. Parameters from one- and two-component fits on average curves, and from fits on non-averaged individual curves are shown. The subcellular location that was analyzed and its corresponding N-value is indicated in the top of each column.

eGFP::DHC-1; Δebp-2		eGFP::DHC-1; Δebp-2 + par-2 RNAi		eGFP::DHC-1; Δebp-2 + par-3 RNAi	
Cortex anterior	Cortex posterior	Cortex anterior	Cortex posterior	Cortex anterior	Cortex posterior
35	35	24	24	21	21
94,66	85,21	90,06	95,4	88,4	84,95
93,95 to 95,36	84,60 to 85,82	89,52 to 90,60	94,73 to 96,07	87,68 to 89,12	84,19 to 85,71
4,47	4,036	3,97	4,08	4,75	4,87
4,35 to 4,59	3,929 to 4,149	3,89 to 4,07	3,98 to 4,20	4,62 to 4,89	4,73 to 5,02
599	599	599	599	599	599
0,96	0,95	0,96	0,95	0,95	0,95
110,8	93,74	95,54	104,5	100,5	100,7
109,6 to 112,0	93,35 to 94,14	95,31 to 95,77	104,2 to 104,9	99,93 to 101,0	99,94 to 101,6
31,33	28,28	23,49	27,63	25,73	27,11
10,92	7,86	6,37	7,75	9,61	11,39
10,47 to 11,41	7,71 to 8,03	6,29 to 6,45	7,62 to 7,89	9,41 to 9,82	11,08 to 11,72
0,94	0,5	0,37	0,5	0,58	0,66
0,90 to 0,1	0,48 to 0,53	0,35 to 0,39	0,48 to 0,53	0,55 to 0,61	0,64 to 0,70
597	597	597	597	597	597
0,9971	0,9978	0,9986	0,9984	0,9983	0,998
Slow phase	Slow phase	Slow phase	Slow phase	Slow phase	Slow phase
116,3	96,88	101,3	113,8	101,3	98,49
105,3 to 127,2	90,77 to 103,0	90,18 to 112,4	99,85 to 127,8	90,96 to 111,6	88,39 to 108,6
11,02	8,28	7,71	9,32	8,67	9,38
8,68 to 13,36	7,20 to 9,36	5,77 to 9,66	7,15 to 11,49	6,95 to 10,38	7,42 to 11,34

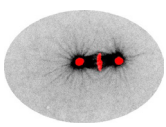

6

Optogenetic dissection of mitotic spindle positioning in vivo

Lars-Eric Fielmich*[1], Ruben Schmidt*[1,2], Daniel J. Dickinson[3,4], Bob Goldstein[3], Anna Akhmanova[2] and Sander van den Heuvel[1]*

* Equal contribution

[1]Developmental Biology, Department of Biology, Faculty of Sciences, Utrecht University, Padualaan 8, 3584 CH, Utrecht, The Netherlands.

[2] Cell Biology, Department of Biology, Faculty of Sciences, Utrecht University, Padualaan 8, 3584 CH, Utrecht, The Netherlands.

[3] Department of Biology and Lineberger Comprehensive Cancer Center, University of North Carolina at Chapel Hill, Chapel Hill, NC, 27599, USA

[4] Current address: Department of Molecular Biosciences, University of Texas at Austin, Austin, TX, USA

Manuscript under revision for publication

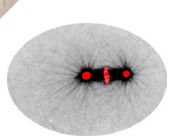

Abstract

The position of the mitotic spindle determines the plane of cell cleavage, and thereby daughter cell location, size, and content. Spindle positioning is driven by dynein-mediated pulling forces exerted on astral microtubules, which requires an evolutionarily conserved complex of Gα·GDP, GPR-1/2$^{Pins/LGN}$, and LIN-5$^{Mud/NuMA}$ proteins. To examine individual functions of the complex components, we developed a genetic strategy for light-controlled localization of endogenous proteins in *C. elegans* embryos. By replacing Gα and GPR-1/2 with a light-inducible membrane anchor, we demonstrate that Gα·GDP, Gα·GTP, and GPR-1/2 are not required for pulling-force generation. In the absence of Gα and GPR-1/2, cortical recruitment of LIN-5, but not dynein itself, induced high pulling forces. The light-controlled localization of LIN-5 overruled normal cell-cycle and polarity regulation and provided experimental control over the spindle and cell-cleavage plane. Our results define Gα·GDP–GPR-1/2$^{Pins/LGN}$ as a regulatable membrane anchor, and LIN-5$^{Mud/NuMA}$ as a potent activator of dynein-dependent spindle-positioning forces.

Introduction

Animal cells control the position of the spindle to determine the plane of cell cleavage. Regulated spindle positioning is therefore critical for asymmetric cell division and tissue formation (Pietro et al., 2016). Early work in *C. elegans* demonstrated that cortical pulling forces position the spindle through a protein complex that consists of a heterotrimeric G protein alpha subunit, GOA-1^{Gαo} or GPA-16^{Gαi} (together referred to as Gα), the TPR-GoLoco domain protein GPR-1/2, and the coiled-coil protein LIN-5 (Colombo et al., 2003; Gotta and Ahringer, 2001; Gotta et al., 2003; Grill et al., 2001; Lorson et al., 2000; Miller and Rand, 2000; Srinivasan et al., 2003). This complex, and the closely related *Drosophila* $Gα_{i/o}$–Pins–Mud and mammalian $Gα_{i/o}$–LGN–NuMA, recruits the microtubule motor dynein to the cell cortex (Bellaïche et al., 2001; Bowman et al., 2006; Du and Macara, 2004; Du et al., 2001; Izumi et al., 2004; Nguyen-Ngoc et al., 2007; Schaefer et al., 2001; Zheng et al., 2010; Zhu et al., 2011) (Fig. 1a). While regulation at the level of individual components has been described, it remains unclear whether these proteins only form a physical anchor for dynein, or whether individual subunits contribute additional functions in spindle positioning.

As a potential additional function, force generation may require a dynein adaptor that activates dynein motility. Such an adaptor is necessary for the processive movement of mammalian cytoplasmic dynein during cargo transport along microtubules (Reck-Peterson et al., 2018). This process differs substantially from dynein-dependent cortical pulling, in which force is generated by shrinking microtubules (Laan et al., 2012). Without adaptor, surface-anchored yeast dynein in contact with depolymerizing microtubules generates pulling forces *in vitro* (Laan et al., 2012). However, yeast dynein moves processively on its own (Reck-Peterson et al., 2006). Hence, it remains unknown whether pulling force generation in animal cells depends just on anchoring of dynein, or whether this requires an additional dynein activator.

The role of $Gα_{i/o}$ subunits in pulling force generation has also remained ambiguous (Fig. 1a). Membrane-attached Gα·GDP associates with GoLoco motifs present in the homologous GPR-1/2, Pins, and LGN proteins (Kimple et al., 2002; Schaefer et al., 2001). This preference for the GDP-bound 'inactive' Gα state explains why RGS-7, a putative GTPase activating protein (GAP), promotes spindle positioning (Hess et al., 2004). However, the role of another conserved regulator of Gα signaling, RIC-8, remains poorly understood (Afshar et al., 2004; Miller and Rand, 2000; Tall et al., 2003). RIC-8 was shown to act as a guanine nucleotide exchange factor (GEF) *in vitro*, while it may function *in vivo* as a Gα chaperone or as both a GEF and chaperone. In addition to RIC-8, G-protein coupled receptors and $Gα_o$·GTP signaling contribute to spindle

positioning in *Drosophila* neuroblasts and sensory organ precursor cells. Therefore, it has been proposed that the Gα·GTP-binding and hydrolysis cycle forms a critical step in cortical pulling force generation (Afshar et al., 2004; Srinivasan et al., 2003; Yoshiura et al., 2012). However, it is difficult to distinguish whether $G\alpha_o$·GTP contributes to force generation, or more indirectly relays cell-cell signaling to the spindle.

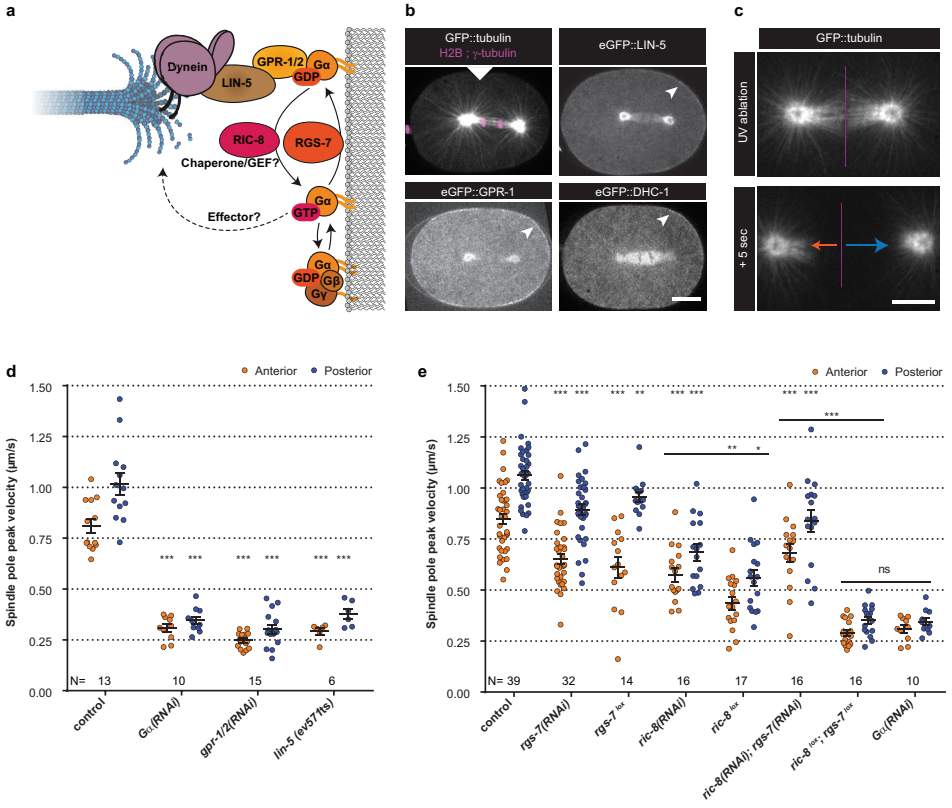

Figure 1 Gα regulation by RIC-8 and RGS-7 is essential for cortical pulling force generation. **(a)** Cartoon model representing mechanisms and functions discussed in the text. Gα·GDP–GPR-1/2–LIN-5–dynein anchors dynamic microtubule plus-ends and generates cortical pulling forces on the mitotic spindle. Gα·GDP can assemble a Gαβγ or Gα–GPR-1/2–LIN-5 trimer. Gα·GDP/GTP nucleotide state is regulated by the GAP RGS-7. For RIC-8, functions as Gα GEF and chaperone are reported. Gα·GTP could promote spindle positioning through unknown downstream effectors. **(b)** Spinning disk confocal images of anaphase spindle positioning away from the cell center (white triangle) in the *C. elegans* zygote. The upper left panel shows the spindle with labeled tubulin and DNA. Other panels: endogenous GPR-1, LIN-5, and dynein (DHC-1) fused to eGFP are present in the cytoplasm, at the cortex (arrowheads), and spindle structures. Scale bar: 10 µm. **(c)** Spinning disk confocal images of the mitotic spindle (marked by GFP::tubulin). Upon UV-laser ablation of the spindle midzone (violet line), spindle poles separate with velocities that represent the respective net force acting on each pole (arrows). Scale bar: 5 µm. **(d)** Spindle pole peak velocities after midzone ablation. Control is *gfp::tubulin* strain. Other conditions: inactivation of Gα, GPR-1/2, and LIN-5. Error bars: s.e.m. Welch's Student's t-test; *** $P < 0.001$. **(e)** Spindle severing experiments in embryos where RIC-8 and RGS-7 were depleted by RNAi or induced tissue specific Cre-lox-mediated knockout of the endogenous gene (lox). Control is *gfp::tubulin* strain, see Supplementary Fig. 1 for knockout method and additional controls. Error bars: s.e.m. Welch's Student's t-test and Mann Whitney U test; * $P < 0.05$, ** $P < 0.01$, *** $P < 0.001$. See Supplementary Table 1 for detailed genotypes. Anterior is to the left in microscopy images.

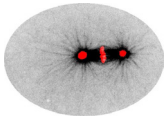

Here, we describe an optogenetic strategy for the systematic examination of individual contributions of cortical pulling force components in vivo. We use the *C. elegans* one-cell embryo (P0), which undergoes reproducible spindle positioning and asymmetric cell division in the absence of cell-cell signaling (Supplementary Video 1) (Rose and Gönczy, 2014). As an initial hurdle, modifying endogenous genes with tunable light-inducible protein-protein interaction tags (TULIPs) induced strong germline silencing. We developed a strategy to promote expression of foreign sequences in the *C. elegans* germline, which is based in part on a new codon usage adaptation method (GLO, GermLine Optimized). This allowed the light-controlled localization of endogenous proteins through ePDZ–LOV domain interactions in the early *C. elegans* embryo. Our results show that Gα·GDP and GPR-1/2 can be replaced with a light-inducible membrane anchor, while LIN-5 is required as activator of dynein-dependent cortical pulling force generation. Local light-controlled LIN-5 recruitment enabled us to manipulate the spindle position and orientation, and thereby the outcome of divisions in the early embryo.

Results

We set out to systematically investigate the individual roles of the proteins involved in cortical pulling force generation. Our previous studies and CRISPR/Cas9-assisted endogenous tagging demonstrated that cytoplasmic dynein and the Gα–GPR-1/2–LIN-5 complex overlap and function together in pulling force generation at the cell cortex of *C. elegans* early blastomeres (Fig. 1b) (Schmidt et al., 2017; van der Voet et al., 2009). As a read-out for pulling forces, we measured spindle pole peak velocities after UV-laser ablation of the spindle midzone (Grill et al., 2001) (Fig. 1c and Supplementary Video 2). Interfering with Gα, GPR-1/2, or LIN-5 function abolished significant force generation, as previously reported (Fig. 1d). RNA interference (RNAi) of *ric-8* or *rgs-7* by dsRNA injection resulted in partial loss of pulling forces (Fig. 1e). Double *ric-8(RNAi); rgs-7(RNAi)* did not further decrease pulling forces as might be expected when RIC-8 and RGS-7 both promote a critical GTPase cycle (Hess et al., 2004; Srinivasan et al., 2003). However, RNAi of *ric-8* and *rgs-7* is known to cause incomplete gene inactivation, which could also explain the limited defects. We generated germline-inducible knock-out alleles to circumvent this caveat. We inserted *lox* sites in the endogenous *ric-8* and *rgs-7* loci by CRISPR/Cas9-assisted recombineering (Fig. S1a), and expressed the CRE recombinase specifically in the germline (Dickinson et al., 2013)(Fig. S1b). Compared to the control without CRE activity, knockout embryos showed reduced spindle pole peak velocities *(ric-8*^{lox}: anterior -50% and posterior -48%; *rgs-7*^{lox}: anterior -29% and posterior -11%), similar to or more defective than the corresponding RNAi embryos (Fig. 1e, Fig. S1c, d, e). Importantly, the double knock-out of *ric-8*^{lox}*; rgs-7*^{lox} showed much reduced spindle pole movements (anterior -68% and posterior -67 %), thereby resembling *Gα(RNAi)* (Fig. 1e). This indicates that RIC-8 and RGS-7 act independently, or partly redundant, as positive regulators of Gα.

To gain further insight into the individual functions of cortical pulling force regulators, we sought to obtain spatiotemporal control of protein localization. To this end, we explored implementing the ePDZ–LOV system, which makes use of exposure to blue light to control protein heterodimerization (Harterink et al., 2016; Strickland et al., 2012). As introduction of *epdz*, *lov*, and *cre* sequences induced strong germline silencing responses, we developed a computational approach to design protein-coding sequences that are resistant to silencing in the germline. Our design algorithm assembles a coding sequence for any desired polypeptide from a list of 12-nucleotide words found in native germline-expressed genes (Fig. S2a). We hypothesized that transgenes designed in this way would mimic native genes and thereby evade the germline silencing machinery. Indeed, using this approach, we could obtain robust expression of

several foreign transgenes that were otherwise silenced (Fig. S2b, c). Although some of these transgenes were stably expressed for many generations, others showed gradual silencing when passaging strains in culture (Fig. S2d); therefore, as a further buffer against silencing, we combined our germline-optimized exons with poly-AT-cluster rich intron sequences, which were recently demonstrated to protect against germline silencing (Frøkjær-jensen et al., 2016; Zhang et al., 2018). This combined approach resulted in stable germline expression of transgenes and enabled implementation of the ePDZ–LOV system for use in the *C. elegans* early embryo.

To characterize the ePDZ–LOV system, we created a strain with a membrane-bound LOV2 domain, expressed as a pleckstrin-homology domain (PH)–eGFP protein fusion (PH::LOV), together with cytosolic ePDZ::mCherry (Fig. 2a). Illumination with a blue (491 nm) laser rapidly induced recruitment of ePDZ::mCherry to PH::LOV, and allowed both global and local cortical enrichment in one-cell embryos (Fig. 2b and Supplementary Videos 3-5). Because GFP is also excited with blue light, experiments that involve GFP imaging imply global and continuous induction of the ePDZ–LOV interaction. To test the reversibility of the ePDZ–LOV interaction, we followed ePDZ::mCherry membrane localization after a global activation pulse, and found dissociation kinetics similar to those reported by others (Hallett et al., 2016) (t ½ = 42 s; Fig. 2c and Supplementary Video 6). Thus, we conclude that the ePDZ—LOV system is suitable for controlled protein localization in the early *C. elegans* embryo.

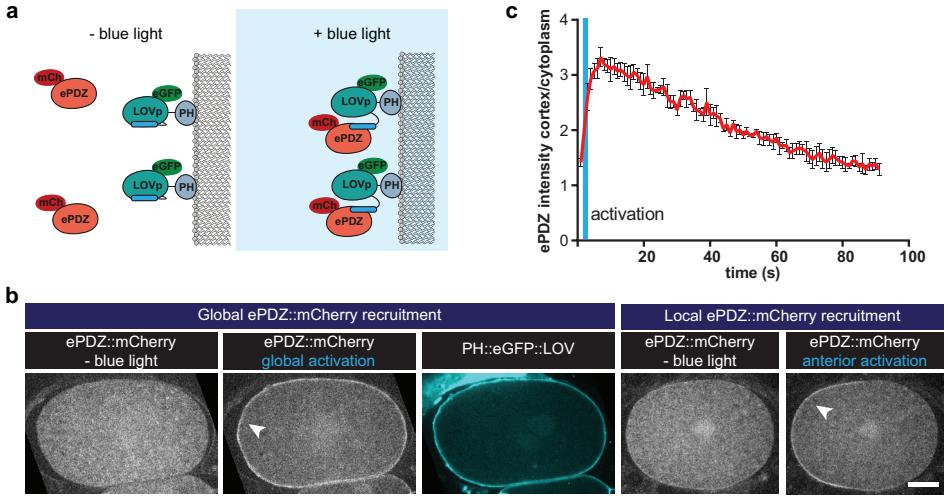

Figure 2 Optimized ePDZ–LOV enables light-inducible control of endogenous protein localization in the *C. elegans* one-cell embryo. **(a)** Cartoon model illustrating the proof of concept wherein cytosolic ePDZ::mCherry is cortically recruited to membrane PH::LOV upon activation with blue light. Blue fields indicate conditions in which an ePDZ- and LOV component are present, and an ePDZ–LOV interaction is induced using blue light. **(b)** Spinning disk confocal images showing light-controlled localization of proteins in the *C. elegans* zygote (arrowheads). Also see Supplementary Movies 3-5. Scale bar: 10 µm. Anterior is to the left in microscopy images. **(c)** Quantification of cortical ePDZ::mCherry enrichment measured over time after a 1 second pulse activation (blue vertical line). Error bars: s.e.m. tP^1P/R_2R calculated with single component non-linear regression.

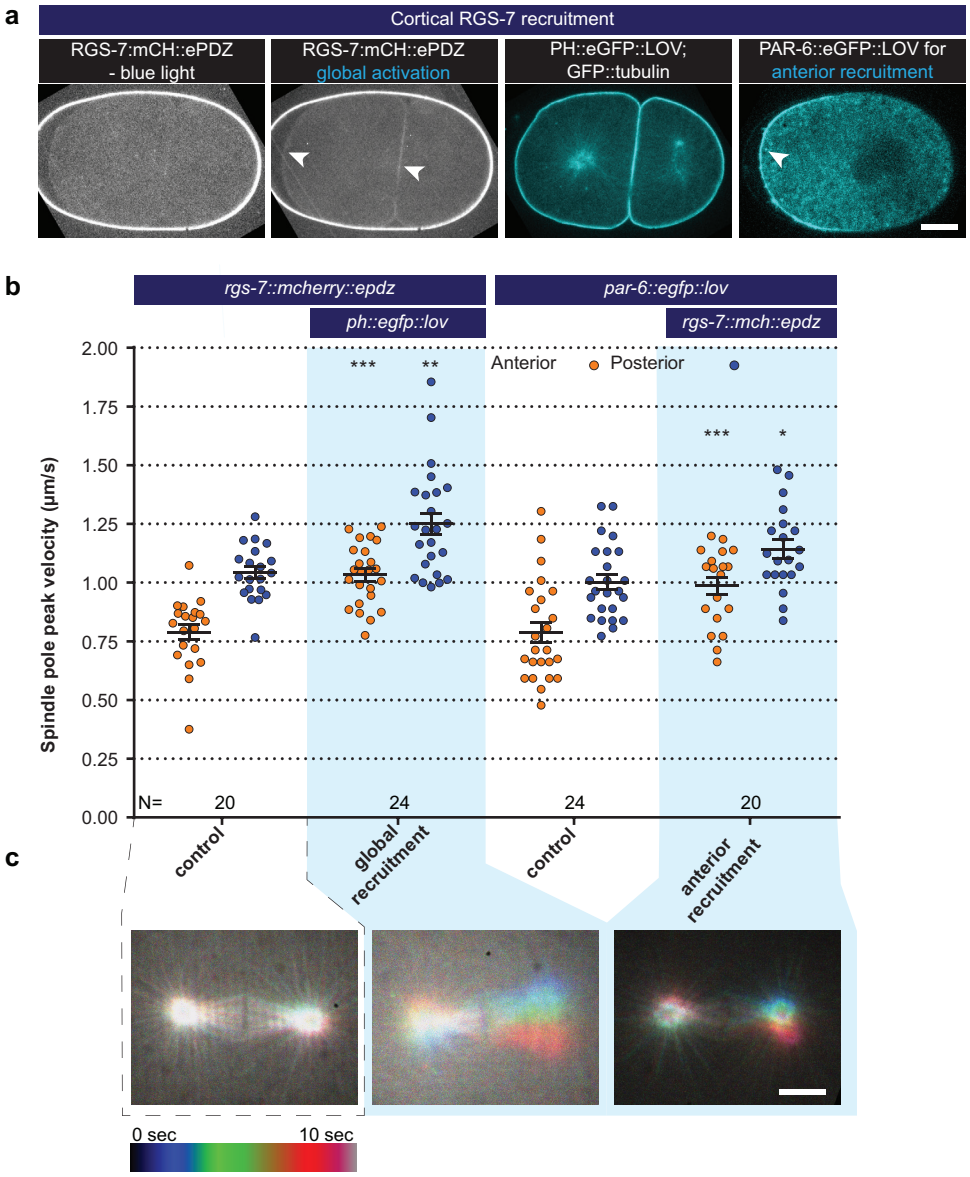

Figure 3 Light-controlled localization of endogenous Gα regulator RGS-7 in the *C. elegans* embryo. **(a)** Light-controlled localization of endogenous RGS-7 to membrane PH::LOV (arrowheads, note that the eggshell shows strong autofluorescence in the red channel). Most right panel: anterior localization of PAR-6::eGFP::LOV. Scale bar: 10 µm **(b)** Spindle severing experiments after light-induced cortical localization of RGS-7 (blue fields). Controls are *rgs-7::mcherry::epdz* and *par-6::egfp::lov* strains. Experimental conditions: combination with *ph::egfp::lov* and *rgs-7::mcherry::epdz*. Blue fields indicate conditions in which an ePDZ- and LOV component are present, and an ePDZ–LOV interaction is induced using blue light. Blue light activation was global and continuous. Error bars: s.e.m. Welch's Student's *t-test*; * $P < 0.05$, ** $P < 0.01$, *** $P < 0.001$. **(c)** Maximum projections of spindle movements for 10 seconds using a temporal color coding scheme to visualize spindle movement. A stationary spindle produces a white maximum projection, whereas a mobile spindle leaves a colored trace. Scale bar: 5 µm.

Next, we examined whether membrane recruitment of RGS-7 and RIC-8 promotes pulling forces. Regulation of the Gα·GDP/GTP cycle normally takes place at the cell membrane, while chaperoning of Gα folding and trafficking is expected to occur in the cytosol and at endomembranes (Gabay et al., 2011). We created strains expressing endogenous RIC-8 and RGS-7 as ePDZ::mCherry protein fusions. When combined with PH::LOV, this resulted in light-inducible membrane recruitment of RIC-8 and RGS-7 (Fig. 3a, 4a, and Supplementary Video 7). Cortical enrichment of RGS-7 enhanced spindle pole movements (anterior +25% and posterior +20%) (Fig. 3b) and spindle oscillations (Fig. 3c). The RGS-7::ePDZ signal was too subtle to reliably control its local recruitment. As an alternative strategy, we fused eGFP::LOV to endogenous PAR-6, which localizes to the anterior cortex of the zygote (Fig. 3a). Following global light exposure, recruitment of RGS-7::ePDZ to PAR-6::LOV enhanced the peak velocities of both spindle poles, but most significantly the movement of the anterior pole (anterior +25% and posterior +14%; Fig. 3b, c). Thus, cortical recruitment of RGS-7 acutely increases pulling forces, in agreement with its proposed function as a GAP that promotes Gα·GDP–GPR-1/2 interaction. In contrast, cortical enrichment of RIC-8 did not significantly enhance pulling forces (Fig. 4b). Thus, in agreement with the *ric-8*^{lox}*; rgs-7*^{lox} synergistic phenotype, our optogenetic localization experiments support a model in which RIC-8 and RGS-7 promote Gα function at different levels. While RGS-7 probably functions as a GAP, our data are in line with RIC-8 acting in vivo as a Gα chaperone, rather than a GEF, thus indirectly promoting force generation.

To directly address whether Gα·GTP might contribute to spindle positioning or if Gα·GDP serves merely as a membrane anchor, we aimed to reconstruct a cortical force generator in the absence of Gα (Fig. 5a). We obtained optogenetic control over the membrane localization of GPR-1 by combining endogenously labeled *epdz::mcherry::gpr-1* (ePDZ::GPR-1) with knockout of *gpr-2*, expression of PH::LOV and Gα RNAi (Fig. 5b, c and Supplementary Video 8, 9). Live imaging and immunohistochemistry confirmed light-induced cortical recruitment of ePDZ::GPR-1 and consequently LIN-5 (Fig. 5b, Fig. S3a). Spindle movements appeared reduced following the tagging of *gpr-1* and knockout of *gpr-2* (anterior -40% and posterior -26%) (Fig. S3b). However, light-induced ePDZ::GPR-1 recruitment increased spindle pole movements (anterior +56% and posterior +10%) (Fig. 5d, f). Moreover, membrane-localized ePDZ::GPR-1 sustained force generation in the absence of Gα (anterior +195% and posterior +232%), indicating that Gα is dispensable for cortical pulling force generation. Recruitment of ePDZ::GPR-1 restored spindle pole movements to a similar degree in *Gα(RNAi)* and *Gα(RNAi); ric-8(RNAi)* embryos (Fig. 5d). Thus, cortical pulling forces can be generated when Gα membrane anchor function is replaced by PH::LOV, and most likely in the absence of $G\alpha_{i/o}$·GTP. We conclude that Gα functions as a membrane anchor and that Gα·GTP does not perform an essential function in pulling force generation.

Light-controlled heterodimerization exhibits a certain level of dark state activity (Hallett et al., 2016). We performed spindle severing experiments in the absence of blue light to confirm the light-specificity of recruitment. Replacement of *gfp::tubulin* with an *mcherry::tubulin* transgene allowed for tracking of the spindle in the absence of blue light and consequently LOV activation. We observed that the scattering of UV-light (355 nm) during midzone ablation also uncages the LOV domain. Nevertheless, the presence of blue light resulted in substantially elevated spindle pulling forces when compared to dark state experiments (anterior +33% and posterior +35%) (Fig. 5e). We conclude that the observed spindle pole movements are light-dependent and the specific result of inducible cortical recruitment of GPR-1.

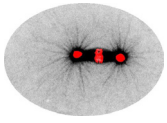

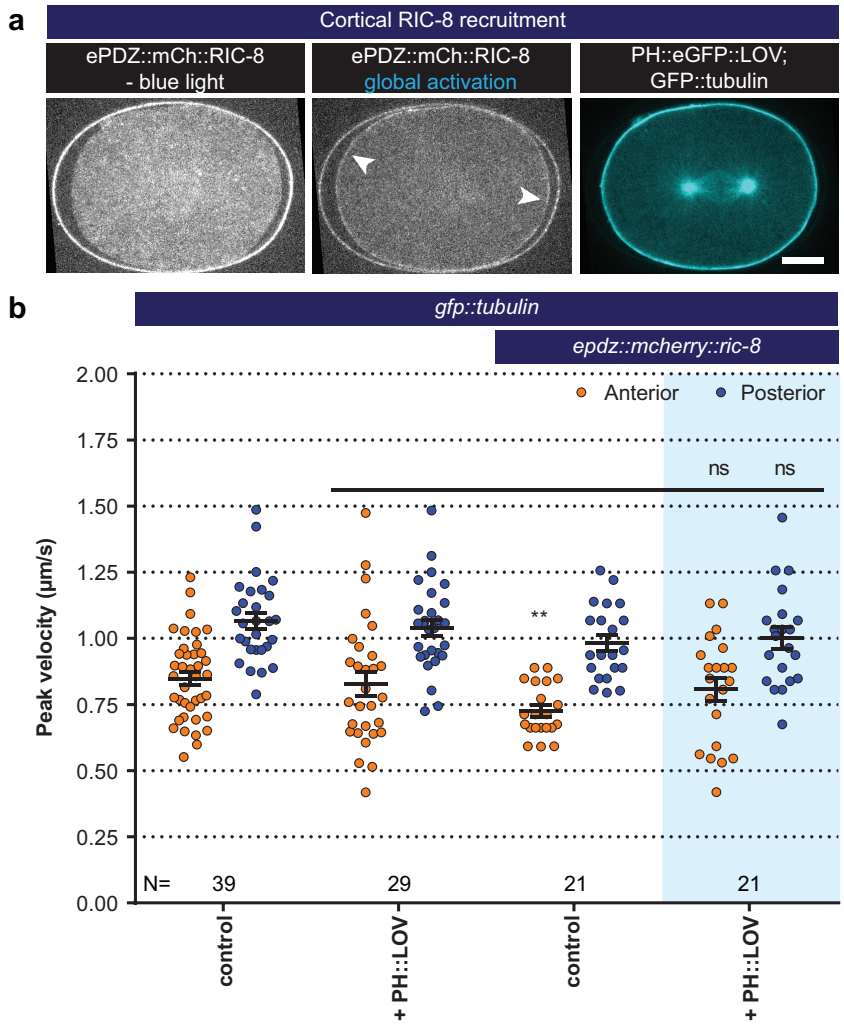

Figure 4 Light-controlled localization of endogenous Gα regulator RIC08 in the *C. elegans* embryo. **(a)** Light-controlled localization of endogenous RIC-8 to membrane PH::eGFP::LOV (arrowheads, note that the eggshell shows strong autofluorescence in the red channel). Scale bar: 10 µm **(b)** Spindle severing experiments after light-induced cortical localization of RIC-8 (blue fields). Controls are *gfp::tubulin* and *epdz::mcherry::ric-8* strains. Experimental conditions: combination with *ph::egfp::lov*. Blue fields indicate conditions in which an ePDZ- and LOV component are present, and an ePDZ–LOV interaction is induced using blue light. Error bars: s.e.m. Welch's Student's t-test; ns $P > 0.05$. See Supplementary Table 1 for detailed genotypes. Anterior is to the left in microscopy images.

Considering that spindle poles moved in three dimensions after recruitment of GPR-1, measuring peak velocities after midzone severing by tracking the poles in two dimensions likely underestimated the resulting pulling forces. Therefore, we utilized an additional read-out of cortical pulling forces. Cortical pulling events cause invaginations of the plasma membrane, which are visible as dots in the sub-cortical plane (Redemann et al., 2010) (Fig. 5g and Supplementary Video 10, 11). Control PH::LOV embryos showed on average 138 membrane invaginations during anaphase in an area covering approximately $^{1}/_{3}$ of the cell surface (Fig. S3d). When plotted along the anterior-posterior axis, the distribution of these invaginations reflected the three described cortical domains: anterior, posterior, and a posterior lateral LET-99 region at ±60% embryo length(Rose and Gönczy, 2014) (Fig. 5h). In this cortical domain, LET-99 antagonizes GPR-1/2 localization and thereby pulling force generation (Krueger et al., 2010). Cortical GPR-1 recruitment resulted in a total number of 174 (+25% compared to *ph::lov* control) invaginations in the presence and 122 (+249% compared to *Gα(RNAi)* invaginations in the absence of Gα (Fig. S3c, d). Interestingly, the absence of invaginations around 60% embryo length was lost following ePDZ::GPR-1 anchoring by PH::LOV. Instead, we observed a milder dip at 50% embryo length. The remaining peaks likely represent the cortical regions closest to the spindle poles, as these sites contact the highest numbers of astral microtubules. Taken together, Gα is not essential for force generation, but the characteristic distribution of force generating events is likely regulated in part at the Gα level.

Gα–GPR-1/2–LIN-5 has been suggested to function as a dynein anchor, but this has not been tested directly (Kotak et al., 2012; Pietro et al., 2016). Our optogenetic approach allows replacing the entire complex by PH::LOV, and examining whether the complex strictly acts as an anchor, or whether individual components have additional functions (Fig. 6a). To directly recruit dynein to the cortex, we generated an *epdz::mcherry* knock-in allele of *dhc-1* (dynein heavy chain). While homozygous *epdz::mcherry::dhc-1* (ePDZ::DHC-1) was viable, its combination with *ph::egfp::lov* was lethal. This effect was also observed for an ePDZ::GFP fusion of DHC-1 in the presence of PH::LOV, but not in the absence of PH::LOV or for mCherry::DHC-1 without the ePDZ domain. Therefore, we attributed the lethality to ePDZ–LOV dark state interactions that disturb essential dynein functions. We circumvented this effect by using *epdz::mcherry::dhc-1* in combination with a wild-type allele (*epdz::mcherry::dhc-1/+*) to control dynein localization (Fig. 6b, c and Supplementary Video 12, 13). We found that induced ePDZ::DHC-1 cortical recruitment in the presence of the wild type complex slightly (but not significantly) increased spindle pole movements (anterior +10% and posterior +5%, 162 membrane invaginations: +17%; Fig. 6d-f). Notably, cortical ePDZ::DHC-1 recruitment in the absence of a wild type complex (*gpr-1/2(RNAi)* or *Gα(RNAi)*) did not result in substantial pulling force generation or spindle movements (Fig. 6e, Fig. S4b, c). Because direct cortical dynein anchoring does not support force generation, it is likely that the LIN-5 complex performs essential functions beyond providing a structural dynein anchor.

In vitro reconstitution studies established that homodimerizing adapters containing extended coiled-coil domains are critical for dynein activity (McKenney et al., 2014; Schlager et al., 2014). LIN-5 and its homologs NuMA and Mud are predicted to contain a long coiled-coil domain, to homodimerize, and to interact with dynein (Kotak et al., 2012; Lorson et al., 2000; Merdes et al., 1996). To investigate if LIN-5 can activate dynein-dependent force generation, we recruited endogenous LIN-5 to the cortex (Fig. 7a-c and Supplementary Video 14, 15). Spindle severing experiments and invagination counting revealed that cortical LIN-5 recruitment greatly increased spindle pulling forces in otherwise wild type embryos (anterior +131% and posterior +68%, 557 invaginations: +303%) (Fig. 7d, e and Fig. S5b-d). *gpr-1/2(RNAi)* embryos also showed strong dynein-dependent forces after cortical recruitment of LIN-5 (anterior +183% and posterior +244%, 429 invaginations: +1488%). In fact, cortical LIN-5 recruitment generated extreme premature pulling forces (Supplementary Video 16) that could result in separation of centrosomes and their associated pronuclei even before formation of a bipolar spindle

(Supplementary Video 17). Therefore, embryos were kept in the absence of blue light until mitotic metaphase. Subsequent blue light exposure induced cortical LIN-5 recruitment within seconds, and the spindles showed excessive movements in all three dimensions well before cortical LIN-5 reached peak levels (Fig. 7c, e). Therefore, the number of membrane invaginations in anaphase probably reflects the pulling forces more accurately than the average peak velocities of the poles (Fig. 7f and Fig. S5b, c). These results identify LIN-5 as a strong activator of dynein in the generation of cortical pulling forces.

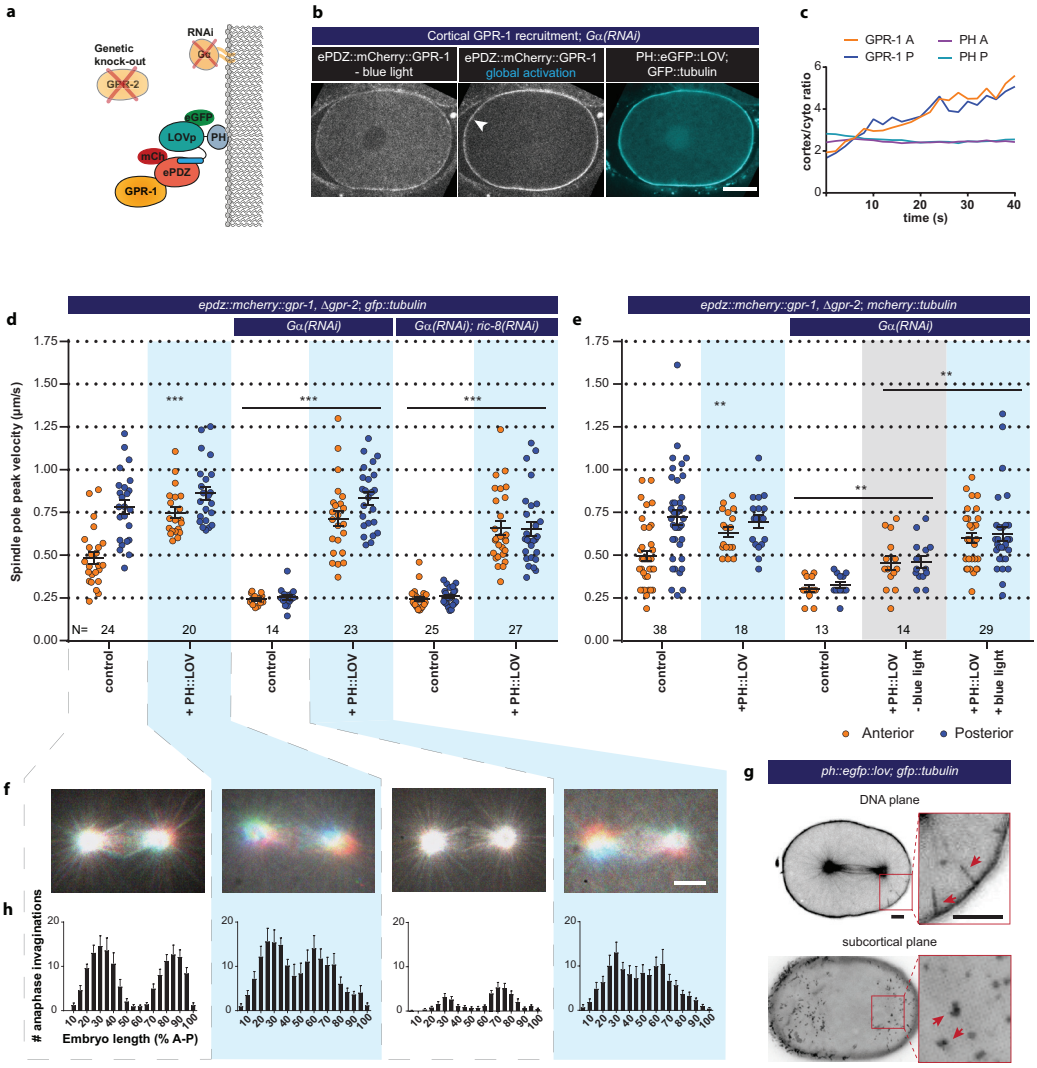

Next, we examined whether we could deploy cortical LIN-5 to manipulate the spindle position and outcome of cell division by local illumination with blue light. In the normal P0 cell, the spindle becomes positioned posteriorly and cell cleavage creates a larger anterior blastomere (AB) and smaller posterior blastomere (P1). Local recruitment of LIN-5 to the anterior cortex caused the P0 spindle to position anteriorly and inverted the AB:P1 asymmetry (Fig. 8a and Supplementary Video 18). In addition, recruiting LIN-5 laterally induced a completely perpendicular spindle position (Fig. 8b and Supplementary Video 19). While this triggered some furrowing at the anterior and posterior cell poles, the spindle switched back to an anterior-posterior orientation during cytokinesis, possibly resulting from geometric constraints. We therefore switched to two-cell embryos with the relatively round AB and P1 blastomeres. In two-cell *gpr-1/2(RNAi)* embryos, the spindle fails to rotate in P1, resulting in a transverse spindle orientation in both blastomeres (Srinivasan et al., 2003). Importantly, local recruitment of LIN-5 to the membranes between AB and P1 promoted anterior-posterior spindle orientations in both blastomeres of *gpr-1/2(RNAi)* embryos (Fig. 8c and Supplementary Video 20, 21). These spindles maintained their anterior-posterior orientation throughout mitosis and induced cleavage furrows that reproducibly followed the spindle positions. These experiments underline the determining role of LIN-5-dependent cortical pulling in spindle orientation and cell cleavage determination.

Our observations fit with and expand on conclusions from studies of LIN-5-related Mud and NuMA, which when tethered to the cortex contributes to spindle positioning (Kotak et al., 2012; Ségalen et al., 2010). Notably, these previous studies considered NuMA to be just a dynein anchor, and were performed in cells that express Gα, GPR-related Pins and LGN, and presumably RIC-8A proteins. We observed similarly high pulling forces upon cortical LIN-5 recruitment in *gpr-1/2(RNAi)* and *Gα(RNAi)* embryos (Fig. S5c, d). Thus, Gα and GPR-1/2 are not per se required for force generation. In addition, we observed that cortical recruitment of LIN-5 localized dynein and vice versa (Fig. S4a, S5a). However, only LIN-5-mediated cortical anchoring of dynein through LIN-5 resulted in pulling forces. Thus, membrane attachment of LIN-5 appears both essential and sufficient for dynein-dependent cortical pulling force generation.

Figure 5 Light-inducible GPR-1 recruitment to the cortex rescues pulling force generation in the absence of Gα. **(a)** Cartoon model illustrating the experiment that localizes GPR-1 directly to the membrane, bypassing the wild type membrane anchor Gα which is inactivated by RNAi. **(b)** Spinning disk confocal images of light-controlled cortical GPR-1 recruitment independent of the wild type anchor Gα (arrowheads; note the auto fluorescent eggshell in the mCherry channel). Scale bar: 10 µm. **(c)** Quantification of cortical GPR-1 recruitment during continuous activation of the ePDZ–LOV interaction, represented as the ratio of cortical/cytoplasmic signal. Also see Supplementary Movie 8, 9. **(d)** Spindle severing experiments in combination with cortical recruitment of endogenous GPR-1. Control is *epdz::mch::gpr-1, Δgpr-2; gfp::tubulin* strains. Experimental conditions: combinations with *ph::egfp::lov*, *Gα(RNAi)*, and Gα(RNAi); *ric-8(RNAi)*. Blue fields indicate conditions in which an ePDZ- and LOV component are present, and an ePDZ–LOV interaction is induced using blue light. Blue light activation was global and continuous. Error bars: s.e.m. Welch's Student's *t-test* and Mann Whitney U test; ** $P < 0.01$, *** $P < 0.001$. **(e)** Spindle severing experiments in combination with cortical recruitment of endogenous GPR-1. Control is *epdz::mch::gpr-1, Δgpr-2; mcherry::tubulin* strains. Experimental conditions: combinations with *ph::egfp::lov, Gα(RNAi)*, and the absence of blue light (grey field). Blue fields indicate conditions in which an ePDZ- and LOV component are present, and an ePDZ–LOV interaction is induced using blue light. Blue light activation was global and continuous. Error bars: s.e.m. Welch's Student's *t-test* and Mann Whitney U test; ** $P < 0.01$, *** $P < 0.001$. **(f)** Maximum projections of spindle movements for 10 seconds using a temporal color coding scheme to visualize spindle movement as in Fig. 3c. **(g)** Plasma membrane invaginations as result of cortical pulling forces are visible as lines in the DNA plane and dots in the subcortical plane (red arrows). Scale bar: 5 µm. (h) Distribution of anaphase membrane invaginations plotted along anterior-posterior embryo length. Conditions were the same as for the connected experiments in d and f, except for the control which was *ph::egfp::lov; gfp::tubulin* strain and not *epdz::mch::gpr-1, Δgpr-2*. Scale bar: 5 µm. Blue fields indicate conditions in which an ePDZ- and LOV component are present, and an ePDZ–LOV interaction is induced using blue light. See Supplementary Table 1 for detailed genotypes. Anterior is to the left in microscopy images.

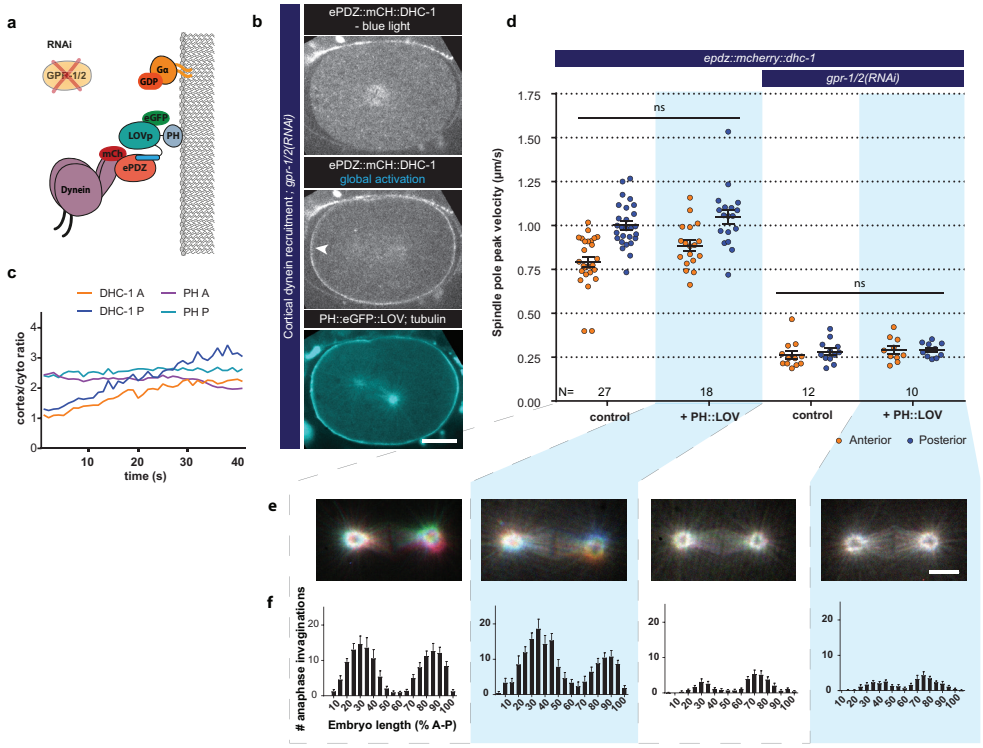

Figure 6 Direct cortical anchoring of dynein (DHC-1) is insufficient for cortical pulling force generation. **(a)** Cartoon model illustrating the experiment where dynein is recruited directly to the cortex. The wild type force generator is inactivated by RNAi. **(b)** Spinning disk confocal images showing light-controlled recruitment of dynein to the cortex (arrowheads, note the auto fluorescent eggshell in the mCherry channel). Scale bar: 10 µm. **(c)** Quantification of cortical dynein recruitment during continuous activation of PH::LOV with blue light. **(d)** Spindle severing experiments with cortical dynein recruitment. Control is *epdz::mch::dhc-1; gfp::tubulin* strain. Experimental conditions: combination with *ph::egfp::lov and gpr-1/2(RNAi)*. Blue light activation was global and continuous. Error bars: s.e.m. Welch's Student's t-test and Mann Whitney U test; ns $P > 0.05$. **(e)** Maximum projections of spindle movements for 10 seconds using a temporal color coding scheme to visualize spindle movement as in Figure 3c. Scale bar: 5 µm. **(f)** Distribution of anaphase membrane invaginations plotted along anterior-posterior embryo length. Conditions were the same as for the connected experiments in d and e, except for the control which was *ph::egfp::lov; gfp::tubulin* strain and not *epdz::mch::dhc-1*. Blue fields indicate conditions in which an ePDZ- and LOV component are present, and an ePDZ–LOV interaction is induced using blue light. See Supplementary Table 1 for detailed genotypes. Anterior is to the left in microscopy images.

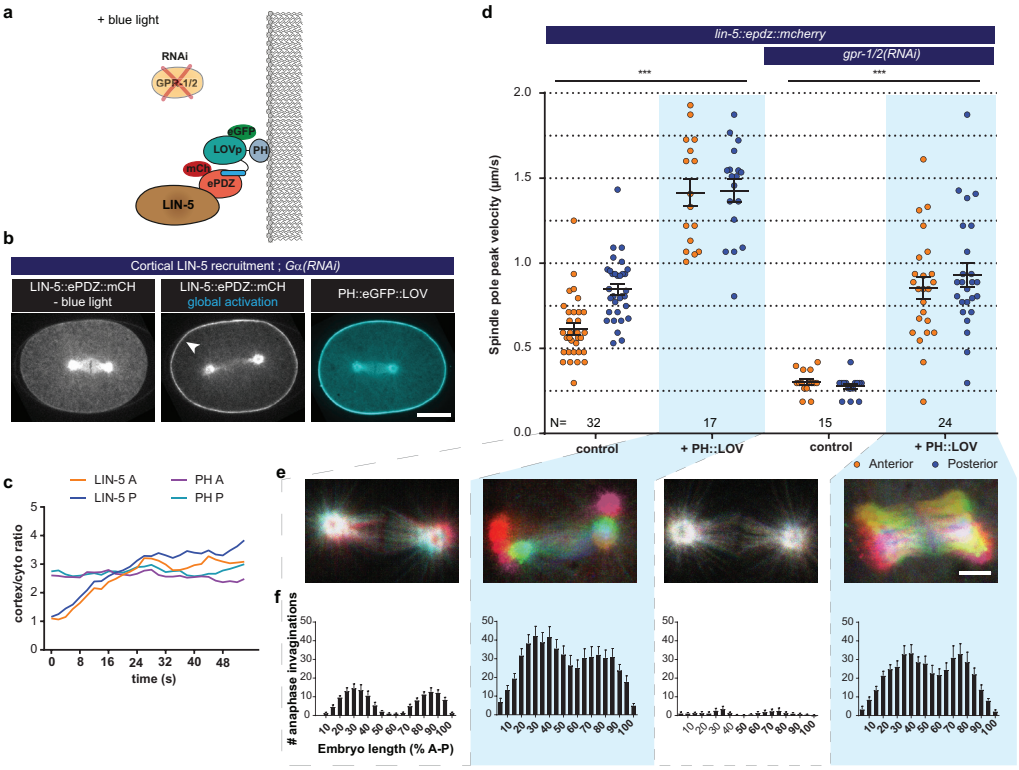

Figure 7 LIN-5 is a strong and essential activator of dynein-dependent cortical pulling forces. **(a)** Cartoon model illustrating the experiment in which LIN-5 is recruited to the cortex independently of the wild type Gα–GPR-1/2 anchor. **(b)** Spinning disk confocal images showing light-controlled recruitment of endogenous LIN-5 in the absence of Gα (arrow head). See also Supplementary Movie 14, 15. **(c)** Cortical LIN-5 recruitment during continuous activation of the ePDZ–LOV interaction, represented as the ratio of cortical/cytoplasmic signal. Scale bar: 10 µm. **(d)** Spindle severing experiments in combination with cortical recruitment of endogenous LIN-5. Control was *lin-5::epdz::mcherry; gfp::tubulin* strain. Experimental conditions: combinations with *ph::egfp::lov and gpr-1/2(RNAi).* Error bars: s.e.m. Welch's Student's t-test and Mann Whitney U test; *** $P < 0.001$. **(e)** Maximum projections of spindle movements for 10 seconds using a temporal color coding scheme to visualize spindle movement as in Fig. 3c. Scale bar: 5 µm. **(f)** Anaphase membrane invaginations plotted along anterior-posterior embryo length. Conditions were the same as for the connected experiments in d and e, except for the control which was *ph::egfp::lov; gfp::tubulin* strain and not *lin-5::epdz::mch.* Blue fields indicate conditions in which an ePDZ- and LOV component are present, and an ePDZ–LOV interaction is induced using blue light. See Supplementary Table 1 for detailed genotypes. Anterior is to the left in microscopy images.

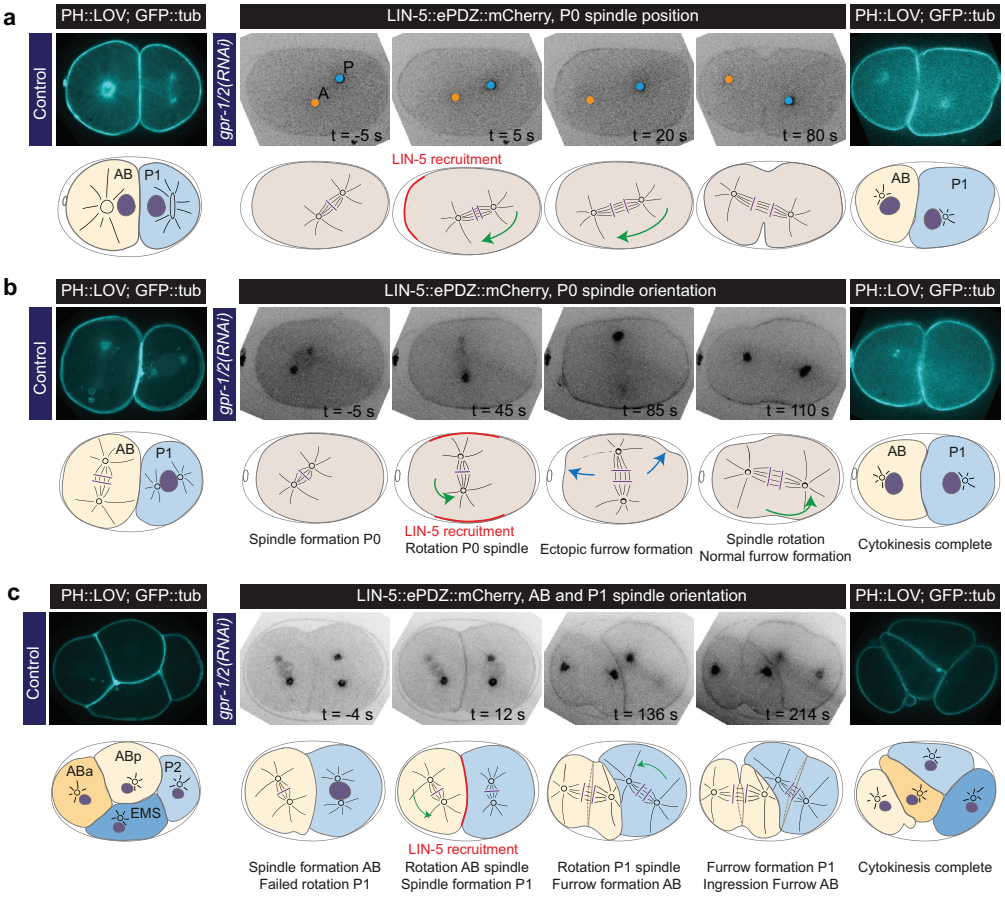

Figure 8 Experimentally induced spindle positioning by controlled localization of endogenous LIN-5. **(a)** Selected time points of Supplementary Movie 18 showing induced anterior displacement of the P0 spindle upon local cortical recruitment of LIN-5. Images are annotated with centrosome positions shown as circles (orange, anterior pole; blue, posterior pole). **(b)** Selected time points of Supplementary Movie 19 showing induced transverse P0 spindle orientation upon local cortical recruitment of LIN-5. Blue arrows, ectopic furrowing. **(c)** Selected time points of Supplementary Movie 20 showing induced AB and P1 spindle rotation upon local cortical recruitment of LIN-5. In a, b, and c panels 1-4 show LIN-5::ePDZ::mCherry fluorescence, panel 5 shows PH::LOV and GFP::tubulin. Cartoons accompanying images illustrate key events. Red, local LIN-5 recruitment. Green arrows, spindle movements. leftmost panels show control two- and four-cell embryos labeled with PH::eGFP::LOV and GFP::Tubulin. See Supplementary Table 1 for detailed genotypes. Anterior is to the left in microscopy images.

Discussion

Recent advances in CRISPR/Cas9-mediated genome engineering and optogenetics hold far-reaching potential for cell- and developmental biology (Johnson and Toettcher, 2018; Waaijers and Boxem, 2014). We combined these strategies to systematically control the localization of endogenous proteins in the *C. elegans* early embryo by light-induced ePDZ–LOV heterodimerization, to determine their individual contributions in spindle positioning. Our quantitative analyses classified LIN-5, but not Gα, RIC-8 and GPR-1/2, as essential for dynein-dependent pulling force generation. Since only LIN-5 is strictly required for cortical pulling force generation, the question arises why a tripartite dynein anchor is conserved from worm to man. In yeast, dynein is localized by the single-component cortical anchor Num1, a coiled-coil domain protein with a PH-domain for membrane localization (Ananthanarayanan, 2016). Our ectopic ePDZ–LOV heterodimerization experiments show that membrane-tethered LIN-5 could suffice as a dynein anchor and activator, and that local regulation is needed to rotate and migrate the spindle. Conceivably, the trimeric dynein anchor/adaptor evolved in metazoans to augment context-specific regulation and reduce stochastic activation of spindle pulling forces. We propose that Gα–GPR-1/2 provides a regulatable membrane anchor, while membrane-bound LIN-5 acts as an obligate adapter and activator of cytoplasmic dynein at the cell cortex, which possibly links dynein and the dynactin complex.

Which factors may normally control the Gα–GPR-1/2 membrane anchor? Our double knockout experiments and optogenetic localization studies support that RIC-8 and RGS-7 regulate Gα anchor function at different levels. RIC-8 was initially characterized as a GEF for $G\alpha_{i/o}$·GDP and Gα·GDP–LGN–NuMA (Tall and Gilman, 2005; Tall et al., 2003). To explain how a GEF could promote spindle pulling forces, it has been proposed that Gα·GDP/GTP cycling is essential for Gα·GDP–GPR-1/2 association. However, experiments in *Drosophila* and mammals suggested a Gα chaperone function for RIC-8, while observations in *C. elegans* supported dual activities as a GEF for GOA-1$^{G\alpha o}$, and a chaperone for the membrane localization of GPA-16$^{G\alpha i}$ (Afshar et al., 2004, 2005; David et al., 2005; Gabay et al., 2011; Hampoelz et al., 2005; Wang et al., 2005). We found no evidence to support direct RIC-8 function in spindle positioning in vivo and favor a model in which RIC-8 indirectly affects force generation by promoting the properly folded membrane-anchored $G\alpha_{i/o}$ conformation, possibly as chaperone. The fact that Gα can be replaced with a PH–membrane anchor dismisses a general requirement for Gα·GTP in pulling force generation. However, we noticed that Gα contributes to the normal distribution of pulling forces: direct cortical anchoring of GPR-1 or LIN-5 coincided with increased membrane invaginations in the region occupied by LET-99. This indicates that LET-99 normally antagonizes Gα·GDP availability or Gα·GDP–GPR-1/2 interaction.

Despite the observed replaceability of Gα, Gα·GTP has been reported to affect the spindle orientation in specific tissues (Katanaev et al., 2005; Schaefer et al., 2001; Yoshiura et al., 2012). In *Drosophila* neuroblasts and sensory organ precursor cells, canonical G-protein signaling probably is used to align cellular polarity with tissue polarity (Katanaev et al., 2005; Yoshiura et al., 2012).

For our in vivo dissection of spindle positioning, we developed and applied methods for germline-specific gene knockout, tagging of endogenous proteins, reliable expression of foreign sequences in the germline, and light-inducible protein heterodimerization. These methods further expand the molecular biology toolbox for in vivo studies and can be broadly applied to other biological processes. Of particular interest is the acquired possibility to experimentally control the position of the spindle, for instance for future studies aimed at deciphering how the spindle determines the plane of cell cleavage.

Materials and methods

C. elegans strains and maintenance

The names and associated genotypes of *C. elegans* strains used in this study are included in supplementary table 1. Animals were maintained at either 15 or 20 °C as described previously (Brenner, 1974). Strains expressing both ePDZ and LOV protein motifs were regarded as light-sensitive and thus cultured in the dark. Animals were kept on plates that contained nematode growth medium (NGM) that had been seeded with OP50 *Escherichia coli* bacteria.

Molecular cloning

DNA vector-based repair templates to be used for CRISPR/Cas-9-mediated genome editing were designed in A plasmid Editor (M. Wayne Davis) to include 500-1500 bp homology arms. These and all other sequences used were generated using either purified *C. elegans* genomic DNA or pre-existing vectors via PCR amplification using Q5 Hot Start High-Fidelity DNA Polymerase (New England Biolabs). A list of all cloning, repair template and genotyping primers (Integrated DNA technologies) and DNA templates used has been included in supplementary table 2. PCR fragments were gel purified (Qiagen), their concentrations measured using a BioPhotometer D30 (Eppendorf) and then ligated into pBSK by Gibson assembly (New England Biolabs). gRNA vectors were generated by annealing of antisense oligonucleotide pairs and subsequent ligation into BbsI-linearized pJJR50 or BsaI-linearized pMB70 using T4 ligase (New England Biolabs). All DNA vectors used for genome editing were transformed into DH5α competent cells and subsequently purified by midiprep (Qiagen).

Design of germline-optimized coding sequences

Custom Perl scripts were written to design germline-optimized coding sequences according to the algorithm described in the legend of Supplementary Fig. 2. After designing each coding sequence, we inserted either 1) normal synthetic introns with the sequence gtaagttt(n36)ttttcag, where n36 is a 36 bp random DNA sequence with 30% GC content; or 2) PATC introns (Frøkjær-jensen et al., 2016). Our design algorithm is accessible via a web interface at http://104.131.81.59/, and the source code can be found at https://github.com/dannyhmg/germline. Germline-optimized sequences were synthesized as gBlocks (Integrated DNA Technologies) and single-copy transgenes were generated using standard methods (Frøkjær-Jensen et al., 2012). Please refer to supplementary table 2 for detailed sequence features of each transgene.

Design of inducible germline-specific knockout

loxP and *loxN* sequences were integrated in the endogenous loci of essential genes (see CRISPR/Cas9-mediated genome editing section for details). For the FLP recombinase, the hyperactive FLP G5D variant (Schwartz and Jorgensen, 2016) was used (pMLS262; Addgene #73718). We used a long version of the *pie-1* promoter including enhancer for germline-specific expression (pAZ132, a kind gift from A. A. Hyman). To initiate the recombination cascade, the germline-specific FLP was injected in P0 mothers with the following protocol to favor germline expression (Personal communication Oliver Hobert, February 21, 2013); linearized FLP construct (2 ng/µl), PvuII digested *E. coli* genomic DNA (150 ng/µl), co-injection marker *Pmyo-2::tdtomato* (2 ng/µl). Transgenic F1 animals were singled and allowed to lay eggs for at least 24 hrs. From F1 with 100% embryonic lethal broods (*ric-8* and *rgs-7* are essential for embryogenesis), early embryos were isolated and used for spindle severing experiments.

CRISPR/Cas9-mediated genome editing

Either the wild type N2 or SV1818 (*pha-1*(*e2123*ts) 4x outcrossed) *C. elegans* genetic background was used for the generation of CRISPR/Cas-9 alleles. Injection mixes with a total volume of 50 µl were prepared in MilliQ HR_2RO and contained a combination of 50 ng/µl *Peft-3-p::cas9* (Addgene ID #46168 (Martin and Weiss, 2015) or 60 ng/µl pJW1285 (61252, Addgene; (Dickinson et al., 2013)), 50-100 ng/µl *u6::sgRNA* (targeting genomic sequences listed in supplementary table 2), 50 ng/µl of (PAGE-purified oligonucleotide) repair template and 2.5 ng/µl of the co-injection pharyngeal marker *myo-2p::tdtomato*, and spun down in a microcentrifuge (Eppendorf) for at least 10 minutes at 13,000 RPM prior to use. Young adult hermaphrodites were injected in the germline using an inverted micro-injection setup (Eppendorf). After injection, animals were singled and grown at 15 or 20 °C. F1 animals were then picked to a total of at least 96, and grown with two or three animals per plate for 7-8 days at 20 °C until freshly starved. Half a plate containing F2 and F3 animals was then washed off with M9 medium supplemented with 0.05% Tween-20, and subsequently lysed to extract genomic DNA. Some knock-ins were obtained using co-CRISPR selection: rescue of *pha-1*(*e2123*ts) (Ward, 2014), generation of visible *unc-22* (Kim et al., 2014) or *dpy-10* (Paix et al., 2015) phenotypes, or integration of an self-excisable cassette carrying a visible marker (Dickinson et al., 2015). Genotyping was carried out by PCR amplification with OneTaq polymerase (New England Biolabs) of genome sequences using primers annealing in the inserted sequence and a genomic region not included in the repair template. Confirmed alleles were subsequently sequenced (Macrogen Europe).

Spinning disk microscopy

Prior to live imaging, embryos were dissected from adult hermaphrodites onto coverslips (Menzel-Gläser) in 0.8x egg salts buffer (94 mM NaCl, 32 mM KCl, 2.7 mM CaCl2, 2.7 mM MgCl2, 4 mM HEPES, pH 7.5; (Tagawa et al., 2001) or M9, and mounted on 4% agarose pads. Spinning disk imaging of embryos was performed using a Nikon Eclipse Ti with Perfect Focus System, Yokogawa CSU-X1-A1 spinning disk confocal head, Plan Apo VC 60x N.A. 1.40 oil and S Fluor 100x N.A. 0.5-1.3 (at 1.3, used for UV-laser photo-ablation) objectives, Photometrics Evolve 512 EMCCD camera, DV2 two-channel beam-splitter for simultaneous dual-color imaging, Cobolt Calypso 491 nm (100 mW), Cobolt Jive 561 nm (100 mW) and Teem Photonics 355 nm Q-switched pulsed laser controlled with the ILas system (Roper Scientific France/ PICT-IBiSA, Institut Curie, used for photo-ablation), ET-GFP (49002), ET-mCherry (49008) and ET-GFPmCherry (49022) filters, ASI motorized stage MS-2000-XYZ with Piezo Top Plate, and Sutter LB10-3 filter wheel. The microscope was operated using MetaMorph 7.7 software and situated in a temperature-controlled room (20 °C). The temperature of the stage and objective was controlled at 25 °C with a Tokai Hit INUBG2E-ZILCS Stage Top Incubator during experiments. Images were acquired in either streaming mode with 250 or 500 ms exposure, or time-lapse mode with 250, 500 or 1500 ms exposure and 2 or 5 second intervals. Laser power and exposure times were kept constant within experiments. For the quantification of membrane invaginations embryos were imaged by 250 ms exposure stream acquisition starting in the DNA plane at anaphase onset, as judged by GFP::Tubulin signal. During anaphase, the spinning disk imaging plane was moved as close to the membrane as possible while keeping the cytosol discernable from the membrane signal. Acquisitions were terminated at early telophase, as judged by the PH::eGFP::LOV signal. For experiments involving balanced *epdz::mcherry::dhc-1/+*, each animal was confirmed to be positive for *epdz::mcherry::dhc-1* by fluorescence before the experiment. Images acquired by spinning disk microscopy were rotated, cropped, annotated, provided with scale bars, and processed further by linear adjustment of brightness and contrast using ImageJ and FIJI. Fluorophores used in this study include (e)GFP, mCherry, Alexa-488 and Alexa-568.

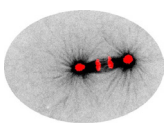

RNA-mediated interference (RNAi)

For immunohistochemistry experiments L4 hermaphrodites were grown on RNAi plates seeded with HT115 *Escherichia coli* bacteria strains generating double-stranded RNA (dsRNA) targeting genes of interest (*goa-1*, *gpa-16*, *gpr-1*) for 48 hours at 15 °C prior to fixation (Timmons and Fire, 1998). For all other gene knock-down experiments, young adult hermaphrodites were injected with dsRNA targeting genes of interest (*goa-1*, *gpa-16*, *gpr-1*, *ric-8*, *rgs-7*) and grown for 48 hours at 15 °C (Fire et al., 1998) prior to experiments. To generate dsRNA, coding regions of genes of interest were PCR amplified using Q5 Hot Start High-Fidelity DNA Polymerase (New England Biolabs). These PCR products were used as templates for *in vitro* dsRNA synthesis (MEGAscript T7 transcription kit, ThermoFisher Scientific). dsRNA was diluted 5x in DEPC HR_2RO prior to micro-injection. ORF clones from the Vidal and Ahringer RNAi libraries were used (Kamath et al., 2003; Rual et al., 2004).

Spindle severing assays

Mitotic spindle severing was performed in essence as described (Grill et al., 2001; Portegijs et al., 2016). One-cell embryos expressing GFP- or mCherry-labeled tubulin were imaged during mitosis using the spinning disk microscope setup described above, equipped with a Teem Photonics 355 nm Q-switched pulsed laser controlled with the ILas system (Roper Scientific France/ PICT-IBiSA, Institut Curie). At anaphase onset, as judged by spindle morphology and mobility, spindles were severed as shown in Figure 1c and Supplementary Movie 2. Centrosome displacement was recorded by 500 ms exposure streaming acquisition, and peak velocities were subsequently extrapolated using the FIJI TrackMate plugin.

Dark state spinning disk microscopy

Dark state experiments were performed on the spinning disk setup described above. For local photoactivation of LOV2 in *C. elegans* embryos, light was applied in a region of variable size depending on each individual experiment using a 491 nm laser controlled with the ILas system (Roper Scientific France/ PICT-IBiSA, Institut Curie). Due to high sensitivity of LOV2 to blue light and variations in laser power, embryos of strain SV2061 (expressing diffuse ePDZ::mCherry and PH::eGFP::LOV) were used to calibrate the amount of laser power required for local activation of LOV2 prior to experiments. During both global and local photoactivation assays and dark state spindle severing experiments embryos were kept away from blue light as much as practically feasible. To this end, aluminum foil was used to cover the microscope setup, and optical filters were inserted in the light path to remove LOV2-activating wavelengths from the transmitted light used to locate embryos on slides. Prior to experimental use of embryos, unintended premature cortical recruitment of ePDZ-mCherry or ePDZ-mCherry-LIN-5 was assessed by observation of mCherry localization patterns.

Antibodies and immunocytochemistry

For immunostaining of *C. elegans* embryos, embryos were dissected from adults in 10 µl MilliQ HR_2RO on slides coated with poly-L-lysine. Samples were then freeze-cracked and fixed in methanol for 5 min. at -20 °C and subsequently in acetone for 5 min. at -20 °C. Embryos were then rehydrated in phosphate buffered saline + 0.05% Tween-20 (PBST), blocked for 1 hour at 4 °C in PBST + 1% bovine serum albumin and 1% goat serum (Sigma-Aldrich), and then incubated at room temperature with primary antibodies for 1 hour and then with secondary antibodies for 45 min., both in blocking solution, with four 10 minute washes in PBST following each antibody mix. Finally, embryos were embedded in ProLong Gold Antifade with DAPI. Primary antibodies used were mouse anti-LIN-5 (1:10, (Lorson et al., 2000)) and rabbit anti-DHC-1 (1:100, (Gönczy et al., 1999); a kind gift from P. Gönczy). Secondary antibodies used were goat anti-rabbit Alexa-488,

goat anti-rabbit Alexa-568, goat anti-mouse Alexa-488 and goat anti-mouse Alexa-568 (Invitrogen), all at 1:500 dilution. Imaging of immunolabeled embryos was performed on the spinning disk setup described above.

Data analysis

All quantitative spinning disk image analyses were performed in either ImageJ or FIJI. For quantification of membrane invaginations, movies were limited to the 200 frames (50 seconds) preceding the onset of telophase. Images were then cropped to include the outer limits of the PH::eGFP signal. Transient cortical dots were tracked manually using the MTrackJ ImageJ plugin. To yield the distribution of invaginations on the length axis of the visible embryo cortex, recorded x coordinates were incremented into groups of 5% embryo length each. To quantify the cortical recruitment and dynamics of ePDZ::mCherry, ePDZ::mCherry::GPR-1, LIN-5::ePDZ::mCherry and ePDZ::mCherry::DHC-1 by PH::eGFP::LOV, multiple 20 px wide linescans were drawn perpendicular to the membrane per analyzed embryo. An intensity profile was plotted per linescan at each acquired time point, from each of which an average of the maximum 3 pixel values was extracted to yield the peak intensity values at the membrane. Each intensity measurement was first corrected for background noise with a value measured outside of the embryo in a 50x50 px region of interest, and cortex to cytoplasm intensity ratios were calculated using average cytoplasmic intensity measurements in a 50x50 or 29x23 px region of interest at all timepoints analyzed. Fluorescence intensity measurements as measure for *Cre(FLPon)* activation (Supplementary Fig. 1e) were taken as total embryo average intensity minus background signal using ImageJ measurement tool. The half time of ePDZ-LOV interaction after a pulse activation was inferred from a non-linear, single component regression. All numerical data processing and graph generation was performed using Excel 2011 (Microsoft) and Prism 7 (GraphPad software, inc.).

Statistical analysis

All data were shown as means with SEM. Statistical significance as determined using two-tailed unpaired Student's t-tests, Mann-Whitney U tests and the Wilcoxon matched-pairs signed rank test. Correlation coefficients between two data sets were calculated using Pearson *r* correlation tests or Spearman rank correlation tests. Data sets were assessed for their fit to a Gaussian distribution using the D'Agostino-Pearson omnibus K2 normality test prior to application of appropriate statistical test. A p-value of <0.05 was considered significant. *, $P<0.05$; **, $P<0.01$; ***, $P<0.001$; ****, $P<0.0001$. All statistical analyses were performed in Prism 7 (GraphPad software, inc.).

Code availability

Our design algorithm is accessible via a web interface at http://104.131.81.59/, and the source code can be found at https://github.com/dannyhmg/germline.

Data availability

The data that support the findings of this study are available from the corresponding author upon reasonable request.

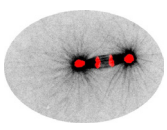

Acknowledgements

We thank S. Jonis, Y. Onderwater, H. Pires, P. van Bergeijk, and M. Harterink for reagents and L. Kapitein for technical advice. We also thank all the members of the Van den Heuvel, Akhmanova, Goldstein, Boxem, and Kapitein groups for helpful discussion and general support. We further thank A. Thomas for critically reading the manuscript. We acknowledge Wormbase and the Biology Imaging Center at the Faculty of Sciences, Department of Biology, Utrecht University. Some strains were provided by the Caenorhabditis Genetics Center (CGC), which is funded by NIH Office of Research Infrastructure Programs (P40OD010440).

Author contribution

L.F., R.S., D.J.D., B.G., A.A., and S.v.d.H. designed the study and analyzed data. L.F. and S.v.d.H. wrote the manuscript. L.F. developed inducible knockout method and performed knockout experiments. L.F. and R.S. carried out optogenetic studies. D.J.D. developed germline-optimization algorithm and performed sequence optimization experiments.

Competing interests statement

The authors declare no competing interests exist.

Supplementary note

Controlled recombination of *C. elegans* transgenes using Cre/lox or FLP/FRT strategies was reported before (Davis et al., 2008; Kage-Nakadai et al., 2014; Ruijtenberg et al., 2015a); reviewed in (Hubbard, 2014). However, our aim to control knockout of essential genes in the germline required the development of novel and improved methods. We designed two-step or bipartite recombination systems, with the goal of enabeling both spatial and temporal control of recombination.

Split-Cre approach

Initially, we developed a Cre-complementation or 'Split-Cre' approach for *C. elegans*, based on a method previously reported for mice (Hirrlinger et al., 2009; Ruijtenberg et al., 2015b). In short, an N-terminal (Cre1) and C-terminal (Cre2) Cre construct are differentially regulated by a germline-specific (*Ppie-1::cre1*) and heat shock-activated promoter (*Phsp-16.48::cre2*); see (Ruijtenberg et al., 2015b) for a more detailed description of the Split-Cre method. A readout construct that switches from mCherry to GFP expression upon Cre-mediated recombination was used to monitor Cre activity as in (Ruijtenberg et al., 2015a). Previously, low-efficiency germline recombination was observed when either the Cre1 or Cre2 construct was expressed from a multicopy extrachromosomal array. Single copy integrants of the constructs were generated using the Mos-SCI method (Frøkjær-Jensen et al., 2012), but these transgenes could not induce reproducible red-to-green-fluorescence switching of the Cre reporter construct (data not shown). We attributed this lack of recombination to possible germline silencing of the germline-specific *Ppie-1*-driven Cre1 construct.

To prevent germline silencing of the *cre1* transgene, we inserted *cre1* at the 3' end of the endogenous *pie-1* coding sequence using CRISPR/Cas9, separated by a T2A self-cleaving peptide sequence, such that expression of *pie-1::t2a::cre1* results in distinct PIE-1 and Cre1 protein products (Ahier and Jarriault, 2014; Dickinson et al., 2013). Although a functional *pie-1::t2a::cre1* knockin was obtained, Cre1 expressed from the *pie-1* locus did not result in robust germline recombination when combined with the heat shock promoter driven *cre2* (data not shown). Since *pie-1::t2a::cre1* is expressed (*pie-1* expression is essential for germline development), we suspected that heat shock-induced expression of *cre2* was too transient or too low to constitute functional Cre1-Cre2 dimers. We therefore seized our attempts to implement a Split-Cre system in the *C. elegans* germline. This decision was also based on experiments with the Split-Cre system in somatic cells. This revealed examples of low recombination efficiencies when *cre1* and *cre2* were expressed under the control of different promoters (Ruijtenberg et al., 2015b). For future follow up studies, improving Cre1-Cre2 dimerization could be considered, for instance by making use of Inteins as in the recently described Split *C. elegans* UAS-GAL4 system (Wang et al., 2018).

FLP-Cre approach

Next, we moved to an approach in which continuous germline expression of Cre is activated by an inducible recombination event (Fig. S1). To this end, we generated and integrated a *cre(FLPon)* construct (*Ppie-1::frt::glo-mcherry::utr::frt::glo-cre::utr*) that switches from germline-specific mCherry (Fig. S6a) to Cre expression upon FLP-mediated recombination between the *frt* sites. Germline-expression of this construct was only achieved after germline-optimization (Fig. S2) of the *mcherry* and *cre* sequences. To control FLP-mediated activation of the recombination cascade, constructs expressing the hyperactive FLP (G5D, see (Schwartz and Jorgensen, 2016)) under different heat shock promoters (*Phsp-16.2, Phsp-16.41*, and, *Phsp-16.48*) were integrated and crossed with the *cre(FLPon)* construct, and the red-to-green Cre reporter or *ric-8*^{loxN} allele. Despite elaborate optimization of the heat shock protocol, heat shock induction of FLP did not

result in robust and reproducible Cre activity (as judged by green fluorescence (Cre readout switched), lethargic (*ric-8* incomplete loss of function), or embryonic lethality (*ric-8* loss of function); data not shown).

To investigate whether FLP expression was the limiting factor for induction of the recombination cascade, we introduced *Ppie-1::flp* on multicopy extrachromosomal arrays (as in (Cochella et al., 2013), personal communication Oliver Hobert) in animals carrying the integrated *cre(FLPon)*, red-to-green Cre-readout, and *Phsp-16.41::flp* or *Phsp-16.48::flp* constructs. We observed 100% recombination efficiency (i.e. green progeny) for 24 transgenic lines generated in the *Phsp-16.41::flp* background and 23 transgenic lines generated in the *Phsp-16.48::flp* background (Fig. S6b). We repeated this approach with animals carrying the *ric-8*^{loxN} allele instead of the Cre-reporter. In these experiments, we frequently observed efficient germline recombination (i.e.: embryonic lethality) (Fig. S6c). We suspected there might be a selection against *Ppie-1::flp* expression in animals carrying loxed alleles of essential genes. This could occur at the level of transgenesis (extrachromosomal arrays that lack *Ppie-1::flp*) or expression (germline silencing). We reasoned that introducing *Ppie-1::flp* in animals that were naïve to *flp* sequences (did not carry a *Phsp::flp* transgene) might reduce silencing responses against the *Ppie-1::flp* transgene. By doing so, we obtained 100% embryonic lethal F2 broods in approximately 50% of the transgenic strains carrying the *ric-8*^{loxN} (N=41), *rgs-7*^{loxP} (N=37), and *ric-8*^{loxN}*; rgs-7*^{loxP} (N=52) alleles (Fig. S 6d). Similarly, we introduced different *Phsp::flp* constructs in worms naïve to *flp* sequences, but did not observe any 100% embryonic lethal F2 broods of heat shocked, staged L1 worms (10 hours after hatching).

Taken together, we concluded that a heat shock-induced recombination cascade was unlikely to be efficient and continued with the extrachromosomally injected *Ppie-1::flp* in animals that are naïve to *flp* sequences for our inducible knock-out experiments described in this chapter. For a future attempt, FLP activation using the binary Q-system could be considered (Hwang et al., 2013).

6

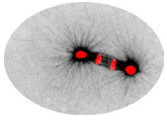

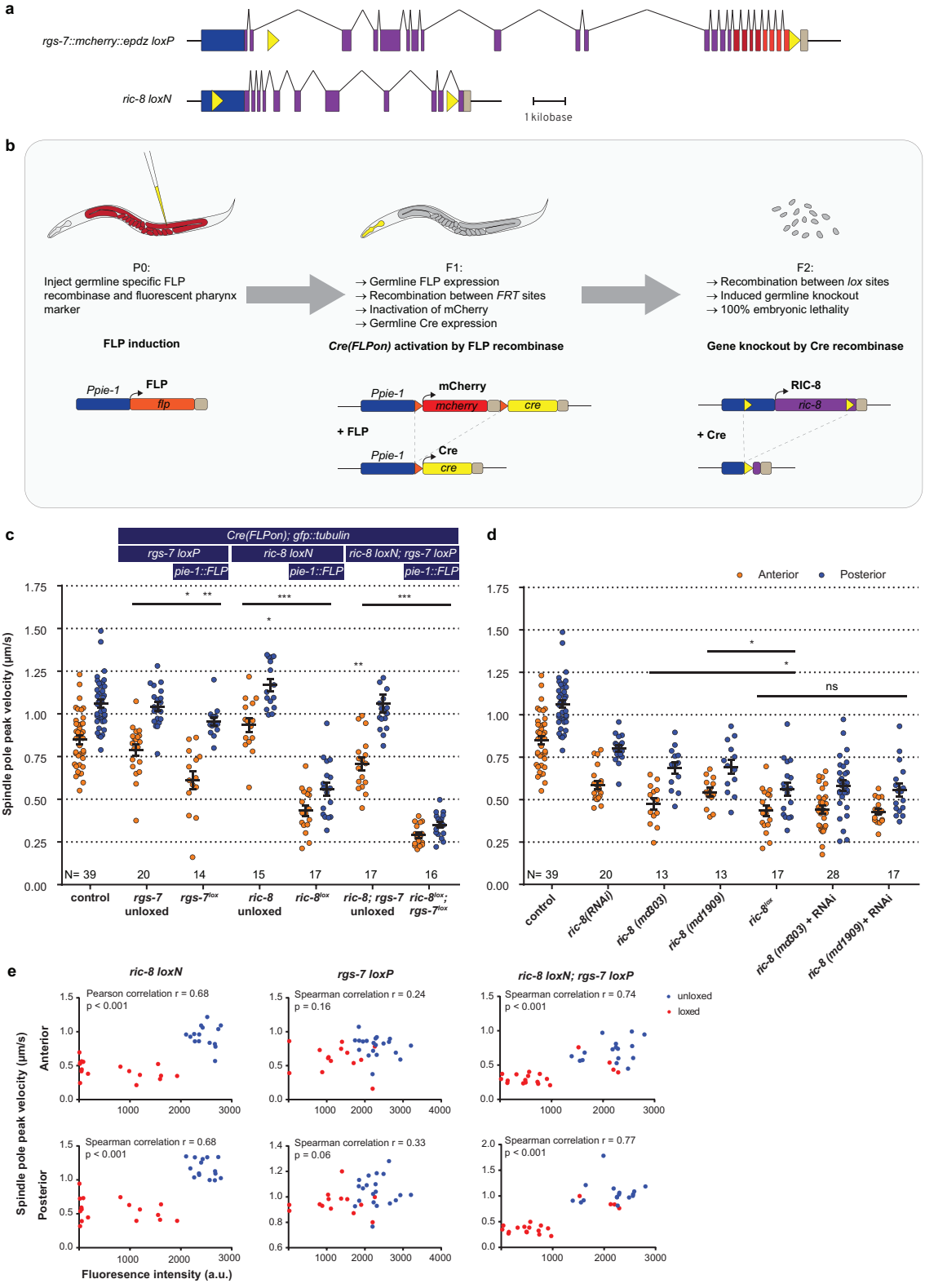
a
rgs-7::mcherry::epdz loxP
ric-8 loxN
1 kilobase
b
P0:
Inject germline specific FLP recombinase and fluorescent pharynx marker
F1:
→ Germline FLP expression
→ Recombination between FRT sites
→ Inactivation of mCherry
→ Germline Cre expression
F2:
→ Recombination between lox sites
→ Induced germline knockout
→ 100% embryonic lethality
FLP induction
Cre(FLPon) activation by FLP recombinase
Gene knockout by Cre recombinase
Ppie-1
FLP
flp
mCherry
mcherry
cre
+ FLP
Cre
+ Cre
RIC-8
ric-8
c
Cre(FLPon); gfp::tubulin
rgs-7 loxP
ric-8 loxN
ric-8 loxN; rgs-7 loxP
pie-1::FLP
Spindle pole peak velocity (µm/s)
N= 39 20 14 15 17 17 16
control
rgs-7 unloxed
rgs-7lox
ric-8 unloxed
ric-8lox
ric-8; rgs-7 unloxed
ric-8lox; rgs-7lox
d
Anterior
Posterior
N= 39 20 13 13 17 28 17
control
ric-8(RNAi)
ric-8 (md303)
ric-8 (md1909)
ric-8lox
ric-8 (md303) + RNAi
ric-8 (md1909) + RNAi
ns
e
ric-8 loxN
rgs-7 loxP
ric-8 loxN; rgs-7 loxP
Pearson correlation r = 0.68
p < 0.001
Spearman correlation r = 0.24
p = 0.16
Spearman correlation r = 0.74
p < 0.001
unloxed
loxed
Spearman correlation r = 0.68
p < 0.001
Spearman correlation r = 0.33
p = 0.06
Spearman correlation r = 0.77
p < 0.001
Anterior
Posterior
Spindle pole peak velocity (µm/s)
Fluoresence intensity (a.u.)

Supplementary figure 1 Inducible knockout of essential genes in the *C. elegans* germline. **(a)** Position of *lox* sites (yellow triangles) in *rgs-7* and *ric-8* loci with promoter (blue), coding sequence (purple), 3' UTR (khaki), mcherry (red), and epdz (orange). We paid attention not to disturb annotated genetic elements and and create splice donor/acceptor consensus sites. Scale bar: 1 kb. **(b)** Flow chart of the inducible tissue-specific knock-out procedure. The system depends on successive expression of two recombinases: FLP and *Cre*. This bipartite nature allows for both spatial and temporal control. For spatial control, we chose the long *Ppie-1* germline-specific promoter including enhancer, which is active in every region of the germline during every developmental stage (Merritt et al., 2008). Temporal control depends on injection of the *Ppie-1::flp* construct (including a fluorescent co-injection marker) in P0 germlines. Transgenic F1 express germline FLP, which recombines between two *FRT sites* (orange triangles). As a result, the integrated tissue-specific *Cre(FLPon)* construct switches expression from *mcherry* to *cre*. *mcherry* and *cre* sequences were germline-optimized for reliable germline expression (see Supplementary Fig. 2). For the *Cre(FLPon)* construct, we chose the *cep-1* 3' UTR because it contains a strong poly-adenylation signal consensus (aataaa) and permits expression in every region and developmental stage of the germline(Merritt et al., 2008). The induced, tissue-specific Cre recombines between *lox* sites (yellow triangles), generating a knockout and 100% embryonic lethal F2 generation. The two-step knockout creates a delay that results in germline Cre activity only in the F1 germline. P0 germline Cre activity generates knockout F1 but does not deplete maternal protein product. **(c)** Spindle severing experiments of the induced *rgs-7*P^{lox}P and *ric-8*P^{lox}P knockout alleles compared to embryos in which FLP and the consequent recombination cascade were not induced. Control is *gfp::tubulin* strain. Error bars: s.e.m. Welch's Student's t-test and Mann Whitney U test; * $P < 0.05$, ** $P < 0.01$, *** $P < 0.001$. **(d)** Spindle severing experiments to compare the induced *ric-8*P^{lox}P knockout phenotype with feeding RNAi, two *ric-8* partial loss of function alleles, and mutants + RNAi. Control is *gfp::tubulin* strain. Error bars: s.e.m. Welch's Student's t-test and Mann Whitney U test; ns $P > 0.05$, * $P < 0.05$. **(e)** Scatter plots showing a correlation between loss of mcherry expression (Cre activation) and reduced spindle pole peak velocities for *ric-8 loxN*, *rgs-7 loxP*, and *ric-8 loxN; rgs-7 loxP*. Embryos were isolated from transgenic F1 (loxed) and control animals that were not injected with the FLP construct (unloxed) embryos. Clearly, some of the *ric-8 loxN; rgs-7 loxP* loxed cluster with the unloxed. These were discarded as outliers from further analyses. Data points were from the same experiment as in c. See Supplementary Table 1 for detailed genotypes.

e

Fluorescent Protein	Codon Adaptation Index	Germline Optimization Score
mTagBFP2 (CAI=1)	0.96	146
mTagBFP2 (GLO)	0.52	531
mTurquoise2 (CAI=1)	0.88	305
mTurquoise2 (GLO)	0.57	728
GFP (from Fire kit)	0.30	76
GFP (CAI=1)	0.96	329
GFP (GLO)	0.57	704
mNeonGreen (CAI=1)	1.00	134
mNeonGreen (GLO)	0.46	481
mScarlet-I (CAI=1)	1.00	341
mScarlet-I (GLO)	0.57	822
mKate2 (CAI=1)	0.97	129
mKate2 (GLO)	0.54	672
HaloTag (CAI=1)	0.93	180
HaloTag (GLO)	0.55	621

Supplementary figure 2 Germline-optimization of coding sequences confers resistance to silencing. **(a)** Strategy for designing germline-optimized coding sequences. We used an RNAseq dataset from one-cell embryos (Gerstein et al., 2014; Hillier et al., 2008) as a proxy for germline-expressed mRNAs, because one-cell embryos are not transcriptionally active and thus their entire mRNA content should be derived from the maternal germline. We made a list of all 12-nucleotide coding words and assigned each word a score that is the sum of the RPKM expression values of the germline mRNAs in which that word appears. Thus, words that appear frequently, or in highly-expressed germline genes, will have high scores. Although the germline silencing machinery is presumably blind to reading frame, we only considered in-frame 12mers so that our design algorithm would implicitly account for codon usage. Finally, we developed an algorithm to assemble any desired coding sequence from our list of coding 12mers. The algorithm is as follows: 1) Based on the desired amino acid sequence, assemble a list of all 12mers that could appear in the coding sequence, and sort these words by score; 2) Assemble a draft coding sequence by plugging in one word at a time, beginning with the highest-scoring possible word and continuing until the sequence is complete; 3) Compute a score for the entire draft sequence by averaging the scores of each word it contains; 4) Refine the sequence by randomly choosing one word at a time, changing it to a different word, and checking whether the overall sequence score improves. Repeat step (4) until no further improvements are found after a certain number of iterations, which is chosen based on the sequence length such that each residue has a 99% chance of being tested at least once. The random optimization in step (4) is necessary because step (2) favors the highest-scoring words without considering context. Choosing a high-scoring word at one position constrains the subsequent choice of words that overlap the high-scoring word. In some cases, a higher overall score results from choosing two moderately- scoring words, rather than a high- and a low-scoring word, when the two words overlap. Random optimization ensures that these cases are found and maximizes the overall score of the designed sequence. **(b)** Images of germline fluorescence in animals carrying either codon-optimized (Redemann et al., 2011) or germline-optimized mNeonGreen::AraD transgenes. AraD is a tetrameric bacterial protein used as a control for single-molecule fluorescence photobleacing experiments (Dickinson et al., 2017). **(c)** Measurements of fluorescence intensity in the germlines of strains carrying either codon-optimized or germline-optimized mNeonGreen::AraD transgenes. Each data point represents one animal. The high expression of the germline-optimized transgenes was stable for >20 generations. **(d)** Images of germline fluorescence in animals carrying GFP::CDK-1 transgenes made with either non-optimized or germline-optimized GFP. *gfp::cdk-1* was tested because this transgene is especially prone to silencing (Lee et al., 2012). A non-transgenic (N2) animal is shown as an example of autofluorescence. We consistently observed expression of germline-optimized GFP::CDK-1 shortly after transgene isolation, although this expression was gradually lost over ~10 generations when we cultured these strains without selecting fluorescent animals at each passage. **(e)** Results of applying our germline optimization algorithm to a selected set of fluorescent protein tags. Codon adaptation index (Redemann et al., 2011) and our germline optimization score are shown for coding sequences designed to maximize optimal codon usage (CAI=1 indicates that sequence was designed to have a codon adaptation index as close as possible to 1.00) or to maximize the germline optimization score (GLO, GermLine Optimized). Germline optimization significantly increases the germline optimization score as expected, at the cost of a moderate reduction in codon adaptation index. Despite the lower codon adaptation index, germline-optimized transgenes were most often expressed at higher levels than their codon-optimized counterparts (see above and our unpublished observations). Constructs containing the listed germline-optimized fluorescent protein sequences will be deposited at Addgene.

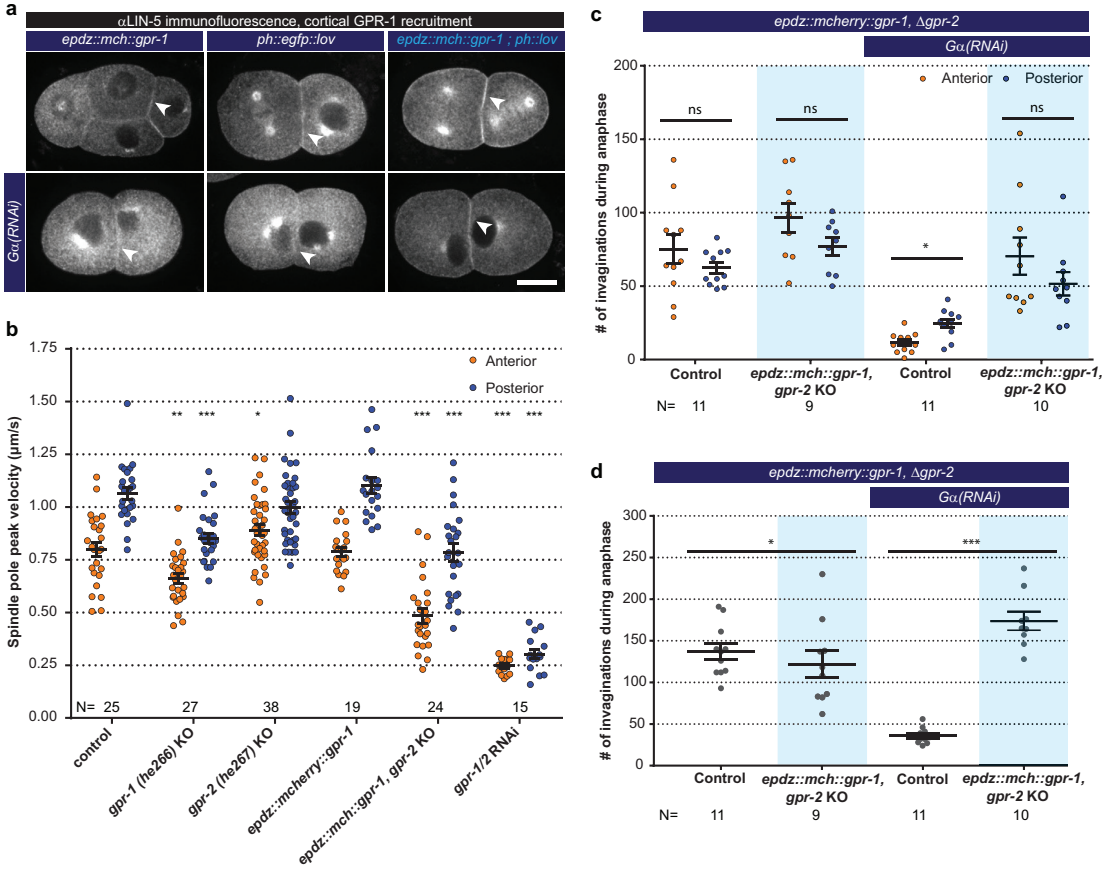

Supplementary figure 3 Cortical GPR-1 recruitment constitutes functional cortical pulling force generators. **(a)** Immunofluorescent staining of LIN-5 in early embryos. Controls are *epdz::mch::gpr*-1 and *ph::egfp::lov* strains. Experimental condition is the combination of the two controls (GPR-1 recruitment to membrane LOV) in otherwise wildtype embryos or Gα RNAi) embryos. Arrowheads indicate cortical LIN-5. Scale bar: 10 µm. **(b)** Spindle severing experiments of CRISPR/Cas9-mediated *gpr-1* and *gpr-2* knockout alleles, and tagged *epdz::mch::gpr-1. egfp::tubulin* (control) and *gpr-1/2(RNAi)* are wildtype and gpr-1/2 loss of function controls. Error bars: s.e.m. Welch's Student's *t-test* and Mann Whitney U test; * $P < 0.05$, ** $P < 0.01$, *** $P < 0.001$. **(c)** Number of membrane invaginations, anterior and posterior compared for indicated genotypes. Control is *gfp::tubulin; ph::egfp::lov* strain. Error bars: s.e.m. Paired, two-tailed Student's *t-test*; ns $P > 0.05$, * $P < 0.05$. **(d)** Total number of membrane invaginations for the indicated genotypes. Control is *gfp::tubulin; ph::egfp::lov* strain. Error bars: s.e.m. Welch's Student's t-test; * $P < 0.05$, *** $P < 0.001$. Blue fields indicate conditions in which an ePDZ- and LOV component are present, and an ePDZ–LOV interaction is induced using blue light. See Table S for detailed genotypes. Anterior is to the left in microscopy images.

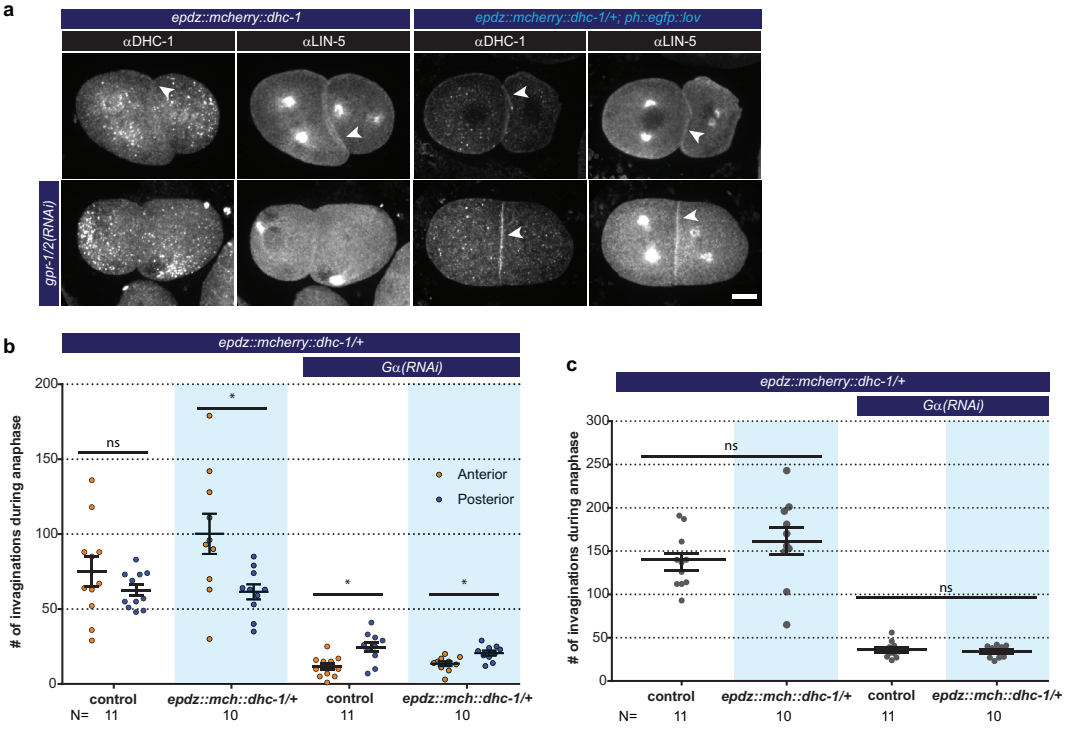

Supplementary figure 4 Cortical dynein (DHC-1) recruitment localizes LIN-5 but does not constitute a functional force generator. Scale bar: 10 µm. **(a)** Immunofluorescent staining of DHC-1 and LIN-5 in early embryos. Control is *epdz::mch::dhc-1/+* strain. Experimental condition is cortical dynein recruitment in *gpr-1/2(RNAi)* or otherwise wildtype embryos. Arrowheads indicate cortical staining. **(b)** Number of membrane invaginations, anterior and posterior compared for indicated genotypes. Control is *gfp::tubulin; ph::egfp::lov* strain. Error bars: s.e.m. Paired, two-tailed Student's t-test; ns $P > 0.05$, * $P < 0.05$. **(c)** Total number of membrane invaginations for the indicated genotypes. Control is *gfp::tubulin; ph::egfp::lov* strain. Error bars: s.e.m. Welch's Student's t-test; ns $P > 0.05$. Blue fields indicate conditions in which an ePDZ- and LOV component are present, and an ePDZ–LOV interaction is induced using blue light. See Supplementary Table 1 for detailed genotypes. Anterior is to the left in microscopy images.

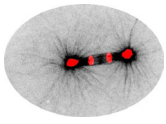

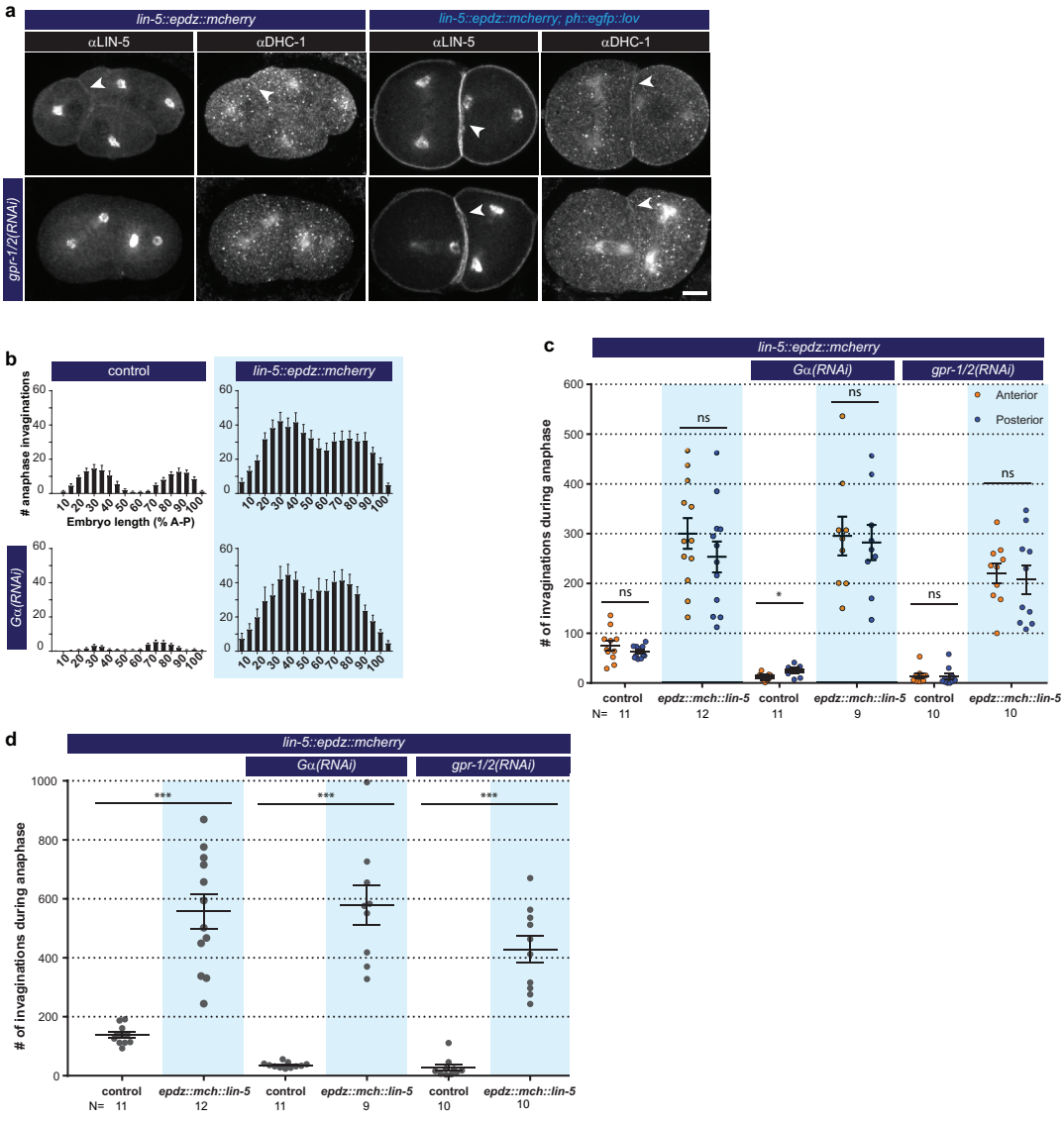

Supplementary figure 5 Cortical LIN-5 recruitment localizes DHC-1 and constitute a minimal force generator. **(a)** Immunofluorescent staining of LIN-5 and DHC-1 in early embryos. Control is *lin-5::epdz::mch* strain. Experimental condition is cortical LIN-5 recruitment in *gpr-1/2(RNAi)* or otherwise wildtype embryos. Arrowheads indicate cortical staining. Scale bar: 10 µm **(b)** Distribution of membrane invaginations along the one-cell embryo anterior-posterior axis. Control is *ph::egfp::lov; gfp::tubulin* strain with and without Gα RNAi. Experimental condition is the combination of control with *lin-5::epdz::mch* for cortical LIN-5 recruitment. **(c)** Number of membrane invaginations, anterior and posterior compared for indicated genotypes. Control is *gfp::tubulin; ph::egfp::lov* strain. Error bars: s.e.m. Paired, two-tailed Student's *t-test*; ns $P > 0.05$, * $P < 0.05$. **(d)** Total number of membrane invaginations for the indicated genotypes. Control is *gfp::tubulin; ph::egfp::lov* strain. Error bars: s.e.m. Welch's Student's *t-test*; *** $P < 0.001$. Blue fields indicate conditions in which an ePDZ- and LOV component are present, and an ePDZ–LOV interaction is induced using blue light. See Supplementary Table 1 for detailed genotypes. Anterior is to the left in microscopy images.

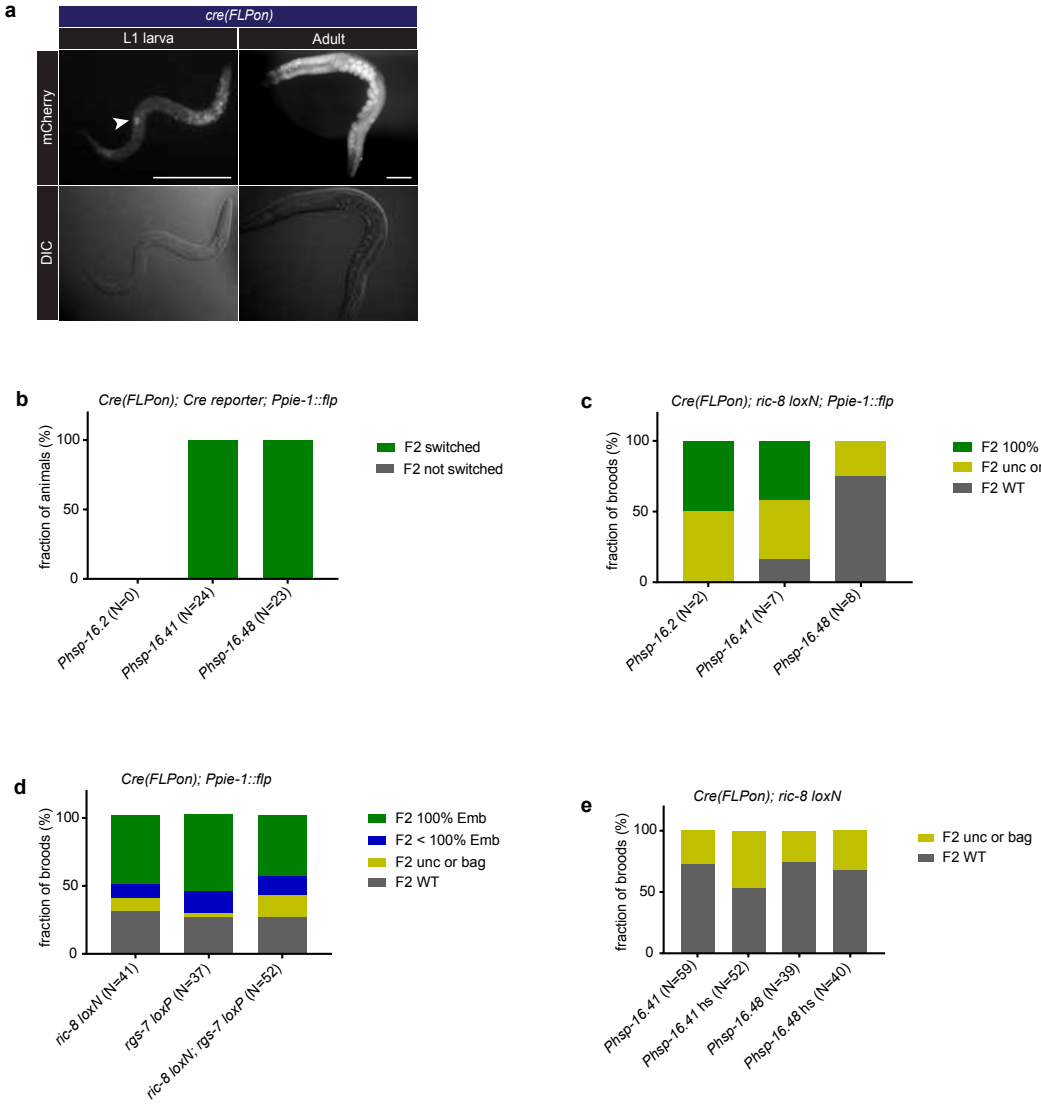

Supplementary figure 6 Different approaches to obtain an inducible germline knockout. **(a)** Germline expression of the *Cre(FLPon)* construct at different developmental stages. **(b)** Efficiency of recombination of the red-to-green switching Cre reporter. The recombination cascade was initiated by constitutive germline expression of FLP. **(c)** Efficiency of recombination of *ric-8 loxN*. The recombination cascade was initiated by constitutive germline expression of FLP. **(d)** Efficiency of recombination of endogenous genes. The recombination cascade was initiated by constitutive germline expression of FLP in worms naïve to FLP sequences. **(e)** Efficiency of recombination of endogenous genes. The recombination cascade was initiated by heat-shocked induced expression of FLP in worms naïve to FLP sequences. Emb: embryonic lethal, unc: uncoordinated movement, bag: bag of worms. See supplementary table 1 for detailed genotypes.

Supplementary Table 1 Genotypes of C. elegans used in this study, listed per figure

Figure	Strain	Genotype	Source
1 b	SA250	tjIs54(Ppie-1::gfp::tbb-2 + Ppie-1::2xmcherry::tbg-1 + unc-119(+)); TjIs57(Ppie-1::mcherry::his-48 + unc-119(+))	CGC
	SV1589	lin-5(he244[co-egfp::lin-5]) II	(Portegijs et al., 2016)
	SV1569	gpr-1(he238[co-fkbp::co-egfp::gpr-1]) III	(Portegijs et al., 2016)
	SV1803	dhc-1 (he263[egfp::dhc-1]) I	(Schmidt et al., 2017)
1 c	AZ244	unc-119(ed3) III; ruIs57[Ppie-1::gfp::tbb-2 + unc119(+)] V	CGC
1 d	AZ244	unc-119(ed3) III; ruIs57[Ppie-1::gfp::tbb-2 + unc119(+)] V	CGC
	SV1485	lin-5(ev571ts) II; ruIs57[Ppie-1::gfp::tbb-2 + unc119(+)] V	
1 e	AZ244	unc-119(ed3) III; ruIs57[Ppie-1::gfp::tbb-2 + unc119(+)] V	CGC
	SV2035	ttTi5605(he312[Ppie-1(long)::frt::glo-mcherry::cep-1(3'UTR)::frt::egl-13nls::glo-cre::cep-1(3'UTR)]) II; ric-8(he280[loxN -741/loxN 4624]) IV; ruIs57[Ppie-1::gfp::tbb-2 + unc119(+)] V; Ppie-1::sv40nls::flp(G5D)::egl-13nls::tbb-2(3'UTR) + Pmyo-2::tdtomato + E. coli DNA c/w PvuII Ex	
	SV2087	ttTi5605(he312[Ppie-1(long)::frt::glo-mcherry::cep-1(3'UTR)::frt::egl-13nls::glo-cre::cep-1(3'UTR)]) II; ruIs57[Ppie-1::gfp::tbb-2 + unc119(+)] V; rgs-7(he300[loxP in intron 2 + -CT co-mcherry::co-epdz::tev::loxP::3xflag]) X; Ppie-1::sv40nls::flp(G5D)::egl-13nls::tbb-2(3'UTR) + Pmyo-2::tdtomato + E. coli DNA c/w PvuII Ex	
	SV2088	ttTi5605(he312[Ppie-1(long)::frt::glo-mcherry::cep-1(3'UTR)::frt::egl-13nls::glo-cre::cep-1(3'UTR)]) II; ric-8(he280[loxN -741/loxN 4624]) IV; ruIs57[Ppie-1::gfp::tbb-2 + unc119(+)] V; rgs-7(he300[loxP in intron 2 + -CT co-mCherry::co-epdz::tev::loxP::3xflag]) X; Ppie-1::sv40nls::flp(G5D)::egl-13nls::tbb-2(3'UTR) + Pmyo-2::tdtomato + E. coli DNA c/w PvuII Ex	
2 b	SV2061	ttTi5605(he314[Ppie-1::glo-epdz::mcherry(smu-1)::tbb-2(3'UTR)]) II; cxTi10816(he259[Peft-3::ph::co-egfp::co-lov::tbb-2(3'UTR)]) IV	

3 a	SV2076	cxTi10816(he259[Peft-3::ph::co-egfp::co-lov::tbb-2(3'UTR)]) IV; ruIs57[Ppie-1::gfp::tbb-2 + unc119(+)] V; rgs-7(he290[rgs-7::co-mcherry::co-epdz]) X	
	SV2062	par-6(he322[par-6::gfp(smu-1 introns)::glo-lov] I	
3 b	SV2074	ruIs57[Ppie-1::gfp::tbb-2 + unc119(+)] V; rgs-7(he290[rgs-7::co-mcherry::co-epdz]) X	
	SV2076	CxTi 10816(he259[Peft-3::PH::eGFP::LOV::tbb-2]) IV ; RuIs57 [Ppie-1::Tub::GFP) V ; rgs-7 (he290[rgs-7::co-mCherry::co-ePDZ]) X	
	SV2109	par-6 (he322 [par-6::gfp(smu-1 introns)::glo-lov]) I ; RuIs57 [Ppie-1::Tub::GFP) V	
	SV2143	par-6(he322[par-6::gfp(smu-1 introns)::glo-lov] I; ruIs57[Ppie-1::gfp::tbb-2 + unc119(+)] V; rgs-7(he290[rgs-7::co-mcherry::co-epdz]) X	
3 c	SV2074	ruIs57[Ppie-1::gfp::tbb-2 + unc119(+)] V; rgs-7(he290[rgs-7::co-mcherry::co-epdz]) X	
	SV2076	CxTi 10816(he259[Peft-3::PH::eGFP::LOV::tbb-2]) IV ; RuIs57 [Ppie-1::Tub::GFP) V ; rgs-7 (he290[rgs-7::co-mCherry::co-ePDZ]) X	
	SV2143	par-6(he322[par-6::gfp(smu-1 introns)::glo-lov] I; ruIs57[Ppie-1::gfp::tbb-2 + unc119(+)] V; rgs-7(he290[rgs-7::co-mcherry::co-epdz]) X	
4 a	SV2147	ric-8(he339[glo-epdz::mcherry(smu-1 introns)::ric-8]) IV; cxTi10816(he259[Peft-3::ph::co-egfp::co-lov::tbb-2(3'UTR)]) IV; ruIs57[Ppie-1::gfp::tbb-2 + unc119(+)] V	
4 b	AZ244	unc-119(ed3) III; ruIs57[Ppie-1::gfp::tbb-2 + unc119(+)] V	CGC
	SV2085	cxTi10816(he259[Peft-3::ph::co-egfp::co-lov::tbb-2(3'UTR)]) IV; ruIs57[Ppie-1::gfp::tbb-2 + unc119(+)] V	
	SV2146	ric-8(he339[glo-epdz::mcherry(smu-1 introns)::ric-8]) IV; ruIs57[Ppie-1::gfp::tbb-2 + unc119(+)] V	
	SV2147	ric-8(he339[glo-epdz::mcherry(smu-1 introns)::ric-8]) IV; cxTi10816(he259[Peft-3::ph::co-egfp::co-lov::tbb-2(3'UTR)]) IV; ruIs57[Ppie-1::gfp::tbb-2 + unc119(+)] V	

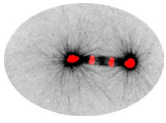

5 b	SV2043	gpr-1(he301[glo-epdz::mcherry(smu-1 introns)::gpr-1]), gpr-2(he311[Δ7 - 1212]) III; cxTi10816(he259[Peft-3::ph::co-egfp::co-lov::tbb-2(3'UTR)]) IV
5 c	SV2043	gpr-1(he301[glo-epdz::mcherry(smu-1 introns)::gpr-1]), gpr-2(he311[Δ7 - 1212]) III; cxTi10816(he259[Peft-3::ph::co-egfp::co-lov::tbb-2(3'UTR)]) IV
5 d	SV2038	gpr-1(he301[glo-epdz::mcherry(smu-1 introns)::gpr-1]), gpr-2(he311[Δ7 - 1212]) III; ruIs57[Ppie-1::gfp::tbb-2 + unc119(+)] V
	SV2059	gpr-1(he301[glo-epdz::mcherry(smu-1 introns)::gpr-1]), gpr-2(he311[Δ7 - 1212]) III; cxTi10816(he259[Peft-3::ph::co-egfp::co-lov::tbb-2(3'UTR)]) IV; ruIs57[Ppie-1::gfp::tbb-2 + unc119(+)] V
5 e	SV2091	weIs21[pJA138 (Ppie-1::mcherry::tubulin::pie-1 + unc-119(+)]; unc-119(ed3) III; gpr-1(he301[glo-epdz::mcherry(smu-1 introns)::gpr-1]), gpr-2(he311[Δ7 - 1212]) III
	SV2099	weIs21(pJA138[Ppie-1::mcherry::tubulin::pie-1(3'UTR)]); gpr-1(he301[glo-epdz::mcherry(smu-1 introns)::gpr-1]), gpr-2(he311[Δ7-1212])III; cxTi10816(he259[Peft-3::ph::co-egfp::co-lov::tbb-2(3'UTR)]) IV
5 f	SV2085	cxTi10816(he259[Peft-3::ph::co-egfp::co-lov::tbb-2(3'UTR)]) IV; ruIs57[Ppie-1::gfp::tbb-2 + unc119(+)] V
	SV2038	gpr-1(he301[glo-epdz::mcherry(smu-1 introns)::gpr-1]), gpr-2(he311[Δ7 - 1212]) III; ruIs57[Ppie-1::gfp::tbb-2 + unc119(+)] V
	SV2059	gpr-1(he301[glo-epdz::mcherry(smu-1 introns)::gpr-1]), gpr-2(he311[Δ7 - 1212]) III; cxTi10816(he259[Peft-3::ph::co-egfp::co-lov::tbb-2(3'UTR)]) IV; ruIs57[Ppie-1::gfp::tbb-2 + unc119(+)] V
5 g	SV2085	cxTi10816(he259[Peft-3::ph::co-egfp::co-lov::tbb-2(3'UTR)]) IV; ruIs57[Ppie-1::gfp::tbb-2 + unc119(+)] V
5 h	SV2085	cxTi10816(he259[Peft-3::ph::co-egfp::co-lov::tbb-2(3'UTR)]) IV; ruIs57[Ppie-1::gfp::tbb-2 + unc119(+)] V
	SV2059	gpr-1(he301[glo-epdz::mcherry(smu-1 introns)::gpr-1]), gpr-2(he311[Δ7 - 1212]) III; cxTi10816(he259[Peft-3::ph::co-egfp::co-lov::tbb-2(3'UTR)]) IV; ruIs57[Ppie-1::gfp::tbb-2 + unc119(+)] V
6 b	SV2090	dhc-1(he255[epdz::mcherry::dhc-1])/+ I; cxTi10816(he259[Peft-3::ph::co-egfp::co-lov::tbb-2(3'UTR)]) IV; ruIs57[Ppie-1::gfp::tbb-2 + unc119(+)] V;

6 c	SV2090	dhc-1(he255[epdz::mcherry::dhc-1])/+ I; cxTi10816(he259[Peft-3::ph::co-egfp::co-lov::tbb-2(3'UTR)]) IV; ruIs57[Ppie-1::gfp::tbb-2 + unc119(+)] V;
6 d	SV2095	dhc-1(he255[epdz::mcherry::dhc-1]) I; ruIs57[Ppie-1::gfp::tbb-2 + unc119(+)] V
	SV2090	dhc-1(he255[epdz::mcherry::dhc-1])/+ I; cxTi10816(he259[Peft-3::ph::co-egfp::co-lov::tbb-2(3'UTR)]) IV; ruIs57[Ppie-1::gfp::tbb-2 + unc119(+)] V;
6 e	SV2095	dhc-1(he255[epdz::mcherry::dhc-1]) I; ruIs57[Ppie-1::gfp::tbb-2 + unc119(+)] V
	SV2090	dhc-1(he255[epdz::mcherry::dhc-1])/+ I; cxTi10816(he259[Peft-3::ph::co-egfp::co-lov::tbb-2(3'UTR)]) IV; ruIs57[Ppie-1::gfp::tbb-2 + unc119(+)] V;
6 f	SV2095	dhc-1(he255[epdz::mcherry::dhc-1]) I; ruIs57[Ppie-1::gfp::tbb-2 + unc119(+)] V
	SV2090	dhc-1(he255[epdz::mcherry::dhc-1])/+ I; cxTi10816(he259[Peft-3::ph::co-egfp::co-lov::tbb-2(3'UTR)]) IV; ruIs57[Ppie-1::gfp::tbb-2 + unc119(+)] V;
7 b	SV2121	lin-5(he330[lin-5::glo-epdz::mcherry(smu-1 introns)]) II; cxTi10816(he259[Peft-3::ph::co-egfp::co-lov::tbb-2(3'UTR)]) IV; ruIs57[Ppie-1::gfp::tbb-2 + unc119(+)] V
7 c	SV2121	lin-5(he330[lin-5::glo-epdz::mcherry(smu-1 introns)]) II; cxTi10816(he259[Peft-3::ph::co-egfp::co-lov::tbb-2(3'UTR)]) IV; ruIs57[Ppie-1::gfp::tbb-2 + unc119(+)] V
7 d	SV2120	lin-5(he330[lin-5::glo-epdz::mcherry(smu-1 introns)]) II; ruIs57[Ppie-1::gfp::tbb-2 + unc119(+)] V;
	SV2121	lin-5(he330[lin-5::glo-epdz::mcherry(smu-1 introns)]) II; cxTi10816(he259[Peft-3::ph::co-egfp::co-lov::tbb-2(3'UTR)]) IV; ruIs57[Ppie-1::gfp::tbb-2 + unc119(+)] V
7 e	SV2120	lin-5(he330[lin-5::glo-epdz::mcherry(smu-1 introns)]) II; ruIs57[Ppie-1::gfp::tbb-2 + unc119(+)] V;
	SV2121	lin-5(he330[lin-5::glo-epdz::mcherry(smu-1 introns)]) II; cxTi10816(he259[Peft-3::ph::co-egfp::co-lov::tbb-2(3'UTR)]) IV; ruIs57[Ppie-1::gfp::tbb-2 + unc119(+)] V
7 f	SV2085	cxTi10816(he259[Peft-3::ph::co-egfp::co-lov::tbb-2(3'UTR)]) IV; ruIs57[Ppie-1::gfp::tbb-2 + unc119(+)] V

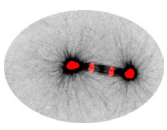

	SV2120	lin-5(he330[lin-5::glo-epdz::mcherry(smu-1 introns)]) II; ruIs57[Ppie-1::gfp::tbb-2 + unc119(+)] V;	
	SV2121	lin-5(he330[lin-5::glo-epdz::mcherry(smu-1 introns)]) II; cxTi10816(he259[Peft-3::ph::co-egfp::co-lov::tbb-2(3'UTR)]) IV; ruIs57[Ppie-1::gfp::tbb-2 + unc119(+)] V	
8 a	SV2121	lin-5(he330[lin-5::glo-epdz::mcherry(smu-1 introns)]) II; cxTi10816(he259[Peft-3::ph::co-egfp::co-lov::tbb-2(3'UTR)]) IV; ruIs57[Ppie-1::gfp::tbb-2 + unc119(+)] V	
8 b	SV2121	lin-5(he330[lin-5::glo-epdz::mcherry(smu-1 introns)]) II; cxTi10816(he259[Peft-3::ph::co-egfp::co-lov::tbb-2(3'UTR)]) IV; ruIs57[Ppie-1::gfp::tbb-2 + unc119(+)] V	
8 c	SV2121	lin-5(he330[lin-5::glo-epdz::mcherry(smu-1 introns)]) II; cxTi10816(he259[Peft-3::ph::co-egfp::co-lov::tbb-2(3'UTR)]) IV; ruIs57[Ppie-1::gfp::tbb-2 + unc119(+)] V	
S1 c	AZ244	unc-119(ed3) III; ruIs57[Ppie-1::gfp::tbb-2 + unc119(+)] V	CGC
	SV2087	ttTi5605(he312[Ppie-1(long)::frt::glo-mcherry::cep-1(3'UTR)::frt::egl-13nls::glo-cre::cep-1(3'UTR)]) II; ruIs57[Ppie-1::gfp::tbb-2 + unc119(+)] V; rgs-7(he300[loxP in intron 2 + -CT co-mcherry::co-epdz::tev::loxP::3xflag]) X ttTi5605(he312[Ppie-1(long)::frt::glo-mcherry::cep-1(3'UTR)::frt::egl-13nls::glo-cre::cep-1(3'UTR)]) II; ruIs57[Ppie-1::gfp::tbb-2 + unc119(+)] V; rgs-7(he300[loxP in intron 2 + -CT co-mcherry::co-epdz::tev::loxP::3xflag]) X; Ppie-1::sv40nls::flp(G5D)::egl-13nls::tbb-2(3'UTR) + Pmyo-2::tdtomato + E. coli DNA c/w PvuII Ex	
	SV2035	ttTi5605(he312[Ppie-1(long)::frt::glo-mcherry::cep-1(3'UTR)::frt::egl-13nls::glo-cre::cep-1(3'UTR)]) II; ric-8(he280[loxN -741/loxN 4624]) IV; ruIs57[Ppie-1::gfp::tbb-2 + unc119(+)] V ttTi5605(he312[Ppie-1(long)::frt::glo-mcherry::cep-1(3'UTR)::frt::egl-13nls::glo-cre::cep-1(3'UTR)]) II; ric-8(he280[loxN -741/loxN 4624]) IV; ruIs57[Ppie-1::gfp::tbb-2 + unc119(+)] V; Ppie-1::sv40nls::flp(G5D)::egl-13nls::tbb-2(3'UTR) + Pmyo-2::tdtomato + E. coli DNA c/w PvuII Ex	

	SV2088	ttTi5605(he312[Ppie-1(long)::frt::glo-mcherry::cep-1(3'UTR)::frt::egl-13nls::glo-cre::cep-1(3'UTR)]) II; ric-8(he280[loxN -741/loxN 4624]) IV; ruIs57[Ppie-1::gfp::tbb-2 + unc119(+)] V; rgs-7 (he300 [loxP in intron 2 + -CT co-mCherry::co-epdz::TEV::loxP::3xFlag]) X ttTi5605 (he312 [long Ppie-1::FRT::glo-mCherry::cep-1 3' UTR::FRT::egl-13 NLS::glo-Cre::cep-1 3' UTR]) II ; ric-8 (he280[loxN -741/loxN 4624]) IV ; RuIs57(Ppie-1::GFP::tubulin)V ; rgs-7 (he300 [loxP in intron 2 + -CT co-mCherry::co-epdz::TEV::loxP::3xFlag]) X; Ppie-1::sv40nls::flp(G5D)::egl-13nls::tbb-2(3'UTR) + Pmyo-2::tdtomato + E. coli DNA c/w PvuII Ex	
S1 d	AZ244	unc-119(ed3) III; ruIs57[Ppie-1::gfp::tbb-2 + unc119(+)] V	CGC
	SV1460	ric-8(md303) I; ruIs57[Ppie-1::gfp::tbb-2 + unc119(+)] V	
S2 b	LP185	cpIs25[Pmex-5::mNeonGreen::AraD::2xStrep::tbb-2 3'UTR + unc-119(+)] II; unc-119(ed3) III	
	LP186	cpIs26[Pmex-5::mNeonGreen::AraD::2xStrep::tbb-2 3'UTR + unc-119(+)] II; unc-119(ed3) III	
	LP187	cpIs27[Pmex-5::mNeonGreen::AraD::2xStrep::tbb-2 3'UTR + unc-119(+)] II; unc-119(ed3) III	
	LP230	cpIs36[Pmex-5::mNeonGreen::3xFlag::AraD::tbb-2 3'UTR + unc-119(+)] II; unc-119(ed3) III	
	LP231	cpIs37[Pmex-5::mNeonGreen::3xFlag::AraD::tbb-2 3'UTR + unc-119(+)] II; unc-119(ed3) III	
	LP232	cpIs38[Pmex-5::mNeonGreen::3xFlag::AraD::tbb-2 3'UTR + unc-119(+)] II; unc-119(ed3) III	
	LP233	cpIs39[Pmex-5::mNeonGreen::3xFlag::AraD::tbb-2 3'UTR + unc-119(+)] II; unc-119(ed3) III	
S2 c	LP185	cpIs25[Pmex-5::mNeonGreen::AraD::2xStrep::tbb-2 3'UTR + unc-119(+)] II; unc-119(ed3) III	
	LP186	cpIs26[Pmex-5::mNeonGreen::AraD::2xStrep::tbb-2 3'UTR + unc-119(+)] II; unc-119(ed3) III	
	LP187	cpIs27[Pmex-5::mNeonGreen::AraD::2xStrep::tbb-2 3'UTR + unc-119(+)] II; unc-119(ed3) III	

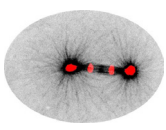

	LP230	cpIs36[Pmex-5::mNeonGreen::3xFlag::AraD::tbb-2 3'UTR + unc-119(+)] II; unc-119(ed3) III	
	LP231	cpIs37[Pmex-5::mNeonGreen::3xFlag::AraD::tbb-2 3'UTR + unc-119(+)] II; unc-119(ed3) III	
	LP232	cpIs38[Pmex-5::mNeonGreen::3xFlag::AraD::tbb-2 3'UTR + unc-119(+)] II; unc-119(ed3) III	
	LP233	cpIs39[Pmex-5::mNeonGreen::3xFlag::AraD::tbb-2 3'UTR + unc-119(+)] II; unc-119(ed3) III	
S2 d	LP288	cpSi22[Pcdk-1::gfp::cdk-1 + unc-119(+)] II; unc-119(ed3) III	
	LP294	cpSi28[Pcdk-1::gfp-GLO::cdk-1 + unc-119(+)] II; unc-119(ed3) III	
S3 a	SV1972	gpr-1(he301[glo-epdz::mcherry(smu-1 introns)::gpr-1]) III	
	SV2085	cxTi10816(he259[Peft-3::ph::co-egfp::co-lov::tbb-2(3'UTR)]) IV; ruIs57[Ppie-1::gfp::tbb-2 + unc119(+)] V	
	SV1982	gpr-1 (he301[glo-epdz::mcherry(smu-1 introns)::gpr-1]) III; cxTi10816(he259[Peft-3::ph::co-egfp::co-lov::tbb-2(3'UTR)]) IV	
S3 b	AZ244	unc-119(ed3) III; ruIs57[Ppie-1::gfp::tbb-2 + unc119(+)] V	CGC
	SV1815	gpr-1(he266[Δgpr-1 -443 to 2039]) III; ruIs57[Ppie-1::gfp::tbb-2 + unc119(+)] V	
	SV1816	gpr-2 (he267[Δgpr-2 368 to 1953]) III; ruIs57[Ppie-1::gfp::tbb-2 + unc119(+)] V	
	SV2075	gpr-1(he301[glo-epdz::mcherry(smu-1 introns)::gpr-1]) III; ruIs57[Ppie-1::gfp::tbb-2 + unc119(+)] V	
	SV2038	gpr-1(he301[glo-epdz::mcherry(smu-1 introns)::gpr-1]), gpr-2(he311[Δ7 - 1212]) III; ruIs57[Ppie-1::gfp::tbb-2 + unc119(+)] V	
S3 c	SV2085	cxTi10816(he259[Peft-3::ph::co-egfp::co-lov::tbb-2(3'UTR)]) IV; ruIs57[Ppie-1::gfp::tbb-2 + unc119(+)] V	
	SV2059	gpr-1(he301[glo-epdz::mcherry(smu-1 introns)::gpr-1]), gpr-2(he311[Δ7 - 1212]) III; cxTi10816(he259[Peft-3::ph::co-egfp::co-lov::tbb-2(3'UTR)]) IV; ruIs57[Ppie-1::gfp::tbb-2 + unc119(+)] V	
S3 d	SV2085	cxTi10816(he259[Peft-3::ph::co-egfp::co-lov::tbb-2(3'UTR)]) IV; ruIs57[Ppie-1::gfp::tbb-2 + unc119(+)] V	

	SV2059	gpr-1(he301[glo-epdz::mcherry(smu-1 introns)::gpr-1]), gpr-2(he311[Δ7 - 1212]) III; cxTi10816(he259[Peft-3::ph::co-egfp::co-lov::tbb-2(3'UTR)]) IV; ruIs57[Ppie-1::gfp::tbb-2 + unc119(+)] V
S4 a	SV1673	dhc-1(he255[epdz::mcherry::dhc-1]) I
	SV2090	dhc-1(he255[epdz::mcherry::dhc-1])/+ I; cxTi10816(he259[Peft-3::ph::co-egfp::co-lov::tbb-2(3'UTR)]) IV; ruIs57[Ppie-1::gfp::tbb-2 + unc119(+)] V;
S4 b	SV2085	CxTi 10816(he259[Peft-3::PH::eGFP::LOV::tbb-2]) IV ; RuIs57 [Ppie-1::Tub::GFP) V
	SV2090	dhc-1(he255[epdz::mcherry::dhc-1])/+ I; cxTi10816(he259[Peft-3::ph::co-egfp::co-lov::tbb-2(3'UTR)]) IV; ruIs57[Ppie-1::gfp::tbb-2 + unc119(+)] V;
S4 c	SV2085	CxTi 10816(he259[Peft-3::PH::eGFP::LOV::tbb-2]) IV ; RuIs57 [Ppie-1::Tub::GFP) V
	SV2090	dhc-1(he255[epdz::mcherry::dhc-1])/+ I; cxTi10816(he259[Peft-3::ph::co-egfp::co-lov::tbb-2(3'UTR)]) IV; ruIs57[Ppie-1::gfp::tbb-2 + unc119(+)] V;
S5 a	SV2100	lin-5(he330[lin-5::glo-epdz::mcherry(smu-1 introns)]) II
	SV2121	lin-5(he330[lin-5::glo-epdz::mcherry(smu-1 introns)]) II; cxTi10816(he259[Peft-3::ph::co-egfp::co-lov::tbb-2(3'UTR)]) IV; ruIs57[Ppie-1::gfp::tbb-2 + unc119(+)] V
S5 b	SV2085	cxTi10816(he259[Peft-3::ph::co-egfp::co-lov::tbb-2(3'UTR)]) IV; ruIs57[Ppie-1::gfp::tbb-2 + unc119(+)] V
	SV2120	lin-5(he330[lin-5::glo-epdz::mcherry(smu-1 introns)]) II; ruIs57[Ppie-1::gfp::tbb-2 + unc119(+)] V;
	SV2121	lin-5(he330[lin-5::glo-epdz::mcherry(smu-1 introns)]) II; cxTi10816(he259[Peft-3::ph::co-egfp::co-lov::tbb-2(3'UTR)]) IV; ruIs57[Ppie-1::gfp::tbb-2 + unc119(+)] V
S5 c	SV2085	cxTi10816(he259[Peft-3::ph::co-egfp::co-lov::tbb-2(3'UTR)]) IV; ruIs57[Ppie-1::gfp::tbb-2 + unc119(+)] V

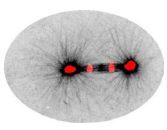

	SV2120	lin-5(he330[lin-5::glo-epdz::mcherry(smu-1 introns)]) II; ruIs57[Ppie-1::gfp::tbb-2 + unc119(+)] V;
	SV2121	lin-5(he330[lin-5::glo-epdz::mcherry(smu-1 introns)]) II; cxTi10816(he259[Peft-3::ph::co-egfp::co-lov::tbb-2(3'UTR)]) IV; ruIs57[Ppie-1::gfp::tbb-2 + unc119(+)] V
S5 d	SV2085	cxTi10816(he259[Peft-3::ph::co-egfp::co-lov::tbb-2(3'UTR)]) IV; ruIs57[Ppie-1::gfp::tbb-2 + unc119(+)] V
	SV2120	lin-5(he330[lin-5::glo-epdz::mcherry(smu-1 introns)]) II; ruIs57[Ppie-1::gfp::tbb-2 + unc119(+)] V;
	SV2121	lin-5(he330[lin-5::glo-epdz::mcherry(smu-1 introns)]) II; cxTi10816(he259[Peft-3::ph::co-egfp::co-lov::tbb-2(3'UTR)]) IV; ruIs57[Ppie-1::gfp::tbb-2 + unc119(+)] V
S6 a	SV2017	ttTi5605 (he312 [long Ppie-1::FRT::glo-mCherry::cep-1 3' UTR::FRT::egl-13 NLS::glo-Cre::cep-1 3' UTR]) II
S6 b		ttTi 4348 (he295 [phsp-16.2 FLP G5D SV40 + EGL-13 NLS]) I ; ttTi5605 (he312 [long Ppie-1::FRT::glo-mCherry::cep-1 3' UTR::FRT::egl-13 NLS::glo-Cre::cep-1 3' UTR]) II ; hels105 [rps-27::plox::nls::mCherry::plox::nls::gfp] IV; Ppie-1::sv40nls::flp(G5D)::egl-13nls::tbb-2(3'UTR) + Pmyo-2::tdtomato + E. coli DNA c/w PvuII Ex ttTi 4348 (he289 [phsp-16.41 FLP G5D SV40 + EGL-13 NLS]) I ; ttTi5605 (he312 [long Ppie-1::FRT::glo-mCherry::cep-1 3' UTR::FRT::egl-13 NLS::glo-Cre::cep-1 3' UTR]) II ; hels105 [rps-27::plox::nls::mCherry::plox::nls::gfp] IV; Ppie-1::sv40nls::flp(G5D)::egl-13nls::tbb-2(3'UTR) + Pmyo-2::tdtomato + E. coli DNA c/w PvuII Ex ttTi 4348 (he299 [phsp-16.48 FLP G5D SV40 + EGL-13 NLS]) I ; ttTi5605 (he312 [long Ppie-1::FRT::glo-mCherry::cep-1 3' UTR::FRT::egl-13 NLS::glo-Cre::cep-1 3' UTR]) II ; hels105 [rps-27::plox::nls::mCherry::plox::nls::gfp] IV; Ppie-1::sv40nls::flp(G5D)::egl-13nls::tbb-2(3'UTR) + Pmyo-2::tdtomato + E. coli DNA c/w PvuII Ex
S6 c		ttTi 4348 (he295 [phsp-16.2 FLP G5D SV40 + EGL-13 NLS]) I ; ttTi5605 (he312 [long Ppie-1::FRT::glo-mCherry::cep-1 3' UTR::FRT::egl-13 NLS::glo-Cre::cep-1 3' UTR]) II; ric-8 (he280[loxN -741/loxN 4624]) IV ; Ruls57(Ppie-1::GFP::tubulin)V Ppie-1::sv40nls::flp(G5D)::egl-13nls::tbb-2(3'UTR) + Pmyo-2::tdtomato + E. coli DNA c/w PvuII Ex

	ttTi 4348 (he289 [phsp-16.41 FLP G5D SV40 + EGL-13 NLS]) I ; ttTi5605 (he312 [long Ppie-1::FRT::glo-mCherry::cep-1 3' UTR::FRT::egl-13 NLS::glo-Cre::cep-1 3' UTR]) II ; ric-8 (he280[loxN -741/loxN 4624]) IV ; Ruls57(Ppie-1::GFP::tubulin)V Ppie-1::sv40nls::flp(G5D)::egl-13nls::tbb-2(3'UTR) + Pmyo-2::tdtomato + E. coli DNA c/w PvuII Ex
	ttTi 4348 (he299 [phsp-16.48 FLP G5D SV40 + EGL-13 NLS]) I ; ttTi5605 (he312 [long Ppie-1::FRT::glo-mCherry::cep-1 3' UTR::FRT::egl-13 NLS::glo-Cre::cep-1 3' UTR]) II ; ric-8 (he280[loxN -741/loxN 4624]) IV ; Ruls57(Ppie-1::GFP::tubulin)V Ppie-1::sv40nls::flp(G5D)::egl-13nls::tbb-2(3'UTR) + Pmyo-2::tdtomato + E. coli DNA c/w PvuII Ex
S6 d	ttTi5605 (he312 [long Ppie-1::FRT::glo-mCherry::cep-1 3' UTR::FRT::egl-13 NLS::glo-Cre::cep-1 3' UTR]) II ; ric-8 (he280[loxN -741/loxN 4624]) IV ; Ruls57(Ppie-1::GFP::tubulin)V + Pmyo-2::tdtomato + E. coli DNA c/w PvuII Ex
	ttTi5605 (he312 [long Ppie-1::FRT::glo-mCherry::cep-1 3' UTR::FRT::egl-13 NLS::glo-Cre::cep-1 3' UTR]) II ; Ruls57(Ppie-1::GFP::tubulin)V ; rgs-7 (he300 [loxP in intron 2 + -CT co-mCherry::co-epdz::TEV::loxP::3xFlag]) X + Pmyo-2::tdtomato + E. coli DNA c/w PvuII Ex
	ttTi5605 (he312 [long Ppie-1::FRT::glo-mCherry::cep-1 3' UTR::FRT::egl-13 NLS::glo-Cre::cep-1 3' UTR]) II ; ric-8 (he280[loxN -741/loxN 4624]) IV ; Ruls57(Ppie-1::GFP::tubulin)V ; rgs-7 (he300 [loxP in intron 2 + -CT co-mCherry::co-epdz::TEV::loxP::3xFlag]) X + Pmyo-2::tdtomato + E. coli DNA c/w PvuII Ex
S6 e	ttTi 4348 (he289 [phsp-16.41 FLP G5D SV40 + EGL-13 NLS]) I; ttTi5605 (he312 [long Ppie-1::FRT::glo-mCherry::cep-1 3' UTR::FRT::egl-13 NLS::glo-Cre::cep-1 3' UTR]) II ; ric-8 (he280[loxN -741/loxN 4624]) IV ; Ruls57(Ppie-1::GFP::tubulin)V + Pmyo-2::tdtomato + E. coli DNA c/w PvuII Ex
	ttTi 4348 (he299 [phsp-16.48 FLP G5D SV40 + EGL-13 NLS]) I; ttTi5605 (he312 [long Ppie-1::FRT::glo-mCherry::cep-1 3' UTR::FRT::egl-13 NLS::glo-Cre::cep-1 3' UTR]) II ; ric-8 (he280[loxN -741/loxN 4624]) IV ; Ruls57(Ppie-1::GFP::tubulin)V + Pmyo-2::tdtomato + E. coli DNA c/w PvuII Ex

Supplementary Table 1 Genotypes of *C. elegans* used in this study, listed per figure

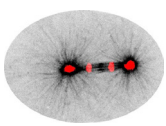

7

Summary and Discussion

Lars-Eric Fielmich and Sander van den Heuvel

Developmental Biology, Department of Biology, Faculty of Sciences, Utrecht University, Padualaan 8, 3584 CH Utrecht, The Netherlands.

The research in this thesis describes the regulation of mitotic spindle positioning in the *C. elegans* zygote. Our results expand on the known phospho-regulation of LIN-5 by cell-cycle-, polarity-, and signaling kinases (Chapter 3). We also provide mechanistic insight into the role of APR-1^{APC} as a cytoskeletal regulator that asymmetrically suppresses cortical microtubule dynamics (Chapter 4). Our work further shows that LIN-5-anchored cortical dynein is the major contributor to spindle positioning, while contribution of the microtubule plus-end tracking dynein pool is modest (Chapter 5). These mechanisms are regulated by the anterior-posterior PAR polarity axis and contribute to asymmetric spindle positioning. In Chapter 6, we identify LIN-5 as an essential activator of dynein-dependent cortical pulling forces and manipulate spindle position with controlled LIN-5 localization. Although not essential for pulling force generation, the wild type anchor Gα—GPR-1/2 is required for the normal distribution of pulling force events. We further provide evidence that RIC-8 and RGS-7 are likely to promote Gα independently, as opposed to both assisting a GTP hydrolysis cycle. And finally, our work introduces new methodologies that will hopefully prove useful to other research.

By increasing the knowledge on Gα—GPR-1/2—LIN-5—dynein regulation, the work in this thesis contributes to a more complete understanding of mitotic spindle positioning during asymmetric cell division *in vivo.* Most aspects of our results are discussed in their respective chapters. In this chapter, we discuss questions that were not addressed in the previous chapters. These concern the mechanisms by which APR-1 is recruited to the cortex, the physical strength of the cortical force generator, and the role of RIC-8 as chaperone for Gα.

Getting a hold of dynamic microtubules

Cortical pulling force generators that are about to capture an AMT encounter its growing plus-end, which is accompanied by a cloud of plus-end tracking proteins (+TIPs). These +TIPs regulate microtubule dynamics and participate in various biological processes (Akhmanova and Steinmetz, 2015). The end-binding proteins (EBP-1, -2, and -3 in *C. elegans*) are master regulators of the +TIP network. Dynein (Vaughan et al., 1999), APC^{APR-1} (Mimori-Kiyosue et al., 2000), and NuMA^{LIN-5} (Seldin et al., 2016) have been described as +TIPs and regulators of AMT anchoring and spindle positioning. The work in this thesis focusses on the cortical localization and functions of dynein, LIN-5, and APR-1. Moreover, we did not observe 'EB-like' comets of GFP-tagged APR-1 and LIN-5 in the *C. elegans* early embryo and show that the plus-end tracking population of dynein is dispensable for spindle positioning. Additionally, loss of all end-binding proteins, and hence the +TIP network, only results in mild phenotypes (Schmidt et al., 2017; Yang et al., 2017). This might hint at compensatory mechanisms. A potential strategy to uncover such redundantly acting mechanisms would be to screen for mutants that are synthetic lethal with the generated EB knock-out alleles.

APC, an 'All Processes Controlling protein'

Adenomatous polyposis coli (APC) tumor suppressor proteins localize to the cytoplasm, cortex, kinetochores, microtubules, plus-ends, and centrosomes (Aoki and Taketo, 2007; Bahmanyar et al., 2009). APC is best known for its role in canonical Wnt signaling as part of the β-catenin destruction complex together with Axin, GSK3β, and casein kinase CK1. Wnt/β-catenin signaling is a conserved regulator of developmental processes and adult tissue stem cell identity (Nusse and Clevers, 2017). Loss of APC function results in hyperactive Wnt/β-catenin signaling, can drive tumorigenesis and is found in most colorectal cancers (Wood et al., 2007). In addition to its regulating function in canonical Wnt/β-catenin signaling, APC was also found to perform

functions as a cytoskeletal regulator. As such, APC stabilizes microtubules (Reilein and Nelson, 2005; Zumbrunn et al., 2001), promotes kinetochore–microtubule interactions (Fodde et al., 2001; Kaplan et al., 2001), guides cytoskeleton polarization and directed cell migration (Etienne-Manneville and Hall, 2003; Näthke et al., 1996; Wen et al., 2004), and interacts with the actin cortex and adherens junctions through α- and β-catenin (Lu et al., 2001; McCartney et al., 2001; Su et al., 1993; Yamashita et al., 2003). Cortical APC has been described to have an instructive role in astral microtubule tethering and spindle orientation, but mechanistic insight was lacking (Lu et al., 2001; McCartney et al., 2001; Yamashita et al., 2003). We have shown that cortical levels of *C. elegans* APR-1^{APC} correlate with astral microtubule residence time. This contributes to spindle positioning in asymmetric cell division by delaying microtubule depolymerization and consequently suppressing spindle pulling forces on one side of the cell. APC's ability to interact with microtubules is inhibited upon phosphorylation by GSK3β (Zumbrunn et al., 2001). Active Wnt signaling thus not only releases β-catenin but also APC. This might explain why APC's function as microtubule regulator is influenced by upstream Wnt signaling (Schlessinger et al., 2007; Sugioka et al., 2011). This link between Wnt-signaling and APC's microtubule function may bridge the gap in our understanding of the links between hyperactive Wnt signaling and chromosome instability (Rusan and Peifer, 2008).

The molecular mechanism through which APC stabilizes microtubules remains obscure. It must be noted that most studies on cortical MT–APC interactions involve interphase cells, in which the microtubule network is less dynamic than in mitotic cells. Also, microtubules in interphase cells interact laterally with the cortex, which can result in sliding behavior (Gusnowski and Srayko, 2011). These interactions are likely to be distinct from the apparently end-on cortex–microtubule interactions during mitosis. As a next step in understanding how APR-1 affects cortical microtubule residence time, it will be interesting to know if this effect depends on the LIN-5–dynein anchor, as this might indicate whether APR-1 tethers and stabilizes microtubules directly or indirectly by modulating cortical microtubule interactions with dynein.

Another remaining question is how APR-1 is localized to the cortex. Human and *Drosophila* APC membrane recruitment proteins (AMER1 and -2) have been described to localize to the plasma membrane via association with phosphatidylinositol-4,5-biphosphate (PIP_2), recruit APC and thereby promote cortical microtubule stability (Grohmann et al., 2007; Pfister et al., 2012). However, AMER proteins are unlikely to contribute to cortical APR-1 localization in the *C. elegans* zygote as the worm does not have a clear AMER ortholog. As an additional cortical localization mechanism for APC, a link through α-catenin and actin or β-catenin and E-cadherin junctions has been described (Lu et al., 2001; McCartney et al., 2001; Yamashita et al., 2003). Cortical HMP-2$^{β\text{-catenin}}$ and HMR-1$^{E\text{-cadherin}}$ localize to the anterior half of the zygote during polarization (Munro et al., 2004). This asymmetry is however only transient and a passive effect of the anterior-directed actomyosin flows. Unless the association between HMP-2 or HMR-1 with APR-1 is asymmetrically regulated, these proteins are unlikely to mediate cortical APR-1 localization. Moreover, we found that depletion of WRM-1$^{β\text{-catenin}}$ did not affect cortical APR-1 localization.

Human and *Drosophila* APC can bind monomeric and filamentous actin (F-actin) directly and stimulate actin nucleation together with the Formin Dia (Jaiswal et al., 2013; Moseley et al., 2007; Okada et al., 2010). Mutant cells that specifically lack the actin nucleation function of APC are defective in directed migration (Juanes et al., 2017). It is unknown if *C. elegans* APR-1 interacts with actin, but the fact that this interaction is conserved between *Drosophila* and humans and that APR-1 is also required for directed cell migration suggests that APR-1 interacts with actin (Hoier et al., 2000).

Actomyosin is asymmetrically localized and enriched at the anterior cortex of mitotic *C. elegans* zygotes (Strome, 1986). This actomyosin polarity is reciprocally regulated by PAR polarity

(Munro et al., 2004). If APR-1 interacts with actin and promotes its nucleation, anterior F-actin and APR-1 could promote each other's anterior enrichment, although APR-1 asymmetry is maintained when the actin asymmetry is lost at the end of mitosis. Notably, both APR-1 and F-actin are negative regulators of cortical pulling force generation (Berends et al., 2013; Sugioka et al., 2017). According to the prevalent model, F-actin dampens pulling force generation by increasing cortical rigidity: force generators are less able to maintain contacts with depolymerizing microtubules in a more rigid cortex (Kozlowski et al., 2007; Redemann et al., 2010; Spiro et al., 2014). This effect is unlikely to be related to the increased cortical residence by APR-1 that we described. Nevertheless, actin could provide the cortical docking site for APR-1, which thereby tethers AMTs to the actin cortex.

Many hands make light work

Cortical force generators can only maintain the interaction with a shrinking AMT for approximately one second (Kozlowski et al., 2007), suggesting that attachments are lost continuously. The impact of pulling on the complex depends on cortical rigidity and can be dampened by invagination of the plasma membrane (Redemann et al., 2010). These invaginations are increased in number and length when the actomyosin cortex is weaker, for instance following *nmy-2* (non-muscle myosin II) knock-down. This enhances pulling force generation by prolonging the cortical anchoring of dynamic AMTs (Afshar et al., 2010; Berends et al., 2013; Kozlowski et al., 2007; Redemann et al., 2010). Why are these cortical AMT—force generator interactions lost? Are force generators not strong enough to wield 5 pN pulling force generated by a cortical dynein—MT interaction (Laan et al., 2012)? The force generated by a dynein-anchored microtubule is less than the force generated by a free depolymerizing microtubule (30-65 pN) (Grishchuk et al., 2005). This difference could be caused by the observed slowing effect of barrier-bound dynein on microtubule depolymerization (Laan et al., 2012). Alternatively, protein-protein interactions or dynein's stalling force are limiting for cortical pulling force generation. To answer this question, we discuss the potential strength of the cortical force generator.

Starting from the base: how strong is the Gα membrane anchor? The $G\alpha_{i/o}$ isoforms involved in mitotic spindle positioning all contain the consensus for N-terminal myristoylation and palmitoylation in addition to a polybasic stretch that enhances membrane affinity (Aicart-Ramos et al., 2011; Marrari et al., 2007). A single myristoylated protein has an adhesion force to a lipid bilayer of 50 pN (Desmeules et al., 2002), so the Gα membrane anchor is definitely strong enough to withstand 5 pN of pulling force. The strengths of the Gα—GoLoco, TPR—NuMA, and NuMA—dynein interactions are not known. Considering that protein—protein interaction rupture forces range from a dozen to several hundred pN (Li et al., 2014; Malkovskiy et al., 2015; Zhang et al., 2009), they are not likely to be a limiting factor in force generation. How strong then is the dynein motor? Measurements of dynein's stalling force vary, but range around 5 pN (Roberts et al., 2013), similar to the force generated by a cortical force generator (Laan et al., 2012). Thus, the ability of dynein to maintain contact with the shrinking AMT may be limiting.

It has been proposed that three dynein motors can bind a MT end-on (Laan et al., 2012). This potentially distributes the force of a single depolymerizing AMT over multiple complexes and amplifies the force generated by a single anchored AMT. The NuMA—LGN interaction has been characterized with crystal structure resolution and has a 1:1 stoichiometry (Culurgioni et al., 2011; Zhu et al., 2011). However, LIN-5 and NuMA have been reported to form homodimers, which together may interact with two GPR-1/2 and LGN proteins. Another amplification occurs at the level of the Gα interaction as biochemical studies and crystal structures indicate that the four GoLoco domains of LGN can each bind a Gα protein simultaneously (Jia et al., 2012). *Drosophila* Pins contains three and *C. elegans* GPR-1/2 one or two GoLoco domains. Therefore, the total

number of components that anchor an AMT could theoretically be 3 x dynein, 6 x NuMA$^{Mud/LIN-5}$, 6 x LGN$^{Pins/GPR-1/2}$, and 24 (human), 18 (*Drosophila*), or 6 to 12 (*C. elegans*) Gα molecules to share the load. It must however be noted that we did not observe increased fluorescence signals of tagged dynein and LIN-5 at the sites of cortical AMT attachment and membrane invaginations (Chapter 5), so these numbers are somewhat speculative.

In yeast spindle positioning, dynein binding and cortical anchoring are the function of a single protein: Num1 (*S. cerevisiae*), Mcp5 (*S. pombe*), or ApsA (*A. nidulans*). These proteins contain an N-terminal coiled-coil domain for dynein binding and a C-terminal pleckstrin-homology (PH) domain for membrane localization (Ananthanarayanan, 2016). Again, the strength of the interaction with dynein is not known, but a PLC-δ1 PH domain—PIP2 interaction can withstand up to 190 pN (Malkovskiy et al., 2015). The PH::LOV2 anchor used in chapter 6 of this thesis contains this PLC-δ1 PH domain and is therefore also not likely to introduce a bottle neck for force generation. Taken together, dynein's strength may be the limiting factor in pulling force generation and the reason that measured dynein-dependent pulling forces are considerably lower than that of a free depolymerizing microtubule.

RIC-8 GEF function: a red herring or conserved regulatory mechanism?

One aspect of spindle positioning that has continued to puzzle researchers ever since it was first described is the role of the GEF RIC-8 and its regulation of Gα. The discovery of a noncanonical function of $G\alpha_{i/o}$·GDP as physical membrane anchor and the conserved regulation by the GEF RIC-8 and GAP RGS-7 in spindle positioning strongly suggested a role for Gα-signaling. Despite the extensive data from many models and systems, a coherent function for RIC-8 that explains the observed phenotypes has not emerged. Most *in vivo* data for RIC-8 function in asymmetric cell division comes from *Drosophila* neuroblasts (NBs) and sensory organ precursor (SOP) cells. An important observation in these studies was that *Ric8A* mutant cells were defective in Gα plasma membrane targeting and in some cases showed globally reduced Gα protein levels (David et al., 2005; Hampoelz et al., 2005; Wang et al., 2005). Similar results were obtained in mouse embryonic stem cells (Gabay et al., 2011) and cell-free lysates (Chan et al., 2013). Interestingly, in *Drosophila* SOP cells and the *C. elegans* early embryo, RIC-8 only promotes plasma membrane targeting of $G\alpha_i^{GPA-16}$ and not of $G\alpha_o^{GOA-1}$ (Afshar et al., 2005; David et al., 2005). Based on these findings, RIC-8 was suggested to function in early Gα biosynthesis. This was eagerly accepted, because no chaperone had yet been identified that aids in the complex folding and intracellular transport of Gα proteins.

As an argument against a function for RIC-8 in early Gα biosynthesis, depletion of GPB-1^{Gβ} was concluded to be epistatic to loss of RIC-8 (Afshar et al., 2004). In addition, RIC-8 preferentially binds Gα in complex with LGN—NuMA (Tall and Gilman, 2005). These findings place RIC-8 function downstream of the assembly of the Gαβγ and Gα—LGN—NuMA trimers. Another hint that RIC-8 may regulate mature and not nascent Gα comes from work describing that RIC-8 prevents Gα polyubiquitination at the C-terminus and subsequent proteasomal degradation (Chishiki et al., 2013; Nagai et al., 2010). Thereby, RIC-8 promotes stability of the Gα protein, but not as a folding chaperone. To investigate the RIC-8—Gα interaction in detail, hydrogen-deuterium exchange mass spectrometry (HDX-MS), a method to assess protein surface exposure, was used. This revealed that the Gα C-terminus (that is ubiquitinated in the absence of RIC-8) is strongly shielded by RIC-8 (Kant et al., 2016). In conclusion, most RIC-8 data is in line with a function for RIC-8 as chaperone, but not in early Gα biosynthesis.

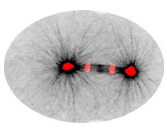

Gα: ·di-P or ·tri-P?

How should RIC-8's 'original' function as a GEF be placed in the mechanism of spindle positioning? In support of a function of Gα·GTP and RIC-8 GEF function in spindle positioning, over-expression of Gα·GTP (Q205L) influenced spindle orientation in SOP cells (Schaefer et al., 2001). In addition, one of the $Pins^{LGN}$ GoLoco domains was shown to have a strong preference for $G\alpha_o$·GTP (Kopein and Katanaev, 2009; Yoshiura et al., 2012). These findings suggest that Gα·GTP and RIC-8 GEF function contribute to spindle positioning through formation of the Gα—$Pins^{LGN}$—Mud^{NuMA} complex. To test the function of Gα·GTP, pertussis toxin (PTX) is commonly used to ribosylate Gα·GDP and prevent the exchange of GDP for GTP (Darby and Falkow, 2001; Mangmool and Kurose, 2011). PTX activity disturbs spindle positioning in HeLa and MDCK cells in culture, *Drosophila* NBs, and chick neuroepithelium cells (Kotak et al., 2012, 2014; Peyre et al., 2011; Woodard et al., 2010; Yoshiura et al., 2012). However, it is disputed whether ribosylated Gα·GDP can interact with GoLoco domains (Machicoane et al., 2014; Woodard et al., 2010), raising the question of whether the observed effect of PTX is the result of disturbed Gα·GTP signaling or Gα—$Pins^{LGN}$ interaction. Moreover, NBs and SOP cells were later shown to also depend on canonical G-protein signaling to align the cell polarity axis with tissue polarity (Katanaev et al., 2005; Yoshiura et al., 2012). This makes it difficult to distinguish between a direct effect of Gα·GTP signaling and an indirect effect of disturbed cell polarity in the observed spindle orientation phenotypes. Therefore, it has remained inconclusive whether Gα·GTP plays a role in spindle positioning. The controlled localization of endogenous RIC-8 enabled the direct testing of RIC-8 function and provides conclusive evidence that RIC-8 does not promote cortical pulling force generation directly (Chapter 6). Moreover, the fact that Gα could be replaced by PH::LOV rejects essential Gα specific functions such as Gα·GTP signaling.

The *in vitro* observed GEF function of RIC-8 might thus simply be a side effect of RIC-8 chaperone function and a red herring that distracted researchers from its true function. In support of this idea, HDX-MS of free versus RIC-8-bound Gα indicated that RIC-8 imposes extensive global conformational changes on Gα during GDP release (Kant et al., 2016). This is a much more elaborate (and slower) nucleotide exchange than applied by a G-protein coupled receptor GEF. This explains why RIC-8 is an inefficient GEF that only accelerates Gα nucleotide exchange twelve fold (Thomas et al., 2008).

Does the search for RIC-8's function get a fatty tail?

Since RIC-8 functions neither as GEF nor as folding chaperone, then what is its function? RIC-8's positive effect on cellular Gα levels can be explained by the shielding of Gα by RIC-8 against C-terminal polyubiquitination. It ten remains unknown how it promotes Gα membrane localization. This is possibly explained by a chaperone function for mature Gα, for instance in the regulation of Gα acylation. Gα proteins are co-translationally myristoylated on the N-terminal glycine after cleavage of the starting methionine. This occurs on free ribosomes in the cytoplasm and offers a moderate membrane affinity. Gα and Gβγ are reciprocally required for membrane targeting: formation of the heterotrimeric G-protein offers an additional membrane targeting signal because Gγ is also acylated in the cytoplasm by enzymatic addition of a C-terminal isoprenyl or geranylgeranyl group. In addition, most Gα proteins are also palmitoylated at their N-terminus (Evanko et al., 2000; Marrari et al., 2007; Wedegaertner et al., 1995). Palmitoylation of proteins is carried out by palmitoyl acyltransferases (PATs) or DHHC proteins (for their characteristic Asp-His-His-Cys motif). DHHC proteins are transmembrane proteins that localize to all cellular membranes, but the Golgi apparatus appears the predominant site of palmitoylation (Salaun et al., 2010). Unique among acylations, palmitoylation is reversible by cytoplasmic acyl palmitate thioesterases (APT). The human genome contains 25 DHHC and three APT genes (Salaun et al., 2010). For *C. elegans*, 15 DHHC and two APT coding genes have been annotated

(Edmonds and Morgan, 2014). There is no precise consensus sequence for palmitoylation: palmitoylation seems to occur on cysteines that are within reach of the membrane-bound DHHC proteins and thus near prior acylations or transmembrane domains (Charollais and Van Der Goot, 2009; Degtyarev et al., 1994; Rodenburg et al., 2017). Multi-acylation strongly increases membrane-affinity. Hence, spatial regulation of palmitoylation/depalmitoylation cycling affects protein sorting to different membrane compartments. How dynamic palmitoylation of Ras and G-proteins affects shuttling between different membrane compartments and signaling dynamics is described in several studies (Aicart-Ramos et al., 2011; Jia et al., 2014; Rocks et al., 2005; Siegel et al., 2009). Could RIC-8 function as part of the dynamic Gα palmitoylation/depalmitoylation cycle?

Depalmitoylation reduces Gα membrane affinity and shifts the equilibrium to a larger protein fraction in the cytosol. From there, the protein stochastically associates with any membrane, until it is repalmitoylated on the Golgi membrane from where it is shuttled back to the plasma membrane (Jia et al., 2014; Rocks et al., 2005). The retrograde shuttling of depalmitoylated Gα from plasma membrane to Golgi possibly requires a chaperone protein to cage the remaining hydrophobic fat modification (Meder and Simons, 2005). Multiple observations could support a role for RIC-8 as chaperone that guides shuttling depalmitoylated Gα through the cytoplasm. Firstly, RIC-8 was found to bind and strongly shield the Gα N-terminus, where the acylations occur (Kant et al., 2016). Such a shielding/caging of remaining lipid moieties was proposed to be required for efficient cytosolic Gα shuttling (Meder and Simons, 2005). Moreover, the loss of Gα plasma membrane localization upon RIC-8 depletion is most striking for $G\alpha_q$, which is only palmitoylated (not myristoylated) and would be more sensitive to a defective palmitoylation cycle (Gabay et al., 2011). Direct experimental evidence is currently lacking for a function for RIC-8 in dynamic Gα palmitoylation. Nevertheless, it is attractive to propose such a function for RIC-8 in chaperoning shuttling Gα that undergoes de-/repalmitoylation because it fits with most published observations and explains a chaperone function for mature Gα, after heterotrimeric G-protein and cortical force generator assembly. This hypothesis could be tested by Gα localization studies and palmitoylation profiling mass spectrometry of native Gα in normal versus *ric-8* loss of function cells (Rodenburg et al., 2017).

Optogenetic tools lighten up experimental biology

The work described in this thesis has deepened our understanding of the regulation of mitotic spindle positioning. In addition, the described tools and methods may open new avenues for future research. The expansion of the light-induced protein-protein interactions toolkit holds great promises for experimental biology (van Bergeijk et al., 2015; Bugaj et al., 2016; Johnson and Toettcher, 2018; Strickland et al., 2012). Although various applications of light-controlled dimerization have been reported, the field is still at an early stage. For instance, gain of function optogenetics in a loss of function genetic background should be the standard for optogenetic localization experiments and was recently pinpointed as an outstanding challenge for the field (Johnson and Toettcher, 2018). Also, control of endogenous proteins in a metazoan had not been reported.

One question that could now be addressed is how the mitotic spindle influences cell cleavage plane positioning. The mitotic spindle sends furrow stimulating signals from the spindle midzone and a negative, cortical relaxing signal from the spindle asters (Galli and van den Heuvel, 2008; Roubinet and Cabernard, 2014). These two signals redundantly position the cleavage furrow (Bringmann et al., 2007; Dechant and Glotzer, 2003). The equatorial stimulating signal is mediated by the centralspindlin complex (Dechant and Glotzer, 2003; Somers and Saint, 2003). The astral relaxing signal depends on AMT anchoring by cortical force generators and their

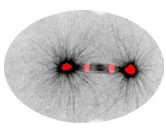

relative absence around the site of furrow induction (Bringmann et al., 2007; Galli et al., 2011b; Kiyomitsu and Cheeseman, 2012; Kotak et al., 2014). The current model assumes that centrosome separation and the local minimum of microtubule density at the cortex trigger furrow formation (Dechant and Glotzer, 2003). Such a model can ideally be tested with light-controlled localization of proteins by manipulating aster position.

Reconstitute pulling force generation to truly understand it

A more in-depth understanding of cortical pulling force generation is expected from the field of biophysics. Although the light-controlled localization studies described in chapter 6 provide interesting insights, *in vivo* systems remain inherently complex. Exactly how cortical force generators are assembled and generate pulling forces that position the spindle can be scrutinized in *in vitro* reconstitution studies to come (Vleugel et al., 2016b, 2016a). Such studies may reveal the composition and stoichiometry of the entire complex and if LIN-5^{NuMA} is an adapter that brings together dynein and dynactin in a manner similar to BICD2, Spindly, and Hook3 (McKenney et al., 2014; Schlager et al., 2014). It will also be interesting to know if the simultaneous interaction of multiple dynein motors with a single depolymerizing microtubule synergistically generates pulling force, to better understand the source of energy for pulling force generation. Most excitingly, the detailed structure of an intact cortical force generator may be in reach, now that structures of large complexes such as dynein—dynactin—BICD in interaction with a microtubule have been solved using Cryo EM/ET (Grotjahn et al., 2018; Urnavicius et al., 2018).

The next frontier

Despite the beauty and relevance of molecular cell biology studies, studying a process one phosphorylation at a time may not ultimately lead to a complete understanding of the studied process. If anything, mitotic spindle positioning has proven to be complex. Therefore, combining molecular cell biology with systems biology and model building appears to be an important next step towards an integrated understanding of the complex processes involved. One such effort is the generation of a mitotic cell atlas (Mitocheck) using an automated, high-throughput imaging platform (Cai et al., 2017). For this inspiring endeavor, a selection of 600 proteins has been endogenously tagged with a fluorescent protein to be monitored by high resolution microscopy and fluorescence correlation microscopy in dividing cells. When complete, this uniform dataset can be combined with other available data (such as phosphorylation) and will hopefully greatly advance our understanding of mitotic cell division. Similar screens can then be performed in asymmetrically dividing cells to create an integrated model of asymmetric spindle positioning. And one day, researchers may prove to understand cell division by recreating it as is being attempted by the 'Building s Synthetic Cell' consortium (BaSyC).

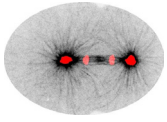

&

Addendum

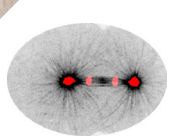

Literature references

Afshar, K., Willard, F.S., Colombo, K., Johnston, C.A., Mccudden, C.R., Siderovski, D.P., Go, P., Hill, C., and Carolina, N. (2004). RIC-8 Is Required for GPR-1/2-Dependent Ga Function during Asymmetric Division of *C. elegans* Embryos. Cell *119*, 219–230.

Afshar, K., Willard, F.S., Colombo, K., Siderovski, D.P., and Gönczy, P. (2005). Cortical localization of the Galpha protein GPA-16 requires RIC-8 function during *C. elegans* asymmetric cell division. Development *132*, 4449–4459.

Afshar, K., Werner, M.E., Tse, Y.C., Glotzer, M., and Gönczy, P. (2010). Regulation of cortical contractility and spindle positioning by the protein phosphatase 6 PPH-6 in one-cell stage *C. elegans* embryos. Development *137*, 237–247.

Ahier, A., and Jarriault, S. (2014). Simultaneous expression of multiple proteins under a single promoter in Caenorhabditis elegans via a versatile 2A-based toolkit. Genetics *196*, 605–613.

Aicart-Ramos, C., Valero, R.A., and Rodriguez-Crespo, I. (2011). Protein palmitoylation and subcellular trafficking. Biochim. Biophys. Acta - Biomembr. *1808*, 2981–2994.

Akhmanova, A., and Steinmetz, M.O. (2015). Control of microtubule organization and dynamics: Two ends in the limelight. Nat. Rev. Mol. Cell Biol. *16*, 711–726.

Albertson, G. (1978). Cell Cycling and DNA Replication in a Mutant in the Nematode Caenorhabditis Blocked in Cell Division elegans. Dev. Biol. *178*, 165–178.

Albertson, D.G., Sulston, J.E., and White, J.G. (1978). Cell cycling and DNA replication in a mutant blocked in cell division in the nematode Caenorhabditis elegans. Dev. Biol. *63*, 165–178.

Ananthanarayanan, V. (2016). Activation of the motor protein upon attachment: Anchors weigh in on cytoplasmic dynein regulation. BioEssays *38*, 514–525.

Ananthanarayanan, V., Schattat, M., Vogel, S.K., Krull, A., Pavin, N., and Tolić-Nørrelykke, I.M. (2013). Dynein Motion Switches from Diffusive to Directed upon Cortical Anchoring. Cell *153*, 1526–1536.

Aoki, K., and Taketo, M.M. (2007). Adenomatous polyposis coli (APC): a multi-functional tumor suppressor gene. J. Cell Sci. *120*, 3327–3335.

Arribere, J. a, Bell, R.T., Fu, B.X., Artiles, K.L., Hartman, P.S., and Fire, A.Z. (2014). Efficient Marker-Free Recovery of Custom Genetic Modifications with CRISPR/Cas9 in Caenorhabditis elegans. Genetics *198*, 837–846.

Bahmanyar, S., Nelson, W.J., and Barth, A.I.M. (2009). Role of APC and its Binding Partners in Regulating Microtubules in Mitosis. Adv Exp Med Biol *656*, 65–74.

Baldwin, A.T., and Phillips, B.T. (2014). The tumor suppressor APC differentially regulates multiple -catenins through the function of axin and CKI during *C. elegans* asymmetric stem cell divisions. J. Cell Sci. *127*, 2771–2781.

Ban, R., Matsuzaki, H., Akashi, T., Sakashita, G., Taniguchi, H., Park, S.Y., Tanaka, H., Furukawa, K., and Urano, T. (2009). Mitotic regulation of the stability of microtubule plus-end tracking protein EB3 by ubiquitin ligase SIAH-1 and aurora mitotic kinases. J. Biol. Chem. *284*, 28367–28381.

Barth, A.I.M., Caro-Gonzalez, H.Y., and Nelson, W.J. (2008). Role of adenomatous polyposis coli (APC) and microtubules in directional cell migration and neuronal polarization. Semin. Cell Dev. Biol. *19*, 245–251.

Beamish, H., de Boer, L., Giles, N., Stevens, F., Oakes, V., and Gabrielli, B. (2009). Cyclin A/cdk2 regulates adenomatous polyposis coli-dependent mitotic spindle anchoring. J. Biol. Chem. *284*, 29015–29023.

Bei, Y., Hogan, J., Berkowitz, L. a, Soto, M., Rocheleau, C.E., Pang, K.M., Collins, J., and Mello, C.C. (2002). SRC-1 and Wnt signaling act together to specify endoderm and to control cleavage orientation in early *C. elegans* embryos. Dev. Cell *3*, 113–125.

Bellaïche, Y., Radovic, A., Woods, D.F., Hough, C.D., Parmentier, M.L., O'Kane, C.J., Bryant, P.J., and Schweisguth, F. (2001). The Partner of Inscuteable/Discs-large complex is required to establish planar polarity during asymmetric cell division in Drosophila. Cell *106*, 355–366.

Berends, C.W.H., Munoz, J., Portegijs, V., Schmidt, R., Grigoriev, I., Boxem, M., Akhmanova, a., Heck, a. J.R., and van den Heuvel, S. (2013). F-actin asymmetry and the ER-associated TCC-1 protein contribute to stereotypic spindle movements in the *C. elegans* embryo. Mol. Biol. Cell *24*.

van Bergeijk, P., Hoogenraad, C.C., and Kapitein, L.C. (2015). Right Time, Right Place: Probing the Functions of Organelle Positioning. Trends Cell Biol. *26*, 121–134.

Bergmann, D.C., Lee, M., Robertson, B., Meng-Fu, B., Rose, L.S., and Wood, W.B. (2003). Bergmann - Embryonic handedness choice in *C. elegans* involves the Gα protein GPA-16.pdf. Development *130*, 5731–5740.

Berlin, V., Styles, C.A., and Fink, G.R. (1990). BIK1, a protein required for microtubule function during mating and mitosis in Saccharomyces cerevisiae, colocalizes with tubulin. J. Cell Biol. *111*, 2573–2586.

Berrueta, L., Tirnauer, J.S., Schuyler, S.C., Pellman, D., and Bierer, B.E. (1999). The APC-associated protein EB1 associates with components of the dynactin complex and cytoplasmic dynein intermediate chain. Curr. Biol. *9*, 425–428.

Bieling, P., Laan, L., Schek, H., Munteanu, E.L., Sandblad, L., Dogterom, M., Brunner, D., and Surrey, T. (2007). Reconstitution of a microtubule plus-end tracking system in vitro. Nature *450*, 1100–1105.

Bisgrove, S.R., Lee, Y.-R.J., Liu, B., Peters, N.T., and Kropf, D.L. (2008). The microtubule plus-end binding protein EB1 functions in root responses to touch and gravity signals in Arabidopsis. Plant Cell *20*, 396–410.

Bosveld, F., Markova, O., Guirao, B., Martin, C., Wang, Z., Pierre, A., Balakireva, M., Gaugue, I., Ainslie, A., Christophorou, N., et al. (2016). Epithelial tricellular junctions act as interphase cell shape sensors to orient mitosis. Nature *530*, 495–498.

Bowman, S.K., Neumüller, R. a, Novatchkova, M., Du, Q., and Knoblich, J. a (2006). The Drosophila NuMA Homolog Mud regulates spindle orientation in asymmetric cell division. Dev. Cell *10*, 731–742.

Boxem, M., Srinivasan, D.G., and van den Heuvel, S. (1999). The Caenorhabditis elegans gene ncc-1 encodes a cdc2-related kinase required for M phase in meiotic and mitotic cell divisions, but not for S phase. Development *126*, 2227–2239.

Boxem, M., Maliga, Z., Klitgord, N., Li, N., Lemmens, I., Mana, M., de Lichtervelde, L., Mul, J.D., van de Peut, D., Devos, M., et al. (2008). A Protein Domain-Based Interactome Network for *C. elegans* Early Embryogenesis. Cell *134*, 534–545.

Brenner, S. (1974). The genetics of Caenorhabditis elegans. Genetics *77*, 71–94.

Bringmann, H., Cowan, C.R., Kong, J., and Hyman, A. a (2007). LET-99, GOA-1/GPA-16, and GPR-1/2 are required for aster-positioned cytokinesis. Curr. Biol. *17*, 185–191.

Bugaj, L.J., O'Donoghue, G.P., and Lim, W.A. (2016). Interrogating cellular perception and decision making with optogenetic tools. J. Cell Biol. 1–4.

Cabernard, C., Prehoda, K.E., and Doe, C.Q. (2010). A spindle-independent cleavage furrow positioning pathway. Nature *467*, 91–94.

Cai, Y., Hossain, J., Heriche, J.-K., Politi, A.Z., Walther, N., Koch, B., Wachsmuth, M., Nijmeijer, B., Moritz, K., Kavur, M.M., et al. (2017). An experimental and computational framework to build a dynamic protein atlas for human cell division. BioRxiv Prepr. 1–1.

Carter, A.P., Diamant, A.G., and Urnavicius, L. (2016). How dynein and dynactin transport cargos: A structural perspective. Curr. Opin. Struct. Biol. *37*, 62–70.

Carvalho, A., Olson, S.K., Gutierrez, E., Zhang, K., Noble, L.B., Zanin, E., Desai, A., Groisman, A., and Oegema, K. (2011). Acute drug treatment in the early *C. elegans* embryo. PLoS One *6*, e24656.

Chan, P., Thomas, C.J., Sprang, S.R., and Tall, G.G. (2013). Molecular chaperoning function of Ric-8 is to fold nascent heterotrimeric G protein α subunits. Proc. Natl. Acad. Sci. U. S. A. *110*, 3794–3799.

Chanet, S., Sharan, R., Khan, Z., and Martin, A.C. (2017). Myosin 2-Induced Mitotic Rounding Enables Columnar Epithelial Cells to Interpret Cortical Spindle Positioning Cues. Curr. Biol. *27*, 1–9.

Charollais, J., and Van Der Goot, F.G. (2009). Palmitoylation of membrane proteins (Review). Mol. Membr. Biol. *26*, 55–66.

Cheeseman, I.M., MacLeod, I., Yates, J.R., Oegema, K., and Desai, A. (2005). The CENP-F-like proteins HCP-1 and HCP-2 target CLASP to kinetochores to mediate chromosome segregation. Curr. Biol. *15*, 771–777.

Chen, C., Fenk, L. a, and de Bono, M. (2013). Efficient genome editing in Caenorhabditis elegans by CRISPR-targeted homologous recombination. Nucleic Acids Res. *41*, e193.

Chishiki, K., Kamakura, S., Yuzawa, S., Hayase, J., and Sumimoto, H. (2013). Ubiquitination of the heterotrimeric G protein α subunits Gαi2 and Gαq is prevented by the guanine nucleotide exchange factor Ric-8A. Biochem. Biophys. Res. Commun. *435*, 414–419.

Cianfrocco, M.A., DeSantis, M.E., Leschziner, A.E., and Reck-Peterson, S.L. (2015). Mechanism and Regulation of Cytoplasmic Dynein. Annu. Rev. Cell Dev. Biol. *31*, 83–108.

Clevers, H., and Nusse, R. (2012). Wnt/β-catenin signaling and disease. Cell *149*, 1192–1205.

Cochella, L., Tursun, B., Stefanakis, N., Rahe, D., Carrera, I., and Hobert, O. (2013). Robust expression of transgenes in the *C. elegans* germline through a simple microinjectino protocol. Worm Breeder's Gaz. *19*.

Colombo, K., Grill, S.W., Kimple, R.J., Willard, F.S., Siderovski, D.P., and Gönczy, P. (2003). Translation of polarity cues into asymmetric spindle positioning in Caenorhabditis elegans embryos. Science *300*, 1957–1961.

Couwenbergs, C., Spilker, A.C.A., and Gotta, M. (2004). Control of Embryonic Spindle Positioning and GÎ± Activity by *C. elegans* RIC-8. Curr. Biol. *14*, 1871–1876.

Couwenbergs, C., Labbé, J.-C., Goulding, M., Marty, T., Bowerman, B., and Gotta, M. (2007). Heterotrimeric G protein signaling functions with dynein to promote spindle positioning in *C. elegans*. J. Cell Biol. *179*, 15–22.

Cowan, C.R., and Hyman, A. a (2007). Acto-myosin reorganization and PAR polarity in *C. elegans*. Development *134*, 1035–1043.

Crowder, M.E., Flynn, J.R., McNally, K.P., Cortes, D.B., Price, K.L., Kuehnert, P. a., Panzica, M.T., Andaya, a., Leary, J. a., and McNally, F.J. (2015). Dynactin-dependent cortical dynein and spherical spindle shape correlate temporally with meiotic spindle rotation in Caenorhabditis elegans. Mol. Biol. Cell *26*, 3030–3046.

Culurgioni, S., Alfieri, A., Pendolino, V., Laddomada, F., and Mapelli, M. (2011). Inscuteable and NuMA proteins bind competitively to Leu-Gly-Asn repeat-enriched protein (LGN) during asymmetric cell divisions. Proc. ....

Culurgioni, S., Mari, S., Bonetti, P., Gallini, S., Bonetto, G., Brennich, M., Round, A., Nicassio, F., and Mapelli, M. (2018). Insc:LGN tetramers promote asymmetric divisions of mammary stem cells. Nat. Commun. *9*, 1025.

Darby, C., and Falkow, S. (2001). Mimicry of a G Protein Mutation by Pertussis Toxin Expression in Transgenic Caenorhabditis elegans. *69*, 6271–6275.

David, N.B., Martin, C. a, Segalen, M., Rosenfeld, F., Schweisguth, F., and Bellaïche, Y. (2005). Drosophila Ric-8 regulates Galphai cortical localization to promote Galphai-dependent planar orientation of the mitotic spindle during asymmetric cell division. Nat. Cell Biol. *7*, 1083–1090.

Davidson, G., Shen, J., Huang, Y.L., Su, Y., Karaulanov, E., Bartscherer, K., Hassler, C., Stannek, P., Boutros, M., and Niehrs, C. (2009). Cell Cycle Control of Wnt Receptor Activation. Dev. Cell *17*, 788–799.

Davis, M.W., Morton, J.J., Carroll, D., and Jorgensen, E.M. (2008). Gene activation using FLP recombinase in *C. elegans*. PLoS Genet. *4*.

Dechant, R., and Glotzer, M. (2003). Centrosome Separation and Central Spindle Assembly Act in Redundant Pathways that Regulate Microtubule Density and Trigger Cleavage Furrow Formation. Dev. Cell *4*, 333–344.

Degtyarev, M.Y., Spiegel, A.M., and Jones, T.L.Z. (1994). Palmitoylation of a G protein αi subunit requires membrane localization not myristoylation. J. Biol. Chem. *269*, 30898–30903.

Desmeules, P., Grandbois, M., Bondarenko, V.A., Yamazaki, A., and Salesse, C. (2002). Measurement of membrane binding between recoverin, a calcium-myristoyl switch protein, and lipid bilayers by AFM-based force spectroscopy. Biophys. J. *82*, 3343–3350.

Dickinson, D.J., Ward, J.D., Reiner, D.J., and Goldstein, B. (2013). Engineering the Caenorhabditis elegans genome using Cas9-triggered homologous recombination. Nat. Methods *10*, 1028–1034.

Dickinson, D.J., Pani, A.M., Heppert, J.K., and Higgins, C.D. (2015). Streamlined genome engineering with a self-excising drug selection cassette. Genetics 1–33.

Dogterom, M., and Yurke, B. (1997). Measurement of the force-velocity relation for growing microtubules. Science (80-.). *278*, 856–860.

Draviam, V.M., Shapiro, I., Aldridge, B., and Sorger, P.K. (2006). Misorientation and reduced stretching of aligned sister kinetochores promote chromosome missegregation in EB1- or APC-depleted cells. EMBO J. *25*, 2814–2827.

Du, Q., and Macara, I.G.G. (2004). Mammalian Pins is a conformational switch that links NuMA to heterotrimeric G proteins. Cell *119*, 503–516.

Du, Q., Stukenberg, P.T., and Macara, I.G. (2001). A mammalian Partner of inscuteable binds NuMA and regulates mitotic spindle organization. Nat. Cell Biol. *3*, 1069–1075.

Duellberg, C., Trokter, M., Jha, R., Sen, I., Steinmetz, M.O., and Surrey, T. (2014). Reconstitution of a hierarchical +TIP interaction network controlling microtubule end tracking of dynein. Nat. Cell Biol.

Edgar, L.G. (1995). Chapter 13 Blastomere Culture and Analysis. In Cuenorhubditis Elegans: Modern Biologcal Analysis of an Organism, H.F. Epstein, and D.C.B.T.-M. in C.B. Shakes, eds. (Academic Press), pp. 303–321.

Edmonds, M.J., and Morgan, A. (2014). A systematic analysis of protein palmitoylation in Caenorhabditis elegans. 1–16.

Eliceiri, K., Schneider, C.A., Rasband, W.S., and Eliceiri, K.W. (2012). NIH Image to ImageJ : 25 years of image analysis HISTORICAL commentary NIH Image to ImageJ : 25 years of image analysis. Nat. Methods *9*, 671–675.

Ellefson, M.L., and McNally, F.J. (2011). CDK-1 inhibits meiotic spindle shortening and dynein-dependent spindle rotation in *C. elegans*. J. Cell Biol. *193*, 1229–1244.

Errico, A., Deshmukh, K., Tanaka, Y., Pozniakovsky, A., and Hunt, T. (2010). Identification of substrates for cyclin dependent kinases. Adv. Enzyme Regul. *50*, 375–399.

Etienne-Manneville, S. (2009). APC in cell migration. Adv Exp Med Biol 30–40.

Etienne-Manneville, S., and Hall, A. (2003). Cdc42 regulates GSK-3 b and adenomatous polyposis coli to control cell polarity. Nature *421*, 753–756.

Evanko, D.S., Thiyagarajan, M.M., and Wedegaertner, P.B. (2000). Interaction with Gbeta gamma Is Required for Membrane Targeting and Palmitoylation of Galpha s and Galpha q. J. Biol. Chem. *275*, 1327–1336.

Ferreira, J.G., Pereira, A.J., Akhmanova, A., and Maiato, H. (2013). Aurora B spatially regulates EB3 phosphorylation to coordinate daughter cell adhesion with cytokinesis. J. Cell Biol. *201*, 709–724.

Fietz, S. a, and Huttner, W.B. (2011). Cortical progenitor expansion, self-renewal and neurogenesis-a polarized perspective. Curr. Opin. Neurobiol. *21*, 23–35.

Fire, A., Xu, S., Montgomery, M.K., Kostas, S.A., Driver, S.E., and Mello, C.C. (1998). Potent and specific genetic interference by double-stranded RNA in Caenorhabditis elegans. Nature *391*, 806–811.

Fisk Green, R., Lorson, M., Walhout, a J.M., Vidal, M., and van den Heuvel, S. (2004). Identification of critical domains and putative partners for the Caenorhabditis elegans spindle component LIN-5. Mol. Genet. Genomics *271*, 532–544.

Fodde, R., Kuipers, J., Rosenberg, C., Smits, R., Kielman, M., Gaspar, C., van Es, J.H., Breukel, C., Wiegant, J., Giles, R.H., et al. (2001). Mutations in the APC tumour suppressor gene cause chromosomal instability. Nat. Cell Biol. *3*, 433–438.

Friedland, A.E., Tzur, Y.B., Esvelt, K.M., Colaiácovo, M.P., Church, G.M., and Calarco, J.A. (2013). Heritable genome editing in *C. elegans* via a CRISPR-Cas9 system. Nat. Methods *10*, 741–743.

Frøkjær-jensen, C., Jain, N., Hansen, L., Dupuy, D., Jorgensen, E.M.M., Fire, A.Z.Z., Frøkjær-jensen, C., Jain, N., Hansen, L., Davis, M.W.W., et al. (2016). An Abundant Class of Non-coding DNA Can Prevent Stochastic Gene Silencing in the *C. elegans* Germline. Cell *166*, 1–15.

Frøkjær-Jensen, C., Davis, M.W., Ailion, M., and Jorgensen, E.M. (2012). Improved Mos1-mediated transgenesis in *C. elegans*. Nat. Methods *9*, 117–118.

Gabay, M., Pinter, M.E., Wright, F.A., Chan, P.Y., Murphy, A.J., Valenzuela, D.M., Yancopoulos, G.D., and Tall, G.G. (2011). Ric-8 proteins are molecular chaperones that direct nascent G protein alpha subunit membrane association. Sci. Signal. *4*, ra79.

Galli, M., and van den Heuvel, S. (2008). Determination of the cleavage plane in early *C. elegans* embryos. Annu. Rev. Genet. *42*, 389–411.

Galli, M., Muñoz, J., Portegijs, V., Boxem, M., Grill, S.W., Heck, A.J.R., and van den Heuvel, S. (2011a). aPKC phosphorylates NuMA-related LIN-5 to position the mitotic spindle during asymmetric division. Nat. Cell Biol. *13*, 1132–1138.

Galli, M., Bodor, D., Etemad, B., Munoz, J., Heck, A., and van den Heuvel, S. (2011b). LIN-5 is required for the aster-derived cytokinesis signal. In Determination of the Cell Cleavage Plane by the LIN-5 Complex, pp. 86–100.

Gallini, S., Carminati, M., De Mattia, F., Pirovano, L., Martini, E., Oldani, A., Asteriti, I.A., Guarguaglini, G., and Mapelli, M. (2016). NuMA Phosphorylation by Aurora-A Orchestrates Spindle Orientation. Curr. Biol. *26*, 1–12.

Garzon-Coral, C., Fantana, H.A., Howard, J., Galli, M., Heuvel, S. van den, Gillies, T.E., Cabernard, C., Campbell, E.K.M., Werts, A.D., Goldstein, B., et al. (2016). A force-generating machinery maintains the spindle at the cell center during mitosis. Science (80-.). *352*, 389–411.

Gassmann, R., Essex, A., Hu, J.-S., Maddox, P.S., Motegi, F., Sugimoto, A., O'Rourke, S.M., Bowerman, B., McLeod, I., Yates, J.R., et al. (2008). A new mechanism controlling kinetochore-microtubule interactions revealed by comparison of two dynein-targeting components: SPDL-1 and the Rod/Zwilch/Zw10 complex. Genes Dev. *22*, 2385–2399.

Gehmlich, K., Haren, L., and Merdes, A. (2004). Cyclin B degradation leads to NuMA release from dynein/dynactin and from spindle poles. EMBO Rep. *5*, 97–103.

Gibson, D.G., Young, L., Chuang, R.Y., Venter, J.C., Hutchison, C.A., and Smith, H.O. (2009). Enzymatic assembly of DNA molecules up to several hundred kilobases. Nat. Methods *6*, 343–345.

Gönczy, P. (2008). Mechanisms of asymmetric cell division: flies and worms pave the way. Nat. Rev. Mol. Cell Biol. *9*, 355–366.

Gönczy, P., Pichler, S., Kirkham, M., and Hyman, A.A. (1999). Cytoplasmic dynein is required for distinct aspects of MTOC positioning, including centrosome separation, in the one cell stage Caenorhabditis elegans embryo. J. Cell Biol. *147*, 135–150.

Gotta, M., and Ahringer, J. (2001). Distinct roles for Galpha and Gbetagamma in regulating spindle position and orientation in Caenorhabditis elegans embryos. Nat. Cell Biol. *3*, 297–300.

Gotta, M., Dong, Y., Peterson, Y.Y.K., Lanier, S.S.M., and Ahringer, J. (2003). Asymmetrically Distributed *C. elegans* Homologs of AGS3/PINS Control Spindle Position in the Early Embryo. Curr. Biol. *13*, 1029–1037.

Gray, D., Plusa, B., Piotrowska, K., Na, J., Tom, B., Glover, D.M., and Zernicka-Goetz, M. (2004). First cleavage of the mouse embryo responds to change in egg shape at fertilization. Curr. Biol. *14*, 397–405.

Green, R.A., and Kaplan, K.B. (2003). Chromosome instability in colorectal tumor cells is associated with defects in microtubule plus-end attachments caused by a dominant mutation in APC. J. Cell Biol. *163*, 949–961.

Green, R.A., Wollman, R., and Kaplan, K.B. (2005). APC and EB1 Function Together in Mitosis to Regulate Spindle Dynamics and Chromosome Alignment. Mol. Biol. Cell *16*, 4609–4622.

Grill, S.W., Gönczy, P., Stelzer, E.H., and Hyman, A.A. (2001). Polarity controls forces governing asymmetric spindle positioning in the Caenorhabditis elegans embryo. Nature *409*, 630–633.

Grill, S.W., Howard, J., Schäffer, E., Stelzer, E.H.K., and Hyman, A. a (2003). The distribution of active force generators controls mitotic spindle position. Science *301*, 518–521.

Grill, S.W., Kruse, K., and Jülicher, F. (2005). Theory of mitotic spindle oscillations. Phys. Rev. Lett. *94*, 1–4.

Grishchuk, E.L., Molodtsov, M.I., Ataullakhanov, F.I., and McIntosh, J.R. (2005). Force production by disassembling microtubules. Nature *438*, 384–388.

Grohmann, A., Tanneberger, K., Alzner, A., Schneikert, J., and Behrens, J. (2007). AMER1 regulates the distribution of the tumor suppressor APC between microtubules and the plasma membrane. J. Cell Sci. *120*, 3738–3747.

Grotjahn, D.A., Chowdhury, S., Xu, Y., McKenney, R.J., Schroer, T., and Lander, G. (2018). Cryo-electron tomography reveals that dynactin recruits a team of dyneins for processive motility. Nat. Struct. Mol. Biol. 182576.

Guilgur, L.G., Prudêncio, P., Ferreira, T., Pimenta-Marques, A.R., and Martinho, R.G. (2012). Drosophila aPKC is required for mitotic spindle orientation during symmetric division of epithelial cells. Development *139*, 503–513.

Gundersen, G.G., Gomes, E.R., and Wen, Y. (2004). Cortical control of microtubule stability and polarization. Curr. Opin. Cell Biol. *16*, 106–112.

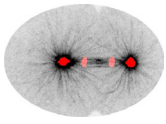

Gusnowski, E.M., and Srayko, M. (2011). Visualization of dynein-dependent microtubule gliding at the cell cortex: implications for spindle positioning. J. Cell Biol. *194*, 377–386.

Habib, S.J., Chen, B.-C., Tsai, F., Anastassiadis, K., Meyer, T., Betzig, E., and Nusse, R. (2013). A localized Wnt signal orients asymmetric stem cell division in vitro. Science *339*, 1445–1448.

Hallett, R.A., Zimmerman, S.P., Yumerefendi, H., Bear, J.E., and Kuhlman, B. (2016). Correlating *in Vitro* and *in Vivo* Activities of Light-Inducible Dimers: A Cellular Optogenetics Guide. ACS Synth. Biol. *5*, 53–64.

Hamaguchi, M.S., and Hiramoto, Y. (1986). Analysis of the Role of Astral Rays in Pronuclear Migration in Sand Dollar Eggs by the Colcemid-UV Method: sperm aster/pronuclear migration/sand dollar/colcemid-UV method. Dev. Growth Differ. *28*, 143–156.

Hampoelz, B., Hoeller, O., Bowman, S.K., Dunican, D., and Knoblich, J.A. (2005). Drosophila Ric-8 is essential for plasma-membrane localization of heterotrimeric G proteins. Nat. Cell Biol. *7*, 1099–1105.

Han, G., Liu, B., Zhang, J., Zuo, W., Morris, N.R., and Xiang, X. (2001). The aspergillus cytoplasmic dynein heavy chain and nudf localize to microtubule ends and affect microtubule dynamics. Curr. Biol. *11*, 719–724.

Hanahan, D., and Weinberg, R.A. (2011). Hallmarks of cancer: The next generation. Cell *144*, 646–674.

Hao, Y., Du, Q., Chen, X., Zheng, Z., Balsbaugh, J.L., Maitra, S., Shabanowitz, J., Hunt, D.F., and Macara, I.G. (2010). Par3 controls epithelial spindle orientation by aPKC-mediated phosphorylation of apical Pins. Curr. Biol. *20*, 1809–1818.

Hara, Y., and Kimura, A. (2009). Cell-Size-Dependent Spindle Elongation in the Caenorhabditis elegans Early Embryo. Curr. Biol. *19*, 1549–1554.

Harborth, J., Weber, K., and Osborn, M. (1995). Epitope mapping and direct visualization of the parallel, in-register arrangement of the double-stranded coiled-coil in the NuMA protein. EMBO J. *14*, 2447–2460.

Harterink, M., Kim, D. h., Middelkoop, T.C., Doan, T.D., van Oudenaarden, A., and Korswagen, H.C. (2011). Neuroblast migration along the anteroposterior axis of *C. elegans* is controlled by opposing gradients of Wnts and a secreted Frizzled-related protein. Development *138*, 2915–2924.

Harterink, M., van Bergeijk, P., Allier, C., de Haan, B., van den Heuvel, S., Hoogenraad, C.C., and Kapitein, L.C. (2016). Light-controlled intracellular transport in Caenorhabditis elegans. Curr. Biol. *26*, R153–R154.

Hawkins, N.C., Ellis, G.C., Bowerman, B., and Garriga, G. (2005). MOM-5 Frizzled regulates the distribution of DSH-2 to control *C. elegans* asymmetric neuroblast divisions. Dev. Biol. *284*, 246–259.

Hendricks, A.G., Lazarus, J.E., Perlson, E., Gardner, M.K., Odde, D.J., Goldman, Y.E., and Holzbaur, E.L.F. (2012). Dynein tethers and stabilizes dynamic microtubule plus ends. Curr. Biol. *22*, 632–637.

Hertwig, O. (1884). Das Problem der Befruchtung und der Isotropie des Eies, eine Theory der Vererbung. Jenaische Zeitschrift Fuer Naturwiss. *18*, 21–23.

Hess, H. a, Röper, J.-C., Grill, S.W., and Koelle, M.R. (2004). RGS-7 completes a receptor-independent heterotrimeric G protein cycle to asymmetrically regulate mitotic spindle positioning in *C. elegans*. Cell *119*, 209–218.

Hirrlinger, J., Requardt, R.P., Winkler, U., Wilhelm, F., Schulze, C., and Hirrlinger, P.G. (2009). Split-CreERT2: Temporal Control of DNA recombination mediated by split-cre protein Fragment Complementation. PLoS One *4*, 2–9.

Hoege, C., and Hyman, A. a (2013). Principles of PAR polarity in Caenorhabditis elegans embryos. Nat. Rev. Mol. Cell Biol. *14*, 315–322.

Hoier, E.F., Mohler, W.A., Kim, S.K., and Hajnal, A. (2000). The Caenorhabditis elegans APC-related gene apr-1 is required for epithelial cell migration and Hox gene expression. Genes Dev. *14*, 874–886.

Holt, L.J., Tuch, B.B., Villen, J., Johnson, A.D., Gygi, S.P., and Morgan, D.O. (2009). Global Analysis of Cdk1 Substrate Phosphorylation Sites Provides Insights into Evolution. Science (80-.). *325*, 1682–1686.

Honnappa, S., Okhrimenko, O., Jaussi, R., Jawhari, H., Jelesarov, I., Winkler, F.K., and Steinmetz, M.O. (2006). Key Interaction Modes of Dynamic +TIP Networks. Mol. Cell *23*, 663–671.

Horvitz, H.R., and Herskowitz, I. (1992). Mechanisms of asymmetric cell division: two Bs or not two Bs, that is the question. Cell *68*, 237–255.

Howard, J., and Garzon-Coral, C. (2017). Physical Limits on the Precision of Mitotic Spindle Positioning by Microtubule Pushing forces: Mechanics of mitotic spindle positioning. BioEssays *39*.

Huang, J., Roberts, A.J., Leschziner, A.E., and Reck-Peterson, S.L. (2012). Lis1 acts as a "clutch" between the ATPase and microtubule-binding domains of the dynein motor. Cell *150*, 975–986.

Hubbard, E.J.A. (2014). FLP/FRT and Cre/lox recombination technology in *C. elegans*. Methods *68*, 417–424.

Hwang, E., Kusch, J., Barral, Y., and Huffaker, T.C. (2003). Spindle orientation in Saccharomyces cerevisiae depends on the transport of microtubule ends along polarized actin cables. J. Cell Biol. *161*, 483–488.

Hwang, W.Y., Fu, Y., Reyon, D., Maeder, M.L., Tsai, S.Q., Sander, J.D., Peterson, R.T., Yeh, J.-R.J., and Joung, J.K. (2013). Efficient genome editing in zebrafish using a CRISPR-Cas system. Nat. Biotechnol. 1–3.

Izumi, Y., Ohta, N., Itoh-Furuya, A., Fuse, N., and Matsuzaki, F. (2004). Differential functions of G protein and Baz-aPKC signaling pathways in Drosophila neuroblast asymmetric division. J. Cell Biol. *164*, 729–738.

Jaiswal, R., Stepanik, V., Rankova, A., Molinar, O., Goode, B.L., and McCartney, B.M. (2013). Drosophila homologues of adenomatous polyposis coli (APC) and the formin diaphanous collaborate by a conserved mechanism to stimulate actin filament assembly. J. Biol. Chem. *288*, 13897–13905.

Jia, L., Chisari, M., Maktabi, M.H., Sobieski, C., Zhou, H., Konopko, A.M., Martin, B.R., Mennerick, S.J., and Blumer, K.J. (2014). A mechanism regulating g protein-coupled receptor signaling that requires cycles of protein palmitoylation and depalmitoylation. J. Biol. Chem. *289*, 6249–6257.

Jia, M., Li, J., Zhu, J., Wen, W., Zhang, M., and Wang, W. (2012). Crystal Structures of the scaffolding protein LGN reveal the general mechanism by which GoLoco binding motifs inhibit the release of GDP from Gαi subunits in G-coupled heterotrimeric proteins. J. Biol. Chem. *287*, 36766–36776.

Johnson, H.E., and Toettcher, J.E. (2018). Illuminating developmental biology with cellular optogenetics. Curr. Opin. Biotechnol. *52*, 42–48.

Johnston, C.A., Hirono, K., Prehoda, K.E., and Doe, C.Q. (2009). Identification of an Aurora-A/PinsLINKER/Dlg Spindle Orientation Pathway using Induced Cell Polarity in S2 Cells. Cell *138*, 1150–1163.

Juanes, M.A., Bouguenina, H., Eskin, J.A., Jaiswal, R., Badache, A., and Goode, B.L. (2017). Adenomatous polyposis coli nucleates actin assembly to drive cell migration and microtubule- induced focal adhesion turnover. J. Cell Biol. *216*, 3327–3335.

Kage-Nakadai, E., Imae, R., Suehiro, Y., Yoshina, S., Hori, S., and Mitani, S. (2014). A conditional knockout toolkit for caenorhabditis elegans based on the Cre/loxP recombination. PLoS One *9*, 1–13.

Kaltschmidt, J. a, Davidson, C.M., Brown, N.H., and Brand, a H. (2000). Rotation and asymmetry of the mitotic spindle direct asymmetric cell division in the developing central nervous system. Nat. Cell Biol. *2*, 7–12.

Kamath, R.S., Fraser, A.G., Dong, Y., Poulin, G., Durbin, R., Gotta, M., Kanapin, A., Le Bot, N., Moreno, S., Sohrmann, M., et al. (2003). Systematic functional analysis of the Caenorhabditis elegans genome using RNAi. Nature *421*, 231–237.

Kant, R., Zeng, B., Thomas, C.J., Bothner, B., and Sprang, S.R. (2016). Ric-8A, a G protein chaperone with nucleotide exchange activity induces long-range secondary structure changes in Gα. Elife *5*, 1–20.

Kaplan, K.B., Burds, A.A., Swedlow, J.R., Bekir, S.S., Sorger, P.K., and Nathke, I.S. (2001). A role for the Adenomatous Polyposis Coli protein in chromosome segregation. Nat Cell Biol *3*, 429–432.

Kardon, J.R., and Vale, R.D. (2009). Regulators of the cytoplasmic dynein motor. Nat. Rev. Mol. Cell Biol. *10*, 854–865.

Katanaev, V.L., Ponzielli, R., Sémériva, M., and Tomlinson, A. (2005). Trimeric G protein-dependent frizzled signaling in Drosophila. Cell *120*, 111–122.

Kemphues, K.J., Priess, J.R., Morton, D.G., and Cheng, N.S. (1988). Identification of genes required for cytoplasmic localization in early *C. elegans* embryos. Cell *52*, 311–320.

Kim, H., Ishidate, T., Ghanta, K.S., Seth, M., Conte, D., Shirayama, M., and Mello, C.C. (2014). A Co-CRISPR strategy for efficient genome editing in Caenorhabditis elegans. Genetics *197*, 1069–1080.

Kimple, R.J., Kimple, M.E., Betts, L., Sondek, J., and Siderovski, D.P. (2002). Structural determinants for GoLoco-induced inhibition of nucleotide release by Galpha subunits. Nature *416*, 878–881.

Kimura, A., and Onami, S. (2005). Computer simulations and image processing reveal length-dependent pulling force as the primary mechanism for *C. elegans* male pronuclear migration. Dev. Cell *8*, 765–775.

Kimura, A., and Onami, S. (2007). Local cortical pulling-force repression switches centrosomal centration and posterior displacement in *C. elegans*. J. Cell Biol. *179*, 1347–1354.

Kimura, A., and Onami, S. (2010). Modeling Microtubule-Mediated Forces and Centrosome Positioning in Caenorhabditis elegans Embryos (Elsevier Inc.).

Kimura, K., and Kimura, A. (2011). Intracellular organelles mediate cytoplasmic pulling force for centrosome centration in the Caenorhabditis elegans early embryo. Proc. Natl. Acad. Sci. U. S. A. *108*, 137–142.

Kirschner, M., and Mitchison, T. (1986). Beyond self-assembly: From microtubules to morphogenesis. Cell *45*, 329–342.

Kiyomitsu, T., and Cheeseman, I.M. (2012). Chromosome- and spindle-pole-derived signals generate an intrinsic code for spindle position and orientation. Nat. Cell Biol. *14*, 311–317.

Kiyomitsu, T., and Cheeseman, I.M. (2013). Cortical Dynein and Asymmetric Membrane Elongation Coordinately Position the Spindle in Anaphase. Cell *154*, 391–402.

Klotz, D.M., Nelson, S.A., Kroboth, K., Newton, I.P., Radulescu, S., Ridgway, R.A., Sansom, O.J., Appleton, P.L., and Näthke, I.S. (2012). The microtubule poison vinorelbine kills cells independently of mitotic arrest and targets cells lacking the APC tumour suppressor more effectively. J. Cell Sci. *125*, 887–895.

Knoblich, J. a (2010). Asymmetric cell division: recent developments and their implications for tumour biology. Nat. Rev. Mol. Cell Biol. *11*, 849–860.

Kobayashi, T., and Murayama, T. (2009). Cell cycle-dependent microtubule-based dynamic transport of cytoplasmic dynein in mammalian cells. PLoS One *4*.

Komarova, Y., De Groot, C.O., Grigoriev, I., Gouveia, S.M., Munteanu, E.L., Schober, J.M., Honnappa, S., Buey, R.M., Hoogenraad, C.C., Dogterom, M., et al. (2009). Mammalian end binding proteins control persistent microtubule growth. J. Cell Biol. *184*, 691–706.

Kopein, D., and Katanaev, V.L. (2009). Drosophila GoLoco-Protein Pins Is a Target of G _ o -mediated G Protein – coupled Receptor Signaling. *20*, 3865–3877.

Korinek, W.S., Copeland, M.J., Chaudhuri, A., and Chant, J. (2000). Molecular linkage underlying microtubule orientation toward cortical sites in yeast. Science (80-.). *287*, 2257–2259.

Kotak, S., Busso, C., and Gönczy, P. (2012). Cortical dynein is critical for proper spindle positioning in human cells. J. Cell Biol. *199*, 97–110.

Kotak, S., Busso, C., and Gönczy, P. (2013). NuMA phosphorylation by CDK1 couples mitotic progression with cortical dynein function. EMBO J. *32*, 1–13.

Kotak, S., Busso, C., and Gönczy, P. (2014). NuMA interacts with phosphoinositides and links the mitotic spindle with the plasma membrane. EMBO J.

Kozlowski, C., Srayko, M., and Nedelec, F. (2007). Cortical microtubule contacts position the spindle in *C. elegans* embryos. Cell *129*, 499–510.

Krueger, L.E., Wu, J.-C., Tsou, M.-F.B., and Rose, L.S. (2010). LET-99 inhibits lateral posterior pulling forces during asymmetric spindle elongation in *C. elegans* embryos. J. Cell Biol. *189*, 481–495.

Kushnirov, V. V. (2000). Rapid and reliable protein extraction from yeast. Yeast *16*, 857–860.

Kwon, M., Bagonis, M., Danuser, G., and Pellman, D. (2015). Direct Microtubule-Binding by Myosin-10 Orients Centrosomes toward Retraction Fibers and Subcortical Actin Clouds. Dev. Cell *34*, 323–337.

Laan, L., Pavin, N., Husson, J., Romet-Lemonne, G., van Duijn, M., López, M.P., Vale, R.D., Jülicher, F., Reck-Peterson, S.L., and Dogterom, M. (2012). Cortical dynein controls microtubule dynamics to generate pulling forces that position microtubule asters. Cell *148*, 502–514.

Labbé, J.-C., Maddox, P.S., Salmon, E.D., and Goldstein, B. (2003). PAR Proteins Regulate Microtubule Dynamics at the Cell Cortex in *C. elegans*. Curr. Biol. *13*, 707–714.

Labbé, J.-C., McCarthy, E.K., and Goldstein, B. (2004). The forces that position a mitotic spindle asymmetrically are tethered until after the time of spindle assembly. J. Cell Biol. *167*, 245–256.

Lansbergen, G., Komarova, Y., Modesti, M., Wyman, C., Hoogenraad, C.C., Goodson, H. V., Lemaitre, R.P., Drechsel, D.N., Van Munster, E., Gadella, T.W.J., et al. (2004). Conformational changes in CLIP-170 regulate its binding to microtubules and dynactin localization. J. Cell Biol. *166*, 1003–1014.

Lechler, T., and Fuchs, E. (2005). Asymmetric cell divisions promote stratification and differentiation of mammalian skin. Nature *437*, 275–280.

Lee, B.H., Schwager, F., Meraldi, P., and Gotta, M. (2018). p37 / UBXN2B regulates spindle orientation by limiting cortical NuMA recruitment via PP1 / Repo-Man. 1–11.

Lee, L., Tirnauer, J.S., Li, J., Schuyler, S.C., Liu, J.Y., and Pellman, D. (2000). Positioning of the Mitotic Spindle by a Cortical- Microtubule Capture Mechanism. Science (80-.). *287*, 2260–2262.

Lee, W.L., Oberle, J.R., and Cooper, J.A. (2003). The role of the lissencephaly protein Pac1 during nuclear migration in budding yeast. J. Cell Biol. *160*, 355–364.

Lenz, J.H., Schuchardt, I., Straube, A., and Steinberg, G. (2006). A dynein loading zone for retrograde endosome motility at microtubule plus-ends. EMBO J. *25*, 2275–2286.

Li, M., Liu, L., Xi, N., and Wang, Y. (2014). Progress in measuring biophysical properties of membrane proteins with AFM single-molecule force spectroscopy. Chinese Sci. Bull. *59*, 2717–2725.

Lorson, M. a, Horvitz, H.R., and van den Heuvel, S. (2000). LIN-5 is a novel component of the spindle apparatus required for chromosome segregation and cleavage plane specification in Caenorhabditis elegans. J. Cell Biol. *148*, 73–86.

Lu, M.S., and Prehoda, K.E. (2013). A NudE/14-3-3 Pathway Coordinates Dynein and the Kinesin Khc73 to Position the Mitotic Spindle. Dev. Cell *26*, 369–380.

Lu, B., Roegiers, F., Jan, L.Y., and Jan, Y.N. (2001). Adherens junctions inhibit asymmetric division in the Drosophila epithelium. Nature *409*, 522–525.

Machicoane, M., de Frutos, C. a., Fink, J., Rocancourt, M., Lombardi, Y., Garel, S., Piel, M., and Echard, a. (2014). SLK-dependent activation of ERMs controls LGN-NuMA localization and spindle orientation. J. Cell Biol. *205*, 791–799.

Malkovskiy, A. V., Wagh, D.A., Longo, F.M., and Rajadas, J. (2015). A strategy for analyzing bond strength and interaction kinetics between Pleckstrin homology domains and PI(4,5)P2 phospholipids using force distance spectroscopy and surface plasmon resonance. Analyst *140*, 4558–4565.

Mangmool, S., and Kurose, H. (2011). Gi/o protein-dependent and -independent actions of pertussis toxin (ptx). Toxins (Basel). *3*, 884–899.

Markus, S.M., and Lee, W.-L. (2011). Regulated offloading of cytoplasmic dynein from microtubule plus ends to the cortex. Dev. Cell *20*, 639–651.

Marrari, Y., Crouthamel, M., Irannejad, R., and Wedegaertner, P.B. (2007). Assembly and trafficking of heterotrimeric G proteins. Biochemistry *46*, 7665–7677.

Martin, K., and Weiss, S.L. (2015). Initial resuscitation and management of pediatric septic shock. Minerva Pediatr. *67*, 141–158.

Maurer, S.P., Fourniol, F.J., Bohner, G., Moores, C.A., and Surrey, T. (2012). EBs recognize a nucleotide-dependent structural cap at growing microtubule ends. Cell *149*, 371–382.

Maurer, S.P., Cade, N.I., Bohner, G., Gustafsson, N., Boutant, E., and Surrey, T. (2014). EB1 accelerates two conformational transitions important for microtubule maturation and dynamics. Curr. Biol. *24*, 372–384.

McCarthy Campbell, E.K., Werts, A.D., and Goldstein, B. (2009). A cell cycle timer for asymmetric spindle positioning. PLoS Biol. *7*, e1000088.

McCartney, B.M., McEwen, D.G., Grevengoed, E., Maddox, P., Bejsovec, A., and Peifer, M. (2001). Drosophila APC2 and Armadillo participate in tethering mitotic spindles to cortical actin. Nat. Cell Biol. *3*, 933–938.

McKenney, R.J., Huynh, W., Tanenbaum, M.E., Bhabha, G., and Vale, R.D. (2014). Activation of cytoplasmic dynein motility by dynactin-cargo adapter complexes. Science (80-.). *345*, 337–341.

McNally, F.J.J. (2013). Mechanisms of spindle positioning. J. Cell Biol. *200*, 131–140.

Meder, D., and Simons, K. (2005). Ras on the roundabout. Science (80-.). *307*, 1731–1733.

Merdes, a, Heald, R., Samejima, K., Earnshaw, W.C., and Cleveland, D.W. (2000). Formation of spindle poles by dynein/dynactin-dependent transport of NuMA. J. Cell Biol. *149*, 851–862.

Merdes, A., Ramyar, K., Vechio, J.D., and Cleveland, D.W. (1996). A complex of NuMA and cytoplasmic dynein is essential for mitotic spindle assembly. Cell *87*, 447–458.

Merritt, C., Rasoloson, D., Ko, D., and Seydoux, G. (2008). 3′ UTRs Are the Primary Regulators of Gene Expression in the *C. elegans* Germline. Curr. Biol. *18*, 1476–1482.

Miller, K.G., and Rand, J.B. (2000). A Role for RIC-8 and GOA-1 in Regulating a Subset of Centrosome Movements During Early Embryogenesis in Caenorhabditis elegans. Genetics *8*, 1649–1660.

Miller, R.K., and Rose, M.D. (1998). Kar9p is a novel cortical protein required for cytoplasmic microtubule orientation in yeast. J. Cell Biol. *140*, 377–390.

Miller, K.G., Alfonso, a, Nguyen, M., Crowell, J. a, Johnson, C.D., and Rand, J.B. (1996). A genetic selection for Caenorhabditis elegans synaptic transmission mutants. Proc. Natl. Acad. Sci. U. S. A. *93*, 12593–12598.

Miller, K.G., Emerson, M.D., McManus, J.R., and Rand, J.B. (2000). RIC-8 (Synembryn): a novel conserved protein that is required for G(q)alpha signaling in the *C. elegans* nervous system. Neuron *27*, 289–299.

Mimori-Kiyosue, Y., Shiina, N., and Tsukita, S. (2000). Adenomatous polyposis coli (APC) protein moves along microtubules and concentrates at their growing ends in epithelial cells. J. Cell Biol. *148*, 505–517.

Minc, N., Burgess, D., and Chang, F. (2011). Influence of cell geometry on division-plane positioning. Cell *144*, 414–426.

Mizumoto, K., and Sawa, H. (2007). Cortical β-Catenin and APC Regulate Asymmetric Nuclear β-Catenin Localization during Asymmetric Cell Division in *C. elegans*. Dev. Cell *12*, 287–299.

Morin, X., and Bellaïche, Y. (2011). Mitotic spindle orientation in asymmetric and symmetric cell divisions during animal development. Dev. Cell *21*, 102–119.

Moseley, J.B., Bartolini, F., Okada, K., Wen, Y., Gundersen, G.G., and Goode, B.L. (2007). Regulated binding of adenomatous polyposis coli protein to actin. J. Biol. Chem. *282*, 12661–12668.

Moser, A.R., Dove, W.F., Roth, K.A., and Gordon, J.I. (1992). The Min (multiple intestinal neoplasia) mutation: Its effect on gut epithelial cell differentiation and interaction with a modifier system. J. Cell Biol. *116*, 1517–1526.

Munro, E., and Bowerman, B. (2009). Cellular Symmetry Breaking during. Cold Spring Harb. Perspect. Biol. 1–21.

Munro, E., Nance, J., and Priess, J.R. (2004). Cortical flows powered by asymmetrical contraction transport PAR proteins to establish and maintain anterior-posterior polarity in the early *C. elegans* embryo. Dev. Cell *7*, 413–424.

Nagai, Y., Nishimura, A., Tago, K., Mizuno, N., and Itoh, H. (2010). Ric-8B stabilizes the α subunit of stimulatory G protein by inhibiting its ubiquitination. J. Biol. Chem. *285*, 11114–11120.

Näthke, I.S., Adams, C.L., Polakis, P., Sellin, J.H., and Nelson, W.J. (1996). to Plasma Membrane Sites Involved in Active Cell Migration. Cell *134*, 165–179.

Nguyen-Ngoc, T., Afshar, K., and Gönczy, P. (2007). Coupling of cortical dynein and G alpha proteins mediates spindle positioning in Caenorhabditis elegans. Nat. Cell Biol. *9*, 1294–1302.

Nicholas, M.P., Höök, P., Brenner, S., Wynne, C.L., Vallee, R.B., and Gennerich, A. (2015). Control of cytoplasmic dynein force production and processivity by its C-terminal domain. Nat. Commun. *6*, 6206.

Niehrs, C., and Shen, J. (2010). Regulation of Lrp6 phosphorylation. Cell. Mol. Life Sci. *67*, 2551–2562.

Nusse, R., and Clevers, H. (2017). Wnt/β-Catenin Signaling, Disease, and Emerging Therapeutic Modalities. Cell *169*, 985–999.

O'Rourke, S.M., Dorfman, M.D., Carter, J.C., and Bowerman, B. (2007). Dynein modifiers in *C. elegans*: light chains suppress conditional heavy chain mutants. PLoS Genet. *3*, e128.

O'Rourke, S.M., Christensen, S.N., and Bowerman, B. (2010). Caenorhabditis elegans EFA-6 limits microtubule growth at the cell cortex. Nat. Cell Biol. *12*, 1235–1241.

Okada, K., Bartolini, F., Deaconescu, A.M., Moseley, J.B., Dogic, Z., Grigorieff, N., Gundersen, G.G., and Goode, B.L. (2010). Adenomatous polyposis coli protein nucleates actin assembly and synergizes with the formin mDia1. J. Cell Biol. *189*, 1087–1096.

Oldenbroek, M., Robertson, S.M., Guven-Ozkan, T., Spike, C., Greenstein, D., and Lin, R. (2013). Regulation of maternal Wnt mRNA translation in *C. elegans* embryos. Development.

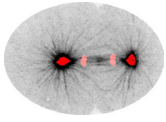

Olsen, J. V, Vermeulen, M., Santamaria, A., Kumar, C., Martin, L., Jensen, L.J., Gnad, F., Cox, J., Jensen, T.S., Nigg, E.A., et al. (2010). Quantitative Phosphoproteomics Reveals Widespread Full Phosphorylation Site Occupancy During Mitosis. *3*, 1–16.

Ou, G., Stuurman, N., D'Ambrosio, M., and Vale, R.D. (2010). Polarized myosin produces unequal-size daughters during asymmetric cell division. Science *330*, 677–680.

Pacquelet, A., Uhart, P., Tassan, J.P., and Michaux, G. (2015). PAR-4 and anillin regulate myosin to coordinate spindle and furrow position during asymmetric division. J. Cell Biol. *210*, 1085–1099.

Paix, A., Folkmann, A., Rasoloson, D., and Seydoux, G. (2015). High Efficiency, Homology-Directed Genome Editing in Caenorhabditis elegans Using CRISPR/Cas9 Ribonucleoprotein Complexes. Genetics *201*, genetics.115.179382-.

Pan, Z., Zhu, J., Shang, Y., Wei, Z., Jia, M., Xia, C., Wen, W., Wang, W., and Zhang, M. (2013). An Autoinhibited Conformation of LGN Reveals a Distinct Interaction Mode between GoLoco Motifs and TPR Motifs. Structure *21*, 1007–1017.

Panbianco, C., Weinkove, D., Zanin, E., Jones, D., Divecha, N., Gotta, M., and Ahringer, J. (2008). A casein kinase 1 and PAR proteins regulate asymmetry of a PIP(2) synthesis enzyme for asymmetric spindle positioning. Dev. Cell *15*, 198–208.

Park, D.H., and Rose, L.S. (2008). Dynamic localization of LIN-5 and GPR-1/2 to cortical force generation domains during spindle positioning. Dev. Biol. *315*, 42–54.

Pecreaux, J., Röper, J.-C., Kruse, K., Jülicher, F., Hyman, A. a, Grill, S.W., and Howard, J. (2006). Spindle oscillations during asymmetric cell division require a threshold number of active cortical force generators. Curr. Biol. *16*, 2111–2122.

Pécréaux, J., Redemann, S., Alayan, Z., Mercat, B., Pastezeur, S., Garzon-Coral, C., Hyman, A.A., and Howard, J. (2016). The Mitotic Spindle in the One-Cell *C. elegans* Embryo Is Positioned with High Precision and Stability. Biophys. J. *111*, 1773–1784.

Pereira, G., and Yamashita, Y.M. (2011). Fly meets yeast: Checking the correct orientation of cell division. Trends Cell Biol. *21*, 526–533.

Peyre, E., Jaouen, F., Saadaoui, M., Haren, L., Merdes, A., Durbec, P., and Morin, X. (2011). A lateral belt of cortical LGN and NuMA guides mitotic spindle movements and planar division in neuroepithelial cells. J. Cell Biol. *193*, 141–154.

Pfister, A.S., Hadjihannas, M. V., Röhrig, W., Schambony, A., and Behrens, J. (2012). Amer2 protein interacts with EB1 protein and adenomatous polyposis coli (APC) and controls microtubule stability and cell migration. J. Biol. Chem. *287*, 35333–35340.

Phair, R., Gorski, S., and Misteli, T. (2003). Measurement of dynamic protein binding to chromatin in vivo, using photobleaching microscopy. Methods Enzymol. *375*, 393–414.

Pietro, F., Echard, A., Morin, X., di Pietro, F., Echard, A., Morin, X., Pietro, F., Echard, A., and Morin, X. (2016). Regulation of mitotic spindle orientation : an integrated view. EMBO Rep. *17*, 1106–1130.

Pinkse, M.W.H., Mohammed, S., Gouw, J.W., Van Breukelen, B., Vos, H.R., and Heck, A.J.R. (2008). Highly robust, automated, and sensitive online TiO2-based phosphoproteomics applied to study endogenous phosphorylation in Drosophila melanogaster. J. Proteome Res. *7*, 687–697.

Plowman, G.D., Sudarsanam, S., Bingham, J., Whyte, D., and Hunter, T. (1999). The protein kinases of Caenorhabditis elegans: a model for signal transduction in multicellular organisms. Proc. Natl. Acad. Sci. U. S. A. *96*, 13603–13610.

Portegijs, V., Fielmich, L.E., Galli, M., Schmidt, R., Muñoz, J., van Mourik, T., Akhmanova, A., Heck, A.J.R., Boxem, M., and van den Heuvel, S. (2016). Multisite Phosphorylation of NuMA-Related LIN-5 Controls Mitotic Spindle Positioning in *C. elegans*. PLoS Genet. *12*, 1–32.

Poser, I., Sarov, M., Hutchins, J.R. a, Hériché, J.-K., Toyoda, Y., Pozniakovsky, A., Weigl, D., Nitzsche, A., Hegemann, B., Bird, A.W., et al. (2008). BAC TransgeneOmics: a high-throughput method for exploration of protein function in mammals. Nat. Methods *5*, 409–415.

Postiglione, M.P., Jüschke, C., Xie, Y., Haas, G. a, Charalambous, C., and Knoblich, J. a (2011). Mouse inscuteable induces apical-basal spindle orientation to facilitate intermediate progenitor generation in the developing neocortex. Neuron *72*, 269–284.

Poulton, J.S., Mu, F.W., Roberts, D.M., and Peifer, M. (2013). APC2 and Axin promote mitotic fidelity by facilitating centrosome separation and cytoskeletal regulation. Development *140*, 4226–4236.

Praitis, V., Casey, E., Collar, D., and Austin, J. (2001). Creation of low-copy integrated transgenic lines in Caenorhabditis elegans. Genetics *157*, 1217–1226.

Raaijmakers, J.A., and Medema, R.H. (2014). Function and regulation of dynein in mitotic chromosome segregation. Chromosoma *123*, 407–422.

Raaijmakers, J. a., Tanenbaum, M.E., and Medema, R.H. (2013). Systematic dissection of dynein regulators in mitosis. J. Cell Biol. *201*, 201–215.

Ramanathan, S.P., Helenius, J., Stewart, M.P., Cattin, C.J., Hyman, A.A., and Muller, D.J. (2015). Cdk1-dependent mitotic enrichment of cortical myosin II promotes cell rounding against confinement. Nat. Cell Biol. *17*, 148–159.

Reck-Peterson, S.L., Yildiz, A., Carter, A.P., Gennerich, A., Zhang, N., and Vale, R.D. (2006). Single-Molecule Analysis of Dynein Processivity and Stepping Behavior. Cell *126*, 335–348.

Reck-Peterson, S.L., Redwine, W.B., Vale, R.D., and Carter, A.P. (2018). The cytoplasmic dynein transport machinery and its many cargoes. Nat. Rev. Mol. Cell Biol.

Redemann, S., Pecreaux, J., Goehring, N.W., Khairy, K., Stelzer, E.H.K., Hyman, A. a, and Howard, J. (2010). Membrane invaginations reveal cortical sites that pull on mitotic spindles in one-cell *C. elegans* embryos. PLoS One *5*, e12301.

Redemann, S., Baumgart, J., Lindow, N., Shelley, M., Nazockdast, E., Kratz, A., Prohaska, S., Brugués, J., Fürthauer, S., and Müller-Reichert, T. (2017). *C. elegans* chromosomes connect to centrosomes by anchoring into the spindle network. Nat. Commun. *8*, 1–13.

Redwine, W.B., DeSantis, M.E., Hollyer, I., Htet, Z.M., Tran, P.T., Swanson, S.K., Florens, L., Washburn, M.P., and Reck-Peterson, S.L. (2017). The human cytoplasmic dynein interactome reveals novel activators of motility. Elife *6*, 1–27.

Reilein, A., and Nelson, W.J. (2005). APC is a component of an organizing template for cortical microtubule networks. Nat. Cell Biol. *7*, 436–473.

Roberts, A.J., Kon, T., Knight, P.J., Sutoh, K., and Burgess, S. a. (2013). Functions and mechanics of dynein motor proteins. Nat. Rev. Mol. Cell Biol.

Rocks, O., Peyker, A., Kahms, M., Verveer, J., Koerner, C., Lumbierres, M., Kuhlmann, J., Waldmann, H., A, W., and Bastiaens, P. (2005). An Acylation Cycle Regulates Localization and Activity of Palmitoylated Ras Isoforms. Science (80-.). *307*, 1746–1752.

Rodenburg, R.N.P., Snijder, J., Van De Waterbeemd, M., Schouten, A., Granneman, J., Heck, A.J.R., and Gros, P. (2017). Stochastic palmitoylation of accessible cysteines in membrane proteins revealed by native mass spectrometry. Nat. Commun. *8*.

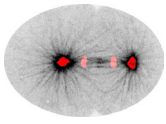

Rose, L., and Gönczy, P. (2014). Polarity establishment , asymmetric division and segregation of fate determinants in early *C. elegans*. 1–43.

Roubinet, C., and Cabernard, C. (2014). Control of asymmetric cell division. Curr. Opin. Cell Biol. *31*, 84–91.

Roubinet, C., Tsankova, A., Pham, T.T., Monnard, A., Caussinus, E., Affolter, M., and Cabernard, C. (2017). Spatio-temporally separated cortical flows and spindle geometry establish physical asymmetry in fly neural stem cells. Nat. Commun. *8*, 1383.

Rual, J.F., Ceron, J., Koreth, J., Hao, T., Nicot, A.S., Hirozane-Kishikawa, T., Vandenhaute, J., Orkin, S.H., Hill, D.E., van den Heuvel, S., et al. (2004). Toward improving Caenorhabditis elegans phenome mapping with an ORFeome-based RNAi library. Genome Res. *14*, 2162–2168.

Ruijtenberg, S., van den Heuvel, S., Heuvel, S. Van Den, and van den Heuvel, S. (2015a). G1/S Inhibitors and the SWI/SNF Complex Control Cell-Cycle Exit during Muscle Differentiation. Cell 1–14.

Ruijtenberg, S., van Rijnberk, L., Boersma, S., and van den Heuvel, S. (2015b). CRE-lox-mediated inducible expression and a split-CRE systen in *C. elegans*. In Coordination of Cell Prolifferation and Differentiation during *C. Elegans* Development, pp. 186–196.

Rusan, N.M., and Peifer, M. (2008). Original CIN: Reviewing roles for APC in chromosome instability. J. Cell Biol. *181*, 719–726.

Saadaoui, M., Machicoane, M., di Pietro, F., Etoc, F., Echard, a., and Morin, X. (2014). Dlg1 controls planar spindle orientation in the neuroepithelium through direct interaction with LGN. J. Cell Biol.

Salaun, C., Greaves, J., and Chamberlain, L.H. (2010). The intracellular dynamic of protein palmitoylation. J. Cell Biol. *191*, 1229–1238.

Schaefer, M., Shevchenko, a, and Knoblich, J. a (2000). A protein complex containing Inscuteable and the Galpha-binding protein Pins orients asymmetric cell divisions in Drosophila. Curr. Biol. *10*, 353–362.

Schaefer, M., Petronczki, M., Dorner, D., Forte, M., and Knoblich, J. a (2001). Heterotrimeric G proteins direct two modes of asymmetric cell division in the Drosophila nervous system. Cell *107*, 183–194.

Schlager, M.A., Hoang, H.T., Urnavicius, L., Bullock, S.L., and Carter, A.P. (2014). *In vitro* reconstitution of a highly processive recombinant human dynein complex. EMBO J. *33*, 1855–1868.

Schlessinger, K., McManus, E.J., and Hall, A. (2007). Cdc42 and noncanonical Wnt signal transduction pathways cooperate to promote cell polarity. J. Cell Biol. *178*, 355–361.

Schmidt, D.J., Rose, D.J., Saxton, W.M., and Strome, S. (2005). Functional analysis of cytoplasmic dynein heavy chain in Caenorhabditis elegans with fast-acting temperature-sensitive mutations. Mol. Biol. Cell *16*, 1200–1212.

Schmidt, R., Fielmich, L.E.L.-E., Grigoriev, I., Katrukha, E.A.E.A., Akhmanova, A., and van den Heuvel, S. (2017). Two populations of cytoplasmic dynein contribute to spindle positioning in *C. elegans* embryos. J. Cell Biol. *216*, 2777–2793.

Schwartz, M.L., and Jorgensen, E.M. (2016). SapTrap, a Toolkit for High-Throughput CRISPR/Cas9 Gene Modification in Caenorhabditis elegans. Genetics *202*, 1277–1288.

Ségalen, M., Johnston, C. a, Martin, C. a, Dumortier, J.G., Prehoda, K.E., David, N.B., Doe, C.Q., and Bellaïche, Y. (2010). The Fz-Dsh planar cell polarity pathway induces oriented cell division via Mud/NuMA in Drosophila and zebrafish. Dev. Cell *19*, 740–752.

Seldin, L., and Macara, I. (2017). Epithelial spindle orientation diversities and uncertainties: recent developments and lingering questions. F1000Research *6*, 984.

Seldin, L., Poulson, N.D., Foote, H.P., and Lechler, T. (2013). NuMA localization, stability, and function in spindle orientation involve 4.1 and Cdk1 interactions. Mol. Biol. Cell *24*, 3651–3662.

Seldin, L., Muroyama, A., and Lechler, T. (2016). NuMA-microtubule interactions are critical for spindle orientation and the morphogenesis of diverse epidermal structures. Elife *5*, 1–18.

Sheeman, B., Carvalho, P., Sagot, I., Geiser, J., Kho, D., Hoyt, M.A., and Pellman, D. (2003). Determinants of S. cerevisiae dynein localization and activation: Implications for the mechanism of spindle positioning. Curr. Biol. *13*, 364–372.

Shi, S.-H., Cheng, T., Jan, L.Y., and Jan, Y.-N. (2004). APC and GSK-3beta Are Involved in mPar3 Targeting to the Nascent Axon and Establishment of Neuronal Polarity. Curr. Biol. *14*, 2025–2032.

Shinar, T., Mana, M., Piano, F., and Shelley, M.J. (2011). A model of cytoplasmically driven microtubule-based motion in the single-celled Caenorhabditis elegans embryo. Proc. Natl. Acad. Sci. *108*, 10508–10513.

Siegel, G., Obernosterer, G., Fiore, R., Oehmen, M., Bicker, S., Christensen, M., Khudayberdiev, S., Leuschner, P.F., Busch, C.J.L., Kane, C., et al. (2009). A functional screen implicates microRNA-138-dependent regulation of the depalmitoylation enzyme APT1 in dendritic spine morphogenesis. Nat. Cell Biol. *11*, 705–716.

Siegrist, S.E., and Doe, C.Q. (2005). Microtubule-induced Pins/Galphai cortical polarity in Drosophila neuroblasts. Cell *123*, 1323–1335.

Siller, K.H., and Doe, C.Q. (2009). Spindle orientation during asymmetric cell division. Nat. Cell Biol. *11*, 365–374.

Siller, K.H., Cabernard, C., and Doe, C.Q. (2006). The NuMA-related Mud protein binds Pins and regulates spindle orientation in Drosophila neuroblasts. Nat. Cell Biol. *8*, 594–600.

Simone, A. De, Spahr, A., Busso, C., and Gönczy, P. (2018). Uncovering the balance of forces driving microtubule aster migration in *C. elegans* zygotes. Nat. Commun.

Slep, K.C., and Vale, R.D. (2007). Structural Basis of Microtubule Plus End Tracking by XMAP215, CLIP-170, and EB1. Mol. Cell *27*, 976–991.

Somers, W.G., and Saint, R. (2003). A RhoGEF and Rho family GTPase-activating protein complex links the contractile ring to cortical microtubules at the onset of cytokinesis. Dev. Cell *4*, 29–39.

Spiro, Z., Thyagarajan, K., De Simone, A., Trager, S., Afshar, K., Gonczy, P., Spiró, Z., Thyagarajan, K., De Simone, A., Träger, S., et al. (2014). Clathrin regulates centrosome positioning by promoting acto-myosin cortical tension in *C. elegans* embryos. Development *141*, 2712–2723.

Splinter, D., Razafsky, D.S., Schlager, M. a, Serra-Marques, A., Grigoriev, I., Demmers, J., Keijzer, N., Jiang, K., Poser, I., Hyman, A. a, et al. (2012). BICD2, dynactin, and LIS1 cooperate in regulating dynein recruitment to cellular structures. Mol. Biol. Cell *23*, 4226–4241.

Srayko, M., Kaya, A., Stamford, J., and Hyman, A.A. (2005). Identification and characterization of factors required for microtubule growth and nucleation in the early *C. elegans* embryo. Dev. Cell *9*, 223–236.

Srinivasan, D.G.D.D.G.D., Fisk, R.M.M.R., Xu, H., and van den Heuvel, S. (2003). A complex of LIN-5 and GPR proteins regulates G protein signaling and spindle function in *C. elegans*. Genes Dev. *17*, 1225–1239.

Stewart, M.P., Helenius, J., Toyoda, Y., Ramanathan, S.P., Muller, D.J., and Hyman, A.A. (2011). Hydrostatic pressure and the actomyosin cortex drive mitotic cell rounding. Nature *469*, 226–231.

Strickland, D., Lin, Y., Wagner, E., Hope, C.M., Zayner, J., Antoniou, C., Sosnick, T.R., Weiss, E.L., and Glotzer, M. (2012). TULIPs: tunable, light-controlled interacting protein tags for cell biology. Nat. Methods *9*, 379–384.

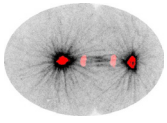

Strome, S. (1986). Fluorescence visualization of the distribution of microfilaments in gonads and early embryos of the nematode caenorhabditis elegans. J. Cell Biol. *103*, 2241–2252.

Strome, S., Powers, J., Dunn, M., Reese, K., Malone, C.J., White, J., Seydoux, G., and Saxton, W. (2001). Spindle dynamics and the role of gamma-tubulin in early Caenorhabditis elegans embryos. Mol. Biol. Cell *12*, 1751–1764.

Su, L.K., Kinzler, K.W., Vogelstein, B., Preisinger, A.C., Moser, A.R., Luongo, C., Gould, K.A., and Dove, W.F. (1992). Multiple intestinal neoplasia caused by a mutation in the murine homolog of the APC gene. Science (80-.). *256*, 668–670.

Su, L.K., Vogelstein, B., and Kinzler, K.W. (1993). Association of the APC tumor suppressor protein with catenins. Science (80-.). *262*, 1734–1737.

Sugioka, K., Mizumoto, K., and Sawa, H. (2011). Wnt regulates spindle asymmetry to generate asymmetric nuclear β-catenin in *C. elegans*. Cell *146*, 942–954.

Sugioka, K., Fielmich, L.-E., Mizumoto, K., Bowerman, B., Van Den Heuvel, S., Kimura, A., and Sawa, H. (2017). The tumor suppressor APC is an attenuator of spindle-pulling forces during *C. elegans* asymmetric cell division. PNAS 1–10.

Sulston, J.E., and Horvitz, H.R. (1981). Abnormal cell lineages in mutants of the nematode Caenorhabditis elegans. Dev. Biol. *82*, 41–55.

Sulston, J.E., Schierenberg, E., White, J.G., and Thomson, J.N. (1983). The embryonic cell lineage of the nematode Caenorhabditis elegans. Dev. Biol. *100*, 64–119.

Suzuki, K., Sako, K., Akiyama, K., Isoda, M., Senoo, C., Nakajo, N., and Sagata, N. (2015). Identification of non-Ser/Thr-Pro consensus motifs for Cdk1 and their roles in mitotic regulation of C2H2 zinc finger proteins and Ect2. Sci. Rep. *5*, 7929.

Tagawa, A., Rappleye, C. a, and Aroian, R. V (2001). pod-2, along with pod-1, defines a new class of genes required for polarity in the early Caenorhabditis elegans embryo. Dev. Biol. *233*, 412–424.

Takeshita, H., and Sawa, H. (2005). Asymmetric cortical and nuclear localizations of WRM-1/beta-catenin during asymmetric cell division in *C. elegans*. Genes Dev. *19*, 1743–1748.

Tall, G.G., and Gilman, A.G. (2005). Resistance to inhibitors of cholinesterase 8A catalyzes release of Gai-GTP and nuclear mitotic apparatus protein (NuMA) from NuMA-LGN-Gai-GDP complexes. Proc. Natl. Acad. Sci. U. S. A. *102*, 16574–16589.

Tall, G.G., Krumins, A.M., and Gilman, A.G. (2003). Mammalian Ric-8A (synembryn) is a heterotrimeric Galpha protein guanine nucleotide exchange factor. J. Biol. Chem. *278*, 8356–8362.

Tame, M.A., Raaijmakers, J.A., Van Den Broek, B., Lindqvist, A., Jalink, K., and Medema, R.H. (2014). Astral microtubules control redistribution of dynein at the cell cortex to facilitate spindle positioning. Cell Cycle *13*, 1162–1170.

Tamura, N., Simon, J.E., Nayak, A., Shenoy, R., Hiroi, N., Boilot, V., Funahashi, A., and Draviam, V.M. (2015). A proteomic study of mitotic phase-specific interactors of EB1 reveals a role for SXIP-mediated protein interactions in anaphase onset. Biol. Open *4*, 155–169.

Thomas, C.J., Tall, G.G., Adhikari, A., and Sprang, S.R. (2008). Ric-8A catalyzes guanine nucleotide exchange on G alphai1 bound to the GPR/GoLoco exchange inhibitor AGS3. J. Biol. Chem. *283*, 23150–23160.

Thyagarajan, K., Afshar, K., and Gönczy, P. (2011). Polarity mediates asymmetric trafficking of the Gbeta heterotrimeric G-protein subunit GPB-1 in *C. elegans* embryos. Development *138*, 2773–2782.

Timmons, L., and Fire, A. (1998). Specific interference by ingested dsRNA [10]. Nature *395*, 854.

Toyoshima, F., and Nishida, E. (2007). Integrin-mediated adhesion orients the spindle parallel to the substratum in an EB1- and myosin X-dependent manner. EMBO J. *26*, 1487–1498.

Tsou, M.-F.B., Hayashi, A., and Rose, L.S. (2003). LET-99 opposes Galpha/GPR signaling to generate asymmetry for spindle positioning in response to PAR and MES-1/SRC-1 signaling. Development *130*, 5717–5730.

Urnavicius, L., Lau, C.K., Elshenawy, M.M., Morales-Rios, E., Motz, C., Yildiz, A., and Carter, A.P. (2018). Cryo-EM shows how dynactin recruits two dyneins for faster movement. Nature *554*, 202–206.

Vaughan, K.T., Tynan, S.H., Faulkner, N.E., Echeverri, C.J., and Vallee, R.B. (1999). Colocalization of cytoplasmic dynein with dynactin and CLIP-170 at microtubule distal ends. J. Cell Sci. *112 (Pt 1*, 1437–1447.

Vaughan, P.S., Miura, P., Henderson, M., Byrne, B., and Vaughan, K.T. (2002). A role for regulated binding of p150(Glued) to microtubule plus ends in organelle transport. J. Cell Biol. *158*, 305–319.

Verbrugghe, K.J.C., and White, J.G. (2004). SPD-1 is required for the formation of the spindle midzone but is not essential for the completion of cytokinesis in *C. elegans* embryos. Curr. Biol. *14*, 1755–1760.

Vidal, M., Brachmann, R.K., Fattaey, A., Harlow, E., and Boeke, J.D. (1996a). Reverse two-hybrid and one-hybrid systems to detect dissociation of protein-protein and DNA-protein interactions. Proc. Natl. Acad. Sci. U. S. A. *93*, 10315–10320.

Vidal, M., Braun, P., Chen, E., Boeke, J.D., and Harlow, E. (1996b). Genetic characterization of a mammalian protein-protein interaction domain by using a yeast reverse two-hybrid system. Proc. Natl. Acad. Sci. U. S. A. *93*, 10321–10326.

Vleugel, M., Kok, M., and Dogterom, M. (2016a). Understanding force-generating microtubule systems through in vitro reconstitution. Cell Adhes. Migr. *10*, 475–494.

Vleugel, M., Roth, S., Groenendijk, C.F., and Dogterom, M. (2016b). Reconstitution of Basic Mitotic Spindles in Spherical Emulsion Droplets. JoVE e54278.

van der Voet, M., Berends, C.W.H., Perreault, A., Nguyen-Ngoc, T., Gönczy, P., Vidal, M., Boxem, M., van den Heuvel, S., Gα, L.-G.P.R., Voet, M. Van Der, et al. (2009). NuMA-related LIN-5, ASPM-1, calmodulin and dynein promote meiotic spindle rotation independently of cortical LIN-5/GPR/Galpha. Nat. Cell Biol. *11*, 269–277.

Vogel, S.K., Pavin, N., Maghelli, N., Jülicher, F., and Tolić-Nørrelykke, I.M. (2009). Self-organization of dynein motors generates meiotic nuclear oscillations. PLoS Biol. *7*, 0918–0928.

Waaijers, S., and Boxem, M. (2014). Engineering the Caenorhabditis elegans genome with CRISPR/Cas9. Methods *68*, 381–388.

Waaijers, S., Portegijs, V., Kerver, J., Lemmens, B.B.L.G., Tijsterman, M., van den Heuvel, S., and Boxem, M. (2013). CRISPR/Cas9-targeted mutagenesis in Caenorhabditis elegans. Genetics *195*, 1187–1191.

Walston, T., Tuskey, C., Edgar, L., Hawkins, N., Ellis, G., Bowerman, B., Wood, W., and Hardin, J. (2004). Multiple Wnt signaling pathways converge to orient the mitotic spindle in early *C. elegans* embryos. Dev. Cell *7*, 831–841.

Wang, H., Ng, K.H., Qian, H., Siderovski, D.P., Chia, W., and Yu, F. (2005). Ric-8 controls Drosophila neural progenitor asymmetric division by regulating heterotrimeric G proteins. Nat. Cell Biol. *7*, 1091–1098.

Wang, H., Liu, J., Yuet, K.P., Hill, A.J., and Sternberg, P.W. (2018). Split cGAL, an intersectional strategy using a split intein for refined spatiotemporal transgene control in *Caenorhabditis elegans*. Proc. Natl. Acad. Sci. 201720063.

Ward, J.D.J.D. (2014). Rapid and precise engineering of the caenorhabditis elegans genome with lethal mutation co-conversion and inactivation of NHEJ repair. Genetics *199*, 363–377.

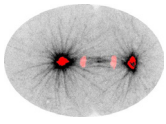

Wedegaertner, P.B., Wilson, P.T., and Bourne, H.R. (1995). Lipid modifications of trimeric G proteins. J. Biol. Chem. *270*, 503–506.

Wen, Y., Eng, C.H., Schmoranzer, J., Cabrera-Poch, N., Morris, E.J.S., Chen, M., Wallar, B.J., Alberts, A.S., and Gundersen, G.G. (2004). EB1 and APC bind to mDia to stabilize microtubules downstream of Rho and promote cell migration. Nat. Cell Biol. *6*, 820–830.

Wildwater, M., Sander, N., de Vreede, G., and van den Heuvel, S. (2011). Cell shape and Wnt signaling redundantly control the division axis of *C. elegans* epithelial stem cells. Development *138*, 4375–4385.

Williams, S.E., and Fuchs, E. (2013). Oriented divisions, fate decisions. Curr. Opin. Cell Biol. 1–10.

Williams, S.E., Beronja, S., Pasolli, H.A., and Fuchs, E. (2011). Asymmetric cell divisions promote Notch-dependent epidermal differentiation. Nature *470*, 353–358.

Williams, S.E., Ratliff, L. a, Postiglione, M.P., Knoblich, J. a, and Fuchs, E. (2014). Par3-mInsc and Gαi3 cooperate to promote oriented epidermal cell divisions through LGN. Nat. Cell Biol. *16*.

Wood, L., Parsons, D., Jones, S.J., Lin, J., Sjoblom, T., Leary, R., Shen, D., Boca, S., Barber, T.D., Ptak, J., et al. (2007). The Genomic Landscapes of Human Breast and Colorectal Cancers. Science (80-.). *318*, 1108–1113.

Woodard, G.E., Huang, N.-N., Cho, H., Miki, T., Tall, G.G., and Kehrl, J.H. (2010). Ric-8A and Gi alpha recruit LGN, NuMA, and dynein to the cell cortex to help orient the mitotic spindle. Mol. Cell. Biol. *30*, 3519–3530.

Wu, G., Huang, H., Garcia Abreu, J., and He, X. (2009). Inhibition of GSK3 phosphorylation of beta-catenin via phosphorylated PPPSPXS motifs of Wnt coreceptor LRP6. PLoS One *4*, e4926.

Wu, H.Y., Nazockdast, E., Shelley, M.J., and Needleman, D.J. (2017). Forces positioning the mitotic spindle: Theories, and now experiments. BioEssays *39*, 1–7.

Wühr, M., Tan, E.S., Parker, S.K., Detrich, H.W., and Mitchison, T.J. (2010). A model for cleavage plane determination in early amphibian and fish embryos. Curr. Biol. *20*, 2040–2045.

Wyatt, T.P.J., Harris, A.R., Lam, M., Cheng, Q., Bellis, J., Dimitracopoulos, A., Kabla, A.J., Charras, G.T., and Baum, B. (2015). Emergence of homeostatic epithelial packing and stress dissipation through divisions oriented along the long cell axis. Proc. Natl. Acad. Sci. *112*, 5726–5731.

Xia, P., Wang, Z., Liu, X., Wu, B., Wang, J., Ward, T., Zhang, L., and Ding, X. (2012). Ensures Accurate Kinetochore – Microtubule Interactions in Mitosis.

Yamashita, Y.M., Jones, D.L., and Fuller, M.T. (2003). Orientation of asymmetric stem cell division by the APC tumor suppressor and centrosome. Science (80-.). *301*, 1547–1550.

Yang, C., Wu, J., de Heus, C., Grigoriev, I., Liv, N., Yao, Y., Smal, I., Meijering, E., Klumperman, J., Qi, R.Z., et al. (2017). EB1 and EB3 regulate microtubule minus end organization and Golgi morphology. J. Cell Biol. *216*, 3179–3198.

Yoshiura, S., Ohta, N., and Matsuzaki, F. (2012). Tre1 GPCR signaling orients stem cell divisions in the Drosophila central nervous system. Dev. Cell *22*, 79–91.

Zanic, M., Widlund, P.O., Hyman, A. a, and Howard, J. (2013). Synergy between XMAP215 and EB1 increases microtubule growth rates to physiological levels. Nat. Cell Biol. *15*, 1–8.

Zeng, X., Tamai, K., Doble, B., Li, S., Huang, H., Habas, R., Okamura, H., Woodgett, J., and He, X. (2005). A dual-kinase mechanism for Wnt co-receptor phosphorylation and activation. Nature *438*, 873–877.

Zhang, D., Tu, S., Stubna, M., Wu, W., Huang, W., Weng, Z., and Lee, H. (2018). The piRNA targeting rules and the resistance to piRNA silencing in endogenous genes. Science (80-.). *592*, 587–592.

Zhang, L., Ward, J.D., Cheng, Z., and Dernburg, A.F. (2015a). The auxin-inducible degradation (AID) system enables versatile conditional protein depletion in *C. elegans*. Development *142*, 4374–4384.

Zhang, R., Alushin, G.M., Brown, A., and Nogales, E. (2015b). Mechanistic origin of microtubule dynamic instability and its modulation by EB proteins. Cell *162*, 849–859.

Zhang, X., Rico, F., Xu, A.J., and Moy, V.T. (2009). Atomic Force Microscopy of Protein--Protein Interactions. In Handbook of Single-Molecule Biophysics, P. Hinterdorfer, and A. Oijen, eds. (New York, NY: Springer US), pp. 555–570.

Zheng, Z., Zhu, H., Wan, Q., Liu, J., Xiao, Z., Siderovski, D.P., and Du, Q. (2010). LGN regulates mitotic spindle orientation during epithelial morphogenesis. J. Cell Biol. *189*, 275–288.

Zhu, J., Wen, W., Zheng, Z., Shang, Y., Wei, Z., Xiao, Z., Pan, Z., Du, Q., Wang, W., and Zhang, M. (2011). LGN/mInsc and LGN/NuMA complex structures suggest distinct functions in asymmetric cell division for the Par3/mInsc/LGN and Gαi/LGN/NuMA pathways. Mol. Cell *43*, 418–431.

Zhu, M., Settele, F., Kotak, S., Sanchez-Pulido, L., Ehret, L., Ponting, C.P., Gonczy, P., and Hoffmann, I. (2013). MISP is a novel Plk1 substrate required for proper spindle orientation and mitotic progression. J. Cell Biol. *200*, 773–787.

Zimniak, T., Stengl, K., Mechtler, K., and Westermann, S. (2009). Phosphoregulation of the budding yeast EB1 homologue Bim1p by Aurora/Ipl1p. J. Cell Biol. *186*, 379–391.

Zonies, S., Motegi, F., Hao, Y., and Seydoux, G. (2010). Symmetry breaking and polarization of the *C. elegans* zygote by the polarity protein PAR-2. Development *137*, 1669–1677.

Zumbrunn, J., Kinoshita, K., Hyman, A.A., and Näthke, I.S. (2001). Binding of the adenomatous polyposis coli protein to microtubules increases microtubule stability and is regulated by GSK3β phosphorylation. Curr. Biol. *11*, 44–49.

Zwaal, R.R., Ahringer, J., van Luenen, H.G., Rushforth, a, Anderson, P., and Plasterk, R.H. (1996). G proteins are required for spatial orientation of early cell cleavages in *C. elegans* embryos. Cell *86*, 619–629.

Nederlandse samenvatting

Cellen vormen de basiseenheid van het leven: bacteriën, schimmels, planten en dieren bestaan uit cellen. Om te leven moet een systeem onder andere in staat zijn zichzelf in stand te houden, te groeien en zich te vermenigvuldigen. Om te vermenigvuldigen deelt een moedercel zich in twee dochtercellen. Tijdens celdeling wordt het verdubbelde erfelijk materiaal (DNA) en de overige cel inhoud over de dochtercellen verdeeld. Deze inhoud kan symmetrisch of asymmetrisch (gelijk of ongelijk) verdeeld worden (zie figuur 1 in hoofdstuk 1). Symmetrische celdeling leidt tot vermenigvuldiging van het aantal cellen van hetzelfde type. Asymmetrische celdeling leidt tot diversificatie van de celpopulatie.

Dierlijke organismen groeien en ontwikkelen uit één cel: de bevruchte eicel. Om van een enkele cel naar de 30 triljoen cellen van een volwassen mens te komen, zijn in principe 50 delingen nodig. In het geval van 50 symmetrische delingen zou een lichaam bestaan uit een homogene klomp cellen. Een lichaam bestaat daarentegen uit vele honderden verschillende soorten cellen, zoals bijvoorbeeld spiercellen, botcellen, darmcellen en zenuwcellen. Deze cellen verschillen in grootte en vorm, maar ook in de eiwitten die ze bevatten. Eiwitten zijn biologische moleculen die een breed scala aan functies vervullen in de cel, onder andere chemische omzetting, transport, structuur en signalering. Tijdens asymmetrische deling kunnen eiwitten verschillend over de dochtercellen verdeeld worden. Hierdoor krijgen de dochtercellen verschillende eigenschappen. Om de toekomstige dochtercellen van elkaar te laten verschillen moet de moedercel een georganiseerde oriëntatie hebben, ofwel polariseren. Polariteit houdt in dat een kant anders is dan de andere kant. Zo kunnen cellen door precies geplaatste polariteitseiwitten niet alleen een voor- en achterkant, maar ook een links, rechts, boven en onder specificeren. De PAR-eiwitten zijn veelvoorkomende polariteitsregulatoren. In figuur 2B van hoofdstuk 1 is een voorbeeld te zien waarin PAR-eiwitten de voor- en achterkant van een cel aangeven. Door signalen van zulke polariteitseiwitten kunnen andere eiwitten asymmetrisch verdeeld worden in een cel, zodat deze na deling slechts in één dochtercel terechtkomen. Voor een juiste verdeling over de dochtercellen is naast de juiste positionering van moleculen bovendien de plaatsing van het delingsvlak van essentieel belang. Hoe het positioneren van het delingsvlak de grootte, inhoud en positie van de dochtercellen beïnvloedt, is geïllustreerd in figuur 1.

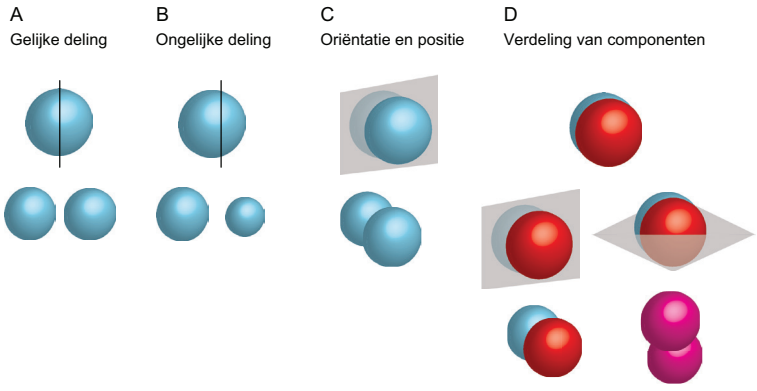

Figuur 1 Een conceptuele benadering van celdeling. Cellen zijn voorgesteld als bollen die door een delingsvlak gesplitst worden. **(A)** Een deling door het midden resulteert in twee dochtercellen van gelijke grootte. **(B)** Een delingsvlak dat afwijkt van het midden resulteert in twee dochtercellen van ongelijke grootte. **(C)** Draaiing van het delingsvlak verandert de positie van de dochtercellen. **(D)** Als componenten (rood en blauw) asymmetrisch verdeeld zijn in de moedercel, bepaalt de positie en oriëntatie van het delingsvlak of de componenten gescheiden of gelijk over de dochtercellen verdeeld worden (rood + blauw = magenta).

De plaats waar de cel in tweeën deelt wordt bepaald door de positie van een spoel, de zogenaamde mitotische spoel (Engels: *mitotic spindle*). De spoel bevat vele trekdraden, microtubuli genaamd (enkelvoud: microtubule), die uitstralen naar de rand van de cel (het celmembraan) (figuur 2). Vanaf het celmembraan wordt er getrokken aan de microtubuli. Hierdoor wordt de spoel en daarmee het delingsvlak van de cel gepositioneerd. De trekkrachten worden geleverd door krachtgeneratoren die de microtubuli verankeren aan het celmembraan. Het onderzoek in dit proefschrift is toegespitst op de vraag hoe de trekkrachten op microtubuli gereguleerd wordt om tijdens asymmetrische celdelingen de spoel en daarmee het delingsvlak correct te positioneren. Foutieve regulatie van celdeling en het positioneren van het delingsvlak kan leiden tot ontwikkelingsfouten en ziekte, zoals bijvoorbeeld kanker.

Voor ons onderzoek gebruikten wij de nematode *Caenorhabditis elegans*, een rondworm die volwassen tot 1 mm groot wordt. Het gebruik van simpele modelorganismen is buitengewoon nuttig voor biologisch onderzoek. Experimenteren met deze dieren is immers eenvoudiger, sneller, goedkoper en minder gebonden aan ethische bezwaren dan experimenteren met grote dieren of mensen. Bovendien worden basale processen als celdeling in alle dieren, van worm tot mens, vergelijkbaar gereguleerd. Daarom is een worm een representatief model om fundamentele biologische vragen te bestuderen. *C. elegans* is daarnaast het enige dier waarvan de identiteit van elke cel, inclusief het moment en de manier van delen, reeds is gekarakteriseerd. Daardoor is het een bijzonder geschikt model om de regulatie van celdeling te bestuderen. Om het positioneren van de spoel te bestuderen, gebruikten wij het vroege embryo als model. In het eencellig embryo wordt de spoel 'naar achteren' of rechts van het midden gepositioneerd (figuur 2). Dit is het resultaat van hogere trekkrachten op de spoel aan de achterkant van de cel. De spoelfiguren in een tweecellig embryo staan haaks op elkaar (figuur 2). Omdat deze posities strak gereguleerd en altijd hetzelfde zijn, kan het proces van spoel positioneren goed bestudeerd worden in vroege *C. elegans* embryos.

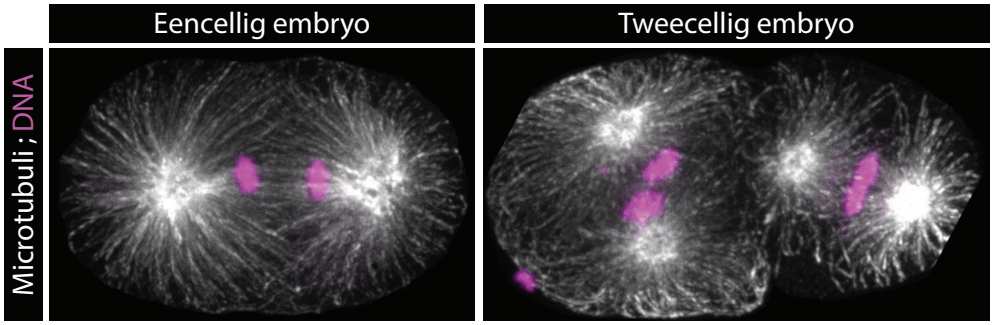

Figuur 2 Fluorescentie microscopie van vroege *Caenorhabditis elegans* embryos met in het wit de trekdraden (microtubuli) van de spoel en in magenta het DNA dat over de dochtercellen wordt verdeeld. In het eencellig embryo (linker afbelding) is de spoel naar achteren (rechts van het midden) geplaatst. Hierdoor deelt deze moedercel in een grotere voorste (linker) en kleinere achterste (rechter) cel. In het resulterende tweecellig embryo wordt de spoel in de voorste cel boven-onder opgezet, terwijl de spoel in de achterste cel voor-achter opgezet wordt. Hierdoor delen deze twee cellen beiden in een andere richting. De correcte positionering van de spoel is het resultaat van asymmetrische trekkrachten op de microtubuli van spoel.

Het positioneren van de spoel wordt uitgevoerd door de krachtgeneratoren die op hun beurt worden gecontroleerd door regulatoren die bepalen waar en wanneer de krachtgeneratoren actief zijn. Waar de generatoren actief zijn wordt gecontroleerd door de PAR-eiwitten, die het onderscheid regelen tussen de verschillen kanten van de cel. Wanneer de generatoren actief zijn wordt gecontroleerd door celdelingsregulatoren, die de voortgang door de verschillende stappen van de celdeling regelen. De krachtgenerator bestaat uit meerdere componenten. Dit zijn de eiwitten Gα, GPR-1/2, LIN-5 en dynein (zie figuur 3). Gα is verankerd in het celmembraan. GPR-1 en GPR-2 zijn twee bijna identieke eiwitten die aan Gα kunnen binden. LIN-5 verbindt GPR-1/2 met dynein, een zogeheten motor eiwit: dynein kan over de microtubuli lopen en verbindt de microtubuli met de krachtgenerator. Ondanks dat het bekend is dat regulatoren van celpolariteit en celdeling het positioneren van de spoel aansturen, is het slechts deels bekend via welke tussenliggende mechanismen en effectoren deze regulatie plaatsvindt.

Voor het onderzoek beschreven in dit proefschrift hebben wij veelvuldig gebruik gemaakt van de nieuwe CRISPR/Cas9 methode om veranderingen (mutaties) in het DNA aan te brengen. De gemaakte mutaties leidden tot het uitschakelen of veranderen van de betrokken eiwitten of delen daarvan. Door het gevolg van de mutaties te bestuderen kon de functie van het eiwit worden afgeleid. Daarnaast hebben wij eiwitten gefuseerd met fluorescente eiwitten om ze te markeren, zodat met behulp van microscopie de eiwitten in de ontwikkelende cel gevolgd en bestudeerd konden worden.

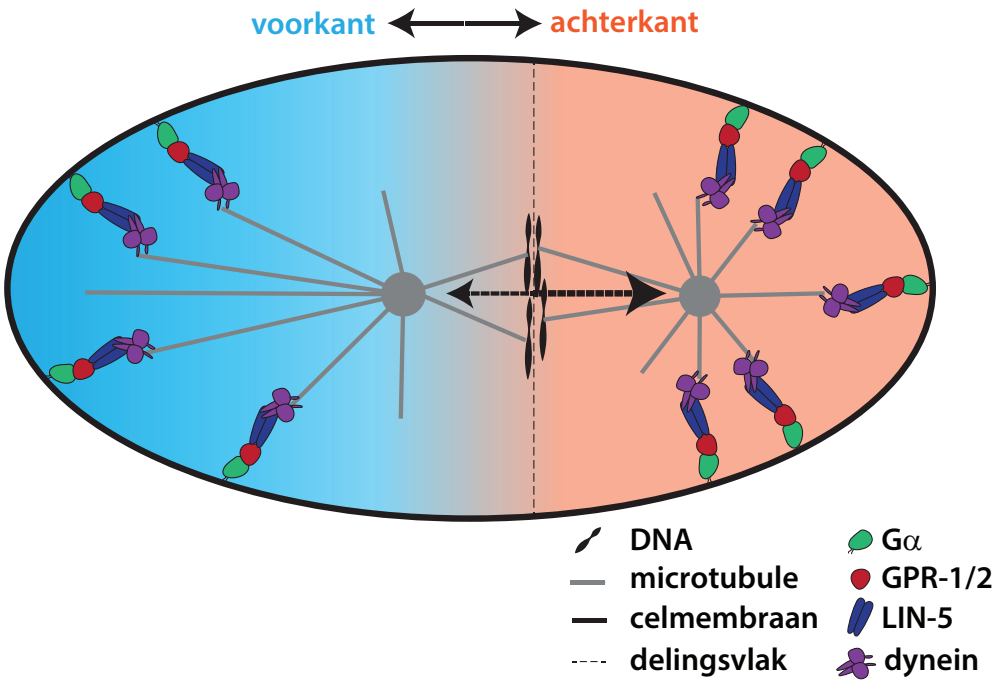

Figuur 3 Schematische weergave van spoelpositionering in het eencellig *Caenorhabditis elegans* embryo (niet op schaal). De krachtgeneratoren aan het celmembraan ankeren en trekken aan de microtubuli van de spoel. Doordat er aan de achterkant (rechts) van de cel harder wordt getrokken (dikkere zwarte pijl), wordt de spoel meer naar achteren getrokken. Hierdoor wordt het delingsvlak achter het midden opgezet.

De aanmaak en afbraak van eiwitten is een belangrijke manier om hun werking in de cel te controleren. De werking van reeds gevormde eiwitten kan gereguleerd worden door modificatie van eiwitten zoals toevoeging van kleine chemische groepen. Een veel bestudeerde modificatie van eiwitten is een fosfaatgroep, die door een kinase wordt toegevoegd. Dit proces heet fosforylering. In hoofdstuk 3 beschrijven wij dat fosforylering op 25 plekken in LIN-5 plaatsvindt. Door specifiek die plekken in LIN-5 te muteren en fosforylering te verhinderen of na te bootsen, is gevonden dat sommige van deze plekken en modificaties bijdragen aan het genereren van trekkrachten en de interacties tussen LIN-5 en GPR-1/2 of tussen LIN-5 en dynein. Voor sommige van deze modificaties is bovendien het verantwoordelijke kinase gevonden. Hieronder bevinden zich kinases waarvan al bekend was dat zij regulatoren van celpolariteit en celdeling zijn. Hierdoor draagt deze studie bij aan het begrip hoe LIN-5 reageert met bindingspartners en hoe regulatie van LIN-5 in plaats (door polariteitskinases) en tijd (door celdelingskinases) bij kan dragen aan de correcte positionering van de spoel.

Microtubuli zijn dynamische polymeren die constant groeien en afbreken aan de uiteinden. De dynamische eigenschappen van microtubuli dragen bij aan het genereren van trekkrachten op de spoel. Immers: microtubuli moeten langer worden om het membraan te bereiken en krimpen om de spoel richting het membraan te kunnen trekken. Hoe dit werkt kan als volgt worden geïllustreerd. Als een mobiel object (spoel) middels een stijve kabel (microtubule) aan een vast object (celmembraan) is gekoppeld, moet de microtubule korter worden om de spoel richting het celmembraan te trekken. In hoofdstuk 4 is beschreven hoe regulatie van de dynamiek van microtubuli kan bijdragen aan de asymmetrie in trekkrachten. Het eiwit APR-1 wordt verrijkt aan de voorkant van de cel en verhindert het krimpen van microtubuli. Hierdoor zijn de gegenereerde trekkrachten aan deze kant van de cel lager en wordt bijgedragen aan een asymmetrische trekkracht waardoor de spoel naar de achterkant van de cel verschuift. Bovendien hebben wij laten zien dat dit mechanisme parallel werkt aan fosforylering van LIN-5 die eveneens de trekkrachten aan de voorkant van de cel vermindert. De mechanismen van asymmetrische APR-1 positionering en LIN-5 fosforylering worden aangestuurd door polariteit van de PAR-eiwitten. Dit werk biedt daardoor meer mechanistisch inzicht in het instrueren van de positie van de spoel middels meerdere effectoren door PAR-polariteit.

Voor het genereren van trekkrachten op de spoel is het verankeren van de microtubuli aan het celmembraan essentieel. Hoe de krachtgeneratoren en de groeiende microtubuli elkaar binden is echter onbekend. Het groeiende einde van een microtubule, plus-eind genaamd, is omgeven door een netwerk van eiwitten die +TIPs worden genoemd (plus-tip interacting proteins). Dynein is een +TIP en komt meer voor aan het groeiende uiteinde van microtubuli. Daarom werd gedacht dat dynein bijdraagt aan het efficiënt ankeren van microtubuli aan het celmembraan: een microtubule plus-eind dat het celmembraan bereikt draagt het ankereiwit dynein al bij zich. In hoofdstuk 5 wordt deze vraag behandeld. Door met CRISPR/Cas9 de eiwitten LIN-5 en dynein te markeren met fluorescente eiwitten, konden LIN-5 en dynein in detail gevolgd worden. Zo konden twee populaties van dynein worden onderscheiden. Eén populatie is via LIN-5 gebonden aan de krachtgeneratoren. Deze populatie bleek door PAR-polariteit verschillend gereguleerd te worden in de voor- en achterkant van de cel. De andere populatie is aan het microtubule plus-eind gebonden via de *end-binding proteins* (EBPs), de centrale regulatoren van het +TIP netwerk. Om de functie van dynein aan het plus-eind te bestuderen, werden mutanten van de EBPs gemaakt. In deze wormen is dynein nog wel aanwezig, maar is de +TIP functie verloren. Dit bleek geen gevolgen te hebben voor het genereren van trekkrachten op de spoel. Echter, als de functie van dynein verminderd werd, leidde het verstoren van de +TIP dynein populatie wel tot vermindering van trekkrachten. De plus-eind bindende dynein populatie vormt dus een buffer die variaties in de cel op kan vangen. Dit soort vangnetten komt veel voor in biologische systemen en helpt processen robuust te maken tegen schommelingen in activiteit.

Als dynein de microtubule-binder is die microtubuli kan verankeren, waarom is dynein dan middels drie andere eiwitten (Gα, GPR-1/2 en LIN-5) aan het celmembraan gekoppeld? Dit lijkt onnodig omslachtig, tenzij de drie eiwitten individuele functies hebben. Een klassieke methode om de functie van een eiwit te bestuderen, is om het eiwit te verwijderen en het effect hiervan te analyseren. Omdat Gα, GPR-1/2 en LIN-5 een onderdeel zijn van de anker structuur van de krachtgenerator, kunnen individuele functies niet bestudeerd worden door het eiwit te verwijderen. Het verwijderen van een van hen resulteert in verlies van het anker en totaal functieverlies van de krachtgenerator. Dankzij een nieuwe techniek hebben wij de individuele bijdrage van Gα, GPR-1/2 en LIN-5 aan trekkrachten op de spoel kunnen testen (zie hoofdstuk 6). Deze nieuwe techniek heet TULIP (tunable light-inducible protein-protein interactions) en maakt gebruik van de licht-induceerbare interactie tussen twee eiwitten, te weten ePDZ en LOV. In afwezigheid van blauw licht zijn ePDZ en LOV ongebonden en bewegen los van elkaar. Onder invloed van blauw licht binden ePDZ en LOV elkaar (figuur 4). Wij hebben deze methode gebruikt om te controleren waar en wanneer de componenten van de krachtgenerator lokaliseren. Door LOV te verankeren aan het celmembraan en ePDZ te fuseren met GPR-1, LIN-5 of dynein konden wij met blauw licht controleren waar en wanneer deze eiwitten aan het celmembraan verankerd worden. Als bijvoorbeeld GPR-1, door schijnen met blauw licht, aan het membraan werd verankerd, lokaliseerde dit ook LIN-5 en dynein. Zo werd een krachtgenerator zonder Gα gebouwd en kon de functie van Gα in de krachtgenerator bestudeerd worden. Zodoende hebben wij ontdekt dat Gα en GPR-1/2 niet nodig zijn voor het genereren van trekkrachten: een krachtgenerator die slechts uit LIN-5 en dynein bestaat is nog steeds functioneel. Onder deze omstandigheden was echter de gebruikelijke verdeling van trekkrachten verloren. Dit geeft aan dat deze verdeling van trekkrachten (gedeeltelijk) via Gα en GPR-1/2 gereguleerd wordt. Verder vonden wij dat enkel dynein geen krachten kan genereren. Het anker van aanvullende eiwitten is dus niet overbodig, maar nodig voor de functie van dynein. Behalve als bindingsplaats dient LIN-5 ook als activator van de dynein-afhankelijke trekkrachten op de spoel. Om te bevestigen dat LIN-5 een belangrijke activator van trekkrachten op de spoel is, hebben wij verder laten zien dat middels zeer gerichte lokalisatie van LIN-5 (door gebundeld licht) de positie van de spoel en het delingsvlak van de cel beïnvloed konden worden.

Het membraancomplex Gα, GPR-1/2, LIN-5 en dynein dat trekkrachten genereert op de microtubuli van de spoel is sterk geconserveerd in de evolutie: in elke cel van elk dier wordt de spoel door deze of nauw verwante eiwitten gepositioneerd. Om de spoel correct te positioneren in de verschillende celtypen moet het systeem adaptief kunnen zijn. Altijd dezelfde positie van spoel en delingsvlak kan immers leiden tot een klomp identieke cellen en niet tot de diversiteit in celtypen die nodig is voor een compleet lichaam. Doordat de krachtgenerator uit meerdere componenten bestaat, wordt de mogelijkheid tot regulatie vergroot. Voor Gα, GPR-1/2, LIN-5 en dynein zijn dan ook verschillende regulatiemechanismen beschreven. Voorbeelden hiervan zijn de fosforylering van LIN-5 en de normale verdeling van trekkrachten die afhankelijk is van het Gα anker. Het werk in dit proefschrift verdiept hiermee het begrip van spoelpositionering in dierencellen.

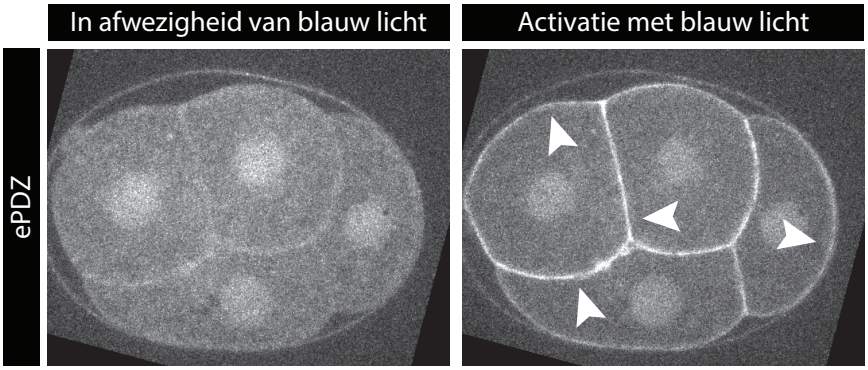

Figuur 4 Gecontroleerde lokalisatie van eiwitten met behulp van blauw licht in het viercellig *Caenorhabditis elegans* embryo. In deze cellen zijn LOV eiwitten aan het celmembraan verankerd (niet zichtbaar). Zichtbaar zijn ePDZ eiwitten gefuseerd met een fluorescent eiwit (grijs). In afwezigheid van blauw licht (linker afbeelding) interacteren LOV en ePDZ niet met elkaar en is ePDZ vrij in de cellen verdeeld. Na activatie met blauw licht binden LOV en ePDZ aan elkaar waardoor ePDZ naar de LOV eiwitten aan het celmembraan van de vier cellen positioneert (rechter afbeelding, pijlpunten).

Curriculum Vitae

Lars-Eric Fielmich is op 19 januari 1987 geboren te Nieuwegein. Hij behaalde in 2006 zijn gymnasiumdiploma aan het Christelijk Gymnasium te Utrecht. Hierna studeerde hij Biomedische Wetenschappen aan de Universiteit Utrecht van 2006 tot en met 2010. Tijdens zijn bacheloropleiding volgde hij een half jaar vakken aan de Universiteit van Tromsø in Noorwegen en een minor Klassieke Cultuur aan de Universiteit van Amsterdam. Ter afronding van zijn bachelor schreef Lars-Eric de scriptie getiteld *'The cell of origin in hepatocellular carcinoma'* onder begeleiding van prof. dr. Alain de Bruin van het departement pathobiologie, faculteit diergeneeskunde, Universiteit Utrecht. Hij vervolgde zijn studie met de master Cancer Genomics and Developmental Biologie aan de Universiteit Utrecht van 2010 tot en met 2012. Onderdeel van deze master waren twee stages. Voor de hoofdstage getiteld *'Molecular mechanisms of angiogenesis and lymphangiogenesis in Zebrafish'* werkte hij een jaar in de groep van prof. dr. Stefan Schulte-Merker in het Hubrecht Instituut in Utrecht, onder begeleiding van dr. Andreas van Impel. Voor de tweede stage ging hij naar Nice en werkte zeven maanden in de groep van dr. Pierre Léopold in het Institute of Biology Valrose, Frankrijk, onder begeleiding van dr. Rénald Delanoue. Het eindverslag was getiteld *'Uncovering the molecular coupling between nutritious state and systemic growth control in Drosophila'*. Ter afronding van de master schreef Lars-Eric een scriptie getiteld *'Non-canonical G-protein signaling in the regulation of asymmetric cell division'* onder begeleiding van prof. dr. Sander van den Heuvel van het Institute of Biodynamics and Biocomplexity en de divisie ontwikkelingsbiologie, departement biologie, faculteit bètawetenschappen van de Universiteit Utrecht. Voor zijn master ontving Lars-Eric het predicaat *cum laude*. In december 2012 begon Lars-Eric als promovendus in de groep van prof. dr. Sander van den Heuvel. Hier bestudeerde hij de regulatie van mitotische spoel positionering in het vroege *C. elegans* embryo met gebruik van moderne methoden in de genetica en microscopie. De resultaten van dit werk zijn gebundeld in het proefschrift *'Pulling apart mitotic spindle positioning in the C. elegans early embryo'* dat op 12 september 2018 verdedigd wordt. Daarnaast is zijn werk gepresenteerd op verschillende nationale en internationale congressen en gepubliceerd in gerenommeerde tijdschriften. Verschillende microscopische opnamen die Lars-Eric voor zijn promotieonderzoek maakte hebben prijzen gewonnen in microscopiewedstrijden. Na zijn promotieonderzoek hervat Lars-Eric zijn werk als postdoctoraal onderzoeker in de groep van dr. Hyun Youk in het Kavli Institute of Bionanoscience aan de TU Delft. Hier zal hij mechanismen van communicatie en besluitvorming in cellen gaan bestuderen in embryonale muizenstamcellen.

List of Publications

L-E Fielmich & S van den Heuvel. 2015 *Cell Polarity: Role in Development and Disease*. K Ebnet. (ed.). 1 ed. Switzerland: Springer International Publishing, Vol. 2, p. 119-141 22p

V Portegijs, **L-E Fielmich***, M Galli*, R Schmidt, J Muñoz, T van Mourik, A Akhmanova, A Heck, M Boxem, S van den Heuvel. 2016 *Multisite Phosphorylation of NuMA-Related LIN-5 Controls Mitotic Spindle Positioning in C. elegans*. PLoS Genetetics 2016 Oct 6;12(10):e1006291. DOI: 10.1371/journal.pgen.1006291

R Schmidt, **L-E Fielmich**, I Grigoriev, E Katrukha, A Akhmanova, S van den Heuvel. 2017, *Two populations of cytoplasmic dynein contribute to spindle positioning in C. elegans embryos*, Journal of Cell Biology Sep 2017, 216 (9) 2777-2793; DOI: 10.1083/jcb.201607038

K Sugioka, **L-E Fielmich**, K Mizumoto, B Bowerman, S van den Heuvel, A Kimura, H Sawa. *Tumor suppressor APC negatively regulates spindle-pulling forces at the cell cortex during C. elegans asymmetric cell division*, Proceedings of the National Academy of Sciences Jan 2018, 115 (5) E954-E963; DOI: 10.1073/pnas.1712052115

L-E Fielmich*, R. Schmidt*, D.J. Dickinson, B. Goldstein, A.A. Akhmanova, S. van den Heuvel. *Optogenetic reconstruction of mitotic spindle positioning in vivo*. Manuscript under revision.

* equal contribution

Acknowledgements/Dankwoord

Now that I have finished this PhD thesis, looking at the final manuscript and thinking about the past five years fills me with satisfaction. Although only my name is printed on the cover, many more people have been involved in this thesis, either directly or indirectly. I hope that I have already expressed my gratitude to all who deserve it, but I wish to explicitly acknowledge some people for their help and support.

First and foremost, my thanks go out to my promotor Sander van den Heuvel. Sander, I can say that we have always had a pleasant connection. From the moment we first met during the Developmental Genetics master course, we got along very well. Nevertheless, I was surprised when you asked me to apply for a position in your lab (exactly six years ago). Maybe this was because I had just decided not to stay in Nice for my PhD and was not yet thinking about my next move. However, some night's sleep and a visit to the Kruyt building made the decision easy: a genetic model to study developmental biology, advanced microscopy, and a pleasant environment… all my wishes were granted in the position you offered! Apart from typical struggles I share with every PhD student I ever spoke to, I have had a very good experience in your lab and there has not been a single day that I was reluctant to go to the Uithof. Your supervision has been paramount for this. I enjoyed your everlasting enthusiasm for science, which was hugely contagious and inspiring to me. Whether we were designing experiments, discussing results, papers or any other event/development: I think I always left your office more enthusiastic than I had entered it. Except for when you killed an idea I proposed, after which I often realized you were probably right. After all, I have always found you open for ideas, new approaches, and not restricted by boundaries when it comes to designing projects and involving people. Finally, I think that you applied the right pressure to steer my attitude and make me realize that I do not work for your but my own career. This also entails your focus on focus. Sander, many thanks for your essential contribution to my early development as a scientist!

When I joined the lab, many of my colleagues were surprised by my lack of certain specific skills: this new guy did two internships with developmental genetics yet does not know how to clone!? Luckily for me there was Vincent. Vincent, for many years you have been the corner stone of the lab. You managed the lab with great care and many benefited from this. I am grateful that you have introduced me to molecular cloning and *C. elegans* work and were always available for help. I cannot thank you enough for this. I hope that I have adopted your precision in experimental work and can thank you by being a worthy offspring of your training. Gladly, I was able to help you in return and could contribute to the LIN-5 phosphorylation work (Chapter 3). Finally, I enjoyed your personality as a close colleague, especially your sense of humor which is characteristic of you but difficult to typify ;)

This humor was shared and often initiated by other colleagues like Ruben and Thijs. Ruben, I greatly valued you as fellow embryo researcher (aka 'the cool people'). I initially feared that our research interests would interfere, but I am happy that this was not the case. Instead, I found our relationship stimulating and motivating, and I am proud that I could be part of the dynein work (Chapter 5). As last of the early embryo people, I count myself very lucky to have had you next to me. Even though we were the smallest subgroup in the lab and had only one cell to talk about, our meetings lasted the longest. This is the result of a positive and constructive atmosphere. And instead of colliding, our work ultimately joined in the TULIP project which turned out more successfully than I had expected for a long time. You and I have very complementary skills that perfectly came together in this project. Ruben, many thanks for all this!

I have also had the pleasure to collaborate internationally and experience the global nature of the scientific endeavor. Kenji, Hitoshi and Bruce from the NIG/RIKEN in Japan and the University of Oregon in the US, thank you for involving us in the APR-1 project (Chapter 4). It was an exciting and valuable experience for me to work together with you, spanning almost all time zones. I also sought international collaboration myself, in the search for weapons to combat my ruthless nemesis called 'germline silencing'. Luckily for me, there were people out there that had managed to harness germline silencing. Christian Frokjaer-Jensen and Andrew Fire from Stanford University, Daniel Dickinson and Bob Goldstein from UNC Chapel Hill, and Heng-Chi Lee from the University of Chicago, thank you so much for sharing your reagents and unpublished data with us. Without this, our work described in chapter 6 would never have been possible. This was a great experience of an ideal open academic community that promotes scientific progress. Dan and Bob, I am honored that our contacts resulted in a true collaboration (chapter 6).

All members of the Developmental Biology division, past and present, thank you for creating such a nice working environment. Our work is exciting and cutting edge; this is the result of continuous hard work by our group of driven people. I enjoyed riding the CRISPR/Cas9 wave that revolutionized experimental biology and put our labs in the spotlight as we were one of the first to successfully apply this technique in the worm. Selma and Mike, I have always been impressed by how much and hard you worked to get the TALENS and CRISPR going. I had just joined the lab and felt excited by witnessing the leading edge of science in action, but I was also intimidated by the competition you had to face. Selma, when I was just starting my PhD, you were finishing yours. Despite this difference, I think we connected well. Mike, you made a huge transition in the time I did my PhD, you gave up your lab bench, to which you seemed very much attached. I always enjoyed the rare occasions on which you came to the lab to do experiments. Also, thank you for being such a positive contributor to almost anything that happens in our labs, for me personally my talks, postdoc application etc. I like the clarity with which you communicate science (written and spoken) and I hope that I adopted some of that. Adri, I have always appreciated your position as being informed and involved yet somewhat independent. Not only for talks and written work, but also for personal conversations (serious or just a chitchat), thanks for all this! Inge, you were always positive, enthusiastic, friendly, and interested both for science and for my personal life. It's nice to have such people around and I am glad to have had you as a colleague. And if I say enthusiasm or being interested, I immediately think of Martin! Your glass is always half full, such a source of positivity. I know no one else who thinks in solutions rather than problems like you do. Thank you so much for all your genuine positive energy and willingness to help with anything. You are always involved in everything and manage to contribute in a positive and meaningful manner to any talk, project, or idea. That is admirable, and I thank you for your support and ideas! I hope that academia will manage to retain you.

Joao, you continued the CRISPR wave in our lab with your characteristic passion and enthusiasm, which was sometimes close to fanatism, but which I admired. Thanks for all your positive contributions in and around the lab and of course the pizza meetings! I'll miss the nonchalance with which you can say that you screened a few (weekend) nights in a row, your eyes barely open. When I speak of hard workers, there are two previous lab members that come to mind. When I was still learning to clone and was trying to find my rhythm in the lab, Thijs was cloning dozens of constructs simultaneously and Suzan was counting cells behind the microscope before the sun rose. Thijs, the way you supervised students set an example to me. Suzan, you have been a great example to me, both personally and professionally. Thank you for your sincere involvement and care. I was excited to experience the development of your project first hand and learned a bit from the entire publication and PhD thesis process. Speaking of spending crazy hours behind a microscope, albeit late at night rather than early in the morning: Suzanne. In my humble opinion,

that machine and room should be named after you. You have shown great perseverance and commitment to your project, which I respect. Also, we were often in the same stage of our PhD and I found it pleasant to be able to share such issues with you: talk in LA, writing thesis etc. Thank you for all this. I'll miss the smileys you used to mark your boxes, they made my days a little better. :)

Jana, you are the microbe and cloning expert in the lab. Thank you for helping me optimize my transformations and spoil those fragile ccdB resistant cells to make them incorporate those insanely large SEC vectors which I had been trying to clone for a long time. And thank you for all our nice conversations about our families, gardens, skiing and many more. Helena, I think we share similar visions for science and life. Therefore, our many long conversations have helped me a lot to shape my ideas, balance my work, and determine my position. Combined with your openness and friendliness, your person is a great contribution to our lab. Thanks a lot, and big hug for that! Juliane, you do your thing with flair and character and I appreciate that. In addition to managing the lab, you have a good radar for 'the things that happen'. I thank you for keeping an eye on me! Aniek, I liked it when you moved lab benches close to mine. I've enjoyed our talks about anything (often cats and fishes :)) and your down to earth take on matters. Also, I have always been fascinated by the way your story evolved, from a 'failure to replicate' to a complete story that offers mechanistic insights. It was great to witness how you made this happen.

Molly! I tried so many times, but I never managed to scare you. But then, you are not easily impressed. You weren't even annoyed when I played loud music in the lab at night. Besides thanks for tolerating my music, also thanks for your cheerful company, your willingness to have lunch outside when it is just under 20C, and of course introducing Quint and me to bouldering. I also liked to witness your start as postdoc and applying for grants, as I knew I would soon find myself in a similar position. I hope I learned from your driven and seemingly stress-less attitude. Amir, you said you would read my entire thesis. In case you made it this far: thanks for your input and contribution to the embryo work during your master. Also to the other 'new' additions to the groups: Janine, Victoria, Amalia, Sanne, and Ben: your addition brought a lot of activity to the lab, which I really enjoyed. Also, your social activities make the lab feel more like a family. I wish you everything I had for your time in the Kruyt building. As last but not the least of Dev Bio, some words for our princess Amalia. To me you brought liveliness with Greek passion to the office. Witnessing how you experienced moving to Holland and staring as a PhD was insightful to me and I hope that I helped a bit to smoothen the process. I also wish you joy and success with the secret tasks you took over from me…

In addition to learning many things, I have also had the pleasure to teach and supervise. Yeszamin and Simon, both of you worked with me on the TULIP project for a year. I lured you in with great promises about exciting experiments involving light-inducible spindle movements. Unfortunately, this only happened years after you two had left the lab. You thereby experienced the unpredictable nature of scientific projects first hand. I am proud of how you managed to each give a personal twist to your projects but also cope with the seemingly endless row of setbacks and failed experiments you had to endure. I am also glad that I could help both of you finding your way to a fitting career path after you left my formal supervision. Yeszamin, you were a very precise and reliable worker. Your personality was also a great addition to the lab. You rose above the student level and truly mixed with the lab members. Simon, your enthusiasm and excitement was energizing to me. You could sometimes loose yourself completely in a search to optimize a protocol or find out new ways to perform an experiment. I hope you'll never lose that. Finally, I would like to thank both of you not only for your direct contributions but also for what you taught me about myself. Supervising you was sometimes like looking into a mirror and has made me a more complete researcher, thanks for that!

I have also enjoyed the interaction with our neighboring division of cell biology, both professionally and personally. Anna, thank you for your honest input and direct contribution to my work (Chapters 5 and 6). I value your opinion and am impressed by your focus and vision for science. Ilya and Eugene: many many many thanks for the way you manage the BioImaging powerhouse. I honestly believe that all the microscopes combined had less down time than the coffee machine on its own, which is a huge compliment to you guys. Your training, help, and aftercare with imaging and analysis is the best I ever experienced. Lukas, I enjoyed the impressive growth and development of your lab. Microscopy rocks and you are among its rock stars. Thank you for your investment in inducible heterodimerization assays to which I devoted my main project (chapter 6). And many thanks for your spirit that energizes the 5th floor of the Kruyt building. Petra, Martin, and Max: thank you for developing and implementing the ePDZ-LOV2 system to be presented to us as a plug-and-play method (apart from hurdles specific to our system). Amelie, Amol, Ankit, Bas, Ben, Catia, Chao, Corette, Dieudonnee, Esther, Fons, Harold, Helma, Ivar, Joanna, Kay, Mariella, Marleen, Maud, Max, Mithila, Paul, Riccardo, Roderick, Sam, Wilco and York: thank you for a fun time and our many chats in which we shared our concerns and joys, personally and profesionally! I hope to continue hearing about your endeavors. Including all others: thanks for a great time. Our science, retreats, and parties are outstanding!

My thanks also go out to colleagues outside the concrete tower of the Kruyt building: the local worm community (organized by Sasha - many thanks!!!), and all of you whom I met through the CSnD and GSLS communities. To the members of my PhD supervisory committee, Anna Akhmanova and Rik Korswagen, thank you for your involvement and input. For the members of the reading committee for assessment of my PhD thesis, Bruce Bowerman, Matilde Galli, Geert Kops, Susanne Lens, and Rene Medema, thank you for your time and effort.

I would probably not have started a PhD without the stimulating experiences I had during my internships. As part of my master, I studied the development of the circulatory system in the zebra fish *Danio rerio*. This work was done in the group of Stefan Schulte-Merker under the supervision of Andreas van Impel. The Hubrecht Institute and academic world impressed and motivated me. As probably every student, I had the feeling that my results were going to change the world. Andreas, I was impressed with your work, which to me set a norm I could not meet. Luckily, you didn't make me feel like I had to meet that norm; instead, you have given me a solid basis as experimentalist and a confident start as young scientist. I always enjoyed fishing in the aquarium and still believe that the embryonic zebrafish vasculature is among the prettiest biological structures. Thanks for your supervision and patience.

I continued my master in the lab of Pierre Leopold under the supervision of Renald Delanoue at the Institute of Biology Valrose in Nice. There I studied how growth is coupled to the nutritious state in the fruit fly *Drosophila melanogaster*. Renald, my interests for genetics will always be linked to the phenotyping mapping you made me do. And I still enjoy showing pictures of the *Drosophila* larval brain to people (not because it's so pretty, but because it looks like a penis and two testicles). Outside the lab, I enjoyed the Cote d'Azur, where I made international friends for life but was also visited by numerous people from The Netherlands. I've always taken this as a huge compliment and was touched with your concerns about my considerations about staying in Nice to do a PhD.

So far, these acknowledgements have focused on my colleagues, who shaped my academic environment. However, as we are recurrently reminded by topics such as 'valorization' and 'societal impact', scientists are a part of society and must justify their work. Moreover, society has recently started to influence the research agenda. Likewise, I have experienced many interactions between my academic and social life and received signals and input from both sides. And although I have spent the majority of my time in the lab, the most important part of my life takes

place outside the lab. As the result of this paradox, my friends and family have received significantly less time and attention than they deserve. I hope that this thesis justifies the time I spent away from you. Finishing a PhD feels like a Tour de France: a long-term criterion that includes sprints, ascends, and descends in every *etappe*. A successful completion requires the strength of a horse, skin of an elephant, and work ethic of a honey bee (Fraser Stoddart, 2016 Nobel laureate in chemistry). To develop and maintain these traits, both professional and social support are essential. The remaining part of these acknowledgements will be continued in Dutch and deliberate on the social support I received from my dear family and friends.

Lieve Pep en Mem, op elk belangrijk moment in mijn leven heb ik jullie liefhebbende zorg en betrokkenheid gevoeld. Dit was tijdens mijn promotie niet anders: nog steeds voelde ik mij geholpen en ondersteund, ondanks jullie eigen zorgen. Irmhild, jij was samen met Pep en Mem deel van de hoogte- en dieptepunten: etentjes om mijn aanstelling en eerste salaris te vieren, verhalen over maanden zonder resultaten, mooie uitjes en praatjes op congressen, de zoektocht naar een volgende baan, en het recente positieve nieuws over de beoordeling van ons paper. Ik ben blij dat ik jullie met Anneke en Quint heb kunnen meenemen naar het lab, om mijn wereld daar en enthousiasme voor de wormen en microscopen te kunnen delen. Het is een kers op de taart dat ik jullie alweer voor de derde keer uit mag nodigen in het Academiegebouw om een mooi moment met mij te delen. Mem, alle verhalen over wetenschap en de Senaatszaal van vroeger maken dit moment zeker extra bijzonder! Lieve Pau, mijn promotie is weer een mijlpaal die we samen mee mogen maken. Het is mij dierbaar dat je hier nog bij bent, je bent absoluut een van de eregasten!

De laatste jaren is er een grote groep mensen bijgekomen die ik familie mag noemen: familie Sanders, bedankt voor jullie warm onthaal. Ik waardeer jullie enthousiasme en medeleven voor mijn werk en begrip als ik eens een samenkomen moest missen om op het lab met wormen te spelen. Gelukkig hebben jullie Karin als andere PhD'er in jullie directe omgeving, waardoor ik niet de enige gekke hobbyist ben die te veel tijd spendeert aan ogenschijnlijk onbeduidende experimenten. Karin, ik vind het leuk en fijn dit met jou te kunnen delen.

Dan mijn vrienden, met in de kern de mannen van jaarclub Polaris. Wie had dat gedacht: van zeer regelmatig samenkomen om te ouwehoeren en de mooiste feestjes te pakken, tot sporadisch een keertje clubeten en dan ook nog te laat aan komen kakken. Ondanks dat onze individuele paden en passies uiteen kunnen lopen, hebben wij dankzij een prachtig intensieve studententijd nog altijd voldoende basis en samenhang om van een groep te kunnen spreken. Zowel als groep als individu waren jullie een belangrijk klankbord en bron van ontspanning voor mij. Bedankt voor jullie begrip en steun, zowel voor persoonlijke als werk gerelateerde onderwerpen, en vooral bedankt voor alle keren dat het niet over serieuze zaken ging: even alles loslaten, genieten van het hier en nu. Ik hoop dit nog veel met jullie te mogen doen.

Robin en Martin, bedankt dat jullie als mijn paranimfen naast mij komen staan. Dankzij jullie niet-aflatende enthousiasme en positivisme zijn de afgelopen jaren soepeler verlopen en zal 12 september een mooie dag worden!

Dan mijn allerliefste Anneke, Quint en Louise. Ik schrijf dit stukje met tranen in mijn ogen en hoop dat dit tranen van geluk zijn. Jullie hebben mij nog veel meer gevormd dan de wormen en de wetenschap hebben kunnen doen: van een zoekende jongeman in een studentenkamer in Utrecht tot een trotse, gelukkige echtgenoot en vader in een hoekhuis met tuin in Houten. Bovenop mijn academische titels zijn de titels 'man' en '(bonus)vader' absoluut diegene die ik het hoogst houd en naar eer en geweten in wil vullen. Anneke en Quint, van jullie heb ik de meest onvoorwaardelijke steun gekregen: altijd positief, stimulerend en opbouwend. Nooit een klacht over mijn afwezigheid, vermoeidheid of stress. Dit heb ik altijd erg bijzonder gevonden en

ik vraag mij nog altijd af waar ik dat aan verdiend heb. Als wrange beloning voor die oneindige steun hebben jullie het meest ingeleverd voor mijn promotie. Het heeft mij laten zien hoe een gezin niet een groep individuen maar een geheel moet zijn. Ik hoop dat ik jullie steun terug kan betalen door te zeggen dat jullie altijd mijn eerste prioriteit en overweging waren en zullen zijn. Lieve Quint, jouw ongecompliceerde plezier en kijk op de wereld was de beste remedie tegen een hoofd vol mislukte experimenten. Als ik thuiskwam en begroet werd door een enthousiaste Quint “goed nieuws Lars, mijn Pokémon is geëvolueerd!”, of jou een (bijna)scoop uitlegde en jij reageerde met “dan weet je de volgende keer dat je op moet schieten” werd ik zo effectief de mooie, echte wereld ingetrokken dat ik alle sores van het promoveren meteen vergat. Lief meisje, jij hebt mij zo veel meer gegeven dan ik ooit had verwacht van iemand te zullen krijgen. Altijd heb jij oog voor het grotere plaatje en weet je me de juiste steun, liefde en zorg te geven. Jij hebt een essentiële bijdrage geleverd aan mijn geluk en gezondheid, en bent daardoor een van de pijlers waar dit proefschrift en ik op steunen. Opdat wij elkaar mogen blijven steunen, sturen en liefhebben. Lieve kleine Louise, zo’n bron van vreugde en geluk. Je kwam op het juiste moment: met het afronden van dit proefschrift en op tijd om het gat tussen twee banen te vullen met luiers en lachjes. Ik hoop dat dit betekent dat je beter met planning en deadlines om kunt gaan dan je vader :)

In conclusion, I consider myself a very fortunate and rich man, thanks to you! Enough words about the past, on to a bright future!

Cheers,
Lars